

Heat Management for Process Intensification of Fast Exothermic Reactions in Microstructured Reactors

THÈSE N° 5887 (2013)

PRÉSENTÉE LE 27 SEPTEMBRE 2013

À LA FACULTÉ DES SCIENCES DE BASE

LABORATOIRE DE GÉNIE DE LA RÉACTION CHIMIQUE

PROGRAMME DOCTORAL EN CHIMIE ET GÉNIE CHIMIQUE

ÉCOLE POLYTECHNIQUE FÉDÉRALE DE LAUSANNE

POUR L'OBTENTION DU GRADE DE DOCTEUR ÈS SCIENCES

PAR

Julien HABER

acceptée sur proposition du jury:

Prof. C. Pulgarin, président du jury

Prof. L. Kiwi, directrice de thèse

Prof. V. Hessel, rapporteur

Dr P. Löb, rapporteur

Dr T. Maeder, rapporteur



ÉCOLE POLYTECHNIQUE
FÉDÉRALE DE LAUSANNE

Suisse
2013

Don't be humble. You're not that great.

Golda Meir

ACKNOWLEDGEMENTS

First of all, I thank Prof. Lioubov Kiwi-Minsker for having agreed to take me as a PhD student in her group. From the professional point of view, these past 3.5 years at GGRC have been a very enriching experience, where I learnt research, being critical, structuring, presentation and many other things within a dynamic and yet pleasant working environment. Last but not least, accepting me in her group in Lausanne also meant a lot of snowboarding in the mountains, boat trips on the lake and fishing in the Swiss rivers, which I am also very thankful for.

I thank Prof. Albert Renken as my unofficial co-supervisor for his continuous advices, ideas and comments all over the time. I always left his office a little wiser than when entering, and generally enjoyed our on and especially off topic discussions.

I thank Madhav, with whom I shared the office during the first 2.5 years, for showing me which metro to take to get home from work after my first day of PhD in Lausanne. Without him I would still be sleeping in the office. I am also thankful for the PhD supervision he took care of after that day.

The last year I worked together with Artur in the office. I want to thank him for his numerous Russian lessons, friendship, and for the day he came to the office with a purple T-shirt (and everything that happened afterwards).

But, I am also very grateful to all of my colleagues at GGRC, who made these 3.5 years a precious and memorable time:

Guillaume Gossip with whom I am trying to become Hulk, Charline Praline who baked cakes without expecting something in return (why would someone do that?), Daniel Samuel with his fascination for Game of Thrones (why?), Mica the “Zen” in the group, Fernando Lorenzo who watches the offices at

night to prevent burglary, Anne-Laure with her 5 iphones and 1 ipad, Igor and Tatiana with their optimized communication.

Furthermore, I thank my two remarkable master students for their valuable participation in this thesis: Charles who danced his way through the master and concluded it with Tecktonic, and Abhishek, the golden Indian who does not need to train to achieve a marathon.

I thank Bo for a great collaboration. I think we helped out each other much more than what was written in the contract. I doubt that I will see many more of this type of collaborations.

I thank some people that make a difference compared to many other universities and departments, namely our crew from the mechanical workshop and from the electrical work shop. I want to specially thank the following people: André, Roger, Gilles, Vladan (“Mr. pompe”), Supardi, Grégoire.

The people from “magasin” who welcome us every day with sweets & chocolates, and therefore, made me buy much more than I needed. Thanks you Jacques and Marie.

I am thankful to all our secretaries that were willing to help us in any administration matter: Maria Szuman, Madeleine Steffen, Nadia Rossi, Rachel Bordelais (Francine).

I thank PAP and Eddy for all the good time that I spent seeing them on the corridor or at “apéros”.

I am grateful to my parents for supporting me during the past 28 years and raising me to this point. Good news: I am not a student anymore after 28 years.

Finally I thank the person who so much wanted to stand on the top of this page: Thank you Veronica for having made it with me through this rough PhD time. You will get a present.

ABSTRACT

Nowadays, the production in fine chemical and pharmaceutical industry is mostly carried out in large scale batch reactors having typically dimensions of a few meters to satisfy the demand of the market. Even though this technology has been widely used and developed for centuries, it is by far not optimal for every type of reaction. For example, when working with exothermic reactions, the produced heat can't be always fully evacuated. To avoid run-aways, high amounts of solvents are used to increase the heat capacity of the mixture, or semi-batch mode with a slow addition of one of the reactants. In both cases, the space-time yield, i.e. mass of product produced per unit of time and per unit of volume, drastically diminishes.

One of the main enabling technologies allowing process intensification are the microstructured devices, characterized by high heat and mass transport rates due to the small characteristic dimensions ($< 1\text{ mm}$). Using this type of equipment, almost isothermal conditions can be achieved while carrying out fast exothermic reactions (with characteristic reaction times down to $t_r \approx 10\text{ s}$). Thereby, the target throughput is reached by numbering-up, i.e. parallel connection of several identical microreactors. For very fast exothermic reactions, especially for quasi-instantaneous reactions, dimensions smaller than $100\text{ }\mu\text{m}$ are needed to prevent the formation of unwanted hot spots. As such small dimensions are not suitable for industrial scale due to possible clogging and high pressure drops, other solutions are warranted.

The aim of this thesis is to develop alternative microstructured reactors enabling quasi-instantaneous reactions to be carried out under intensified conditions while suppressing the large hot spots. The work is divided into two main parts: determination of suitable strategies for the microstructured reactor design via numerical simulations (Chapter 3) and the experimental validation of the best microstructured reactor concept (Chapter 4-6).

Three strategies for enhanced temperature control within microstructured reactors for quasi-instantaneous reactions are taken for analysis using numerical simulation: 1) reduction of hot spot temperature by increased axial heat transfer in the reactor wall, 2) by injection of one reactant in multiple points along the reactor length and 3) by continuous injection of one reactant through a porous wall in a concentric reactor geometry. The multi-injection reactor (option 2) is the most effective design since with an optimized dosing with only 4 injection points the temperature rise is 5-fold smaller as compared to the adiabatic temperature rise. Furthermore, the key design requirements for an efficient multi-injection reactor are identified: 1) complete mixing after each injection and 2) evacuation of the produced heat before reaching the next injection point.

To experimentally validate the simulation results, in the subsequent chapter, an experimental method to monitor temperature in microstructured reactors is developed (Chapter 4). To track axial temperature profiles quantitatively, a method based on non-intrusive infrared thermography is developed yielding a resolution of 100 points/mm² and a precision of 1 °C. In the first validation experiments, the heat transfer coefficient determined in a micro heat exchanger (574 W/m²K) is in good agreement with prior estimations. While carrying out the hydrolysis of tetraethoxysilane as a fast model reaction, incomplete mixing of the reactants is detected via the temperature profile, and is ascribed to the high difference in density of the inlet flows.

Applying the method of quantitative IR-thermography to a T-micromixer with circular cross section gives insight into the mixing phenomenon (Chapter 5). The latter is studied via the temperature profile of the reactions strongly controlled by mixing, i.e. dilution of sulfuric acid with water and cyclization of pseudoionone.

The mass transfer coefficients determined are in the order of 0.1-9 1/s. It is shown that at high Fourier numbers $Fo = t_{diff}/\tau$ (mixing by shearing), the Damköhler number $DaI = \tau/t_{mix}$ remains constant with respect to flow rate at the reactor outlet, as both, mixing time and residence time decrease proportionally

with the latter parameter. To enhance the mixing performance, two approaches are applied: 1) the introduction of a carrier phase leading to travelling micro-batches with up to 4-fold faster mixing and 2) the structuring of the channel walls leading to the formation of vortices, and thus, to a substantially improved mixing efficiency.

For efficient mixing in the multi-injection reactor (Chapter 6), two types of mixing structures, i.e. the tangential mixer and the herringbone mixer, are developed using low temperature co-fired ceramics, and compared using quantitative infrared thermography. The best mixing performance is obtained by the herringbone structure, providing efficient mixing in a large range of flow rates corresponding to Reynolds numbers $Re = 20-130$.

Finally, a multi-injection reactor comprising three injection points and the herringbone microstructure is developed. Using the quasi-instantaneous and exothermic cyclisation of pseudoionone to α -ionone and β -ionone as model reaction, it is demonstrated that the temperature rise can be reduced 8-fold compared to the adiabatic temperature rise due to 1) the high volumetric heat transfer coefficient in the order of $4 \cdot 10^6 \text{ W}/(\text{m}^3\text{K})$, 2) the reduced overall transformation rate due to gradual mixing within the herringbone structure and 3) the injection of pseudoionone at three injection points. Yields of α -ionone and β -ionone above 98 % are achieved at a residence time of 3.7 s while efficiently avoiding the unwanted consecutive polymerization in a temperature range of 30-60 °C. Compared to the conventional semi-batch process, where such high yields can only be attained at temperatures below 10 °C, a 500-fold increased space-time-yield is achieved. In addition to the intensification of the process, the required mass of solvent is halved while maintaining good temperature control, rendering the overall process safe.

KEYWORDS: Process intensification, multi-injection, microstructured reactor, exothermic, temperature, infrared, pseudoionone

ZUSAMMENFASSUNG

Damit die Nachfrage des Marktes gestillt werden kann, findet heutzutage die Produktion der feinchemischen und pharmazeutischen Industrie in großen Rührkesselreaktoren statt. Diese weisen typischerweise Dimensionen in der Größenordnung von einigen Metern auf. Obwohl diese Technologie schon seit Jahrhunderten genutzt und weiterentwickelt wird, handelt es sich dabei bei weitem nicht um die beste Lösung für alle Reaktionstypen. Bei stark exothermen Reaktionen zum Beispiel, kann die produzierte Wärme nur sehr langsam evakuiert werden. Um ein thermisches Durchgehen des Reaktors zu verhindern, werden große Mengen an Lösungsmitteln eingesetzt, die die Wärmekapazität des Gemisches erhöhen. Eine andere Möglichkeit stellt das langsame Hinzudosieren eines der Reaktanden im sogenannten „Semi-Batch Modus“ dar. Beide Fälle führen zu einer drastisch reduzierten Raum-Zeit Ausbeute, d.h. Masse an Produkt pro Zeiteinheit und pro Volumeneinheit.

Eine der wichtigsten und aussichtsreichsten Technologien zur Prozessintensivierung sind mikrostrukturierte Reaktoren, deren kleine charakteristische Dimensionen von unter einem Millimeter hohe Massen- und Wärmetransportraten ermöglichen. Anhand solcher Apparate können beim Durchführen von schnellen exothermen Reaktionen (mit charakteristischen Reaktionszeiten bis hinunter zu $t_r \approx 10$ s) fast isotherme Bedingung erreicht werden. Dabei wird der benötigte Durchsatz durch das „Numbering-up“-Konzept erzielt, bei dem mehrere Mikroreaktoren parallel geschaltet sind. Für sehr schnelle Reaktionen, insbesondere für quasi-instantane Reaktionen, werden Dimensionen unter $100 \mu\text{m}$ benötigt, um sogenannte Hot Spots, d.h. einen unerwünschten Anstieg der Temperaturen, zu vermeiden. Da sich solche kleinen Kanäle wegen des hohen Druckverlustes und des Risikos der Verstopfung für eine Produktion auf industrieller Ebene nicht eignen, werden andere Lösungen benötigt.

Die Zielsetzung dieser Arbeit ist die Entwicklung alternativer Mikroreaktoren, die es ermöglichen, quasi-instantane Reaktionen unter intensivierten Bedingungen auszuführen. Dabei gilt es, die Temperatur auf ein möglichst konstantes Niveau zu halten, d.h. Hot Spots zu unterdrücken. Die Arbeit lässt sich hauptsächlich in zwei Teile gliedern:

- die Ermittlung geeigneter Mikroreaktordesigns mittels numerischer Simulation (Kapitel 3) und
- die experimentelle Validierung des besten Mikroreaktorkonzepts (Kapitel 4-6).

Folgende drei Strategien zur verbesserten Temperaturkontrolle von quasi-instantanen Reaktionen in Mikroreaktoren werden mittels numerischer Simulationen untersucht: Die Verminderung der Hot Spot Temperatur 1) durch eine Erhöhung der axialen Leitfähigkeit in der Reaktorwand, 2) durch Hinzudosieren einer der Reaktanden an mehreren diskreten Punkten entlang des Reaktors und 3) durch das kontinuierliche Hinzugeben einer der Reaktanden durch eine poröse Wand in einem konzentrisch aufgebauten Reaktor. Der Multi-Injektionsreaktor (Option 2) stellt sich als die effektivste Variante heraus, da mit optimierter Dosierungsstrategie mit lediglich 4 Injektionspunkten der Temperaturanstieg im Vergleich zum adiabaten Temperaturanstieg um ein 5-faches verringert werden kann. Des Weiteren werden die Anforderungen an das Design eines effizienten Multi-Injektionsreaktors ermittelt: 1) eine vollständige Vermischung der Ströme nach jeder Injektion und 2) das Abführen der durch die Reaktion produzierten Wärme vor Erreichen des nachfolgenden Injektionspunktes.

Zur experimentellen Validierung der Ergebnisse wird im darauffolgenden Kapitel 4 eine Methode zur quantitativen Vermessung von Temperaturprofilen in mikrostrukturierten Reaktoren entwickelt. Diese basiert auf berührungsfreier Infrarotthermographie und erzielt eine Auflösung von 100 Punkten/mm² mit einer Präzision von 1 °C. In den ersten Validierungsexperimenten mit einem Mikrowärmetauscher, wird eine gute Übereinstimmung zwischen dem experimentell ermittelten (574 W/m²K) und dem aus Korrelationen geschätzten Wert erhalten. Darüberhinaus wird das Temperaturprofil einer schnellen Modellreaktion vermessen, nämlich der Hydrolyse von Tetraethoxysilan. Das ermittelte Profil ermöglicht

es, unvollständiges Mischen der Eingangsströme im Reaktorinneren festzustellen. Diese kann auf den hohen Dichteunterschied zwischen den Strömen zurückgeführt werden.

Die zuvor entwickelte Methode wird in Kapitel 5 auf einen Mikro-T-Mischer mit kreisförmigem Querschnitt angewandt, um Einsicht in den Verlauf des Mischungsphänomens zu erhalten. Dieses wird mittels des Temperaturprofils von mischungskontrollierten Reaktionen untersucht: die Verdünnung von Schwefelsäure in Wasser und die Cyclisierung von Pseudojonon.

Es werden Stoffübergangskoeffizienten in der Größenordnung von 0.1-9 1/s ermittelt. Dabei wird festgestellt, dass bei großen Fourierzahlen $Fo = t_{diff}/\tau$ (Mischung durch Scherung), die Damköhlerzahl $DaI = \tau/t_{mix}$ am Reaktorauslass bezüglich der Flussrate konstant ist: sowohl die Verweilzeit als auch die charakteristische Mischzeit nehmen umgekehrt proportional mit der Flussrate ab. Um die Vermischungsqualität zu verbessern, werden zwei Ansätze angewendet: 1) Das Hinzufügen einer Trägerphase die zur Bildung von kontinuierlich strömenden „Mikro-Batches“ mit bis zu 4-fach erhöhter Mischgeschwindigkeit führt und 2) das Erzeugen von Strukturen in der Kanalwand die zur Bildung von Sekundärströmungen führen, die eine deutliche verbesserte Mischung zur Folge haben.

Um eine effiziente Mischung im Multi-Injektionsreaktor in Kapitel 6 sicherzustellen, werden zwei Typen von Mischstrukturen untersucht, nämlich der Tangentialmischer und der Herringbonemischer. Beide Strukturen werden mit Low Temperature Co-Fired Ceramics hergestellt und unter Nutzung der quantitativen Infrarotthermographie verglichen. Die beste Vermischung wird mittels der Herringbonestruktur erreicht, die in einem breiten Bereich von Reynoldszahlen $Re = 20-130$ zur vollständigen Vermischung führt.

Die in den vorherigen Kapiteln gesammelten Daten führen zur Entwicklung eines effizienten Multi-Injektionsreaktors (Kapitel 6), der 3 Injektionspunkte und die Herringbonestruktur beinhaltet. Bei der Durchführung der quasi-instantanen und stark exothermen Cyclisierung von Pseudojonon zu α -Jonon und β -Jonon im Multi-Injektionsreaktor, wird eine im Vergleich zur adiabaten Temperaturerhöhung 8-fach

reduzierte Maximaltemperatur erzielt. Die gute Temperaturkontrolle kann auf folgende Punkte zurückgeführt werden: 1) ein hoher volumetrischer Wärmeübergangskoeffizient von ca. $4 \cdot 10^6 \text{ W}/(\text{m}^3\text{K})$, 2) eine verringerte effektive Transformationsrate die sich aus der graduellen Vermischung innerhalb der Herringbonestruktur ergibt und 3) die Injektion des Pseudojonons an 3 unterschiedlichen Injektionspunkten. Bei Verweilzeiten von 3.7 s werden Ausbeuten von α -Jonon und β -Jonon von über 98 % erzielt. Gleichzeitig kann die unerwünschte Folgepolymerisation in einem Temperaturbereich von 30-60 °C unterbunden werden. Im Vergleich zu einem konventionellen Semi-Batch Prozess, wo solche hohe Ausbeuten lediglich bei Temperaturen unter 10 °C erreicht werden, wird eine 500-fach erhöhte Raum-Zeit Ausbeute erreicht. Zusätzliche zur Prozessintensivierung, wird die benötigte Masse an Lösungsmittel halbiert. Dabei wird die Temperatur stets in einem kontrollierten Bereich gehalten, was zu einem rundum sicheren Prozess führt.

STICHWÖRTER: Prozessintensivierung, Multi-Injektion, Mikrostrukturierte Reaktoren, exotherm, Temperatur, Infrarot, Pseudojonon

TABLE OF CONTENTS

Acknowledgements	iii
Abstract	v
Zusammenfassung	ix
Table of Contents	xiii
Chapter 1 : Introduction	1
1.1 Sustainable Development in Chemical Industry	1
1.2 Objective and Structure of the Present Work	3
1.2.1 Objective	3
1.2.2 Structure of the Work	4
1.2.3 Overview of the Reactors	6
Chapter 2 : State of the Art	11
2.1 Introduction to Microstructured Reactors	11
2.1.1 Microstructured Reactors as Tool for Process Intensification.....	11
2.1.2 Main Benefits of Microstructured Reactors	15
2.1.3 Remaining Challenges for Microstructured Reactors	17
2.1.4 Scale-out of Microstructured Reactors	18
2.2 Moving from Macro- to Microdimensions.....	20
2.2.1 Validity of Continuum Assumption	20
2.2.2 Scaling Effects.....	22
2.3 Mass and Energy Transfer.....	24
2.3.1 Residence Time Distribution in Microstructured Reactors	24
2.3.2 Mass and Heat Balance in Microchannels.....	28
2.3.3 Safety and Stability of Microstructured Reactors.....	31
2.4 Mixing in Microstructured Reactors	36
2.4.1 Passive Micromixers	36
2.4.2 Estimation of Mixing Time	39

2.5	Notations	43
Chapter 3 : Numerical Simulation of Microstructured Reactors.....		47
3.1	Introduction	47
3.2	Microchannel with Highly Conducting Walls.....	52
3.2.1	Model Description.....	52
3.2.1.1	<i>Differential Equations</i>	53
3.2.1.2	<i>Estimation of the Radial Heat Transfer Coefficients</i>	54
3.2.1.3	<i>Boundary Conditions</i>	57
3.2.1.4	<i>Default Parameters Used in the Simulations</i>	57
3.2.2	Results	59
3.2.2.1	<i>Variation of Radial Wall Conductivity</i>	60
3.2.2.2	<i>Variation of Axial Wall Conductivity</i>	61
3.2.2.3	<i>Variation of Isotropic Thermal Conductivity</i>	64
3.2.2.4	<i>Introduction of a Heat Sink</i>	66
3.3	Multi-injection Microreactor	69
3.3.1	Model Description.....	69
3.3.1.1	<i>Differential Equations</i>	70
3.3.1.2	<i>Default Parameters Used in the Simulations</i>	72
3.3.2	Results	73
3.3.2.1	<i>Number of Injection Points</i>	74
3.3.2.2	<i>Choice of Limiting Reactant</i>	76
3.3.2.3	<i>Unequal Flow Partition</i>	77
3.3.2.4	<i>Pressure Drop and Flow Distribution</i>	78
3.4	Micro-annular Reactor	80
3.4.1	Model Description.....	81
3.4.2	Results	85
3.4.2.1	<i>Axial Molar Flow and Temperature Profiles</i>	86
3.4.2.2	<i>Variation of the Ratio Residence Time/Cooling Time</i>	87
3.4.2.3	<i>Variation of the Ratio Residence Time/Reaction Time</i>	88
3.4.2.4	<i>Reaction Limited by Mixing</i>	89
3.5	Conclusion.....	91

3.6	Notations	93
Chapter 4 : Quantitative Infrared Imaging of Temperature Profiles in Microreactors		97
4.1	Introduction	97
4.2	Infrared Thermal Mapping	99
4.2.1	Basic Principles of Measurements.....	100
4.2.2	Challenges in Infrared Thermography.....	101
4.2.3	Application to Microsystems.....	104
4.3	Experimental	105
4.3.1	Setup for Thermal Imaging of Microstructured Reactors.....	105
4.3.2	Calibration of the Setup.....	109
4.3.3	Experimental Conditions	110
4.4	Results	111
4.4.1	Characterization of Heat Losses.....	112
4.4.2	Temperature Profiles of the Reactive System	116
4.4.2.1	<i>Calibration for 1st Generation Reactor</i>	116
4.4.2.2	<i>Temperature Profiles in 1st generation reactor</i>	118
4.4.3	Temperature Profiles in the Non-reactive System.....	120
4.5	Conclusions	124
4.6	Notations	125
Chapter 5 : Reactive Mixing Profiles in a Micro-cross Mixer		129
5.1	Introduction	129
5.2	Experimental Part.....	132
5.2.1	Experimental Setup	133
5.2.1.1	<i>Overview of the Setup</i>	133
5.2.1.2	<i>The Micro-cross Mixer</i>	134
5.2.2	The Model Reaction Systems.....	136
5.2.2.1	<i>Model Reactions</i>	136
5.2.2.2	<i>Flow Pattern</i>	139
5.2.3	Quantitative Thermal Imaging of Multi-phase Flows	141

5.3	Results	144
5.3.1	Heat losses	144
5.3.2	Reproducibility of the Temperature Profiles	146
5.3.3	Mixing in homogeneous systems	148
5.3.3.1	<i>Dilution of Sulfuric Acid</i>	148
5.3.3.2	<i>Cyclization of Pseudoionone</i>	153
5.3.4	Mixing in Micro-batch Flow System	155
5.3.4.1	<i>Dilution of Sulfuric Acid</i>	155
5.3.4.2	<i>Cyclization of Pseudoionone</i>	157
5.3.5	Comparison of the Systems	159
5.4	Conclusion	161
5.5	Notations	162
Chapter 6 : Development and Experimental Investigation of a Multi-injection Reactor ...		165
6.1	Introduction	165
6.1.1	Multi-Injection Reactor	166
6.1.2	Cyclization of Pseudoionone	168
6.1.3	Scope of the work	172
6.2	Design of the Multi-injection Reactor	173
6.2.1	List of Requirements	173
6.2.2	Microstructured Reactor from Low Temperature Co-fired Ceramics	174
6.2.3	Mixing zone	176
6.2.4	The Multi-injection Reactor Design	179
6.3	Experimental Part	181
6.3.1	Experimental Setup	182
6.3.1.1	<i>Embedding the Reactor into the Setup</i>	182
6.3.1.2	<i>Overview of the Setup</i>	183
6.3.2	Methods of Analysis	185
6.3.2.1	<i>Quantitative Infrared Measurement</i>	186
6.3.2.2	<i>Gas chromatography</i>	187

6.4	Experimental Results.....	188
6.4.1	Mixing structure	188
6.4.1.1	<i>Tangential Mixer</i>	189
6.4.1.2	<i>Herringbone Mixer</i>	191
6.4.1.3	<i>Comparison of the Structures</i>	192
6.4.2	Characterization of Heat-Transfer in the Multi-Injection Reactor	194
6.4.3	Thermal Characterization of the Cyclization of Pseudoionone in the Multi-injection Reactor	199
6.4.4	Product Distribution in the Multi-injection Reactor.....	202
6.4.4.1	<i>Yield as Function of Flow Rate</i>	203
6.4.4.2	<i>Yield as Function of Temperature</i>	204
6.4.4.3	<i>Reducing the Amount of Solvent</i>	207
6.5	Conclusions	209
6.6	Notations	211
Chapter 7 : General Conclusions.....		213
References		I
Curriculum Vitae		XV

Chapter 1

INTRODUCTION

In this first part of the thesis, the subject and the problematic are introduced. It summarizes the aim, the objectives and the chosen strategy to achieve them.

1.1 Sustainable Development in Chemical Industry

Sustainable development is defined as a development that meets the needs of the present without compromising the ability of future generations to meet their own needs [1]. This definition was formulated in a report of the United Nations General Assembly in 1987. It shows the acute state of awareness of the threats of industrial progress to future generations already back in the eighties. Nevertheless, a constant increase in consumption of natural resources and waste production has been denoted in the past decades, as depicted in Figure 1.1. Already nowadays, consumption of natural resources is much higher than their rate of replacement, leading to their depletion. To meet the rate of consumption of natural resources in 2013, we would need 1.5 planets for our supply. As only one planet Earth is available, we must drastically change our habits. Thereby, the transition from the business as usual to a more sustainable regime is one of the main barriers, since it is often complex to find agreement between economic targets and sustainable development [2].

Due to the obvious adverse effects of chemical products and processes on the global ecology, it is mandatory for the chemical industry to induce some drastic changes, and to strive for a more sustainable

future [3]. A.W. Hofman, a German chemist and founder of the Royal College of Chemistry in London, illustrated already in 1866 that [4]:

“In an ideal chemical factory (...) there is, strictly speaking, no waste but only products (...). The closer (...) it gets to its ideal, the bigger is the profit.”

In contrast to many other industries, a sustainable development in chemical industry is well in accordance with economic success, which should be an incitement for this sector to do pioneering work within this field. With E factors (kg waste/ kg product) above 25 [5-7], especially the current fine chemical and pharmaceutical industries are industries of waste generation [8].

To overcome the high E factors, the industry needs to take decisive steps forward on several levels [9]. One main concern is to move from a chemistry carried out under highly diluted conditions to intensified processes at high concentrations and temperatures allowing high product yield [8].

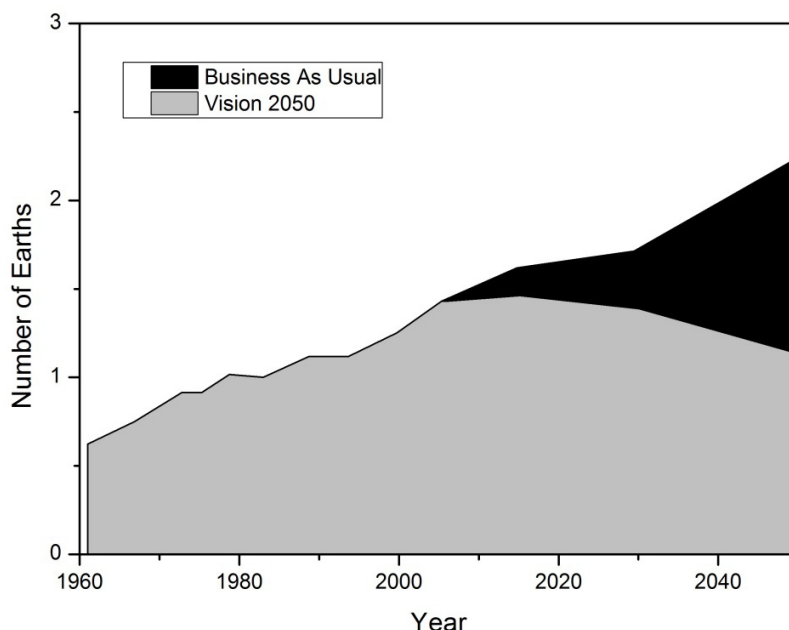


Figure 1.1: Diagram illustrating two possible scenarios for the future development: continuing with the business as usual (black) or making radical changes of approach as described by “Vision 2050” [10].

1.2 Objective and Structure of the Present Work

In this section, the objectives of the present work are formulated. Subsequently, the overall structure of the thesis is addressed before giving an overview of the reactors used and developed within this work.

1.2.1 Objective

A common approach to handle fast exothermic reactions is by 1) dilution of the reactants using solvent or by 2) semi-batch mode, which is the slow addition of one of the reactants. In both cases, the space-time yield, i.e. mass of product produced per unit of time and per unit of reactor volume, drastically diminishes. Furthermore, the first approach results in the enormous E-factors (kg waste/ kg product) found in the pharmaceutical and fine chemical industry, as mentioned in the introduction. Using innovative reactor designs, such fast and exothermic reactions can be carried out in a much more efficient way, i.e. at drastically increased space-time yield.

The microstructured reactor (MSR) is one key component to fulfill the needs of substantial intensification of chemical transformation in the fine chemical and pharmaceutical industry [8, 11-13]. Its most significant advantage is the improved heat evacuation compared to the conventional large scale reactors [14-16]. Under the predominant laminar regime, the volumetric heat transfer resistance at the reactor channel side is proportional to the square of the reactor diameter [17].

In principle, by using the strong dependence of the heat transfer rates on the reactor diameter, any exothermic reaction can be controlled by adjusting the reactor diameter to the reaction properties. When carrying out exothermic reactions with effective characteristic reaction times < 10 s, almost isothermal profiles can be achieved by the use of MSR with diameters in the range of 1000 μm to 100 μm . However, for faster reactions, particularly quasi-instantaneous with characteristic reactions times in the order of 1 s, this approach leads to sizes smaller than 100 μm . For a production on industrial scale, such small channel

sizes are not viable as they are highly sensitive to clogging, cause high pressure drops when passing liquids and are expensive to scale-out [17].

The aim of this project is to enable process intensification of rapid and highly exothermic reactions with characteristic reaction times of a few seconds or even smaller than 1 s, referred to as quasi-instantaneous. Thereby, alternative strategies of temperature management in microstructured reactors have to be found to minimize the temperature rise, i.e. suppress the formation of hot spots, while avoiding the use of excessively small reactor diameters. The task is addressed on a theoretical level by carrying out numerical simulations and experimentally by demonstrating the proof of concept.

1.2.2 Structure of the Work

The reader is introduced to the fundamentals of microstructured reactors to give an insight in the advantages and constraints encountered with microstructured reactors (Chapter 2).

Following the first brainstorming, three strategies having the potential to reduce hot spot temperature in microstructured reactors are selected and analyzed in detail using numerical simulation (Chapter 3): 1) temperature control by axial conduction of heat, 2) by distinct injections of one reactant along the length and 3) by continuous injection along the length of a concentric reactor. Using numerical simulation as tool for elaboration of the best concept, the multiple injections at distinct positions is identified. Furthermore, the key design parameters of an efficient multi-injection reactor are determined: To avoid accumulation of heat and mass, it is crucial to assure complete mixing of the reactants, and to evacuate the produced heat before reaching the subsequent injection point. Thereby, an entire chapter (Chapter 5) of the thesis is devoted to mixing, which remains challenging under the predominant laminar flow regime in micro-capillaries.

For the experimental validation of the simulation results obtained with the multi-injection reactor, a non-intrusive experimental method to monitor temperature in microstructured reactors is developed and validated in the following chapter (Chapter 4).

As complete mixing between the injection points is crucial, the newly developed thermal mapping method is used to get further insight into the rate of homogenization in a T-shaped micromixer with circular cross section (Chapter 5).

Finally, in Chapter 6, the development and testing of a multi-injection reactor is presented. Thereby, the cyclization of pseudoionone is used as a model reaction to demonstrate the degree of process intensification that can be achieved with this type of reactor while keeping temperature in a controlled range.

The findings of the study are summarized in the concluding chapter (Chapter 7).

1.2.3 Overview of the Reactors

Table 1.1: Overview of the reactors developed during the present study.

Nr.	Reactor Type	Chapter	Aim	Material	Cross Section [μm]	Length [mm]	Structures/ Integrated Cooling
1	Caterpillar mixer	4	Mixing upstream of the monitored reactor	Stainless steel	Split & Recombine, 150 x 150	5	Yes/No
2	Capillary	4	Validation of Setup	Perfluoroalkoxy (PFA)	Circular, $\phi = 1000$	50	No/No
3	IMM heat exchanger	4	Validation of Setup	Polyether ether ketone (PEEK)	Rectangular, 500 x 200	100	No/Yes
4	Cross Junction	5	Mixing efficiency in circular channels	Polytetrafluoroethylene (PTFE)	Circular, $\phi = 500$	16	No/No
5	Tangential Mixer	6	Mixing efficiency in structured channels	DuPont 951 ceramic tape	Rectangular, 500 x 500	32	Yes/No
6	Herringbone Mixer	6	Mixing efficiency in structured channels	DuPont 951 ceramic tape	Rectangular, 560 x 500	68	Yes/No
7	Multi-Injection Reactor	6	Process intensification	DuPont 951 ceramic tape	Rectangular, 560 x 500	300	Yes/Yes
8	3 Glass Mixers	-	Mixing as function of contact angle	Glass	Trapezoidal, $\approx 500 \times 130$	300	No/No
9	Multi-Injection Reactor	-	Process intensification	Stainless steel	Circular, $\phi = 500$	270	No/No
10	Micro-Annular Reactor	-	Mixing efficiency	Polycarbonate	Annular, i.d. 6 mm, o.d. 7 mm	75	No/No
11	Cooled Tangential Mixer	-	Development of an integrated cooling	DuPont 951 ceramic tape	Rectangular, 500 x 500	32	Yes/Yes

Table 1.1 gives an overview of the 11 main reactors that were bought (reactor 1&2) or developed during the present thesis. While reactors 1 to 7 are thoroughly described in the thesis (see Figure 1.2), reactors 8-11 are only mentioned in the present section (Figure 1.3).

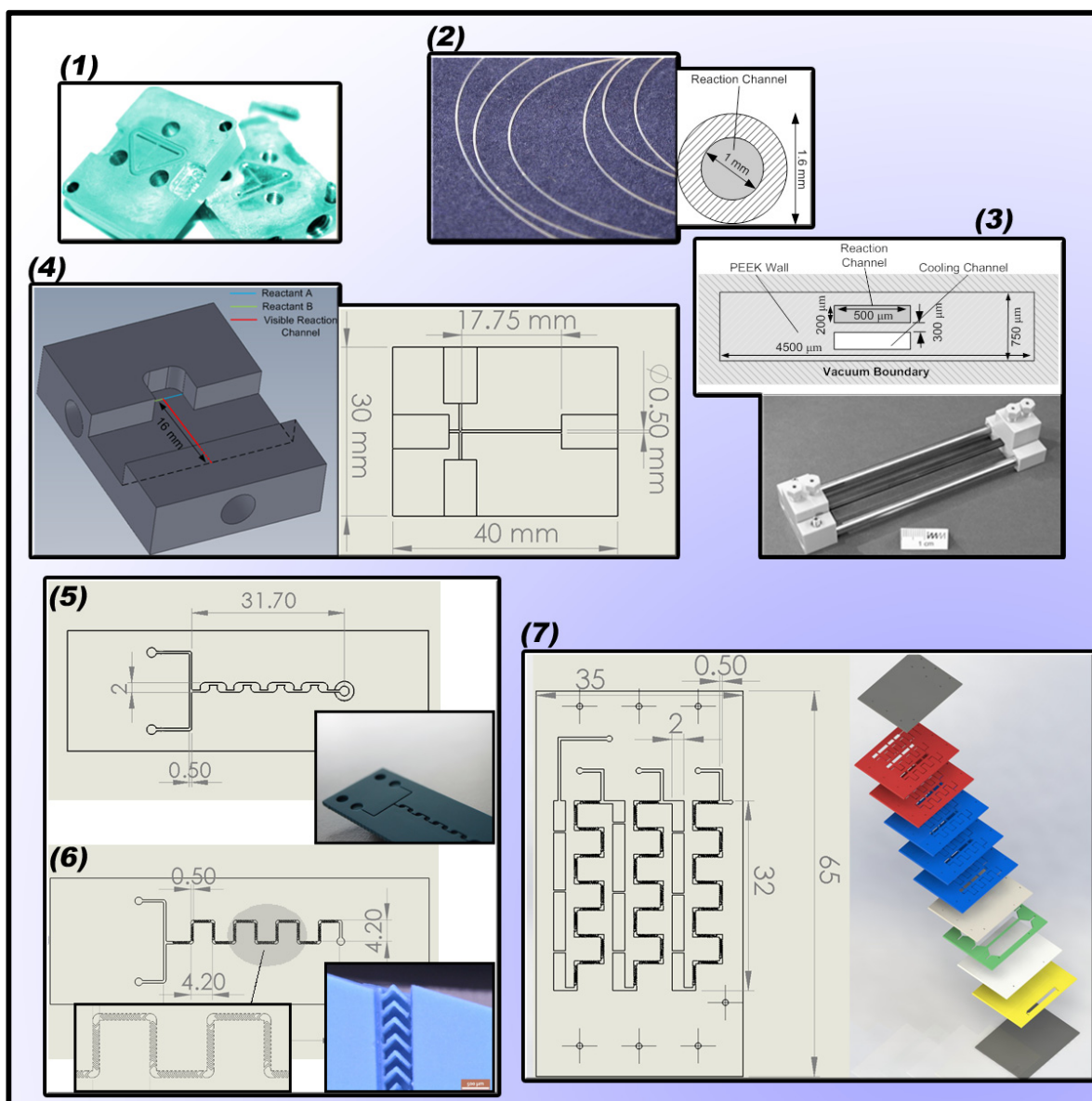


Figure 1.2: Overview of the reactors developed within the PhD project and presented in the upcoming chapters. If not further specified, the dimensions are given in millimeter.

The main challenge encountered while developing the reactors was to ensure sufficient mixing of the relative viscous inlet flows under the predominant laminar flow regime. When working with the glass

reactors (reactors 8), which had three different contact angles for the incoming flows, it was quickly noticed that the high ratio of channel width/channel height (about 3.5) prevented the flows to mix even at Reynolds numbers of a few hundreds. Any mixing would occur only in the capillaries attached at the reactor outlet.

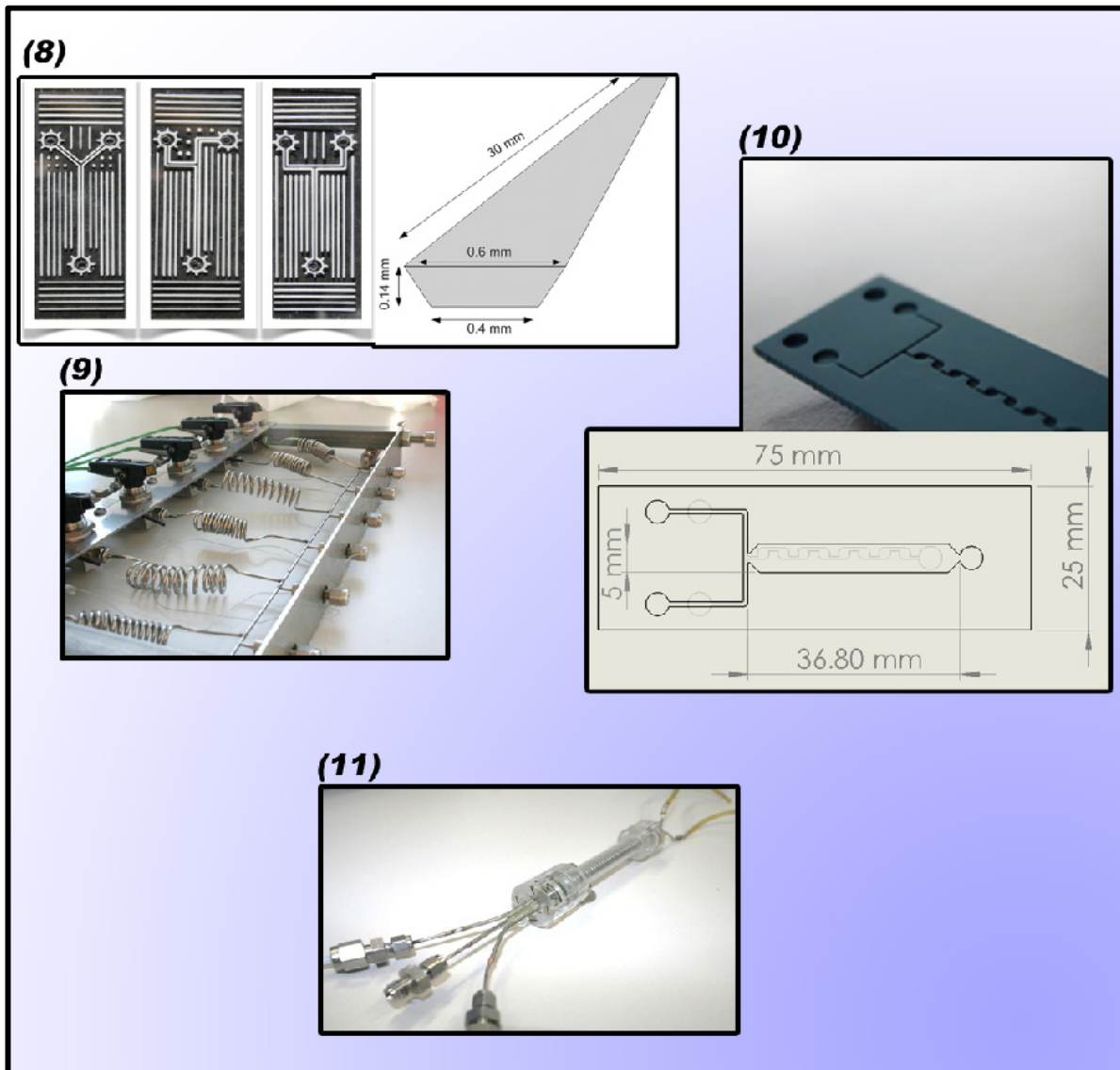


Figure 1.3: Overview of the reactors developed within the PhD project. The results obtained with the represented reactors are not addressed in the present study.

In the first version of a multi-injection reactor (reactor 9), mixing in circular cross sections was found to be insufficient, which would have led to dangerous accumulation of the reactants along the length. Finally,

a similar behavior was observed for the prototype of the micro-annular reactor (11), where the streams in annular space were found to mix solely by slow diffusion.

Chapter 2

STATE OF THE ART

This chapter will give the reader an introduction to microstructured reactors (MSR). At first, a simplified overview of the entire field is given, establishing when and how to use this type of equipment. In the subsequent section, the different aspects of mass and heat balance inside microchannels are addressed, showing on the one hand similarities, and on the other hand, the differences between the conventional and the microreactor scale. As up to now a lot of effort has been done to understand and improve mixing in MSR, this on-going subject is addressed in a separate section.

2.1 Introduction to Microstructured Reactors

In this section, the reader is introduced to the concept of microreactors. Starting with a definition, the main motivations for their use and challenges to overcome are elucidated. As this type of equipment cannot be scaled-up in the classical sense, the last part of this section is devoted to the “scaling-out” approach which allows the production on a pilot and industrial scale.

2.1.1 Microstructured Reactors as Tool for Process Intensification

Process intensification was described by C. Ramshaw as “a strategy for making dramatic reductions in the size of a chemical plant so as to reach a given production objective” [12, 13]. This significant reduction in

size can be reached by two ways: (1) Reducing the amount of apparatuses involved in one process or by (2) reducing the size of the pieces of equipment. Later on, A. Stankiewicz reformulated C. Ramshaws concept in a broader sense: “Any chemical engineering development that leads to a substantially smaller, cleaner and more energy efficient technology is process intensification”. This vision of the future of chemical engineering was the main impulse for the rapid development of microreactors, as one of the main tools of process intensification.

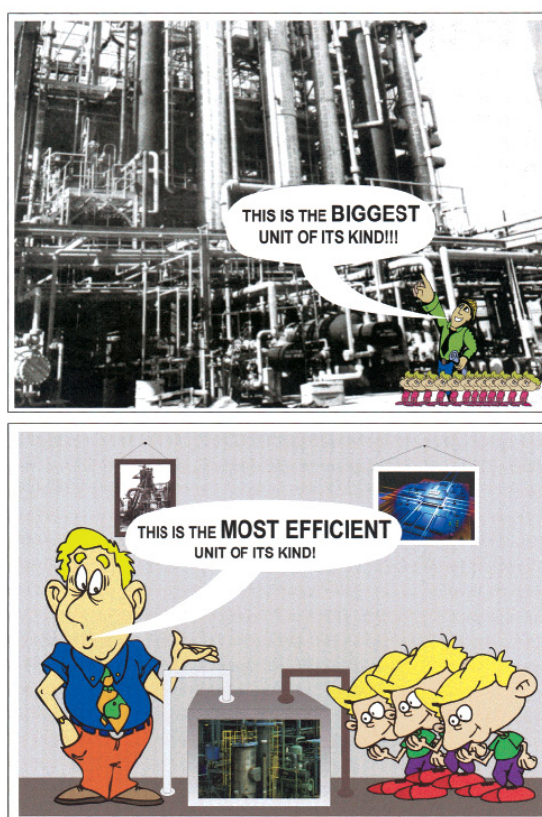


Figure 2.1: Illustration depicting in an exaggerated manner a school excursion to a chemical plant in the present (top) and in the future (bottom). Adopted from Stankiewicz *et al.* [12].

Microstructured reactors are usually defined as miniaturized reaction systems which have at least one characteristic dimension in the submillimeter range, i.e. typically 10-1000 μm [18-20]. Reactors with dimensions approaching the upper boundary are usually referred to as milli- or minireactors, whereas for smaller reactors the term nanoreactors can be found. When referring to microreactors or microstructured

reactors in the present study, systems to carry out chemical transformation aiming at the production of fine chemicals or pharmaceuticals on an industrial scale are described.

The first activities of micro process technology occurred in the 1980s, when this technology was used to enhance heat exchange capacity [14, 20, 21]. In 1990, the Institut für Mikrotechnik Mainz (IMM) was founded [22], which played an essential role in the future development of this field. Initially, micro-fabricated equipment was used to create so called Lab-on-Chip devices for biochemical and analytical tasks [20, 23, 24]. Thereby, several working steps are integrated on one chip creating a miniature working station. The idea of carrying out chemical and biochemical synthesis for pilot plant and larger applications became mature in a workshop which took place in 1995 at Institut für Mikrotechnik Mainz, Germany [25]. This was the birth of a separate class of microfluidic devices which are the subject of this dissertation. In 1997, the first International Conference on Microreaction Technology (IMRET1) was held in Frankfurt, Germany [26]. Since then, 12 IMRETs have been organized all over Europe, USA and Japan, and a dramatic increase in research activity took place leading to a yearly growing amount of publications and patents [27], as can be seen in Figure 2.2.

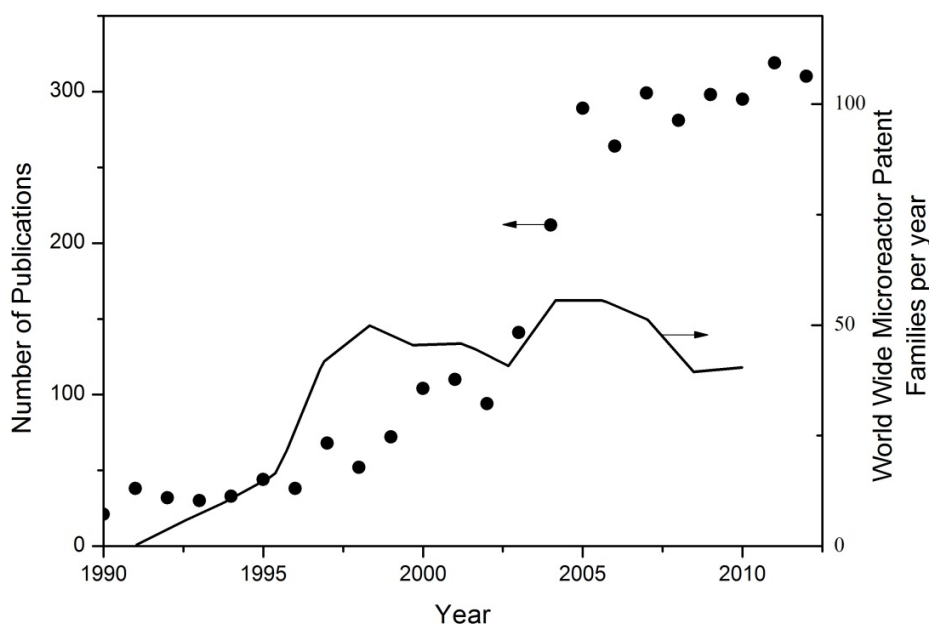


Figure 2.2: Amount of publications on “microreactor” found on Scopus [28] in 2013 (dots) and amount of worldwide patent families published per year on microreactors (edited from Dencic *et al.* [27]).

As mentioned in the previous paragraph, microreactors can be divided in different categories according to their function. On one extreme there are the analysis systems, designed as a tool to gather information (Lab-on-Chip), uniting several functions on one single plate. One example for this category is a device developed to measure concentration of metal containing aerosols in air [29].

The second category is constituted of reaction systems which are used for chemical or biochemical synthesis, but solely to collect data for a process that is meant to be carried out on conventional macro scale equipment. In this, the classical scale-up step separates the lab scale experiment from the pilot plant or large scale production. A typical example for the latter category would be the determination of kinetic data of a reaction that is industrially carried out in a batch or semi-batch reactor [30, 31]. Finally, on the other extreme one finds microstructured reactors that are used to carry out chemical or biochemical synthesis on a small production scale. Thereby, transfer from laboratory experiment to larger scales is done by so called “scale-out” or “numbering-up” (see section 2.1.4). Especially within the two latter

categories, several of the following components are arranged in series/parallel to create a set-up or mini-plant [18]:

- Micromixer
- Micro heat exchanger
- Microseparators
- Gas phase reactors
- Liquid phase reactors
- Gas/Liquid Reactors

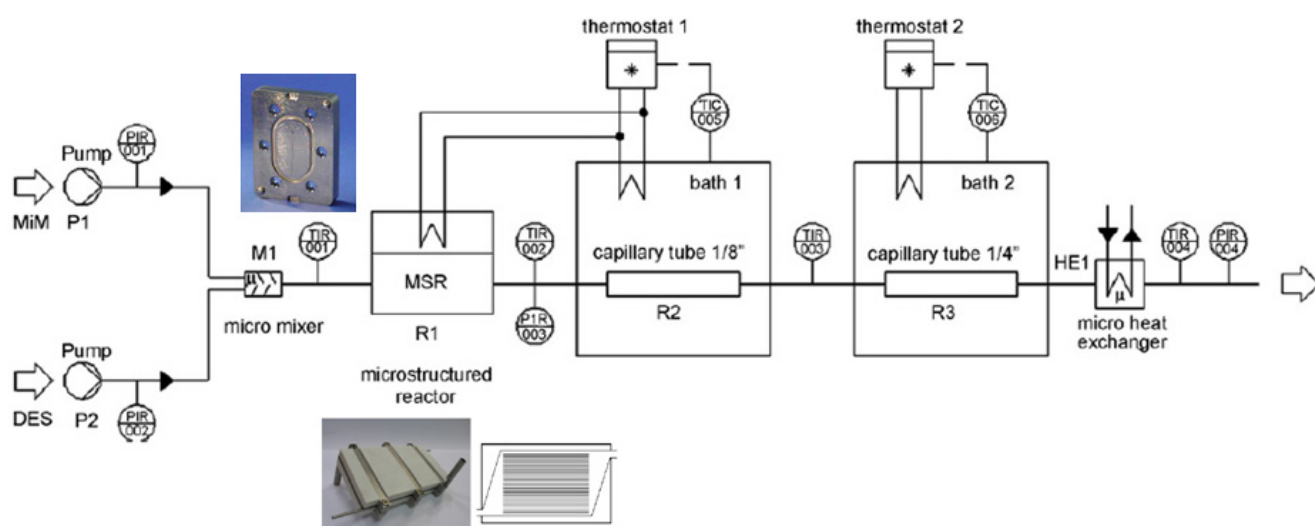


Figure 2.3: Typical arrangement of several microdevices forming a set-up or mini-plant. This plant was designed for the synthesis of ionic liquids. Image adopted from Renken *et al.* [32].

2.1.2 Main Benefits of Microstructured Reactors

In the previous section, the rising amount of effort put in the development of microstructured reactors was demonstrated. The motivations behind this are numerous, and can be ascribed to essentially three main characteristics:

- a) Enhanced reliability
- b) Advantages related to the small characteristic dimensions
- c) Scale-up is replaced by Scale-out

In the fine chemical and pharmaceutical industry, most of the liquid phase processes are conventionally carried out in batch reactor. By implementing such reactions in microstructured reactors, generally a shift from a discontinuous process to a continuous flow process takes place [33-35]. In the continuous mode, quality can be controlled continuously and a fast response to unwanted changes of parameters can be supplied. According to Sergio Pissavini, Business Director of Reactor Technologies at Corning SAS (France), three out of ten batches don't pass quality control as the outcome of a whole batch can only be verified at the very end of the reaction [36]. In addition, the integration of automation system can increase the operator safety and reduce the risk of human error.

The small sizes lead to an improvement of the mass and heat transport phenomena: due to the radical reduction of transport length, the diffusion gradients are intensified, which in turn results in higher surface specific flux according to Fick's and Fourier's law [37, 38]. At the same time, the volumetric contact surface between two phases is high, leading to high absolute transfer rates. Better transfer rates mean better reaction control, which at the end of the process results in higher yields and diminished waste. From the point of view of fluid dynamics, due to the small channel, very defined flow in the case of single and multiple phase flows are observed [25, 39-41]. In the former case, the Reynolds number encountered lie well below the transition regime and are in the order of $Re = 1 \dots 1000$ [14, 42]. Numerical simulation of the fluid behavior is more accessible than on large scale reactors which are often operated in a turbulent regime. The small hold-up volume of microstructured reactors [43-45] represents a tremendous advantage from the safety perspective. The amount of involved reacting mass as compared to large scale batch reactors reduces the consequences in the case of an uncontrolled situation. Hence, hazardous reactions (e.g. toxic reactions) can be carried out in microstructured reactors with much higher safety. At the same

time, reactions can be operated under harsh conditions (higher temperature and pressure) to benefit from higher productivity, which is usually referred to as “novel process windows” [11, 46].

The third aspect promoting the success of microtechnology is the fundamental change of the approach towards the step from laboratory scale to industrial scale. Whereas classically the size of the laboratory reactor (the beaker) is upgraded to a few cubic meter to meet the target productivity, the scale-out concept consists in an increase of the number of parallel operating units (more details can be found in section 2.1.4) [17, 47-52]. Thereby, omitting the cost and time expensive step of scaling up allows a company a faster presence on the market with a newly developed product [36, 53]. A shorter time to market goes along with reaching the break-even point of the cash flow curve at an earlier point of time, which renders the whole concept more appealing. Furthermore, the main advantage of batch reactor compared to classical continuous flow reactors is its flexibility: several reactions can be carried out in one and the same batch reactor. Building up modular mini-plants based on microtechnology brings up a whole new degree of freedom in terms of flexibility: using the same basic modular units, different products can be synthesized [8, 36, 54, 55]. Producing a chemical in smaller plants also offers the opportunity of decentralized on-site on-demand production, as common practice nowadays in the automotive industry (“Just in Time Delivery”) [54, 56].

2.1.3 Remaining Challenges for Microstructured Reactors

Several incentives for the use of microdevices have been revealed so far. According to a study published by Roberge *et al.* [57], about 44 % of the synthesis processes would benefit from a transfer to processes partly designed with microstructured reactors. However, this technology still has to face some challenges when implemented in reality. A considerable drawback while using the currently available microdevices is the handling of solids or solid containing solutions, as depositions can quickly lead to clogging of the whole channel [58]. In addition, to be viable on the market, this new concept needs to be economically

advantageous compared to conventional equipment. Recent studies have shown that for smaller scale production, the equipment costs are of the same order [59]. If a larger amount of product is needed, the microstructured reactor technology turns out to demand higher investment compared to a classical vessel [57]. The latter phenomenon can be explained by the extremely low scale up factor of a batch reactor, which can be hardly reached with the numbering-up strategy. In this case, the use of microstructured reactor can be economically justified solely in the case of higher yields, as raw materials represent the major part of the operating costs [35]. Besides the economical question concerning the scale-out strategy, there also remains some doubt about the best technical solution, as will be discussed in the upcoming section. Finally, the use of microstructured reactor requires a shift of thinking from the side of the industry, which has to open up and try to benefit from the advantages that can be brought to them by this yet young technology (as illustrated in Figure 1.1) [36].

2.1.4 Scale-out of Microstructured Reactors

As a traditional scale-up of such microstructured reactors would eliminate their inherent advantages, one has to “scale-out” or “number-up” (Figure 2.4) [8, 48, 49, 60, 61] . There are two classic ways of numbering-up: internal and external [48]. For external numbering-up, multiple identical units are operated in parallel. The advantage is that each single unit is independent of the other and performs as the developed lab-scale unit. However, as each unit will need individual equipment (such as pumping, tubing, etc.), the costs of external numbering-up are considerable. When numbering-up is carried out internally, the amount of equipment needed is reduced and thus the costs. The fluids are mixed in a mixing zone and subsequently distributed into the reaction channels, where conditions are similar to the lab-scale single microchannel. The two main drawbacks of internal numbering-up shall be illustrated in the following.

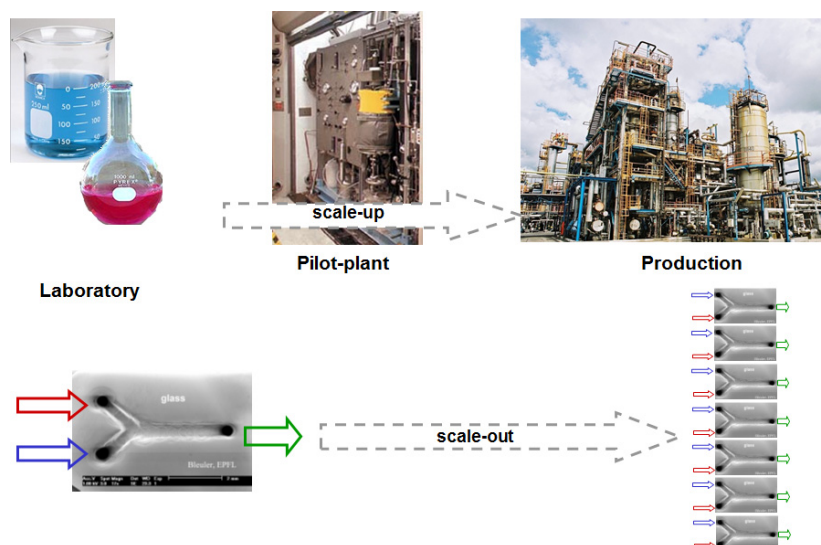


Figure 2.4: Scale-up versus numbering-up (image from A. Renken 2006).

The distribution of fluids to the multiple channels turns out to be complex, as every single molecule needs to experience the same conditions (i.e. temperature, residence time) to obtain optimal reactor performance, efficiency [62] and safety. Saber *et al.*[61] analyzed the effect of maldistribution in catalytic wall microchannel reactor using a theoretical model and showed the negative effect of clogging on selectivity. In the past, a lot of work has been carried out to minimize the flow non-uniformities, which are generally due to two reasons: a poor design of the distribution unit and manufacturing tolerances. Whereas manufacturing tolerances usually cause variations of local temperature in the range of about $\pm 5\%$, the former reason can cause flow ratios in different channels more than a factor 4. An overview over various flow equalization devices is given in Rebrov *et al.* [63]. When numbering up multiphase flows such as slug flow, additional complexity is added to the problem due to the high sensitivity of the flow pattern to variation of flow rate [64]. In these cases, low fabrication tolerances are mandatory and a considerable amount of energy has to be invested in the distribution of the liquids [65, 66]. An about 4 to 50-fold higher pressure drop is required for the distribution of the fluids as compared to the overall pressure drop over one single channel.

The second disadvantage of internal numbering-up is reaction control in the mixing zone. As soon as both reactants are contacted, reaction is initiated and heat is generated. However, efficient heat removal is acquired only in the channels placed after the distribution section. This effect can be reduced to some extent by decreasing Damköhler number ($DaI = \tau / t_r$) in the distribution section. However, for very fast exothermic reactions other solutions are required for higher throughput with limited increase in temperature.

Roberge *et al.*[8, 55, 67] proposed a novel modular multi-scale approach. As most of the reactions form deposits which lead to unpredictable increases in pressure drop, their primary target was to avoid channel parallelization to maximize control over the reactor. Hence, they rejected the concept of “numbering-up” and instead carried out the reaction in one single channel at high flow rates. The channel size increases along the length, thus optimizing temperature control and diminishing pressure drop.

2.2 Moving from Macro- to Microdimensions

After the introduction to microreactors, this section focuses on the change of scale. By moving from the classical scale of typically several meters for batch reactors and at least a few centimeters for tubular reactors to the microscale, the dimensions change with a factor of 100 to 10000. Naturally, this substantial transformation can affect the properties of interaction between reactor and reaction to a certain extent. The first part of this section shows that this type of equipment can still be described with the conventional Navier-Stokes equations [68]. In the second part, some examples are illustrated where terms usually neglected on larger scale gain importance on the microscale, referred to as “scaling effects”.

2.2.1 Validity of Continuum Assumption

Due to the small size of MSR, one has to investigate whether a model of continuous and indefinitely divisible matter is still valid at a channel size as low as 100 μm , which is the smallest relevant scale for

industrial production. For gases, continuum models can be used to describe a system as long as the mean free path λ' is much smaller than the characteristic length of the MSR (L'_{MSR}). A criterion is defined using the Knudsen coefficient ($Kn < 10^{-3}$) [69] which is given as follows.

$$Kn = \frac{\lambda'}{L'_{MSR}} \quad (2.1)$$

For a gas under atmospheric pressure at 298 K, the mean free path of an air molecule corresponds to $\lambda' = 6.7 \cdot 10^{-8}$ m [70]. In this case, the system can be modeled with the continuum equations down to a characteristic size of $L'_{MSR} = 67$ μm . As for an ideal gas λ' is proportional to T and p^{-1} [71], the modeling of small reactors at high temperatures or low pressures can become critical. In liquid systems, describing the limits to non-Newtonian behavior is more problematic. An attempt to approximate this boundary is given by Loose *et al.* [72]. According to their criterion, the fluid behavior becomes non-Newtonian when the shear rate $\dot{\gamma}$ exceeds twice the molecular frequency:

$$\dot{\gamma} = \frac{\partial u}{\partial y} \geq \frac{2}{\tau'} \quad (2.2)$$

with

$$\tau' = \left(\frac{M \cdot \sigma^2}{\varepsilon'} \right)^{0.5} \quad (2.3)$$

where τ' is the molecular time scale, M is the molecular mass, σ is the molecular length and ε' the molecular energy scale [69, 73]. Thereby, u indicates the flow in x -direction and y is a coordinate normal to x . For water under standard temperature and pressure $\tau' = 8.31 \cdot 10^{-13}$ s. In this case, only very high shear rates would cause the continuum assumption to fail. Experimental results given in literature predict a Newtonian behavior down to films of 10 molecular layers for non-polar molecules and to characteristic lengths < 1 μm for polar molecules [74-76]. Therefore, the assumption of continuous and indefinitely divisible matter is valid for liquids in most of the cases.

2.2.2 Scaling Effects

As discussed before, MSR can be described using a continuum model i.e. the Navier-Stokes equations. Although the same equations as for a “macro” reactor can be applied to an MSR, the importance of different terms in the Navier-Stokes equation changes due to “scaling effects” [77-80]. For example, radial temperature gradients in liquid phase MSR can be neglected, whereas they need to be considered in conventional scale reactor (see section 2.3.2)

One of the most pronounced scaling effect is the axial conduction of heat. There are two different pathways: axial heat conduction through the fluid and axial conduction through the reactor wall. The former one can be neglected if the Péclet number ($Pe_t = d_h \cdot u / \alpha_{Fluid}$) > 10 and is only of importance within the channel length (z) such that [73, 81, 82].

$$\frac{z}{d_h} Pe_t \leq 20 \quad (2.4)$$

where d_h is the hydraulic channel diameter and α_{Fluid} is the thermal diffusivity, defined as:

$$\alpha_{Fluid} = \frac{\lambda_{Fluid}}{\rho \cdot c_p} \quad (2.5)$$

where ρ is the average density, c_p is the average heat capacity and λ_{Fluid} is the thermal conductivity of the fluid.

For most of the fluids axial heat conduction does not need to be considered due to their low heat conductivity (i.e. water at 290 K, $\lambda_{Fluid} = 0.59$ W/m·K [83]). However, heat conductivity in the walls of the channels is very high (for silicon at 298.2 K, $\lambda_{Wall} = 149$ W/m·K [83]). Because of the small channel diameter of MSR, the significant wall thickness needed to give mechanical stability to the device results in a non-negligible axial conductivity through the walls. This effect has been thoroughly analyzed in the literature for non-reacting systems demonstrating for example that the heat exchange efficiency of a micro

heat exchanger has an optimum heat conductivity, and decreases for higher heat conducting materials [84-86]. For the geometry analyzed by Stief *et al.* [86], the optimal conductivity was given at about 1 W/(m K), corresponding to glass as material. An example of different thermal wall resistances for hydrogen/air combustion is shown in Figure 2.5. The hot spot was reduced from ~850 °C to ~675 °C and finally to ~590 °C upon diminishing the thermal resistance of the wall material [87]. Horny *et al.* [88] run the oxidative steam-reforming of methanol in autothermal mode. The axial heat conductivity was increased by inserting multiple catalytically active brass wires into a 9 mm glass tube reactor. She managed to transfer the heat released from the fast exothermic partial oxidation of methanol to the downstream mixture for acceleration of the slower endothermic steam-reforming. The temperature profile initially containing a hot spot at the inlet of the reactor followed by a cold spot, was transformed in a nearly isothermal profile. The effect of axial heat conduction through the reactor wall is more extensively discussed in a literature review [63] and in Chapter 3 of the present thesis.

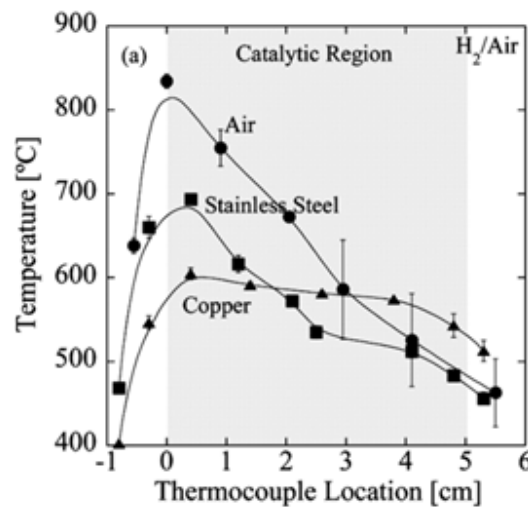


Figure 2.5: Effect of different wall resistances (“thermal spreaders”) on the temperature profile of H₂/air combustion. The thermal spreaders consist in additional wall material added on top of the stainless steel reactor. Adapted from Norton *et al.* [87].

Due to the strong velocity gradients in MSR, the energy losses due to viscous dissipation resulting in a temperature rise need to be considered under certain circumstances. This effect becomes dominant with decreasing channel diameter and with increasing fluid viscosity as well as flow velocity. Many studies

have shown the relevance of this effect by experimental and theoretical analysis [89-93]. To get measurable results, the experiments were carried out in a microchannel with size of 10-100 μm . The experimental work of Celata *et al.* [90] concluded that the viscous dissipation effects are not important when working with diameters above 100 μm . A theoretical analysis carried out by Morini *et al.* [80, 94, 95] reported that for water with Reynolds number (Re) around 1000 and d_h of 100 μm the adiabatic temperature rise is 1 K per 5 cm of tube. Thus, it can be concluded that for the heat balance of MSR working under $Re < 1000$ and $d_h > 100 \mu\text{m}$ this scaling effect can be neglected.

Various other effects such as the formation of an electric double layer at the fluid solid interface have been described in literature but their influence is minor as compared to the abovementioned effects [96, 97].

2.3 Mass and Energy Transfer

In the upcoming section the reader is introduced to the different characteristics of mass and energy transfer in microchannels. It was demonstrated previously that a set of continuous equations with no-slip boundary conditions can be applied to describe the behavior inside a microfluidic channel. As a first aspect, residence time distribution (RTD) in MSR is considered. The conclusions of that part are used to simplify the heat and mass balance in microchannels. At the end of this section, safety issues are addressed, and by using the dimensionless form of the heat and mass balance, a criterion for a priori estimation of reactor stability is developed.

2.3.1 Residence Time Distribution in Microstructured Reactors

An MSR is an open system and its performance can be compared to ideal plug-flow, meaning that all molecules at the reactor outlet exhibit an identical residence time. A deviation of an MSR from ideal plug-flow behavior can be analyzed using different classic models described in the literature [98].

The laminar flow in a tube is characterized by a parabolic velocity profile resulting in fluid dispersion along the length of the reactor. This effect is more pronounced in the microchannels with liquid phase [99, 100] than with gas phase [101] (see Figure 2.6). The fast radial diffusion of the molecules efficiently suppresses the formation of a concentration profile similar to the laminar flow profile. The extent of this effect depends on operating conditions such as characteristic dimension of the reactor (d_h), flow velocity (u) and molecular diffusivity (D_m) [102, 103].

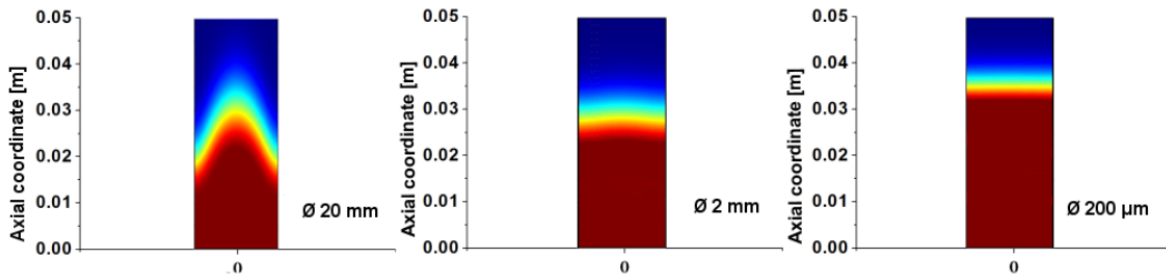


Figure 2.6: Simulated concentration profiles in gas phase laminar flow for tubular reactors with different tube diameters d_R ; ($v = 10^{-5} \text{ m}^2/\text{s}$, $D_m = 10^{-5} \text{ m}^2/\text{s}$, $Re = u \cdot d_R / v = 10$). Adapted from [17].

This effect can be easily explained by using one of the commonly used models, the axial dispersion model. The residence time distribution is described by one single parameter, i.e. the dimensionless Bodenstein number (Bo), representing the ratio of characteristic axial dispersion time ($t_{diff,ax}$) to residence time (τ), as

$$Bo = \frac{u \cdot L}{D_{ax}} = \frac{t_{diff,ax}}{\tau} \quad (2.6)$$

where u is the mean velocity, L is the total channel length and D_{ax} is axial dispersion coefficient. In the case of negligible axial dispersion (ideal plug-flow), the Bo tends to infinity. In reality, plug-flow behavior can be assumed for $Bo > 100$. For complex systems, the axial dispersion coefficient has to be determined experimentally. However, an *a priori* estimation of the axial dispersion coefficient in laminar flow in a cylindrical channel with diameter d_R is possible if the molecular diffusion coefficient D_m is known [104, 105]:

$$D_{ax} = D_m + \frac{u^2 \cdot d_R}{192 \cdot D_m} \quad (2.7)$$

By putting equation (2.7) into the definition of Bo, one obtains a simple approximation while assuming that the contribution of molecular diffusion in axial direction (the first term) is negligible compared to convection effects:

$$Bo \approx 50 \cdot \frac{D_m}{(d_R / 2)^2} \cdot \frac{L}{u} = 50 \cdot \frac{\tau}{t_{diff,rad}} \quad (2.8)$$

Hence, plug flow behavior can be assumed for liquid phase ($D_m = 10^{-9} \text{ m}^2/\text{s}$) in tubular reactors if:

$$\frac{\tau}{d_R^2} > 5 \cdot 10^8 \text{ s/m}^2 \quad (2.9)$$

and in gas phase ($D_m = 10^{-5} \text{ m}^2/\text{s}$) if:

$$\frac{\tau}{d_R^2} > 5 \cdot 10^4 \text{ s/m}^2 \quad (2.10)$$

To visualize the link between residence time and reactor diameter needed for ideal plug flow behavior, equations (2.9) and (2.10) were plotted in Figure 2.7. It has to be pointed out that this relation is solely valid for channels under laminar flow in absence of radial secondary flows (e.g. vortices), whereas it cannot be applied to structured channels, where generally higher Bo are obtained.

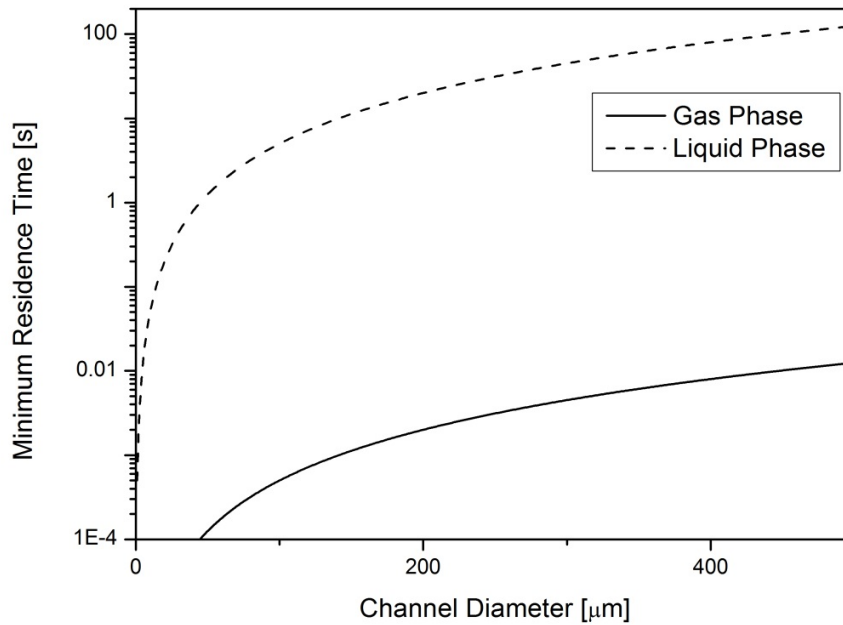


Figure 2.7: Minimum residence time required to acquire plug flow behavior ($Bo > 100$) in gasphase ($D_m = 10^{-5} \text{ m}^2/\text{s}$) and liquid phase ($D_m = 10^{-9} \text{ m}^2/\text{s}$) microchannels.

Whereas for gas phase reactions even at diameters as high as 500 μm plug flow can be assumed already at residence times as low as 0.01 s, for liquid microfluidics a residence time of 10 s is necessary already at an inner diameter of 100 μm . If fast liquid phase reactions (low residence time in the order of seconds) are carried out in such channels, residence time distribution induced by the laminar flow profile has to be taken into account when operating with channel diameters above 100 μm [100, 106, 107]. Trachsel *et al.*[105] measured the axial dispersion by injecting a pulse in a liquid flow channel with rectangular cross section ($d_h = 178.6 \mu\text{m}$) and reported that the plug flow behavior can be readily assumed at $\tau > 70$ s. As expected, a relatively high Bo was obtained ($Bo_{\text{measured}} \approx 83$ at $\tau = 70$ s) due to long residence time (see equation (2.9)). The discrepancy between the measured and the calculated Bo ($Bo_{\text{calculated}} \approx 431$ at $\tau = 70$ s) is attributed to partly the cross section, which is rectangular and not circular as assumed in the approximation, and partly to the non-ideality of the injected pulse.

To reduce residence time distribution of liquids, two strategies have been proposed. On the one hand, a second phase is introduced into the MSR in order to obtain a segmented flow pattern (slug flow) [105, 108]. In this case, each slug of the dispersed phase can be seen as a microsized perfectly mixed batch reactor travelling through the microchannel. All the molecules of one “micro-batch” exhibit the same residence time resulting in a high Bo number. In residence time distribution experiments, Kuhn *et al.* [108] demonstrated that the narrowest distribution is attained for the molecules in the non-wetting phase, thus, avoiding the communication between two “micro-batches” through the liquid film. The second strategy to narrow down residence time is the use of mixing elements [109, 110]. By creating secondary flows, the radial interchange of molecules disturbs the laminar flow profiles. Hence, when carrying out a fast reaction in a micromixer, plug-flow behavior can be attained even for liquid phase reactions.

2.3.2 Mass and Heat Balance in Microchannels

In order to develop the mass and heat balance inside gas and liquid phase cylindrical microchannels, plug flow behavior is assumed in the following. As already demonstrated in section 2.3.1, it is valid for most of the gas phase reactions and for liquid phase channels operated under presence of secondary flows. Hence, no radial gradients of concentrations need to be considered. In the gas phase, mass and heat transport have the same characteristic time. The value of Prandtl number (Pr) and Schmit number (Sc) is typically $Pr \approx Sc \approx 1$.

$$\frac{Sc}{Pr} = \frac{t_{diff,ax}}{t_{therm.diff,ax}} = \frac{\alpha}{D_m} \approx 1 \quad (2.11)$$

The analogy between heat and mass transfer [104] allows the above equations to be applied for heat transfer in gas phase reactions resulting in high Pe_t , and, in turn, in small radial temperature gradients. However, this assumption has to be reconsidered for fast gas phase reactions with high activation energies such as combustions where radial temperature gradients exist [87, 111]. In the liquid phase, heat transport

rates are much higher compared to the mass transfer (e.g. for water $Sc/Pr = 1200/7 = 171$), and therefore, the assumption of an isothermal radial temperature can be readily applied.

To simplify the system, the scaling effects described in the previous sections are neglected and only axial dispersion of mass and heat is addressed. Assuming plug flow behavior [16], the material balance for a small volume element (ΔV) at the reactor steady state is written as

$$-\frac{d\dot{n}_i}{dV} + \nu'_i \cdot r = 0 \quad (2.12)$$

with \dot{n}_i being the molar flux of the i -th chemical compound, ν'_i the stoichiometric coefficient of the i -th reactant for a reaction with reaction rate r .

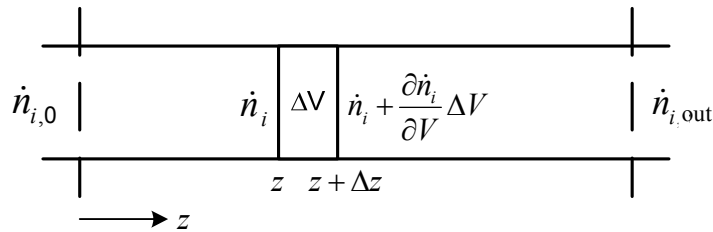


Figure 2.8: Mass balance for an ideal plug flow reactor.

Assuming the cross sectional area S ($dV = S \cdot dz$) and the flow velocity u in z -direction to be constant, the above equation can be written for each concentration c_i as:

$$u \frac{dc_i}{dz} = \nu'_i \cdot r \quad (2.13)$$

For heat transfer, neglecting the work done on the reacting fluid and assuming constant heat capacity and reaction enthalpy, the energy balance equation can be written as given in the following

$$\frac{dT}{dV} = \frac{dT}{S \cdot dz} = \underbrace{\frac{r \cdot (-\Delta H_r)}{\dot{m} \cdot c_p}}_{\text{Heat produced due to the reaction}} - \underbrace{\frac{U \cdot a \cdot (T - T_w)}{\dot{m} \cdot c_p}}_{\text{Heat removed by maintaining constant wall temperature}} \quad (2.14)$$

In this equation, \dot{m} represents the mass flow rate, U is the global surface specific heat transfer coefficient and a is the surface area per volume. Assuming constant cross section, the above equation can be written as

$$\frac{dT}{dz} = \frac{r}{c_{1,0} \cdot u} \cdot \Delta T_{ad} - \frac{U \cdot a \cdot (T - T_w)}{u \cdot \rho \cdot c_p} \quad (2.15)$$

where ΔT_{ad} is the adiabatic temperature rise:

$$\Delta T_{ad} = \frac{c_{1,0} \cdot (-\Delta H_r)}{\rho \cdot c_p} \quad (2.16)$$

and $c_{1,0}$ is the inlet concentration of the limiting reactant.

If axial dispersion of heat and of mass in the fluid is considered, a second derivative of concentration and temperature appears in equations (2.13) and (2.15), respectively. While mass can disperse axially only through the fluid, heat is also transporter through the walls. The mass and heat balance become [86, 112]:

$$D_{ax} \frac{d^2 c_i}{dz^2} - u \frac{dc_i}{dz} + v'_i \cdot r = 0 \quad (2.17)$$

$$\alpha \frac{d^2 T}{dz^2} - u \frac{dT}{dz} + \frac{r}{c_{1,0}} \Delta T_{ad} - \frac{U \cdot a \cdot (T - T_w)}{\rho \cdot c_p} = 0 \quad (2.18)$$

In order to approximate the real behavior of a MSR where thermal conductivity occurs in the fluid and in the wall, it is recommended to work with a lumped heat conductivity whose value is located between the value of the wall and the pure fluid.

The heat transfer coefficient U includes all the resistances to the evacuation of heat i.e. the resistance between channel wall and fluid h_{in} , the channel wall itself h_{wall} and the resistance located between the outer wall and the cooling fluid h_{out} [113].

$$\frac{1}{U} = \frac{1}{h_{in}} + \frac{(d_{out} - d_R)}{\lambda_{wall} \cdot 2} \frac{a}{a_m} + \frac{1}{h_{out}} \frac{a}{a_{out}} \quad (2.19)$$

where a_{out} is the ratio of outer reactor surface to inner reactor volume, d_R and d_{out} are the inner and outer channel diameter respectively, and a_m is the average specific area of the walls, which is defined as follows for cylindrical channels:

$$a_m = \frac{4 \cdot (d_{out} - d_R)}{\ln\left(\frac{d_{out}}{d_R}\right) \cdot d_R^2} \quad (2.20)$$

The heat transfer coefficient between a fluid and a wall can be estimated using correlations for the Nusselt number (Nu) which is defined as [37]:

$$Nu = \frac{h_{in} \cdot d_t}{\lambda_{Fluid}} \quad (2.21)$$

Especially when looking at the inner volumetric heat transfer coefficient, the substantial increase of heat evacuation gained by decreasing channel size becomes obvious. On the one hand, the specific surface area is proportional to d_h^{-1} and on the other hand, the inner heat transfer coefficient is also proportional d_h^{-1} . Hence, if the inner resistance is rate limiting, the overall volumetric heat transfer coefficient increases with d_h^{-2} . Thereby, one has to keep in mind that for very small diameters, the heat transfer is likely to be limited by the walls for low conducting material or by the outer resistance in a simple tempered bath.

2.3.3 Safety and Stability of Microstructured Reactors

The improved temperature control and reduced risk of runaway in MSR allows operating under new reaction conditions like higher temperature and pressure. The kinetics are speeded up which allows a drastically reduced characteristic reaction time ($t_r = 1/k \cdot c_0^{n-1}$). As mentioned in the introduction, this concept is called ‘‘Novel process windows’’ [11, 46]. Due to the short quenching distance, an operation in

the classical explosive regime becomes possible [114, 115]. The recombination of propagating radicals at the channel walls prevents an ignition of the mixture which makes this type of reactor safe regarding the initiation of a propagating explosion. An example of reaction under explosive regime, the catalytic oxidation of hydrogen with pure oxygen, was demonstrated in MSR without run-away of the reactor [45, 116]. Leclerc *et al.* [117] also studied the oxidation of cyclohexane with pure oxygen which was carried out by working with a mixture above the flammability limit of 4 % in a capped silicon etched MSR. However, for a propagating explosion front entering the microchannel from the inlets/outlets, no quenching of the reaction was observed [114].

Despite the safety gained through the use of MSR, Etchells [118] raised some important issues that need to be considered. Due to the short residence time in the order of seconds, the system is much more responsive to changes than classical equipment requiring control and monitoring specially developed for this new environment. The process monitoring and control technology need to be adapted and the operators should be trained to fit into the new required specificities. In addition, the reactor channels are very sensitive to clumping or fouling, which can lead to dangerous variations of the system conditions, which, in turn, can even result in a run-away. Besides, the reaction rate varies with the modification in parameters. The unexpected increase of reaction rate can lead to self-acceleration of the reaction, or a decrease of the reaction rate can lead to accumulation of reactive substances and provoke an uncontrolled reaction in downstream equipment. Thus, the operator and the monitoring equipment have to assure that the reaction conditions are maintained within a narrow tolerable range [114].

The stability criteria developed for conventional continuous reactors by Semenov and Barkelew [119-121] can be applied to MSR (see section 2.1.4), assuming that the axial dispersion of heat is negligible (low conducting wall material). As the criteria were developed for plug flow behavior, they are still valid (yet too conservative) for reactors with axial dispersion. Other sensitivity criteria yielding similar results as the one described in the following can be found in Varma *et al.* [122].

The criterion is based on a dimensionless form of mass and energy balance (equations (2.13) and (2.15)) of an n^{th} order reaction:

$$\frac{dX}{dt'} = \exp\left(\frac{\Delta T'}{1 + \Delta T'/\gamma}\right) \cdot (1-X)^n \quad (2.22)$$

$$\begin{aligned} \frac{d\Delta T'}{dt'} &= q'_{prod} - q'_{rem} \\ &= S' \cdot \exp\left(\frac{\Delta T'}{1 + \Delta T'/\gamma}\right) \cdot (1-X)^n - N' \cdot \Delta T' \end{aligned} \quad (2.23)$$

with

$$\begin{aligned} \Delta T' &= \frac{(T - T_0)}{T_0} \cdot \gamma; \quad t' = \frac{z}{u} \cdot k(T_0) \cdot c_0^{n-1}; \quad \gamma = \frac{E_A}{R \cdot T_0}; \quad S' = \frac{(-\Delta H_r) \cdot c_0}{\rho \cdot c_p \cdot T_0} \cdot \gamma; \quad t_r = \frac{1}{k(T_0) \cdot c_0^{n-1}}; \\ t_c &= \frac{\rho \cdot c_p}{U \cdot a}; \quad N' = \frac{t_r}{t_c} \end{aligned}$$

where, N' is the ratio of characteristic reaction time (t_r) to cooling time (t_c) and S' is heat production potential. The change in temperature along dimensionless time t' is a result of the difference of heat produced and removed. An isothermal operating point is obtained when the dimensionless heat produced q'_{prod} is entirely removed q'_{rem} by the cooling system:

$$q'_{prod} = q'_{rem} \quad (2.24)$$

An operation point is called stable if a small variation in cooling temperature does not affect the systems working temperature. This inherently safe behavior of a system is provided at the operating points where

$\frac{d}{d\Delta T'}(q'_{prod}) \leq \frac{d}{d\Delta T'}(q'_{rem})$. The upper boundary of this condition is the critical case:

$$\frac{d}{d\Delta T'}(q'_{prod}) = \frac{d}{d\Delta T'}(q'_{rem}) \quad (2.25)$$

By solving equations (2.24) and (2.25) for a zero order reaction and by assuming $\Delta T' \gamma \ll 1$ (Frank-Kamenetskii [123]), the following condition for safe operation is obtained for a reaction of the order $n = 0$:

$$N' S' \geq 2.72 \quad (2.26)$$

If applied to higher order reactions, this criterion is still valid but becomes too conservative. The consumption of reactants results in a decrease of the reaction rate with time t' , and thus, the heat production will diminish with time, which is not accounted for in equation (2.26). As an analytical solution is not possible for $n \neq 0$, a numerical method is applied.

The numerical simulations were carried out by Renken *et al.*[112, 124] and a modified criterion was proposed. It states that a reactor will run-away for a dimensionless temperature rise $(\Delta T') \geq 1.2$, independently of the reaction order. In terms of N' and S' , the following correlations were proposed for safe operation:

$$N' S' \geq 2.72 - \frac{B}{\sqrt{S'}}$$
$$\begin{aligned} n = 0.5 : B = 2.60 \\ n = 1 : B = 3.37 \\ n = 2 : B = 4.57 \end{aligned} \quad (2.27)$$

Figure 2.9 shows a plot of the correlations given in equation (2.27). The grey area included within the dashed lines represents the results of literature correlations [122] for safe operation of a first order reaction. As can be seen from the comparison, the presented criterion is relatively conservative compared to others.

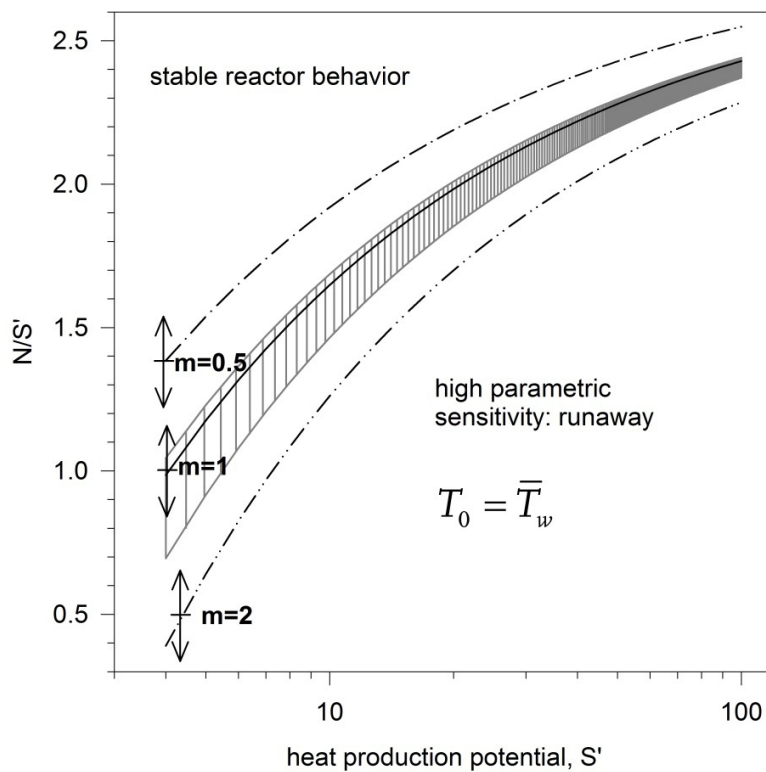


Figure 2.9: Parametric sensitivity of a plug flow reactor for different reaction orders. Adopted from [125].

Thereby, m denotes the reaction order n .

It has to be pointed out that this criterion initially proposed by Semenov [120, 121] was developed for a zero order reaction. In this case, temperature rises until equilibrium of heat production and heat removal, forming a plateau until complete consumption of the reactants. Whereas, when working with higher order reactions, temperature continuously diminishes after reaching the aforementioned equilibrium. Accordingly, the reaction rate strongly decreases on the one hand due to temperature effect, and on the other hand, due to the reduced concentration. Thus, reaching high conversion with a “safe” reactor requires extremely high residence times due to this quenching effect. In order to maintain acceptable productivity, other strategies such as a stepwise increase of temperature have to be applied [32].

To assess safety of a complete process, Klais *et al.*[126] adopted a “HAZOP-LIKE” method for risk analysis in MSR which combines the advantages of the process hazard analysis (PHA) and the hazard

operability study (HAZOP). It provides a systematic way with well-defined and codified guiding words to evaluate a process. Its main advantage is that it can be carried-out at the early stages of a process design which allows an *ab initio* integration of the safety measures. This method was applied to two demonstration projects, i.e. oxidation of SO₂ to SO₃ by air and synthesis of an Ionic liquid (1-ethyl-3-methyl imidazolium ethyl sulfate).

2.4 Mixing in Microstructured Reactors

Often the reaction kinetics in novel process windows [11, 46] are accelerated to a point where they are influenced or completely limited by mass and heat transport. To avoid an effect of mixing on product quality in complex reactions, mixing time needs to be at least one order of magnitude below characteristic reaction time [127, 128]. Therefore, devices achieving fast mixing of the reactants are required. In the past, much effort has been devoted to the development of efficient micromixers [38, 93, 129]. In general, one distinguishes between two types of mixers: passive and active mixers. The former type works essentially with energy provided by pumping while the latter uses an external energy source such as acoustic fields [130-132], electric fields (electro-kinetic instability) [133-135], magnetic fields [136-138] or microimpellers [139, 140]. Although fast mixing can be achieved with passive mixing devices, they often require complex and expensive control units [128]. For this reason, only passive mixers will be considered in the following. Furthermore, the considered mixers have essentially been developed for liquid phase, which is more challenging compared to gas phase due to the four orders of magnitude lower diffusion coefficient.

2.4.1 Passive Micromixers

The simplest passive mixers are Y- and T-type mixers, which provide a contact of two flows in one point, i.e. single-injection mixers. With increasing flow rate, mixing time decreases due to vortex formation

[141]. Kashid *et al.*[142] investigated the effectiveness of various mixers and found the square shaped T-mixer to be the best compromise between short mixing time and efficient use of energy. In this type of mixer, three flow regimes were identified as shown in Figure 2.10 [143-146]:

- Stratified flow: a clear interface separates the two flows (lamination) and mixing occurs entirely by diffusion
- Vortex flow: the vortex creates secondary surface area
- Engulfment flow: the axial symmetry of the flow breaks apart.

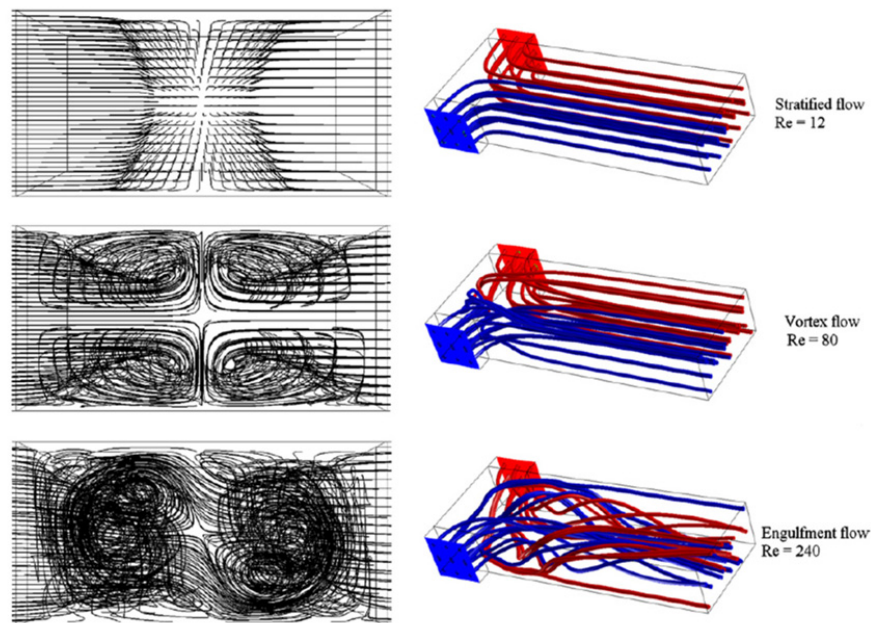


Figure 2.10: Three types of flow patterns observed in a simple T-mixer. Image adopted from Soleymani *et al.* [147].

The transition from one flow regime to another depends not only on the Reynolds number, but also on the geometrical aspects of the reactor [141, 147-149]. When working with fast chemical reactions (in the order of seconds), sufficiently low mixing times can only be attained in the vortex or engulfment flow regime. If lower flow rates are chosen, the diffusion process will be limiting the overall conversion due to small interfacial area and a long diffusion path (half of the channel width). Hence, the crucial point of any mixer is the creation of secondary flow patterns which are superposed to the typical laminar flow profile.

One way to improve mixing quality at Reynolds numbers in the range of a few hundred is the design of curved channels [38, 150, 151]. Thereby, the mixing quality is improved by creating secondary flows for Dean numbers (De) > 140 , where

$$De = Re \left(\frac{d_h}{R''} \right)^{0.5} \quad (2.28)$$

In this equation, R'' designates the radius of the channel curve. The same effect is observed for zigzag channels [152].

All of the mixing principles mentioned so far are based on the fact that the inertia forces break the laminar flow profile at some point, leading to homogenization. However, when working at low Reynolds numbers, the inertia forces are not sufficient. In this regime, different strategies of mixer design have to be applied. By increasing the number of lamellae of alternate concentrations, the so called striation thickness is decreased resulting in lower diffusion time. This principle is used by multi-laminating mixers, which work also at very low Reynolds number, as they only rely on mixing by diffusion. They can be further divided into the parallel and the serial approach. A detailed overview of this type of mixers is given by Hessel *et al.*[38]. Another remarkable structure which is used to mix two liquids at low Reynolds number is the use of grooved channels [153-157]. The grooves create a transverse velocity component at the bottom of the channel which leads to a swirling motion in the upper part of the channel. Interestingly, this type of mixer loses efficiency with increasing Reynolds number, as the flow ceases to follow the grooves.

Due to the small dimensions, the type of pump used plays an essential role in MSR. When two fluids are introduced in a T-junction, a distinct lamination appears and mixing occurs by diffusion. This type of injection is typically observed with discontinuous syringe pumps, which provide a relatively constant flow rate. For comparison, Glasgow and Aubry [158] applied a sinusoidal inlet flow at both inlets resulting in a remarkable increase in mixing quality being maximal for a phase shift of 180° between the pulsations of the two inlets. Pulsations typically appear when working with continuous pumps such as HPLC pumps.

Ducry and Roberge [159] observed very strong effect when the change of pulsation frequency masked the efficiency difference between various mixer types.

2.4.2 Estimation of Mixing Time

By comparing different type of mixers, Falk and Commenge [160] developed general rules for mixing in MSR. The mixing at low Re (< 1000) can be reduced to two distinct phenomena, which are (I) the deformation of lamellae due to the shear field increasing the interfacial surface area followed by (II) complete homogenization due to diffusion. In the case of a T-mixer operated in the stratified flow regime, mixing occurs only by diffusion and the mixing time constant is described as [160, 161]:

$$t_{diff,rad} = A' \cdot \left(\frac{d_{half}^2}{D_m} \right) \quad (2.29)$$

where d_{half} is the half thickness of the aggregate and A' is a shape factor defined as

$$A' = \frac{1}{((p' + 1)(p' + 3))} \quad (2.30)$$

with $p' = 0$ for a slab, $p' = 1$ for a cylinder and $p' = 2$ for a sphere. The aggregate behaves like a first order dynamic system with time constant $t_{diff,rad}$ as shown in Figure 2.11. It can be seen that for the assumption of pure mixing in liquid phase ($D_m = 10^{-9} \text{ m}^2/\text{s}$) a slab size of $50 \text{ }\mu\text{m}$, i.e. a channel size of about $100 \text{ }\mu\text{m}$ is required in order to get $t_{diff} \approx 1 \text{ s}$. For gas phase reactions, mixing by diffusion is much faster ($D_m = 10^{-5} \text{ m}^2/\text{s}$).

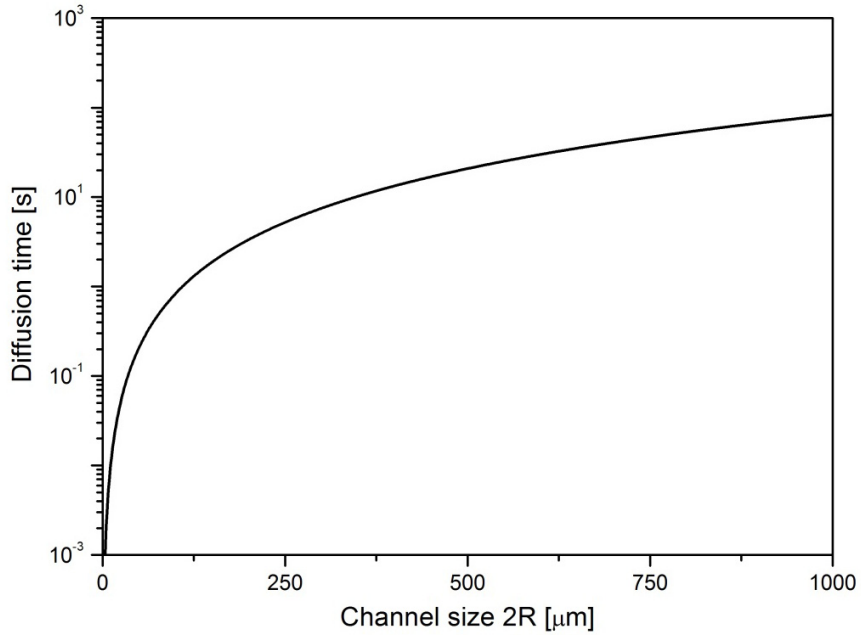


Figure 2.11: Diffusion time constant in liquid phase in a slap ($p = 1$) according to equation (2.29).

Based on the model of Baldyga and Bourne [162], Falk and Commenge [160] developed an expression assuming that all the energy dissipated in a tube (mainly due to shearing) is used for mixing, which results in the shortest possible mixing time for laminar flow. In this case, characteristic mixing time can be described by the following expression:

$$t_{diff+shear} = \frac{1}{\sqrt{2}} \left(\frac{\nu}{\varepsilon} \right)^{0.5} \ln(1.52 \cdot Pe_m) \quad (2.31)$$

where, ν is kinematic viscosity, Pe_m ($= d_h \cdot u / D_m$) is the Péclet number and ε is the power dissipation per unit mass of fluid:

$$\varepsilon = \frac{Q \cdot \Delta p}{\rho \cdot V} \quad (2.32)$$

The pressure drop can be estimated according to the Hagen-Poiseuille flow equation:

$$\frac{\Delta p}{L} = \frac{32 \cdot \rho \cdot \nu \cdot u}{d_h^2} \quad (2.33)$$

Combining the equations above, an expression for mixing time constant as a function of Pe_m , D_m and d_i is obtained.

$$t_{diff+shear} = \frac{d_h^2}{D_m \cdot 8 \cdot Pe_m} \ln(1.52 \cdot Pe_m) \quad (2.34)$$

By comparing the above relation with experimentally measured data, the energetic efficiency of mixing (η) can be defined as the ratio between shear rate effectively used for mixing and total shear rate used for the flow:

$$\eta = \frac{\dot{\gamma}}{\dot{\gamma}_{max}} = \frac{\dot{\gamma}}{\sqrt{\varepsilon / (2 \cdot \nu)}} \quad (2.35)$$

Falk and Commenge [160] compared the performance of different mixers studied in literature and obtained very low energetic efficiency $\eta = 3 \%$ (see Figure 2.12). Baldyga *et al.*[163] yielded similar values for mixing efficiency, i.e. $\eta = 0.75 \%$ for a twin-screw extruder and $\eta = 5 \%$ for a semi-batch reactor. With the existing micromixers, the mixing time and specific energy input are correlated as

$$t_m = 0.15 \cdot \varepsilon^{-0.45} \cdot s \cdot (\text{kg/W})^{0.45} \quad (2.36)$$

The reason for the poor energetic efficiency of mixers is that most of the mechanical energy used to achieve the flow is dissipated in zones of pure component which does not contribute in mixing of two zones of alternate concentrations.

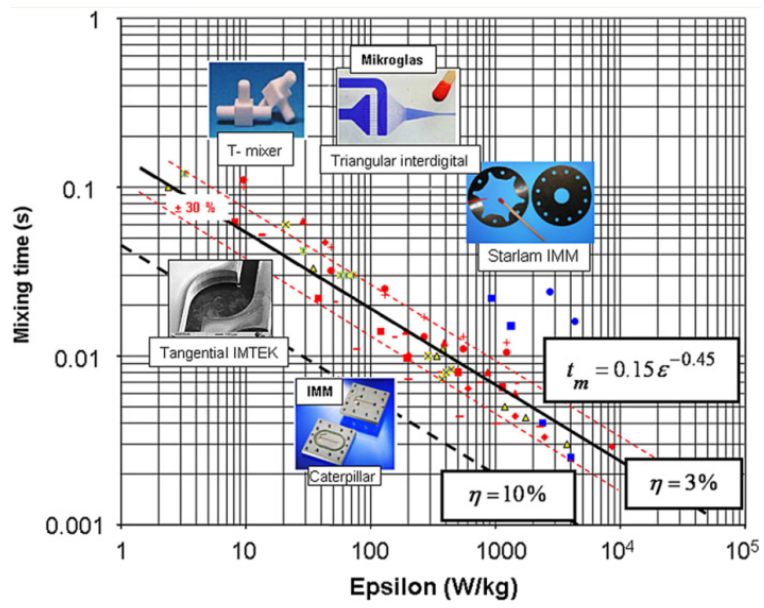


Figure 2.12: Experimental determination of mixing time with resulting energetic efficiency of mixing. Adapted from Falk and Commenge [160].

2.5 Notations

a	Specific surface area, [m^2/m^3]
A'	Shape factor [-]
B	Fit parameter [-]
c_p	Mean heat capacity, [$\text{J}/(\text{kg K})$]
c	Concentration, [mol/m^3]
d_h	Hydraulic diameter, [m]
d_R	Reactor diameter, [m]
D_{ax}	Axial diffusion coefficient, [m^2/s]
D_m	Molecular diffusion coefficient, [m^2/s]
E_A	Activation Energy, [m^2/s]
h	Heat transfer coefficient, [$\text{W}/(\text{m}^2\text{K})$]
H_r	Reaction enthalpy, [J/mol]
k	Rate constant, [$(\text{m}^3/\text{mol})^{n-1}/\text{s}$]
L	Total length of the reactor, [m]
L'	Characteristic length, [m]
M	Molecular weight, [kg/mol]
m	Reaction order (same as n)
\dot{m}	Mass flow rate, [kg/s]
n	Reaction order
\dot{n}	Molar flow rate, [mol/s]
N'	Heat removal potential, [-]
p	Pressure, [Pa]
p'	Parameter, [-]
q'	Dimensionless energy flow, [-]

2 State of The Art

Q	Volumetric flow rate, [m^3/s]
r	Reaction rate, [$\text{mol}/(\text{s m}^3)$]
R''	Curve radius, [m]
S	Cross section area, [m^2]
S'	Heat production potential, [-]
t	Characteristic time, [s]
t'	Dimensionless time, [-]
T	Temperature, [K]
T'	Dimensionless temperature, [-]
u	Velocity, [m/s]
U	Heat transfer coefficient, [$\text{W}/(\text{m}^2\text{K})$]
V	Volume, [m^3]
X	Conversion, [-]
y	Ordinate, [m]
z	Axial coordinate, [m]

Greek

α	Thermal diffusivity [m^2/s]
γ	Arrhenius number, [-]
$\dot{\gamma}$	Shear rate, [1/s]
Δ	Symbol for difference
ε	Specific power dissipatio, [W/kg]
ε'	Molecular energy scale, [J/mol]
η	Energetic efficiency of mixing, [-]
λ	Thermal conductivity, [$\text{W}/(\text{m K})$]
λ'	Mean free path, [m]

ν	Kinematic viscosity, [m ² /s]
ν'	Stoichiometric coefficient, [-]
ξ_{NC}	Non-circular coefficient, [-]
ρ	Mean density, [kg/m ³]
σ	Molecular length scale, [m]
τ	Residence time, [s]
τ'	Molecular time scale, [s]

Dimensionless numbers

Bo	Bodenstein number $u \cdot L / D_{ax}$, [-]
Da_I	Damköhler number τ / t_r , [-]
De	Dean number $Re \cdot (d_h / R')^{0.5}$, [-]
Kn	Knudsen coefficient, [-]
Nu	Nusselt number $h \cdot d_h / I_{fluid}$, [-]
Pe_t, Pe_m	Péclet number heat/mass $u \cdot L / a$ respectively $u \cdot L / D_m$, [-]
Pr	Prandtl number ν / a , [-]
Re	Reynolds number $u \cdot d_h / \nu$, [-]
Sc	Schmidt number ν / D_m , [-]

Subscript

0	Initial condition
ad	Adiabatic
ax	Axial
c	Cooling
diff	Diffusion
i	Index designating a component
in	Inside
m	Mean or mixing

2 State of The Art

max	Maximal
MSR	Microstructured reactor
out	Outside
p	Production
rad	Radial
rem	Removal
r	Reaction
s	At the outlet
therm	Thermal
w	Wall

Chapter 3

NUMERICAL SIMULATION OF MICROSTRUCTURED REACTORS

In this chapter, the numerical simulations of three different strategies of temperature management are explained in detail and their results evaluated. For this study, numerical simulations were carried out a priori allowing the performance of the respective concepts to be judged before building up an experimental system. To simplify the reading, each concept is treated separately with the results directly following the description of the numerical model. At the end of the chapter, the three strategies of heat management are directly compared, and the most suitable concept, i.e. the multi-injection reactor, maintained for further experimental evaluation. A part of the results described in the following have been published in the master thesis written by Charles Guinand [164].

3.1 Introduction

The hot spot in a chemical reactor is the maximum value of temperature resulting from the interchange between heat release and heat evacuation during the reaction. According to Arrhenius equation [165], in a homogeneously cooled reactor the hot spot occurs at the point where the reaction rate is maximum. Although a high reaction rate leads to higher conversion, in general the hot spot temperature must be limited for several reasons:

3 Numerical Simulation of Microstructured Reactors

- In complex reactions, the increase of temperature favors the reaction with highest activation energy. In many cases, this leads to a loss of selectivity towards the desired product [166].
- If the reactor parameters are not chosen accordingly, a slight change of parameters can have dramatic consequences in terms of safety such as the run-away of the reactor [17, 67, 114, 126, 167, 168].
- At high temperature, the material required for construction should be able to hold high thermal stresses meaning increased costs of the reactor.
- When working in a catalytic reaction, several catalyst deactivation processes such as sintering or coking are induced thermally [169]. Thus, high temperature is unfavorable in such cases.

Within the present thesis, especially the first reason is of interest.

Looking at the heat balance of a simple tubular reactor, the most advantageous way to reduce the temperature rise in the reactor is to increase the specific surface area or the global heat transfer coefficient.

The easiest way to put this idea into practice is the use of microreactors, typically having hydraulic diameters below 1 mm [18-20]. Although this concept seems very straight-forward at the first sight, it can be applied only to a limited extent. In the case of quasi-instantaneous reactions with characteristic reaction times in the order of 1 s and less [55, 57, 149], diameters smaller than 100 μm are required to maintain thermal control. Working with extremely small diameter has mainly three disadvantages:

- According to the Hagen-Poiseuille equation [17], the pressure drop increases with $1/d_R^2$ for a constant flow velocity. The specific power consumption from pressure drop ε in W/kg is investigated using equation (3.1) [160]:

$$\varepsilon = \frac{Q \cdot \Delta p}{\rho \cdot V} = 32 \cdot \nu \cdot u^2 \cdot \frac{1}{d_R^2} \quad (3.1)$$

The target throughput for a production on an industrially relevant scale Q_{tot} is obtained by numbering up the channels.

- In addition, working with very small diameter increases the risk of channel clogging which can lead not only to higher friction losses but also to an uncontrolled behavior of the reactor.
- For a fixed target throughput, due to the small volume of the reactor, the numbering-up costs increase significantly with decreasing diameter, as more parallel units need to be set up.

Hence, for thermal management, it is essential to design a microchannel with an optimal diameter that on the one hand, is small enough to remove the heat produced, and on the other hand, large enough to avoid unnecessary energy losses. One viable solution to reduce energy consumption is the use of small channels where necessary [17, 170, 171], followed by a gradual increase of channel size. In this case, the channel diameters are kept small only in the part where high heat removal (or intensive mixing) is required, the residence time needed to finish the reaction is provided by a channel with larger diameter lowering pressure drop [32, 55]. However, even with this approach, one cannot operate with channel diameters smaller than 100 μm .

To enhance thermal control when carrying out rapid exothermic reactions, alternative strategies of reactor design can be imagined:

- Active heat exchange or mixing elements like fins or static mixers [172]: they increase the overall heat exchange coefficient. However, the gained benefits should not increase the technical complexity [171].
- Use of highly heat conducting material for microchannel wall: On the one hand, reduce the heat evacuation resistance, and on the other hand, distribute the locally produced heat along the length of the microreactor.
- Multi-injection concept: spread heat production along the channel length to reduce local heat density and thus diminish the magnitude of the hot spot.

In this chapter, numerical simulation is used as a tool to assess the efficiency of different approaches to reduce hot spot temperature. The first strategy is not further analyzed as it is a widely known concept which comes from the domain of active heat exchangers [172], and its effectiveness is rather a question of

feasibility from the manufacturing point of view. Hence, three specific reactor designs are modeled based on the two latter of the listed strategies:

1. The microchannel reactor with highly conductive walls
2. The multi-injection microreactor
3. The micro-annular reactor (MAR)

The first reactor is a simple microchannel corresponding to the geometry of commercially available tubing [173, 174] with an inner channel diameter of 500 μm and an outer diameter of 1600 μm . The model contains conduction terms (second derivatives of mass and temperature) allowing evaluation of the impact of thermal conductivity on the magnitude of the hot spot. A similar analysis was carried out by Stief *et al.* [86] for micro heat exchanger. They modeled the impact of wall conductivity on heat exchange efficiency and found glass to be the most efficient material. Furthermore, Norton *et al.* [87, 111] studied the stability of methane/air and H_2 /air combustion flames in microchannels with different thermal conductivities, demonstrating the reduced hot spot temperature in the wall by using higher conductive material. Horny *et al.* [88] managed to homogenize temperature during the oxidative steam reforming of methanol by introducing highly conductive brass wires, transferring heat from the fast exothermic partial oxidation of methanol to the cold reforming part.

In the multi-injection microreactor, the limiting reactant is fed at several injection points along the length, thereby spreading heat production resulting in several small hot spots. It can be seen as the continuous form of a periodic fed semi-batch reactor. This concept, which has been proved to work on macro scale reactors [175-177] has been recently adapted for liquid phase reactions in microreactors with promising results [17, 170, 171]. The numerical simulation of this reactor will help to identify the potential of this strategy and the optimal set of parameters to be used.

Finally, the last model represents a novel type of multi-injection reactor developed during this study. Compared to the conventional multi-injection reactor, the geometry is altered and the amount of injection points is increased up to infinite, leading to a continuous distribution of the limiting reactant along the length. This type of reactor is referred to as “micro-annular reactor”, owing to its geometry consisting of a

concentric metal or ceramic filter and a cylindrical case as shown in Figure 3.1. One liquid flows through the filter while the other flows through the annular space between the filter and the cylindrical case. The high porosity with small pore size of the filter allows uniform distribution of the fluid through it. As soon as both reactants contact each other in the annular region, the reaction takes place. A mathematical model was developed and the simulations were carried out to investigate the concentration and thermal behaviour for fast exothermic reactions.

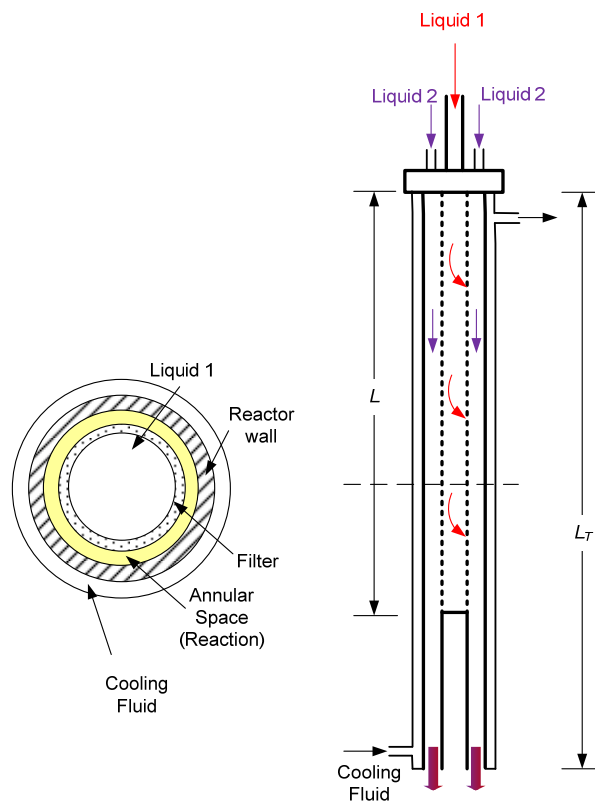


Figure 3.1: Scheme of the micro-annular reactor.

The three strategies, i.e. the axially conductive microchannel reactor, the multi-injection microreactor and the micro-annular reactor, are presented separately in the following. For each reactor type, the model is described followed by the results. The results obtained are compared in the conclusion, where the different approaches are discussed in terms of applicability.

3.2 Microchannel with Highly Conducting Walls

The model of a microchannel with highly conducting walls is described in the first part of this section, followed by the results presented in the second part. Thereby, the wall material is considered as anisotropic with thermal conductivity being different in radial and axial direction in order to separately analyze their respective effects. As model reaction, a fast and exothermic synthesis of Ionic liquid was chosen.

3.2.1 Model Description

The aim of the pseudo 2-D model of a microchannel is to describe the interactions between wall, reaction and cooling medium on the development of the axial temperature gradient inside the reaction channel. For this reason, the continuous mass and heat balance is considered in the three domains as follows:

- The reaction channel with a diameter of $d_R = 0.5$ mm (Figure 3.2)
- The cooling channel with an outer diameter of $d_C = 50$ mm and an inner diameter of $d_W = 1.6$ mm
- The wall separating cooling channel from reaction channel with an inner diameter of $d_R = 0.5$ mm and an outer diameter of $d_W = 1.6$ mm (brown)

The model is entitled “pseudo 2-D” as a full resolution is given in axial direction, whereas in radial direction the temperature and concentration are only given at three distinct points (as listed above).

Thereby, the following assumptions are made:

- No radial gradients of temperature and concentration in the reaction channel except for the boundary layer to the wall.
- Axial conduction of heat through the wall is considered using the temperature in the center of the wall
- Anisotropic wall material whose thermal conductivity is different in radial and axial direction.

- Constant cooling temperature of the coolant

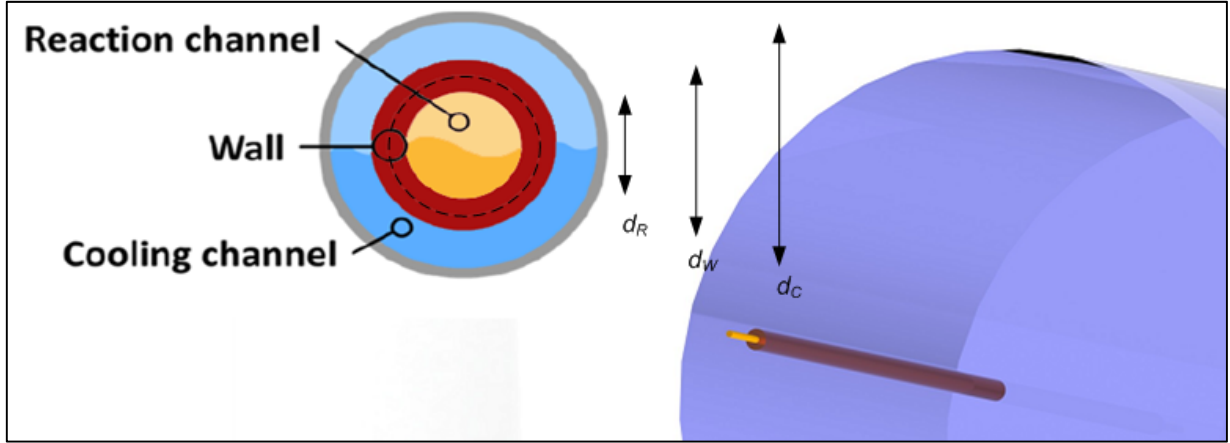


Figure 3.2: Illustration of the pseudo 2-D model used for the simulation of a microchannel reactor. Top part: Cross section of the channels including the dimensions used for simulation. Bottom part: A 3-D scheme drawn to scale.

3.2.1.1 Differential Equations

The equations to be solved in each domain have been partly developed in the previous chapter. In principle, only the steady state solutions are of interest. However, a direct solution of the system of steady state differential equations is numerically extremely challenging. For this reason, the mass and heat transfer equations presented in the following are time dependent. The concentration and temperature profiles presented in the results section (3.2.2) were taken at a time t corresponding to the equilibrium of the system, i.e. at steady state.

Starting from the reaction channel (index “R”), the heat and mass balance are:

$$D_{ax,R} \frac{d^2 c_i}{dz^2} - u_R \frac{dc_i}{dz} + v_i \cdot r = \frac{dc_i}{dt} \quad (3.2)$$

$$\lambda_R \frac{d^2 T_R}{dz^2} - u_R \cdot \rho_R \cdot c_{p,R} \cdot \frac{dT_R}{dz} + r \cdot (-\Delta H_r) - \frac{UA_{R-W}}{V_R} \cdot (T_R - T_W) = \frac{dT_R}{dt} \cdot \rho_R \cdot c_{p,R} \quad (3.3)$$

The second derivative describes the conduction of heat/mass in axial direction, the first derivative designates the axial transport by convection and the remaining terms are the source terms. In this case, the

source terms consist of the transformation/heat formed by the reaction and the exchange of heat with the neighboring wall (index “W”). The axial diffusion coefficient $D_{ax,R}$ is kept low enough to avoid influence of backmixing of mass (ideal plug-flow, see Chapter 2) as it is not the primary target of this study.

As no mass is exchanged in the wall, only the heat balance has to be considered in this domain. Furthermore, no convection occurs, which eliminates the term containing the first derivative of temperature. Thereby, in equation (3.4) the temperature in the middle of the wall T_W is considered, as depicted by the dashed line in Figure 3.2.

$$\lambda_{W,ax} \frac{d^2 T_W}{dz^2} + \frac{UA_{R-W}}{V_W} \cdot (T_R - T_W) + \frac{UA_{W-C}}{V_W} \cdot (T_C - T_W) = \frac{dT_W}{dt} \cdot \rho_W \cdot c_{p,W} \quad (3.4)$$

The source term contains the heat exchange between reaction channel and wall (index “R-W”) on the one hand, and between the coolant and the wall (index “W-C”) on the other hand.

Finally, for the outer channel, a constant temperature is assumed and no mass balance needs to be considered as no reaction is occurring in this channel:

$$0 = \frac{dT_C}{dt} \quad (3.5)$$

3.2.1.2 Estimation of the Radial Heat Transfer Coefficients

For the heat transfer from the reaction channel to the cooling channel, an overall of three serial resistances are taken into account:

- The convective heat transfer at the liquid-solid interface between reaction channel and the wall (index “conv,R-W”)
- The radial conduction inside the wall (index “W”)
- The convective heat transfer at the solid-liquid interface between wall and coolant (index “conv,W-C”)

To obtain the temperature in the center of the wall, i.e. at $d_{W,center} = (d_R + d_W)/2$, the wall resistance is split into two parts: the inner wall resistance and the outer wall resistance as shown in Figure 3.3.

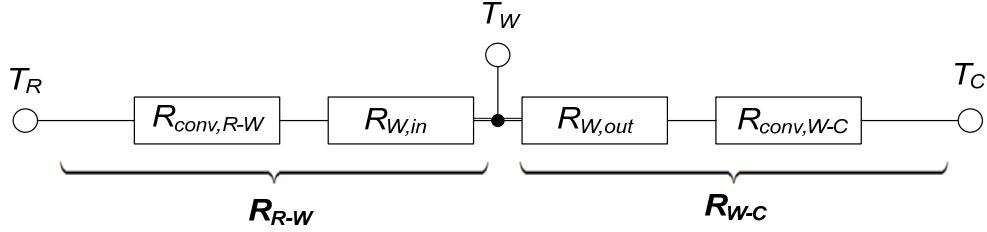


Figure 3.3: Serial arrangement of the radial heat transfer resistances R .

The values for the resistances R_{R-W} and R_{W-C} are calculated according to the following equations:

$$R_{R-W} = \frac{1}{UA_{R-W}} = \frac{1}{h_{conv,R-W} \cdot A_{conv,R-W}} + \frac{\delta / 2}{\lambda_{W,rad} \cdot \bar{A}_{R-W}} \quad (3.6)$$

$$R_{W-C} = \frac{1}{UA_{W-C}} = \frac{1}{h_{conv,W-C} \cdot A_{conv,W-C}} + \frac{\delta / 2}{\lambda_{W,rad} \cdot \bar{A}_{W-C}} \quad (3.7)$$

Where h is the convective heat transfer coefficient, δ the thickness of the wall and $\lambda_{W,rad}$ the conduction in radial direction. Thereby, \bar{A} is the logarithmic average of the surface area (see Figure 3.4) [17, 113]:

$$\bar{A}_{R-W} = \pi \cdot L \cdot \frac{d_{W,center} - d_R}{\ln\left(\frac{d_{W,center}}{d_R}\right)} \quad \text{and} \quad \bar{A}_{W-C} = \pi \cdot L \cdot \frac{d_W - d_{W,center}}{\ln\left(\frac{d_W}{d_{W,center}}\right)} \quad (3.8)$$

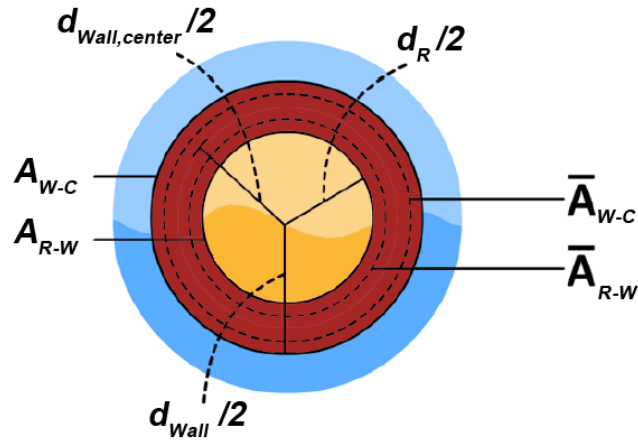


Figure 3.4: Cross section of the channel showing the geometric parameters of the described model.

The Nusselt number in a developed laminar flow inside a tube can be calculated by the means of empirical correlations such as proposed by Hausen [178]:

$$Nu_{R-W} = \frac{h_{R-W} \cdot d_R}{\lambda_R} = 3.65 + \frac{0.19 \cdot (Re \cdot Pr \cdot d_R / L)^{0.8}}{1 + 0.117 \cdot (Re \cdot Pr \cdot d_R / L)^{0.467}} \quad (3.9)$$

In the above equation, L designates the total length of the reactor and Pr is the Prandtl number which is defined in equation (3.11). To calculate the heat transfer coefficient between the wall and the cooling channel, the following correlation is proposed for laminar flow in concentric tubes with an adiabatic outer wall [37]:

$$Nu_{W-C} = \frac{h_{W-C} \cdot d_{h,C}}{\lambda_C} = \left[Nu_{\infty} + f\left(\frac{d_W}{d_C}\right) \frac{0.19 \left(Re \cdot Pr \frac{d_W}{L} \right)^{0.8}}{1 + 0.117 \left(Re \cdot Pr \frac{d_W}{L} \right)^{0.467}} \right] \left(\frac{Pr}{Pr_w} \right)^{0.11} \quad (3.10)$$

where

$$Nu_{\infty} = 3.66 + 1.2 \cdot f\left(\frac{d_W}{d_C}\right)^{0.5} \quad \text{with } f\left(\frac{d_W}{d_C}\right) = 1 + 0.14 \cdot \left(\frac{d_W}{d_C}\right)^{1/2} \quad (3.11)$$

$$Re = \frac{\rho \cdot u \cdot (d_C - d_W)}{\mu}; Pr = \frac{c_p \cdot \mu}{\lambda}; d_{h,C} = d_C - d_W$$

Pr_w is the Prandtl number at the reactor wall temperature and μ the dynamic viscosity.

3.2.1.3 Boundary Conditions

To solve the described system of equations, the initial values and the boundary conditions have to be defined for the different domains. Two types of boundary conditions were chosen for this model [179]:

- Dirichlet boundary condition fixing the value of the variable at the boundary.
- Neumann boundary condition fixing the value of the first derivative of the variable at the boundary.

The boundary conditions applied to the different domains are summarized in Table 3.1.

Table 3.1: Boundary conditions used for the simulation.

	Reaction Channel	Wall	Cooling Channel
Initial Condition	$c = c_0; T_R = T_{C,0}$	$T_W = T_{C,0}$	$T_C = T_{C,0}$
Inlet Boundary Condition	$c = c_0; T_R = T_{C,0}$	$dT_W/dz = 0$	$T_C = T_{C,0}$
Outlet Boundary Condition	$dc/dz = 0; dT_R/dz = 0$	$dT_W/dz = 0$	$dT_C/dz = 0$

3.2.1.4 Default Parameters Used in the Simulations

The model reaction used for the simulation has to be fast and exothermic, with a characteristic reaction time in the order of a few seconds. Besides, a high activation energy is required to form a sharp hot spot in the temperature profile enabling axial heat transfer to take place. For this reason, the synthesis of the Ionic liquid 1-ethyl-3-methylimidazolium ethylsulfate was chosen as model reaction (see Figure 3.5), whose kinetics is described in literature [32, 180]. The reaction parameters used for the simulations are summarized together with the default values of the other parameters in Table 3.2.



Figure 3.5: Synthesis of the Ionic liquid 1-ethyl-3-methylimidazolium ethylsulfate.

Table 3.2: Default parameters used during the simulations with the pseudo 2-D model.

Parameter	Value
Channel diameter, d_R [mm]	0.5
Outer wall diameter, d_W [mm]	1.6
Outer diameter of cooling channel, d_C [mm]	50
Reactor length, L [m]	0.1
Frequency factor, k_0 [$\text{m}^3/(\text{mol}\cdot\text{s})$]	$1.28\cdot 10^9$
Activation energy, E_A [kJ/mol]	89
Reaction enthalpy, ΔH_r [kJ/mol]	-100
Initial concentration of methylimidazole, $c_{1,0}$ [mol/m ³]	4800
Initial concentration of diethylsulfate, $c_{2,0}$ [mol/m ³]	4800
Working temperature, $T_{R,0}$ [°C]	77
Axial thermal conductivity of wall, $\lambda_{w,ax}$ [W/mK]	2
Radial thermal conductivity of wall, $\lambda_{w,rad}$ [W/mK]	2
Thermal conductivity of reaction mass, λ_R [W/mK]	0.58
Thermal conductivity of coolant, λ_C [W/mK]	0.17
Density of wall, ρ_W [kg/m ³]	8960
Density of reaction mixture, ρ_R [kg/m ³]	1100
Heat capacity of wall, $c_{p,W}$ [J/(kg·K)]	390
Heat capacity of reaction mixture, $c_{p,R}$ [J/(kg·K)]	2600
Volumetric Flow rate, Q_R [ml/min]	0.5
Dynamic viscosity of water, μ_{water} [kg/(m·s)]	0.001

3.2.2 Results

The curves shown in this section represent each the system at steady state. Furthermore, the wall material is treated as anisotropic regarding the thermal conductivity. The thermal conductivity in radial direction ($\lambda_{W,rad}$) and in axial direction ($\lambda_{W,ax}$) are varied separately in some simulations to explicitly demonstrate the origin and the significance of some effects. In Figure 3.5, the profiles obtained from the model solved using the default parameters (as listed in Table 3.2) are depicted.

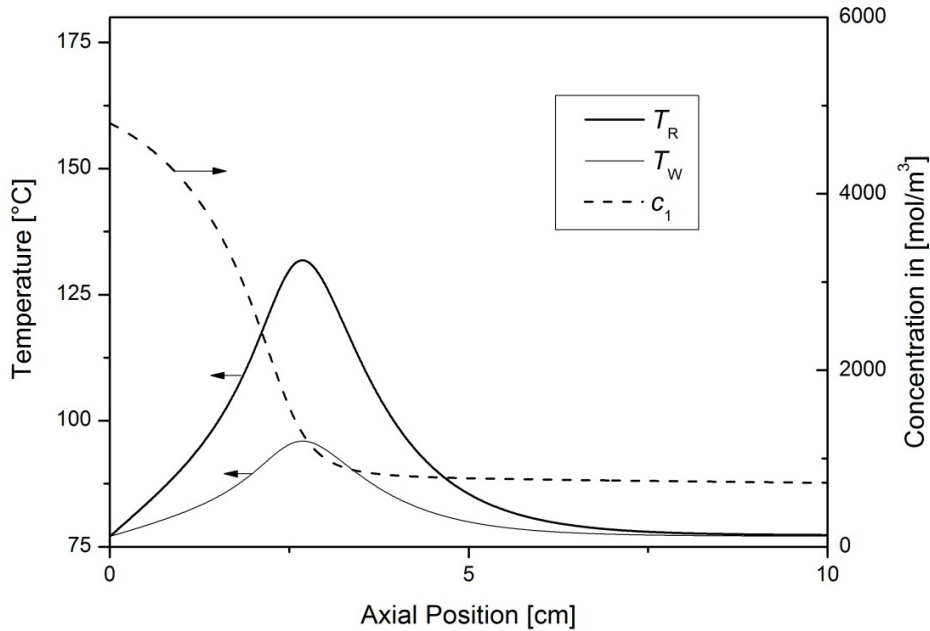


Figure 3.6: Axial profiles of the Pseudo 2-D model using the set of default parameters as indicated in Table 3.2. T_R : Temperature in the reaction channel; T_W : Temperature inside the wall; c_1 : Concentration of methylimidazole.

As expected, a sharp hot spot is formed under the described conditions. The temperature rise is $\Delta T_R = 88$ °C, which is about half of the adiabatic temperature rise ($\Delta T_{ad} = 168$ °C). At these temperatures, the reactor is thermally extremely sensitive to a small change of parameters (see Chapter 2). At the same time, this kind of profile promotes the axial conduction of heat. The profile in the wall is similar to the axial profile in the reaction channel, with the temperature lying between the reactor and the coolant temperature. As the temperature in the wall is closer to the coolant temperature than to the reactor

temperature, one can deduce that in this case, the internal resistance R_{R-W} is higher than the external resistance R_{W-C} . The concentration of the reactants decreases drastically during the formation of the hot spot, leading to a plateau of almost constant concentration due to the strong decrease of reaction rate of this second order reaction. Due to the relatively low values of thermal conductivity, the effect of axial heat conductivity is not visible.

3.2.2.1 Variation of Radial Wall Conductivity

As a first parameter, the radial thermal conductivity of the wall is varied in Figure 3.7 while keeping the axial conductivity at a constant value of $\lambda_{W,ax} = 2$.

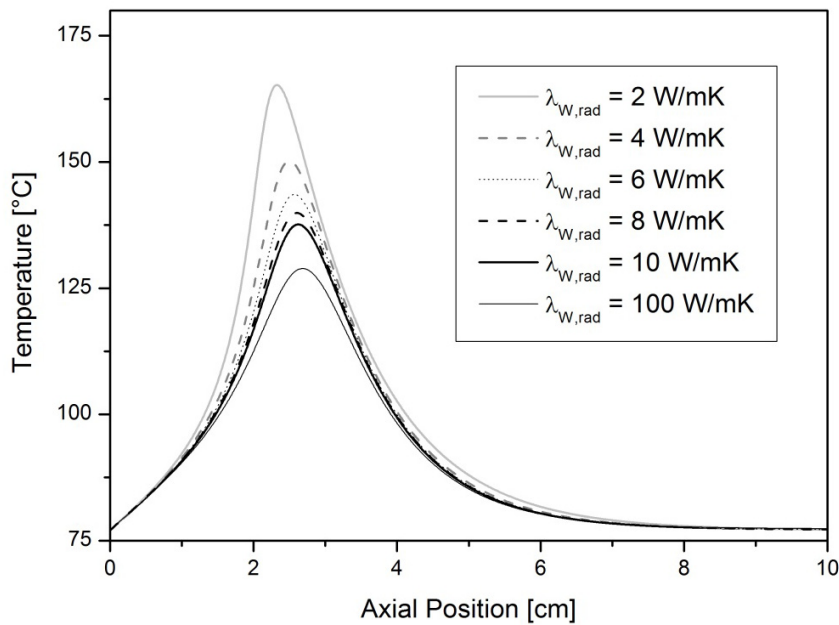


Figure 3.7: Axial temperature profiles obtained in the reaction channel using the set of default parameters as indicated in Table 3.2. The radial thermal conductivity ($\lambda_{W,rad}$) is varied as only parameter.

Varying the radial thermal conductivity directly affects the overall resistance to the evacuation of heat from the reaction channel. Better radial conductivity in the wall leads to an increased heat transport, thus, efficiently reducing the magnitude of the hot spot from initially 168 °C to 129 °C. The main sensitivity to this parameter is observed at thermal conductivities below 20 W/(mK). At higher values the heat transfer

becomes limited by the inner and outer convective resistances ($R_{\text{conv,R-W}}$ and $R_{\text{conv,W-C}}$). The improved temperature control simultaneously has the effect of a slight delay of the hot spot.

3.2.2.2 Variation of Axial Wall Conductivity

In Figure 3.8, analogical to the previous graph, the axial thermal conductivity is varied keeping the other parameters constant.

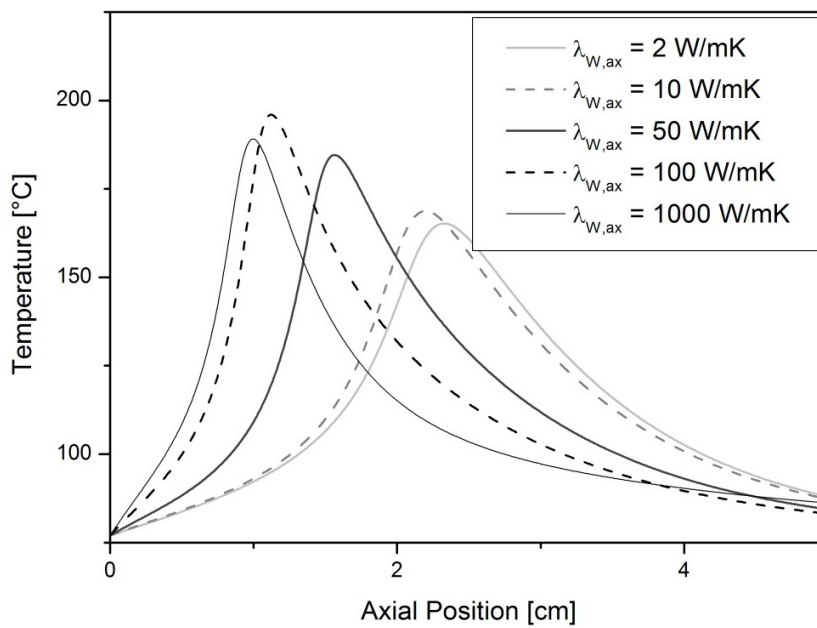


Figure 3.8: Axial temperature profiles obtained in the reaction channel using the set of default parameters as indicated in Table 3.2. The axial thermal conductivity ($\lambda_{W,ax}$) is varied as only parameter.

Two opposing effects are observed: the increase of hot spot temperature with conductivity at values below $\lambda_{W,ax} = 100 \text{ W/(mK)}$ and a decrease of the maximal temperature at higher values. The hot spot temperature at $\lambda_{W,ax} = 2 \text{ W/(mK)}$ is $31 \text{ }^\circ\text{C}$ lower than the ones simulated at $\lambda_{W,ax} = 100 \text{ W/(mK)}$. At the same time, in the former case, the hot spot is located 1 cm further than in the latter case. The explanation for this phenomenon can be found in Figure 3.9.

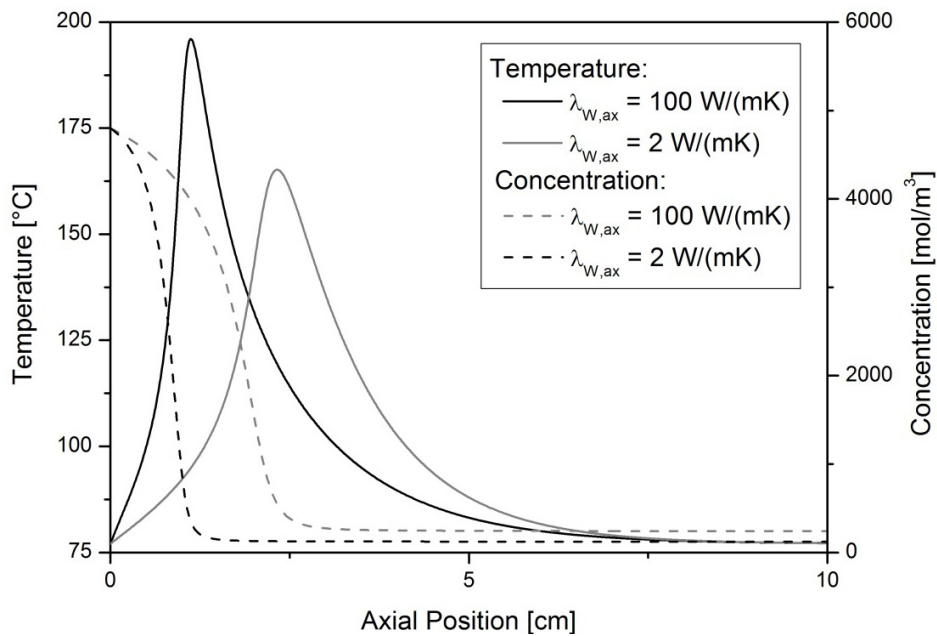


Figure 3.9: Temperature and concentration profiles obtained at low ($\lambda_{W,ax} = 2 \text{ W/(mK)}$) and high ($\lambda_{W,ax} = 100 \text{ W/(mK)}$) axial thermal conductivity.

As mentioned before, the formation of the temperature peak overlaps with a sudden decrease of reactant concentration. At increased axial conductivity, heat is conducted through the walls from the hot spot towards the cold inlet. As the wall at the inlet heats up, consecutively the inlet temperature rises causing an earlier and more pronounced run-away of the reactor. This effect is well reflected by the transient solution of the differential equation shown in Figure 3.10, where one can observe the shift of the hot spot towards the inlet with time. Finally, a further increase of $\lambda_{W,ax}$ above 200 W/(mK) leads to a reduction of the peak temperature (Figure 3.8). Thereby, the heat is evacuated from the hot spot diminishing the wall

temperature at this precise position. The higher gradient between wall and reactor results in a more efficient cooling.

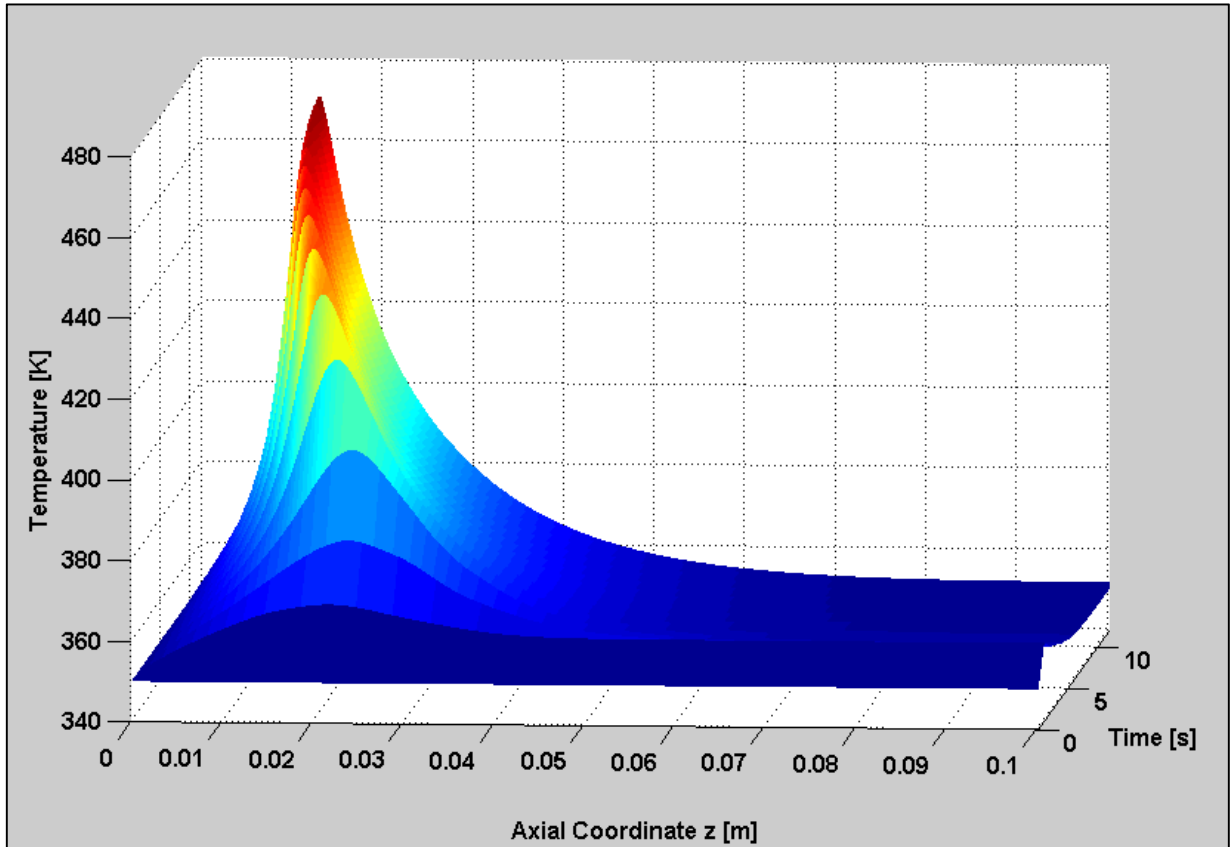


Figure 3.10: Temporal development of the temperature profile at $\lambda_{w,ax} = 100$ W/(mK).

3.2.2.3 Variation of Isotropic Thermal Conductivity

The maximum temperatures seen while varying the axial (Figure 3.8) and the radial (Figure 3.7) thermal conductivity respectively are summarize in Figure 3.11.

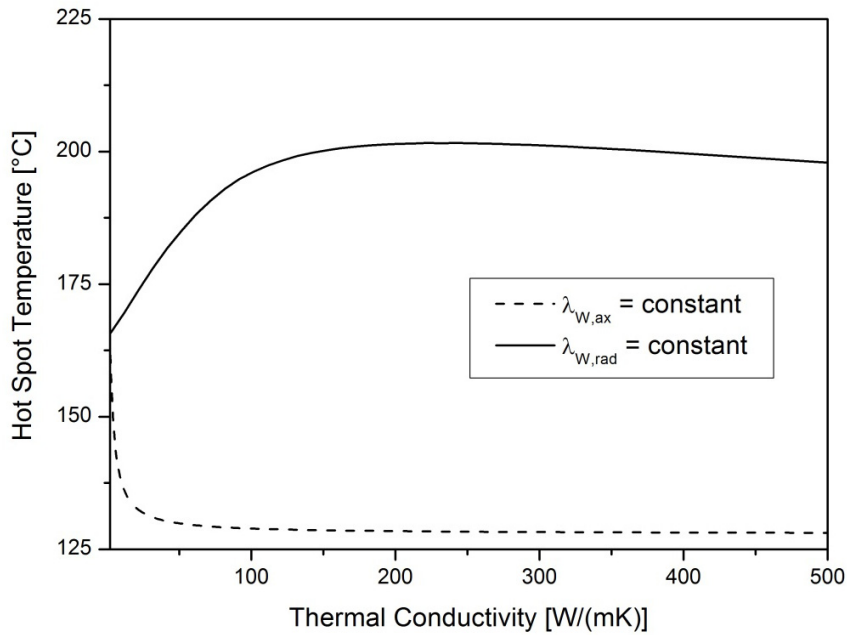


Figure 3.11: Maximum temperature observed while varying the axial respectively the radial thermal conductivity while keeping all the others parameters constant.

While rising axial conductivity leads to higher hot spot temperatures (up to $\lambda_{W,ax} = 200$ W/(mK)) , rising radial conductivity decreases the maximum temperature. When working with isotropic wall material, i.e. $\lambda_{W,ax} = \lambda_{W,rad}$, the presence of these two opposing effect leads to an optimization problem. Accordingly, the simulation of isotropic material results in the curve as shown in Figure 3.12.

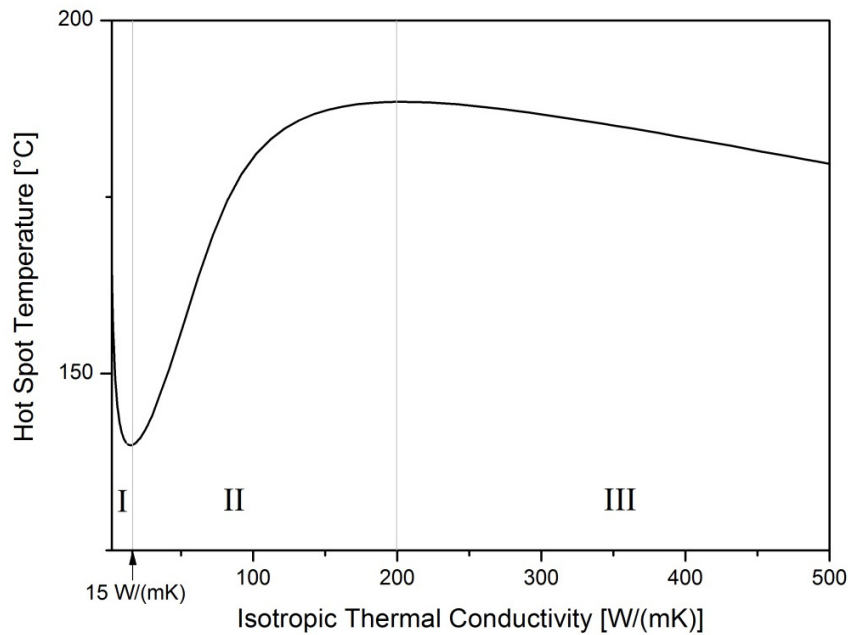


Figure 3.12: Hot spot temperature as function of heat conductivity in the wall. I: Radial conductivity dominates; II: Axial conductivity leads to an increase of inlet temperature; III: High axial conductivity evacuates heat from the hot spot.

The three regions visible on the curve can be explained with the phenomena described above. In the region denoted as “I”, the effect of axial conduction is small whereas the increase of radial conduction very efficiently reduces hot spot temperature yielding a minimum temperature of 140 °C. The effect of axial heat conductivity becomes much more pronounced if the thermal conductivity is further raised (region “II”), leading to an increased inlet temperature and, in turn, to higher temperatures. Finally, when working at conductivities above 200 W/(mK), a decrease of the peak temperature is denoted, which can be explained by the evacuation of heat from the hot spot. Thereby, the minimum temperature reached in region “III” for a reasonable heat conductivity is 183 °C for $\lambda_w = 400$ W/(mK) corresponding to copper [181] as wall material. Hence, for the parameters chosen in this model, the hot spot temperature is minimized by using a rather low conducting wall material such as stainless steel [182]. The benefits of the radial heat conduction outstrip the advantages gained from evacuation of heat from the point of highest temperature.

At last, the impact of the outer thermal resistance $R_{\text{conv,W-C}}$ on the shape of the hot spot temperature curve was analyzed in Figure 3.13. $R_{\text{conv,W-C}}$ contains one convective terms and one conductive term (equation (3.7)). Under default conditions, 75 % of the resistance comes from the convective term.

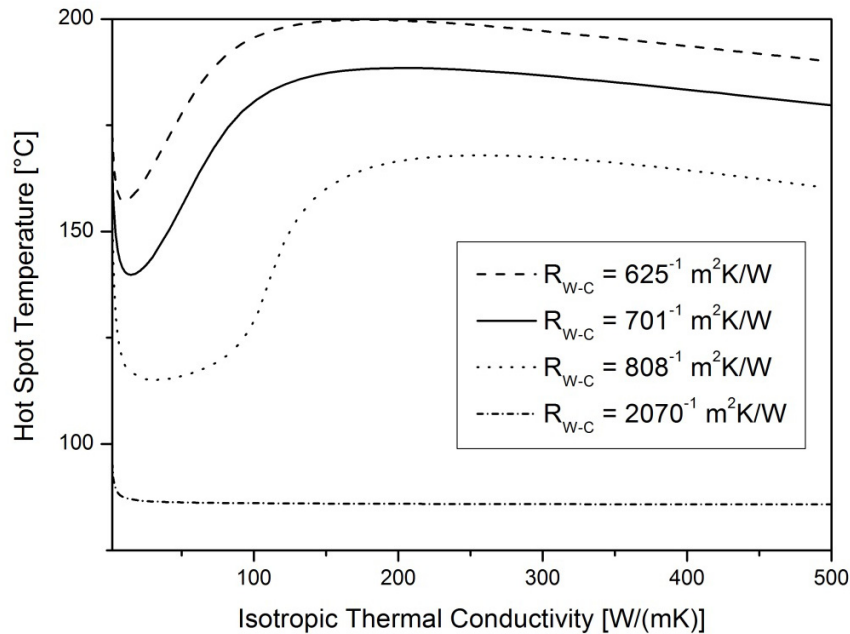


Figure 3.13: Hot spot temperature curve as function of the isotropic thermal conductivity for different outer heat transfer resistances $R_{\text{conv,W-C}}$. The variation of the outer heat transfer resistance is modeled by changing the heat conductivity of the cooling fluid.

The lower the external heat transfer resistance, the broader becomes the region of optimum temperature and the least pronounced the effect of axial conductivity is. In general, stainless steel seems to be the optimal choice of material for the tested geometry. For the case of an efficient external cooling medium, the reactor can be entitled as “stable” (see in Chapter 2), and no more effect of axial heat conduction is visible.

3.2.2.4 Introduction of a Heat Sink

From the results previously shown, one can deduce that too high thermal conductivities are rather unfavorable for the thermal control of the reactor when operating in region II of Figure 3.12. The heat is conducted to the front of the reactor, where it causes an earlier and more pronounced run-away. This

effect disappears only at very high conductivities (region III of Figure 3.12), where sufficient heat can be evacuated through the back end of the reactor.

To benefit from the axial conduction already in region II, a heat sink needs to be introduced into the reactor. Such a heat sink can be an endothermic reaction such as used by Horny *et al.*[88] or a cold inlet stream that needs to be heated up [87, 183]. It has to be noted that these works were done without cooling channel. In the following, the simulations shown in Figure 3.12 are repeated while maintaining the inlet at a temperature of 27 °C instead of 77 °C, which corresponds to a scenario where the reactants enter the reactor without pre-heating room temperature. The remaining parameters, in particular the “coolant” temperature of 77 °C, remain unchanged. The curves obtained are plotted in Figure 3.14 and Figure 3.15.

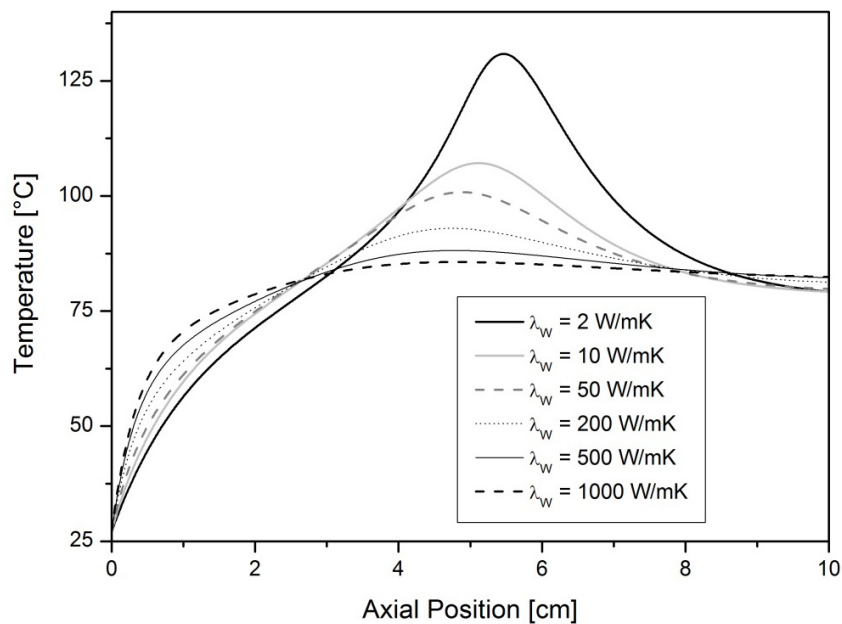


Figure 3.14: Axial temperature profiles obtained in the reaction channel using the set of default parameters as indicated in Table 3.2 with the only difference being the inlet temperature of 27 °C. The isotropic thermal conductivity (λ_w) is varied as only parameter

The presence of a heat sink in the reactor leads to a continuous decrease of hot spot temperature with thermal conductivity in the reactor wall. To understand the phenomenon behind this, one can compare an ideal not conducting wall to a highly conductive wall. In the former case, the coolant supplies heat to the

incoming flows until they reach the reaction temperature, where heat is produced by the reaction leading to the hot spot. In the latter case, the heat of the hot spot is used to heat up the streams, which diminishes the overall heat supplied by the “coolant” to the incoming streams compared to the former case. Thus, hot spot temperature is reduced.

As can be seen in Figure 3.15, an optimum point is not observed anymore, as both, axial and radial conduction, are favorable to diminish hot spot temperature. Thus, the higher the thermal conductivity of the wall material, the more hot spot temperature can be reduced.

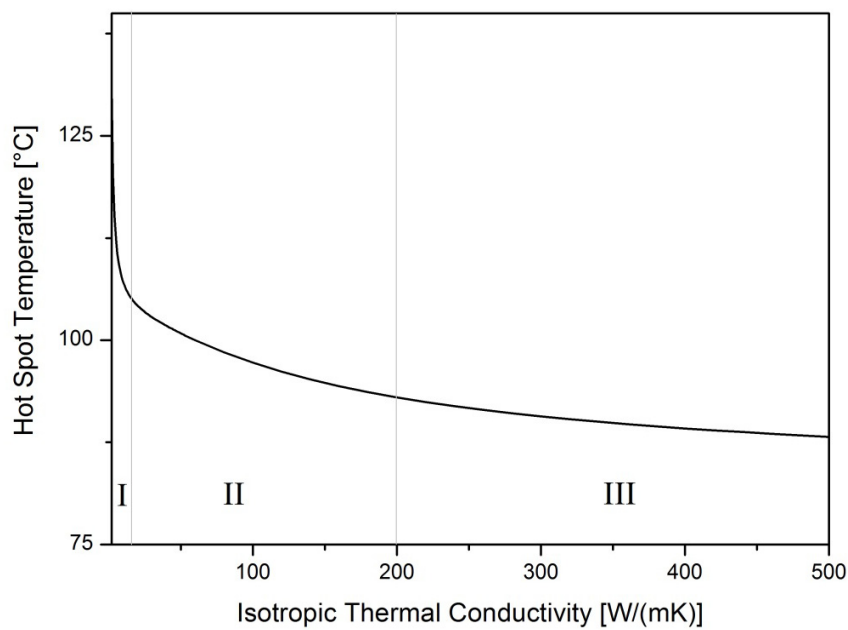


Figure 3.15: Hot spot temperature as function of heat conductivity in the wall. I: Radial conductivity dominates; II: Axial conductivity leads to a further decrease of hot spot temperature; III: Axial conductivity leads to a continuous decrease of hot spot temperature (same as region II).

3.3 Multi-injection Microreactor

In this section, the model of a multi-injection reactor is described followed by the obtained results. The model reaction is the same as in the previous section (synthesis of Ionic liquid), although, for some runs the reaction kinetics were modified to simulate a quasi-instantaneous reaction.

3.3.1 Model Description

For a multi-injection microreactor with a total of N injection points as shown in Figure 3.16, the mass balance can be derived with a similar approach as for a single-injection MSR (equations (3.2), (3.3)). For simplification, the second order terms i.e. axial dispersion of mass and heat are neglected in the following. Hence, the set of partial differential equation is transformed in a set of ordinary differential equations.

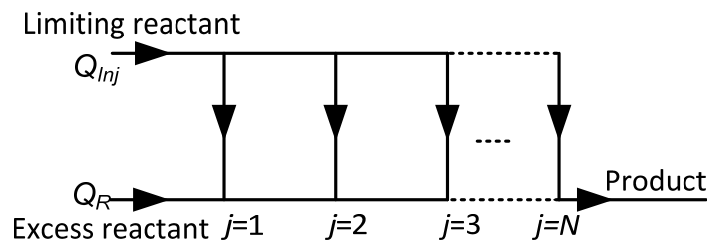


Figure 3.16: Scheme of a multi-injection reactor with N injection points.

3.3.1.1 Differential Equations

The only difference from the model described in the previous section is a sudden change in temperature and reaction mass at each injection point j , which can be described by using a Dirac pulse $\delta(z)$ and the Heaviside function $\sigma(z)$. Reactant 1 contained in the injected flow (index “Inj”) is considered to be the limiting reactant which is added into the excess reactant in the main reaction channel (index “R”). For clarification it has to be pointed out that the use of the terms “limiting/excess reactant” only describe the state of the reactants before reaching the last injection point, where the stoichiometric balance is attained. It is assumed that the volume of limiting reactant injected is equal at each injection point and mixes instantaneously in the main stream.

$$\frac{d\dot{n}_1}{dz} = S_R \cdot \nu_1' \cdot r + \delta\left(z - \frac{L}{N} \cdot (j-1)\right) \cdot \frac{\dot{n}_1}{N} \quad (3.12)$$

$$\begin{aligned} \frac{dT}{dz} = & S_R \cdot \frac{r \cdot (-\Delta H_r)}{\left(Q_R + \sum_{j=1}^N \sigma\left(z - \frac{L}{N} \cdot (j-1)\right) \cdot \frac{Q_{Inj}}{N}\right) \cdot \rho \cdot c_p} - S_R \cdot \frac{Ua_{in} \cdot (T - T_C)}{\left(Q_R + \sum_{j=1}^N \sigma\left(z - \frac{L}{N} \cdot (j-1)\right) \cdot \frac{Q_{Inj}}{N}\right) \cdot \rho \cdot c_p} \\ & + \delta\left(z - \frac{L}{N} \cdot (j-1)\right) \cdot \frac{Q_{Inj}}{Q_R \cdot N} (T_{Inj} - T) \end{aligned} \quad (3.13)$$

In the second term, the only resistance to evacuation of heat is assumed to be the convective resistance between the channel and the wall, which can be estimated assuming an average $Nu_{in} = 3.66$. The third term of the heat balance is the heat added to the system due to the temperature difference between the injected flow and the main flow denoted as $(T_{Inj} - T)$. The above equations can be solved using a simple ordinary differential equation solver for each interval between two injection points. In this case, the boundary conditions of the j^{th} interval have to be adapted considering the reaction mass injected at point j and its temperature as well as the temperature and concentrations at the end of the interval $j-1$. After the first injection point ($j = 1$) equation (3.12) and (3.13) are:

$$\frac{d\dot{n}_1}{dz} = S_R \cdot v_1 \cdot r + \frac{\dot{n}_1}{N} \cdot \delta(z) \quad (3.14)$$

$$\frac{d\dot{n}_2}{dz} = S_R \cdot v_2 \cdot r \quad (3.15)$$

$$\frac{dT}{dz} = S_R \cdot \frac{r \cdot (-\Delta H_r)}{\left(Q_R + \frac{Q_{Inj}}{N}\right) \cdot \rho \cdot c_p} - S_R \cdot \frac{Ua_{in} \cdot (T - T_w)}{\left(Q_R + \frac{Q_{Inj}}{N}\right) \cdot \rho \cdot c_p} + \delta(z) \cdot \frac{Q_{Inj}}{Q_R \cdot N} (T_{inj} - T) \quad (3.16)$$

These equations are solved using the initial molar fluxes $\dot{n}_{2,0} / \dot{n}_{1,0}$ and the initial temperature T_0 in the main reaction channel as boundary conditions. Subsequently, the solutions obtained at $z = 1 \cdot L / N$, i.e. $\dot{n}_1(1 \cdot L / N)$ and $T(1 \cdot L / N)$ are used together with the molar flux and temperature coming from injection point $j = 2$ to calculate the boundary condition for equation (3.15) and (3.16) within the second interval ($j = 2$):

$$\dot{n}_{1,0,j=2} = \dot{n}_1(1 \cdot L / N) + \frac{Q_{Inj}}{N} \cdot c_{1,0} \quad (3.17)$$

$$\dot{n}_{2,0,j=2} = \dot{n}_2(1 \cdot L / N) \quad (3.18)$$

$$T_{0,j=2} = \frac{T(1 \cdot L / N) \cdot (Q_{Inj} + Q_R) \cdot \rho \cdot c_p + T_{inj} \cdot Q_{Inj} \cdot \rho \cdot c_p}{(Q_{Inj} + Q_R) \cdot \rho \cdot c_p + Q_{Inj} \cdot \rho \cdot c_p} \quad (3.19)$$

3.3.1.2 Default Parameters Used in the Simulations

In order to illustrate the behavior of the multi-injection reactor, simulations were carried out for the Ionic liquid synthesis described in section 3.2 [32, 180] with an inner channel diameter of 800 μm . The properties of the reaction used for the simulations are summarized in Table 3.3.

Table 3.3: Parameters used for the simulation of a multi-injection reactor.

Parameter	Value
Volumetric flow rate, Q_R [m^3/s]	3
Volumetric flow rate, Q_{Inj} [m^3/s]	1.83
Initial conc. of methylimidazole, $c_{1,0}$ [mol/m^3]	12540
Initial conc. of diethylsulfate, $c_{2,0}$ [mol/m^3]	7633
Frequency factor, k_0 [$\text{m}^3/\text{mol}\cdot\text{s}$]	$1.28 \cdot 10^9$
Activation energy, E_A [kJ/mol]	89
Density of reaction mixture, ρ_R [kg/m^3]	1100
Heat capacity of reaction mixture, $c_{p,R}$ [$\text{J}/(\text{kg}\cdot\text{K})$]	2600
Nussel number, Nu_{in} [-]	3.66
Thermal conductivity of coolant, λ_C [W/mK]	0.17
Channel diameter, d_R [mm]	0.8

3.3.2 Results

The temperature of the injected fluids, the initial temperature and the cooling temperature are assumed to be equal. A typical simulation profile for a multi-injection reactor with 4 injection points is given in Figure 3.17.

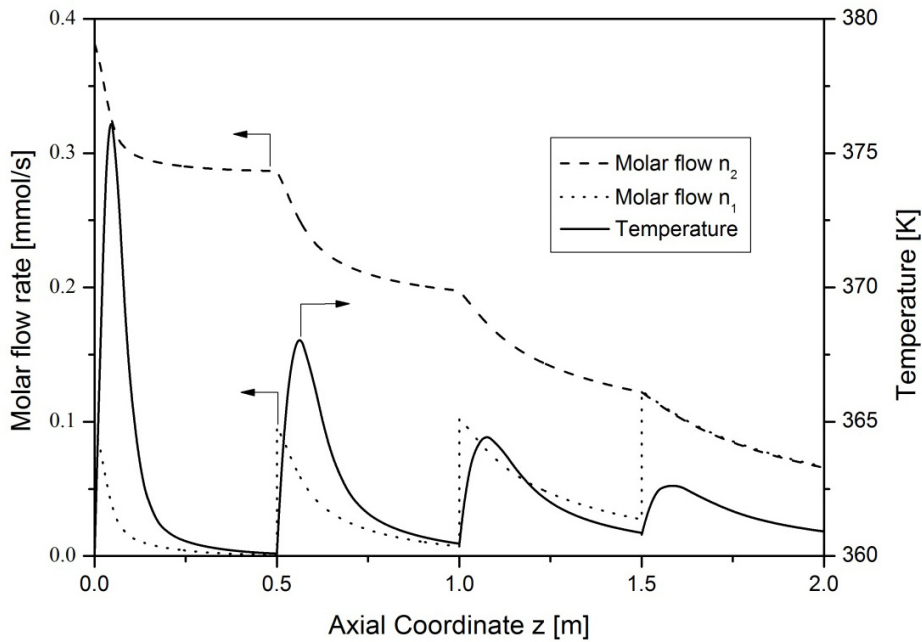


Figure 3.17: Temperature profile of the synthesis of Ionic liquid in a multi-injection reactor with $N = 4$ and $T_0 = T_{inj} = T_W = 360$ K. The injection points are separated by a distance of 0.5 m in order to have a sufficient heat removal. ($\tau = S_R \cdot L / (Q_R + Q_{inj}/2) = 15.4$ s, $t_R = 1 / (k \cdot c_{2,0}) = 0.84$ s, $t_{cool} = \rho \cdot c_p / (U \cdot a_{in}) = 0.22$ s).

In order to successfully run a multi-injection reactor, the concentration of the limiting reactant should be close to 0 before reaching the subsequent injection point. In this case, the limiting reactant is the molar flow n_1 which experiences a sharp rise at each injection followed by decay due to the reaction. As the excess reactant is also consumed along the length, the reaction rate becomes slower at every injection point. The temperature rise is at its maximum at the first injection point reaching about 10 % of the adiabatic temperature rise ($\Delta T_{ad} = 168$ °C). Due to efficient cooling, the temperature can be brought back almost to the initial temperature before the next injection point. The hot spot temperature diminishes from

one injection point to another on the one hand, due to the increased reaction mass, and on the other hand, due to the reduced reaction rate. In the following, the different parameters allowing further reduction of the maximum temperature are presented.

3.3.2.1 Number of Injection Points

The hot spot value within a multi-injection reactor is mainly controlled by the amount of injection points (N). For a first approximation of the temperature rise at each injection point, a simplified system can be considered [170]. In the case of instantaneous mixing and reaction with an equally distributed flow among the injection points, the temperature rises quasi-adiabatically at each injection point. To avoid a high temperature rise, the heat produced at each injection point j is removed before reaching the next injection point $j+1$. For such a system, temperature rise at each injection point can be described as

$$\Delta T_{ad,N,j} = \frac{\frac{Q_{inj}}{N} \cdot c_{1,0} \cdot (-\Delta H_r)}{\left(Q_R + \sum_{jj=1}^j \frac{Q_{inj}}{N} \right) \cdot \rho \cdot c_p} = \frac{1}{\left(N \cdot \frac{Q_R}{Q_{inj}} + j \right)} \cdot \frac{c_{1,0} \cdot (-\Delta H_r)}{\rho \cdot c_p} \quad (3.20)$$

The adiabatic temperature rise for a single-injection MSR is defined as

$$\Delta T_{ad,N=j=1} = \frac{\frac{c_{1,0} \cdot Q_{inj}}{Q_R + Q_{inj}} \cdot (-\Delta H_r)}{\rho \cdot c_p} \quad (3.21)$$

Thus, the temperature rise at each injection point can be expressed relative to the adiabatic temperature rise obtained in a single-injection reactor ($N = 1$) as

$$\frac{\Delta T_{ad,N,j}}{\Delta T_{ad,N=j=1}} = \frac{\left(\frac{Q_R}{Q_{inj}} + 1 \right)}{\left(N \cdot \frac{Q_R}{Q_{inj}} + j \right)} \quad (3.22)$$

In Figure 3.18, the temperature profile of equation (3.22) is compared to the simulation at an initial temperature of 360 K (fast reaction) and to the same reaction carried out at 420 K (instantaneous reaction).

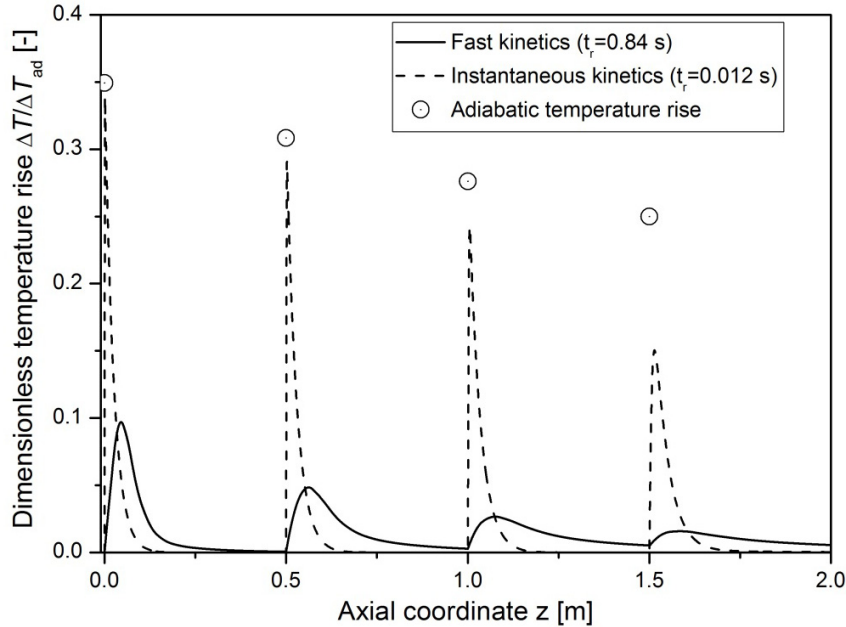


Figure 3.18: Temperature profile in a multi-injection reactor with $N = 4$ and $T_0 = T_{inj} = T_W$ for the synthesis of Ionic liquid. The injection points are separated by a distance of 0.5 m in order to have sufficient heat removal.

($\tau = S_R \cdot L / (Q_R + Q_{inj}/2) = 15.4$ s, $t_R = 1 / (k \cdot c_{2,0}) = 0.84$ s, $t_{cool} = \rho \cdot c_p / (U \cdot a) = 0.22$ s); Fast reaction: $t_R = 1 / (k \cdot c_{D,0}) = 0.84$ s. Instantaneous reaction: $t_R = 1 / (k \cdot c_{D,0}) = 0.012$ s). The other simulation parameters are summarized in Table 3.3.

From equation (3.22) it is obvious that the highest temperature rise occurs at the first injection point ($j = 1$), which is due to the fact that the overall flow rate increases with j for a constant heat release at every injection point, which in turn leads to an increased heat capacity at each injection point. Figure 3.19 shows the adiabatic temperature rise at the first injection point as a function of total injection points N .

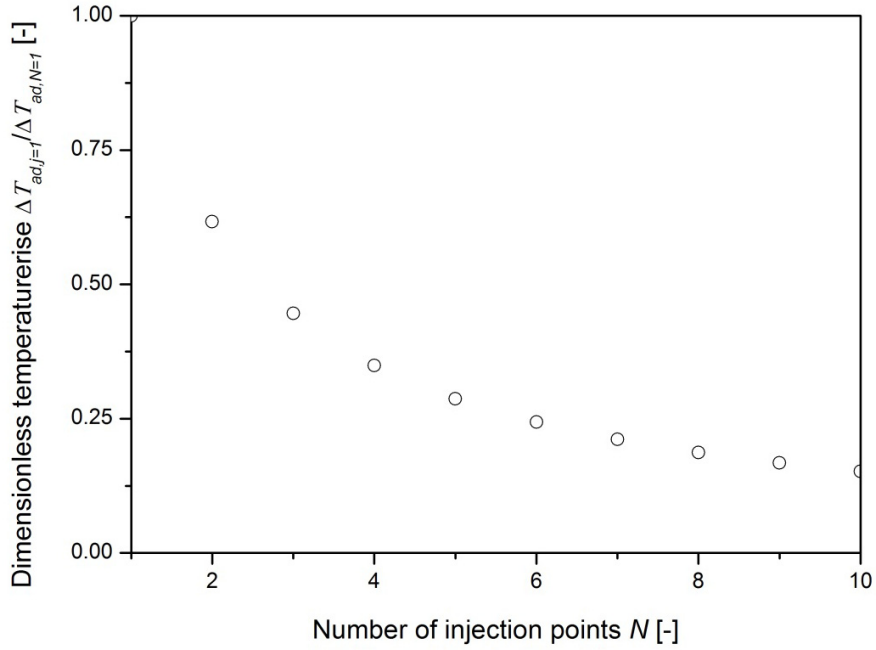


Figure 3.19: Temperature rise at the first injection point as a function of total amount of injection points N for $Q_{inj}/Q_R = 0.61$ and $j = 1$.

3.3.2.2 Choice of Limiting Reactant

In the case of unequal flow rates, a further reduction in hot spot temperature can be obtained

$$\frac{\Delta T_{ad,N,j}}{\Delta T_{ad,N=j=1}} = \frac{(1/F + 1)}{(N \cdot 1/F + j)} = \frac{(1 + F)}{(N \cdot 1 + F \cdot j)} \quad (3.23)$$

Thereby, F is the ratio of Q_{inj}/Q_R . For $F \rightarrow 0$, the normalized temperature rise at each injection point is limited to $1/N$. Rewriting equation (3.23), the maximum number of injection points required to avoid a temperature rise higher than $\Delta T_{ad,N,j=1}$ can be estimated as a function of F and the adiabatic temperature rise of the reaction $\Delta T_{ad,N=j=1}$ in the case of a single-injection reactor ($N = j = 1$):

$$N = (1 + F) \frac{\Delta T_{ad,N=j=1}}{\Delta T_{ad,N,j=1}} - F \quad (3.24)$$

To apply this simple equation, one has to carefully choose characteristic cooling time to avoid the accumulation of heat in the reactor.

3.3.2.3 Unequal Flow Partition

In the previous sections, the flow through the injection channels was assumed to be equal. It was shown that this type of design results in a temperature profile as given in Figure 3.18, which leads to a maximum temperature at the first injection point. In order to further reduce this maximum temperature in a multi-injection reactor, one can design the MSR in order to obtain N equally high hot spots by increasing the injected volume along the length. The optimal flow distribution can be calculated using the model above. For a multi-injection reactor with N injection points, the adiabatic temperature rise at each injection point has to be equal:

$$\Delta T_{ad,N,1}^{(1)} = \Delta T_{ad,N,2}^{(2)} = \Delta T_{ad,N,3}^{(3)} = \dots = \Delta T_{ad,N,N}^{(N-1)} \quad (3.25)$$

It leads to a set of $N-1$ equations for N unknown normalized injection flow rates $F_j = Q_{inj,j}/Q_R$. Solving equations (3.25) leads to the following expression for the normalized injection flow rates as a function of F_1 :

$$F_j = F_1 \cdot (F_1 + 1)^{j-1} \quad (3.26)$$

Thus the growth factor for the volumetric flow rate between two injection points j and $j+1$ is $(F_1 + 1)$.

Assuming a constant density along the length:

$$F = \sum_{j=1}^N F_j \quad (3.27)$$

From the above equations, F_j can be determined for a known value of F . Using the above example ($F = 0.61$ and $N = 4$), the injection flow rate at $j = 1$ is $F_1 = 0.126$ resulting in a growth factor of $G = 1.126$ and a 20 % reduced temperature rise as compared to an equally distributed multi-injection reactor. Especially in cases with high F or a low amount of injection points N this kind of channel design can be beneficial. The reduction in hot spot temperature is demonstrated in Figure 3.20, where the temperature attained with quasi-instantaneous reaction kinetics is compared to the adiabatic case. Even though in the

latter case four peaks of equal temperature would form, under real conditions a decrease of the peaks is observed. This can be explained by the gradually decreasing concentration of the reactants in the main channel, leading to reduced reaction rates.

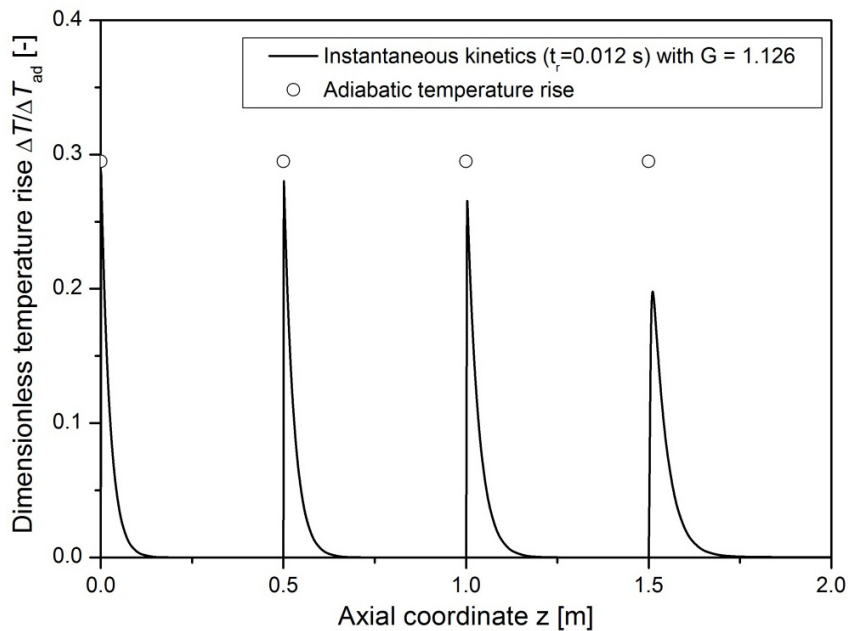


Figure 3.20: Temperature rise for a multi-injection reactor with instantaneous kinetics and gradually increasing injection volume (Factor $G = 1.126$ from one injection point to the next). The simulation parameters are summarized in Table 3.3.

3.3.2.4 Pressure Drop and Flow Distribution

As a multi-injection reactor allows operating with bigger channel diameters for the same temperature rise as in a single-injection reactor, they may be seen as method of scaling-out. To carry out the reaction with quasi-instantaneous kinetics as shown in Figure 3.20, a reactor diameter smaller than $65 \mu\text{m}$ (calculated using the numerical simulation) would be required when working with a single-injection reactor. Hence, by using a multi-injection reactor in this case, the gain in reactor volume is factor 150 for a comparable efficiency in heat removal.

In the sections above, a well-defined distribution of the flow among the injection channels was assumed. However, precise distribution of fluids through multiple channels is not straightforward. As this problem

has already been well discussed in the case of the numbering-up of MSR (see Chapter 2), the same theories can be applied to multi-injection reactors. The pressure drop can be *a priori* described using computational fluid dynamics (CFD) simulations. The main advantage of this method is accurate results. However, the simulation of the whole device requires a lot of computational power, and therefore, a simpler approach is warranted. Several studies [47, 63, 184-187] described the pressure drop in the channel as resistances analogous to electrical networks. When numbering up, internal numbering-up is more cost effective compared to external numbering-up. The comparison for energy input needed for the distribution of the flows between the former and the multi-injection MSR can be made. In addition, both require a comparable set of accessories (mainly pumps and piping). The following simplified flow resistance model is considered (see Figure 3.21).

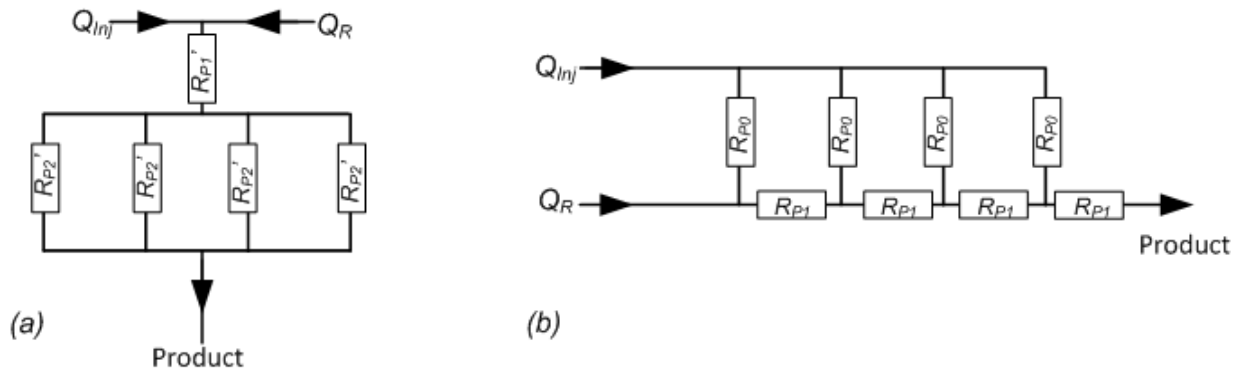


Figure 3.21: Simplified flow resistance model for (a) internal numbering-up of four channels and (b) multi-injection reactor with four injection points.

The resistance R_p and the pressure drop Δp are defined according to Pan *et al.* [186, 187]:

$$R_p = \frac{32 \cdot \nu \cdot L \cdot \xi_{NC}}{d_h \cdot S_R} \quad \text{and} \quad \Delta p = R_p \cdot Q \quad (3.28)$$

As a first approach, the pressure drop between the inlet of Q_R and the outlet is compared, assuming $R_{p1}' = R_{p2}' = R_{p0} = R_{p1} = R_p$ and $Q_R = Q_{inj} = Q$. Hence for case (a):

$$R_{p,tot,a} = R_{p1} + \frac{1}{4/R_{p2}} = \frac{5}{4}R_p \quad (3.29)$$

$$\Rightarrow \Delta p_{tot,a} = \frac{5}{4}R_p Q$$

and for case (b)

$$\begin{aligned} \Delta p_{tot,b} &= R_{p1} (Q_R + 1/4Q_{inj}) + R_{p1} (Q_R + 2/4Q_{inj}) + R_{p1} (Q_R + 3/4Q_{inj}) + R_{p1} (Q_R + 4/4Q_{inj}) \\ &= \frac{13}{2}R_p Q \end{aligned} \quad (3.30)$$

Due to the serial arrangement of the resistances, the pressure drop in the multi-injection reactor is about five times higher for the shown example. The parallel alignment of resistances in case (a) leads to a diminished pressure drop. In addition to the demonstrated effect, some other factors must be taken into account in order to provide the best solution in terms of pressure drop (multi-injection reactor or internal scale-up). Especially in liquid phase, fast mixing of two fluids requires high pressure drop (see section Chapter 2), thus R_{p1} is much higher than in a conventional tube. The resistance of the injection channel will generally be designed much bigger than the main channel resistances ($R_{p0} \gg R_{p1}$) in order to provide an almost equal flow for every injection channel. On the other hand, the small diameter needed for temperature control of multiple parallel microchannels increases the resistance ($R_p \propto 1/d_R^4$). Thus, pressure drop is a critical issue that needs to be considered when making a choice of reactor.

3.4 Micro-annular Reactor

As mentioned in the introduction, this novel reactor concept has not been described in literature yet. The model and results presented in the following are a first proof of concept. The model reaction used to carry out the simulation is an imaginary instantaneous pseudo-first order reaction.

3.4.1 Model Description

A homogenous distribution of the fluid at the inlets of the core and at the annular region was assumed. Thus, no dependence of the system on the angular coordinate needs to be considered. Furthermore, it was assumed that the molar flux through the filter is homogeneously distributed and ideal mixing is insured, resulting in a reaction controlled by its intrinsic kinetics.

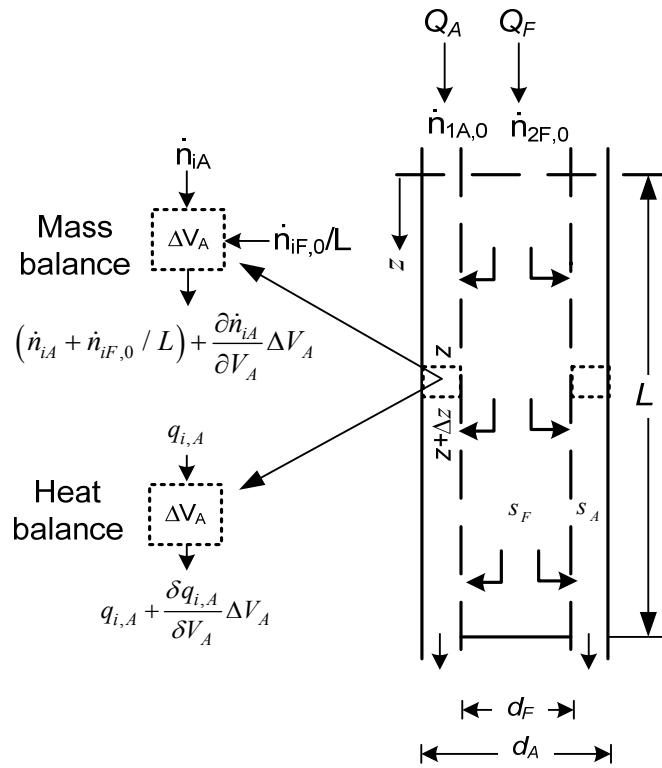


Figure 3.22: Mass- and energy balance in the micro-annular reactor.

In order to keep the model simple, a pseudo first order reaction was assumed: $A_1 + A_2 \rightarrow A_3$ with A_1 being the excess reactant fed through annular space and A_2 the limiting reactant entering through the filter. At steady state, the balance of species i in a small volume element in the annular region (dV_A) is written as

$$\frac{d\dot{n}_{iA}}{dV} = R_{iA} + \frac{\dot{n}_{iF,0}}{V_A} \quad (3.31)$$

3 Numerical Simulation of Microstructured Reactors

Where, R_{iA} is the rate of generation or consumption and \dot{n}_{iA} is the molar flow of the i^{th} species in the annular region. V_A describes the volume in the annular space until the end of injection. The subscript A and F stand for the flow of reactant through annular region and through the filter of length L , respectively. As through the filter solely diluted A_2 is fed, and diluted A_1 through annular space, the initial molar flows are:

$$\dot{n}_{1F,0} = \dot{n}_{2A,0} = 0 \quad (3.32)$$

The cross section area of the annular region S_A remains constant. Therefore, the above equation can be written as

$$\frac{d\dot{n}_{iA}}{dz} = R_{iA} \cdot S_A + \frac{\dot{n}_{iF,0}}{L} \quad (3.33)$$

The volumetric flow rate in annular space Q_A increases linearly along the length until a total flow of $Q_A = Q_{A,0} + Q_{F,0}$ is reached. As the total volumetric flow rate $Q(z) = Q_A(z) + Q_F(z)$ is constant, accordingly Q_F decreases with axial coordinate z . The increase of flow in annular space results in a dilution of the reactants in the reaction zone.

For the heat balance, the cross section of the whole reactor including the filter is considered as isothermal. Thus heat produced in annular space is absorbed by the total volume $Q = Q_A + Q_F$ and evacuated solely at the outer wall of annular space by maintaining it at constant temperature. Neglecting the work done on the reacting fluid, the energy balance can be written as given in the following

$$\frac{d(\dot{m} \cdot c_p \cdot T)}{dV_A} = \frac{d(\rho \cdot \dot{V} \cdot c_p \cdot T)}{S_A \cdot dz} = r \cdot (-\Delta H_R) - Ua_m (T - T_w) \quad (3.34)$$

Where, ρ , Q , c_p and Ua_m are the density, total volumetric flow rate through the central and annular region ($Q_A + Q_F$), specific heat capacity and heat transfer coefficient of reacting mixture, respectively. For a

constant tube diameter, the specific heat exchange surface a is the ratio of surface area of the outer tube to the total annular space:

$$a = \frac{4 \cdot d_A}{(d_A^2 - d_F^2)} \quad (3.35)$$

Where, d_F and d_A are the outer diameter of the filter and inner diameter of the outer wall, respectively. As mentioned before, total volumetric flow rate is used to absorb heat released in the reaction. Assuming constant density, specific heat capacity and volumetric flow rate (no change due to reaction), the above equation can be written as

$$\frac{dT}{dz} = \frac{S_A}{\rho \cdot c_p \cdot \dot{V}} \cdot r(-\Delta H_R) - \frac{U a_{in} \cdot S_A}{\rho \cdot c_p \cdot \dot{V}} \cdot (T - T_w) \quad (3.36)$$

Since the reaction does not take place in the whole cross section of the reactor, the inner heat transfer coefficient h_C of the system is different from the tubular reactor. The Nusselt number in the annular flow depends on Reynolds and Prandtl number, and it is calculated using the correlation proposed for laminar flow in concentric tubes with an adiabatic inner wall [37]:

$$Nu_A = \left[Nu_\infty + f \left(\frac{d_F}{d_A} \right) \frac{0.19 \left(Re \cdot Pr \frac{d_h}{L} \right)^{0.8}}{1 + 0.117 \left(Re \cdot Pr \frac{d_h}{L} \right)^{0.467}} \right] \left(\frac{Pr}{Pr_w} \right)^{0.11} \quad (3.37)$$

where:

$$Nu_\infty = 3.66 + 1.2 \left(\frac{d_F}{d_A} \right)^{0.5}; f \left(\frac{d_F}{d_A} \right) = 1 + 0.14 \left(\frac{d_F}{d_A} \right)^{1/3} \quad (3.38)$$

$$Re = \frac{\rho \cdot u \cdot d_h}{\mu}; Pr = \frac{c_p \mu}{\lambda}; d_h = d_A - d_F$$

Pr_w is the Prandtl number at the outer wall temperature. Thus, the heat transfer coefficient is calculated as

$$U_{in} = \frac{Nu_A \cdot \lambda_A}{d_h} \quad (3.39)$$

3 Numerical Simulation of Microstructured Reactors

In order to better understand the origin of some effect, equations (3.33) and (3.36) were put into dimensionless form, assuming an initial temperature equal to cooling temperature $T_0 = T_W$ and a pseudo-first order reaction ($n = 1$).

$$\frac{dN_{iA}}{dZ} = \frac{\tau}{t_r'} + N_{iF,0} \quad (3.40)$$

$$\frac{d\theta}{dZ} = \frac{\tau}{t_r'} \Delta\theta_{ad} - \frac{\tau}{t_{cool}} \theta \quad (3.41)$$

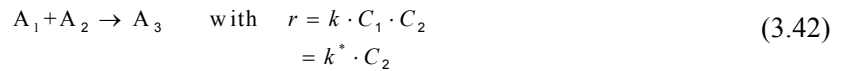
where

$$N_{ij} = \frac{\dot{n}_{ij}}{\dot{n}_{2F,0}}; \quad Z = \frac{z}{L}; \quad t_r' = \frac{\dot{n}_{2F,0}}{r \cdot Q}; \quad r = k_0 \cdot e^{-\gamma} \cdot c_{2A}; \quad \gamma = \frac{E_A}{R \cdot T_W}; \quad t_r = \frac{1}{k_0 \cdot e^{-\gamma}};$$

$$t_c = \frac{\rho \cdot c_p}{h_A \cdot a}; \quad \theta = \frac{T - T_W}{T_W}; \quad \tau = \frac{S_A \cdot L}{Q}; \quad \Delta\theta_{ad} = \frac{-\Delta H_R \cdot \dot{n}_{2F,0}}{\rho \cdot c_p \cdot Q \cdot T_W}$$

Here t_r' represents the ratio between moles fed to the reactor and rate of mole change in annular space. Characteristic cooling time is denoted as t_c . The space time of the micro-annular reactor τ is defined as the ratio between total volume of annular space along the filter and total flow rate. N_{ij} is the dimensionless molar flow rate of the component i in annular space ($j = A$) or in the filter ($j = F$). The index $i = 2$ describes the limiting reactant that is inserted at the filter inlet.

To simulate reactor behaviour in the case of a reaction controlled by kinetics, a pseudo first order reaction was modelled:



Reactant A_1 is the limiting reactant fed through the filter, reactant A_2 is introduced in excess in annular space in order to get a pseudo-first order reaction. Furthermore, it is assumed that the product A_3 is stable i.e. there are no consecutive reactions. The physical properties and operating conditions used for simulation are given in Table 3.4.

The above set of equations was solved using a commercial numerical solver, Mathworks Matlab [149].

Table 3.4: Properties used for simulation of micro-annular reactor.

Parameter	Value	Normalized parameter	Value
Density ρ [kg/m ³]	1000	$N_{IF,0}$ [-]	1
Specific heat c_p [kJ/kgK]	4.18	$N_{2F,0}$ [-]	0
Thermal conductivity of fluid λ_R [kW/m K]	4.844×10^{-4}	t_r [ms]	36
Inlet temperature T_{in} [K]	378	t_c [ms]	816
Wall temperature T_w [K]	378	γ [-]	33.6
Heat of reaction ΔH_R [kJ/mol]	-690	$\Delta\theta_{ad}$ [-]	1.1
Activation energy E_a [kJ/mol]	105.5	τ [s]	10.2
Frequency factor (k_0) [1/s]	1.05×10^{16}	Z [-]	1
Filter diameter d_F [m]	6×10^{-3}		
Cylindrical case diameter d_A [m]	7×10^{-3}		
Filter length L [m]	0.8		
Total length L_{Tot} [m]	1.6		
Flow rate at filter inlet $Q_{F,0}$ [m ³ /s]	4×10^{-7}		
Flow rate at annular inlet $Q_{A,0}$ [m ³ /s]	4×10^{-7}		
Initial concentration $c_{1,0}$ [mol/L]	16		
Initial concentration $c_{2,0}$ [mol/L]	5		

3.4.2 Results

The simulations were carried out for different operating conditions. Only one parameter was varied at the time, the other parameters were kept constant as given in Table 3.4. At first, the profile of molar flow and temperature are shown under default conditions to demonstrate the principle of the micro-annular reactor. Subsequently, the effect of the ratio of residence time to characteristic cooling time is shown. The effect of reaction kinetics is analysed by simulating slower reactions on the one hand, and mixing limited reactions

on the other hand (low activation energy). Finally, the performance of micro-annular reactor is compared to the performance of a microchannel of comparable size.

3.4.2.1 Axial Molar Flow and Temperature Profiles

The fluid keeps on accumulating in the annular region along the length of the reactor and the flow velocity changes due to constant annular space. At the dimensionless length (Z) equal to 1, the flow velocity stays constant as there is no more addition of fluid. In Figure 3.1 the concentration of the limiting reactant is zero all over the length due to quasi-instantaneous reaction. It shows that the reaction is limited by the continuous addition of the limiting reactant, which causes a linear decrease of molar flow of reactant 2 due to reaction. The heat production is constant along the length (for $0 \leq Z \leq 1$) as it is governed by the constant addition of the limiting reactant. Accordingly, the temperature rises until heat production and heat removal equilibrium is reached (at $Z = 0.3$). At $Z = 1$ the addition of the limiting reactant stops and thus heat production becomes zero.

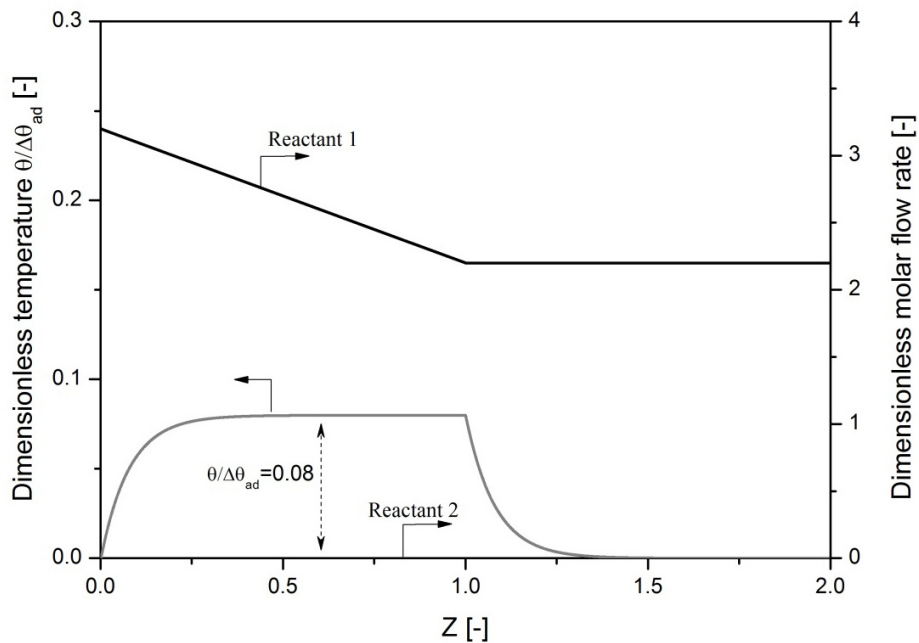


Figure 3.23: Molar flow rates of reactants and temperature along the micro-annular reactor

The isothermal working point can be easily calculated using equation (3.41):

$$\frac{\theta}{\Delta\theta_{ad}} = \frac{t_{cool}}{\tau} = \frac{0.816}{10.2} = 0.08 \quad (3.43)$$

3.4.2.2 Variation of the Ratio Residence Time/Cooling Time

The change in residence time can be realised as a variation of filter length or the volumetric flow rate inside the filter. By reducing residence time for a given set of initial/operating conditions, the amount of reactant dosed per unit filter area increases (see equation (3.44)).

$$J = \frac{\dot{n}_{IF,0}}{L \cdot \pi \cdot d_F} \quad (3.44)$$

A variation of cooling time can be practically achieved either by diminishing the size of annular space or by improving radial heat conductivity of the wall/cooling fluid.

The temperature profile resulting from a change of the ratio of residence time by characteristic cooling time is given in Figure 3.24. For a small ratio $\tau/t_{cool} = 1$, temperature rise is similar to a single-injection reactor: as the characteristic cooling time is in the same order of magnitude as the time needed to accomplish reaction, the temperature rise is relatively high. With increasing ratio τ/t_{cool} , heat removal is enabled and a maximum temperature of less than 5 % of adiabatic temperature rise is achieved for a ratio of 30.

However, a key advantage of this reactor is not only the reduced temperature rise, but its quasi isothermal behaviour. For a ratio $\tau/t_{cool} = 9.3$, the temperature is constant between $Z = 0.3$ and $Z = 1$. With increasing residence time or decreasing characteristic cooling time, the temperature of equilibrium between heat production and heat removal is reached earlier and thus the isothermal part of the reactor becomes longer. To operate the micro-annular reactor under isothermal conditions, residence time should be set one order of magnitude higher than characteristic cooling time.

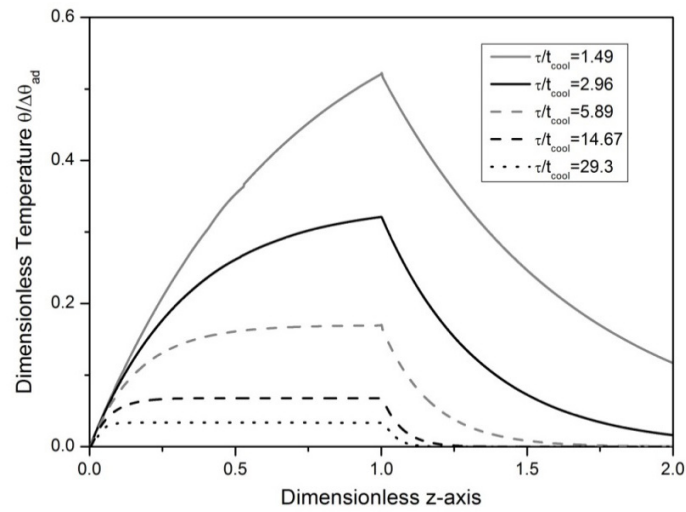


Figure 3.24: Influence of the ratio of residence time and characteristic cooling time on temperature.

3.4.2.3 Variation of the Ratio Residence Time/Reaction Time

For quasi-instantaneous reactions, heat release is solely controlled by the addition of limiting reactant. For low Damköhler I numbers ($Dal' = \tau/t_r$), i.e. slow reactions or higher dosing rates, heat production is governed by the reaction kinetics resulting in accumulation of reactant 1 in the annular space and causing hot spots or even reactor run-away (see Figure 3.23).

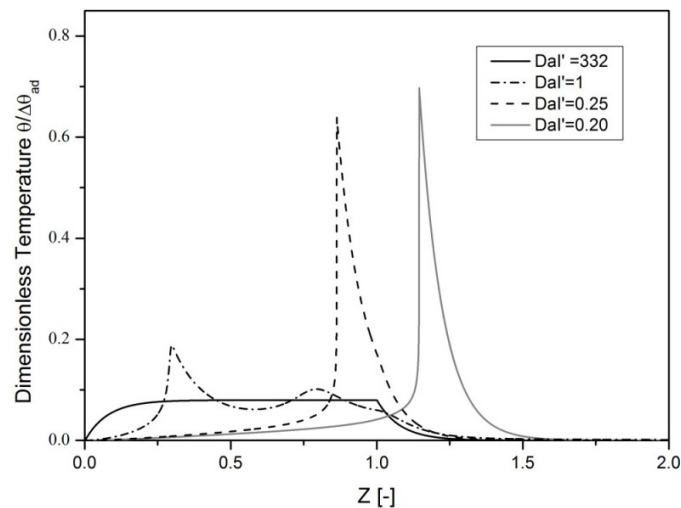


Figure 3.25: Influence of the ratio of residence time and characteristic reaction time $Dal' = \tau/t_r$ on temperature (Arrhenius number $\gamma = 33.6$).

3.4.2.4 Reaction Limited by Mixing

In order to analyse the effect of mixing on MAR performance, reaction activation energy and thus, Arrhenius number was used. Simulations were carried out for zero Arrhenius number to model the case of mixing being the rate limiting step (see Figure 3.26).

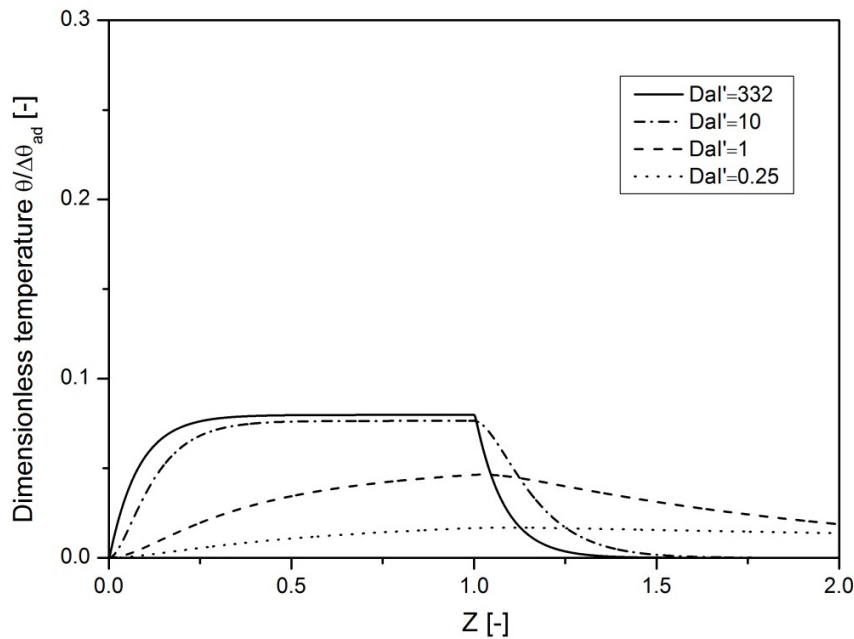


Figure 3.26: Influence of the ratio of residence time and characteristic reaction time on temperature. Here $\gamma = 0$ while the rest of the parameters were set according to Table 3.4.

For the case of $DaI' = 332$, the observed profile is the same as for the instantaneous case, as the reaction rate is high enough to assure an instantaneous consumption. With lower DaI' , more and more reactant is accumulated along the length which reacts after the dosing part. The most apparent difference between Figure 3.25 and Figure 3.26 is the absence of a runaway behaviour in the latter one. The accumulated reactant only proportionally accelerates the reaction, the exponential increase of reaction rate due to temperature is not occurring (as $\gamma = 0$). Instead of a runaway behaviour, with decreasing DaI' (especially below $DaI' = 10$) a decrease in maximum temperature is observed. The reactants consumption is spread along the length requiring more time to complete the reaction due to mixing limitations. However, as soon

3 Numerical Simulation of Microstructured Reactors

as the streams get mixed in downstream equipment, a run-away is likely to occur, which is why the reactor cannot be operated under conditions of slow mixing.

To work efficiently with micro-annular reactor and avoid run-away in down-stream equipment due to accumulation of reactants, characteristic mixing time has to be at least one order of magnitude lower than residence time

$$DaII_{mix}' = \frac{\tau}{t_{mix}} = \frac{S_A \cdot L}{Q} \geq 10 \quad (3.45)$$

For extremely fast reactions, mixing of the reactants is the limiting step. In order to estimate this effect, one can proceed with a simplified calculation.

As residence time equals to 10 s in the considered case, the mixing time has to be in the order of 1 s. An approximate value of mixing time can be calculated for the poor mixing case considering characteristic diffusion time:

$$t_{mix} \approx t_{diffusion} \approx \frac{(d_A - d_F)^2 / 4}{D_m} \quad (3.46)$$

For a gas phase reaction ($D_{m,gas} = 10^{-5} \text{ m}^2/\text{s}$) and an annular width of 0.5 mm one obtains a characteristic mixing time of 25 ms, which is small enough. However, if a liquid system is considered, the characteristic mixing time is about 250 s.

In order to overcome the slow mixing in liquid phase, there are two solutions:

- improve the quality of mixing by inserts
- reducing the annular distance in order to enhance the mixing by diffusion

3.5 Conclusion

In this chapter, three models representing distinct strategies were screened for their potential to reduce hot spot temperature in microstructured reactors: the axially conductive microchannel reactor, the multi-injection microreactor and the micro-annular reactor.

In the thermally conducting microchannel reactor, the modification of thermal conduction showed that the optimal conductivity for this type of geometry lies in the range of stainless steel ($15 \text{ W}/(\text{m}^2\text{K})$) for a pre-heated inlet stream. It was found to be the best tradeoff between sufficient thermal conductivity for radial heat evacuation and a minimization of axial conductivity leading to higher inlet temperatures, which in turn lead to more pronounced run-aways. To benefit from axial conduction through the reactor wall, a heat sink needs to be added. One possibility is to feed the reactor with cold solution: in this case, the heat from the hot spot is used to pre-heat the inlet streams, leading to an almost isothermal temperature profile.

The concept of step-wise injection was shown to be a very powerful approach especially for quasi-instantaneous reactions. The hot spot temperature was progressively reduced with the amount of injection points. Thereby, the maximum temperature is reached at the first injection point owing to the lowest heat capacity and the high concentrations. As countermeasure, it was proposed to gradually increase the flow rate of injected reactant. Carrying out a quasi-instantaneous reaction with a multi-injection reactor can be seen as a scale-out approach as for a given maximum temperature rise, it replaces hundreds of microchannels with a diameter below $100 \mu\text{m}$. Thereby, the serial arrangement of flow resistances needed for distribution requires a substantial amount of pumping energy. Nevertheless, the data obtained from this strategy are very promising. Thus, it is selected for an experimental investigation in the following chapters. It is essential to keep in mind that for a specific amount of injection points, the best results is obtained if between two injection points, the reactants are nearly completely consumed and the heat evacuated. In the case of quasi-instantaneous reactions, the consumption of the reactants can be brought back to the problem of efficient mixing of the two streams (see chapter 5).

3 Numerical Simulation of Microstructured Reactors

The micro-annular reactor is an extreme form of the multi-injection reactor. It shows zero-order shaped temperature profiles with higher throughput for a given temperature rise. As for the multi-injection reactor, a high heat evacuation rate is required. To benefit from a flat temperature profile, it is crucial to have a residence time (equivalent to dosing time) that is one order of magnitude higher than characteristic cooling time. At the same time, to avoid dangerous accumulation of reactants, residence time needs to be one order of magnitude higher than characteristic reaction time, i.e. characteristic mixing time for the case of quasi-instantaneous liquid phase reaction. From the practical point of view, it is more likely to fulfill the latter criterion with mixing insert than by narrowing the hydraulic diameter of annular space, as the precise construction of concentric tubes remains challenging.

As mentioned, the two latter strategies show enormous potential for lower hot spot temperature at increased throughput, especially in the case of reactions with characteristic reaction time in the order of 1 s or less. Initially, both concepts, i.e. the multi-injection and micro-annular reactor, were built-up. The first trials showed that mixing of two liquids, especially when having different densities and/or higher viscosities is challenging. As the modification of the annular space to improve mixing quality turned out to be technically challenging, it was decided to built-up a reactor based on multiple injection points.

3.6 Notations

a	Specific surface area, [m^2/m^3]
A	Surface area, [m^2]
\bar{A}	Average surface area in a cylindrical channel, [m^2]
c_p	Mean heat capacity, [$\text{J}/(\text{kg K})$]
c	Concentration, [mol/m^3]
d	Channel diameter, [m]
d_h	Hydraulic diameter, [m]
D	Effective diffusion coefficient, [m^2/s]
D_m	Molecular diffusion coefficient, [m^2/s]
E_A	Activation Energy, [m^2/s]
h	Heat transfer coefficient, [$\text{W}/(\text{m}^2\text{K})$]
H_r	Reaction enthalpy, [J/mol]
i	Index denoting chemical compound, [-]
j	Index denoting Injection point, [-]
J	Surface specific molar flow rate, [$\text{mol}/(\text{m}^2 \text{s})$]
k_0	Frequency Factor, [$(\text{m}^3/\text{mol})^{n-1}/\text{s}$]
L	Length of the reactor/filter, [m]
\dot{m}	Mass flow rate, [kg/s]
n	Reaction order
\dot{n}	Molar flow rate, [mol/s]
N	Total amount of injection points, [-]
N_{ij}	Dimensionless molar flow rate, [-]
p	Pressure, [Pa]
q	Heat flow, [W]

3 Numerical Simulation of Microstructured Reactors

Q	Volumetric flow rate, [m^3/s]
r	Reaction rate, [$\text{mol}/(\text{s m}^3)$]
R	Transformation rate, [$\text{mol}/(\text{s m}^3)$]
R	Ideal gas constant, [$\text{J}/(\text{mol K})$]
R	Heat Transfer resistance, [K/W]
R_p	Flow resistance, [$\text{Pa s}/\text{m}^3$]
S	Cross section area, [m^2]
t	Time, [s]
t_r	Characteristic reaction time, [s]
t_r	Dimensionless characteristic reaction time, [-]
t_{cool}	Characteristic cooling time, [s]
T	Temperature, [K]
u	Flow velocity, [m/s]
U	Global heat transfer coefficient, [$\text{W}/(\text{m}^2\text{K})$]
V	Volume, [m^3]
X	Conversion, [-]
z	Axial coordinate, [m]
Z	Dimensionless axial coordinate, [-]

Greek

α	Thermal diffusivity [m^2/s]
γ	Arrhenius number, [-]
δ	Wall thickness, [m]
δ	Dirac pulse, [$1/\text{m}$]
Δ	Symbol for difference
ε	Specific power dissipation, [W/kg]

λ	Thermal conductivity, [W/(m K)]
μ	Dynamic viscosity, [Pa s]
ν	Kinematic viscosity, [m ² /s]
ν'	Stoichiometric coefficient, [-]
θ	Dimensionless temperature, [-]
ρ	Mean density, [kg/m ³]
σ	Heaviside function, [-]
τ	Residence time, [s]
ζ_{NC}	Non-circular coefficient, [-]

Dimensionless numbers

DaI'	Modified Damköhler number τ/t_r' , [-]
DaI_{mix}	Mixing Damköhler number τ/t_{mix}
Nu	Nusselt number $h \cdot d_h / l_{Fluid}$, [-]
Pr	Prandtl number ν/a , [-]
Re	Reynolds number $u \cdot d_h / \nu$, [-]

Subscript

0	Initial condition
A	Annular space
ad	Adiabatic
ax	Axial
c / cool	Cooling
conv	convective
F	Filter
i	Index designating a component
in	Inside
Inj	Injection

3 Numerical Simulation of Microstructured Reactors

mix	Mixing
out	Outside
rad	radial
R	Reactor
R-W	Reactor-Wall
Tot	Total
w	Wall
W-C	Wall-Cooling

Chapter 4

QUANTITATIVE INFRARED IMAGING OF TEMPERATURE PROFILES IN MICROREACTORS

To experimentally validate the simulation results obtained in the previous chapter, an experimental method was developed for quantitative measurement of temperature profiles in microstructured reactors. This infrared based approach is the main tool applied within this thesis to monitor mixing of exothermic reactions (chapter 5) and the temperature profile in a multi-injection reactor (chapter 6).

4.1 Introduction

The axial temperature profile within thin channels depends on several parameters, like the kinetics and thermodynamics of the reaction, the design of the reactor, physical properties of the reactants and the quality of mixing achieved. In microchannels the relative importance of some effects is very different as compared to conventional reactors, which is usually referred to as “scaling effect”. For example, when working with conventional batch reactors with relatively slow reactions, mixing time is negligible compared to reaction time and hence, does not affect the overall rate of transformation. However, reactions carried out in microreactors are generally so fast that they may be influenced or totally controlled by mixing.

So far, only a limited amount of studies on thermal behavior of microreactors are available in open literature. Furthermore, most of the work is done by numerical simulation which can only reflect the temperature profile under ideal conditions.

Measuring temperature profiles within microchannels by classical method, such as thermocouples, has two major limitations: i) measurement only at distinct points and ii) the sensor changes the fluid behavior leading to artifacts. To get accurate and reliable characteristics of microdevices, non-intrusive methods of monitoring temperature are required. A common way of carrying out such experiments is the addition of temperature sensitive tracers to the fluid, as done in laser-induced fluorescence [188, 189]. However, this method is only applied to non-reacting microfluidic systems, since the tracers are usually cross-sensitive to the reaction conditions (such as a variation of pH). Another method is based on liquid crystal thermometry where temperature is monitored by liquid crystals whose color changes according to temperature. The liquid crystals can be added to the reactant solutions or coated on the reactor wall and are also used to track temperature in reactive media [190-193]. Iles *et al.* used liquid crystals to determine temperature during the Reimer-Tiemann reaction [192]. The range of suitable sensitivity of this system was limited to a window between 60 °C and 70 °C. Using the dependence of the refractive index on temperature, Fan *et al.* determined temperature profiles by laser [194, 195]. However, this method is also strongly sensitive to changes in concentration. Other methods presented in the literature are based on Raman spectroscopy [196, 197], nuclear magnetic resonance (NMR) [198] and ultrasound [199].

In this study, a method based on infrared thermometry allowing quantitative mapping of temperature has been developed. To use this technique quantitatively, several challenges have to be overcome including the right choice of optics to optimize the resolution, the calibration of the IR camera and the system, etc. [200]. Quantitative application of this technique in microchannels is mostly found in studies on characterization of thermal parameters of non-reacting mixtures. Recently Barber *et al.* [201] used thermal mapping of the channel walls in combination with high speed imaging and pressure sensors to describe the unsteady state fluctuations occurring during two phase heat transfer in microchannels. Using quantitative infrared imaging of channel walls, Xu *et al.* [202] could demonstrate the increased overall Nusselt number

obtained by periodically forcing the thermal profile of the fluid to redevelop. To measure directly the temperature of the fluid, a channel designed with infrared transparent covers, such as sapphire, silicon, germanium or zinc selenide is used [200]. However, a careful calibration of the system is required as the radiation losses by absorption and reflection of the window lead to distortion of the IR signal. Mishan *et al.* [203] determined non-reactive fluid temperature in 16 microchannels with hydraulic diameter of 440 μm covered by sapphire glass window. From the temperature profiles they deduced the heat transfer properties of developing flow. Infrared thermometry studies carried out on reactive microsystems are scarcer and generally only used for qualitative interpretation. Norton *et al.* [87] determined temperature profiles of the catalytic hydrogen combustion to demonstrate the effect of axial heat conduction in the reactor wall. Antes *et al.* [204] monitored the hot spots resulting from flow maldistribution inside their silicon microreactor during the nitration of *N,N*-diethyl-thioureas. A successful application of quantitative IR imaging on reactive systems in microreactors was published by Pradere *et al.*[205]. They used IR thermography to determine the Péclet numbers inside microchannels. From this data, they deduced the field of flow velocity and of heat source term.

In the present work, a quantitative infrared thermometry method initially developed for semiconductors is presented and applied to microstructured reactors [206]. Instead of a single point calibration where homogeneous emissivity is assumed all over the image, a pixel-by-pixel calibration leading to higher accuracy is carried out. The reactor was enclosed in a vacuum box having an infrared transparent window to reduce heat losses, and the temperature profiles were measured for both non-reacting and reacting systems using two generations of microreactors. The heat losses in the system were characterized, and heat transfer coefficients were investigated for different operating conditions.

4.2 Infrared Thermal Mapping

In this section, the reader is introduced to the fundamentals of infrared thermal imaging. At the first sight, this more and more prevalent method seems straightforward in its application, offering precise monitoring

of temperature at high resolution. However, the lack of awareness of certain limitations of this technique induces errors and misinterpretations. The challenges and the correct approach for the use of this technique are explained in the second part of this section. Finally, its application to microsystems, i.e. microstructured reactors is discussed.

4.2.1 Basic Principles of Measurements

Every object that has a temperature above absolute zero (0 K) emits a spectrum of thermal radiation, i.e. electromagnetic waves [207, 208]. To simplify the illustration in the following, the object is assumed to behave as an ideal black body, meaning that it absorbs every incident radiation, and the emitted spectrum is solely a function of temperature. The radiance $L_{\lambda'}(T)$ emitted by a blackbody can be described by Planck's theory of emission [209]:

$$L_{\lambda'}(T) \cdot d\lambda' = \frac{2 \cdot h' \cdot c'^2}{\lambda'^5} \cdot \frac{1}{e^{\frac{h' \cdot c'}{\lambda' \cdot k_B \cdot T}} - 1} d\lambda' \quad (4.1)$$

Where c' designates the speed of light, h' Planck's constant, k_B the Boltzmann constant, λ' the wavelength and T the absolute temperature of the body. The exemplary curves obtained at four different temperatures are plotted in Figure 4.1.

The wavelength at which the radiance is maximal for a certain temperature can be deduced from Wien's displacement law [209]:

$$\lambda'_{\max} \cdot T = 2897.8 \mu\text{m} \cdot \text{K} \quad (4.2)$$

For a fixed wavelength, the radiance emitted by a black body continuously increases meaning that two spectra of different temperatures will never cross. The detector of any infrared thermal camera converts the incoming radiation (irradiance) within the detection band (Figure 4.1) into an electrical signal. Due to

the strictly monotone character of the function that links radiance and temperature, the temperature can be deduced from the incoming radiation, which corresponds to an integral function of equation (4.1).

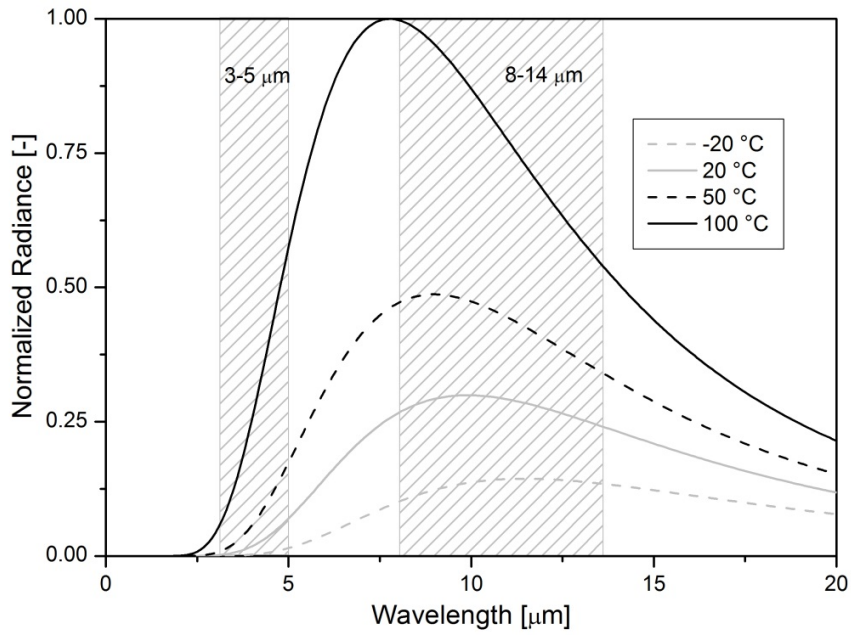


Figure 4.1: Radiance as function of wavelength emitted by an ideal black body. The most common working windows used for infrared thermal imaging are indicated as striped areas.

4.2.2 Challenges in Infrared Thermography

The application of the above described principle into practice is slightly more complex. When pointing the thermal camera at an object, one does not necessarily measure the temperature of the object as illustrated in Figure 4.2.

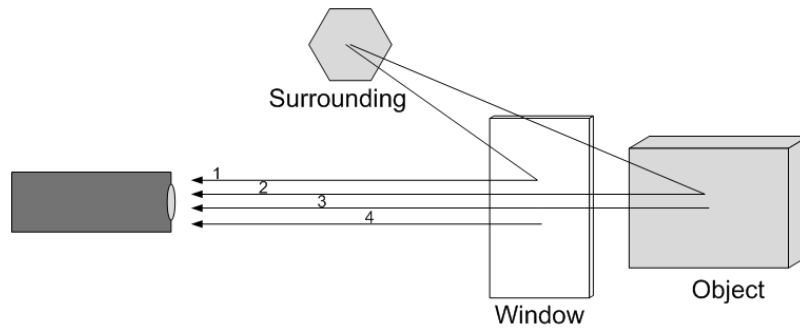


Figure 4.2: Schematic of the signal entering an IR camera: 1) Reflection on the window surface, 2) Reflection on the object surface, 3) Emission from the object, 4) Emission from the window.

Typically, when working with materials such as glass, for wavelengths above $7\ \mu\text{m}$, 99% of the signal is emitted by a layer of $10\ \mu\text{m}$ of the objects surface [210]. The signal transmitted to the camera is deformed by reflections on various surfaces and absorption within the crossed media. The original signal emitted by the object, which is assumed to be a black body, is a function of wavelength as previously described. When travelling from the object to the camera, this signal denoted as (3) in the picture is partly absorbed and reflected by the window, partly absorbed by the crossed medium. Hence, the radiation entering the camera is weaker compared to the emission of the object. At the same time, radiation provided by other sources can perturb the signal. The radiation of a surrounding object, as for example the person carrying out the measurements could be reflected by the window (4) or by the object (2). Finally, as the window has a temperature which is above absolute zero, it also emits radiation. Hence, when measuring, all of these components need to be carefully considered, and in a given case suppressed [200].

The calibration of an infrared camera is generally done using a black body source, which resembles almost perfectly an ideal black body. Real objects, however, have an emission which differs from this ideal behaviour [209]. The ratio of radiation emitted by a surface and radiation emitted by a black body is defined as emissivity. According to Kirchhoff's law [211], at a fixed wavelength, the amount of radiation absorbed by a body equals the amount of radiation emitted by a body, that is:

$$\alpha(\lambda') = \varepsilon(\lambda') \quad (4.3)$$

Every surface has an emissivity between 0 and 1. When measuring temperatures of real surfaces, the emissivity needs to be known to draw quantitative conclusions of the image. Unfortunately, the emissivity of a surface is a function of many variables [209, 212]:

- **Material:** Depending on the chemical composition of the material, the emissivity can strongly vary. In general, one can state that most non-metallic materials (skin, paper, stone, etc.) behave as gray emitters with emissivities in the order of 0.8. In contrast, metals can reach well below 0.2.
- **Surface structure and geometry:** Depending on the surface structure, different values can be obtained for the same material. This effect is especially pronounced for metals, where polishing a rough surface can reduce the emissivity up to one order of magnitude. By creating specific surface geometries, this dependency can be used to increase emissivity.
- **Angle of emission:** An ideal black body emits a radiance which is independent of the direction into which it is emitted. Any real surface shows a dependency of radiance on emission angle, i.e. a decrease of emissivity with increasing angle between surface normal and camera. However, in most of the cases the emissivity can be assumed to be constant up to an angle of 45°.
- **Wavelength:** The dependence on wavelength can be best illustrated with the example of glass, which is transparent in the visible range and behaves as a gray body at long wavelengths.
- **Temperature:** Finally, as many physical parameters, the emissivity is a function of temperature.

Several approaches were developed to obtain quantitative data from infrared thermal mapping. One way to overcome the imprecision due to variation in emissivity, is to cover the target surface with tape or paint with known emissivity. The emissivity can be easily obtained by calibrating the camera with a contact probe. Another approach relies on a direct calibration of the studied object by attaching several contact probes. Both presented strategies can only be applied if good thermal contact between tape/paint/probe and object is assured, and if their thermal impact on the measured object is negligible.

4.2.3 Application to Microsystems

Due to the change of object size, useful data can only be retrieved with additional close-up lenses or microscope optics providing sufficient resolution. Thereby, resolutions as low as a few micrometers can be reached. However, when using these additional components, the distance between camera and object has to be reduced, leading to the so called “Narcissus Effect”. Thereby, the reflection of the thermal camera respectively the close-up lens is seen on an infrared window or directly on the objects surface. One simple way to avoid this effect is a change of viewing angle or a calibration of the image such a presented in section 4.3.2.

In general, microsystems are built up from material with complex emissivity properties such as metals, plastics or glass. Surface modification by tape or paint is often not an option as it would influence the thermal characteristics of the studied system. Hence, other solutions need to be found depending on the specificities of the system [200, 209].

In the present study, a solution regarding the quantitative monitoring of temperature in microfluidic devices is proposed. Thereby, the reactor is placed under vacuum to reduce heat losses and create well-defined boundary conditions. At the same time, the upper cover of the channel is chosen thin enough ($< 500 \mu\text{m}$) resulting in a small gradient between the surface temperature and the inner channel temperature. By carrying out a “pixel-by-pixel calibration” (section 4.3.2), the value of inner temperature can directly be derived from the camera signal observed on the reactors surface.

To measure the temperature profile under cooled conditions, a special reactor was developed and constructed where the cooling channel is located under the reaction channel, and hence, does not interfere with the infrared signal passing through the IR window.

4.3 Experimental

This part of the chapter aims, on the one hand, at describing the setup used to validate the “pixel-by-pixel” approach, and on the other hand, the “pixel-by-pixel” calibration method is explained in detail. Finally, the model reaction used to validate the method under reaction condition is presented together with an overview of the experiments carried out.

4.3.1 Setup for Thermal Imaging of Microstructured Reactors

The setup used for thermal imaging of temperature profile in MSR is depicted in Figure 4.3. It consists of two pumps, a plug-in microreactor, a vacuum box connected to a vacuum pump and a thermal camera. The microreactor was placed in the vacuum box which is connected to a standard rotary vane pump and a sufficient vacuum of 10^{-2} mbar (see section 4.4.1) was achieved. To have visible access to the reactor which is placed inside the vacuum box, an IR-window of size $50\text{ mm} \times 20\text{ mm} \times 1.8\text{ mm}$ was mounted on the box top. As infrared camera, a ThermovisionTM Alert MC with a 320×240 pixels uncooled Focal Plane Array (FPA) detector was used with a temporal resolution of 50 Hz. An optimal compromise between spatial resolution and a large field of vision was obtained at 2500 data points/cm² (close-up lens LW 64/150) leading to a field of vision of $64\text{ mm} \times 48\text{ mm}$. The analysis of smaller structures than presented in this work can be done by exchanging the magnifying lens. The spectral range of analysis is 7.5-13 μm where temperature is detected between $-20\text{ }^{\circ}\text{C}$ and $2000\text{ }^{\circ}\text{C}$ with a sensitivity of $0.1\text{ }^{\circ}\text{C}$. As the camera measures radiation at a wavelength from 7.5-13 μm , a material that has high transmittivity in that range and shows sufficient mechanical stability had to be used as window providing visible access to the box. Zinc selenide (ZnSe) was found to be the most suitable due to its relatively high and constant transmittivity of 70 % in that range [213] as shown in Figure 4.4. The losses of 30 % of radiation due to the window lead to a slight deformation of the signal, which can be corrected by calibration as described in the next section.

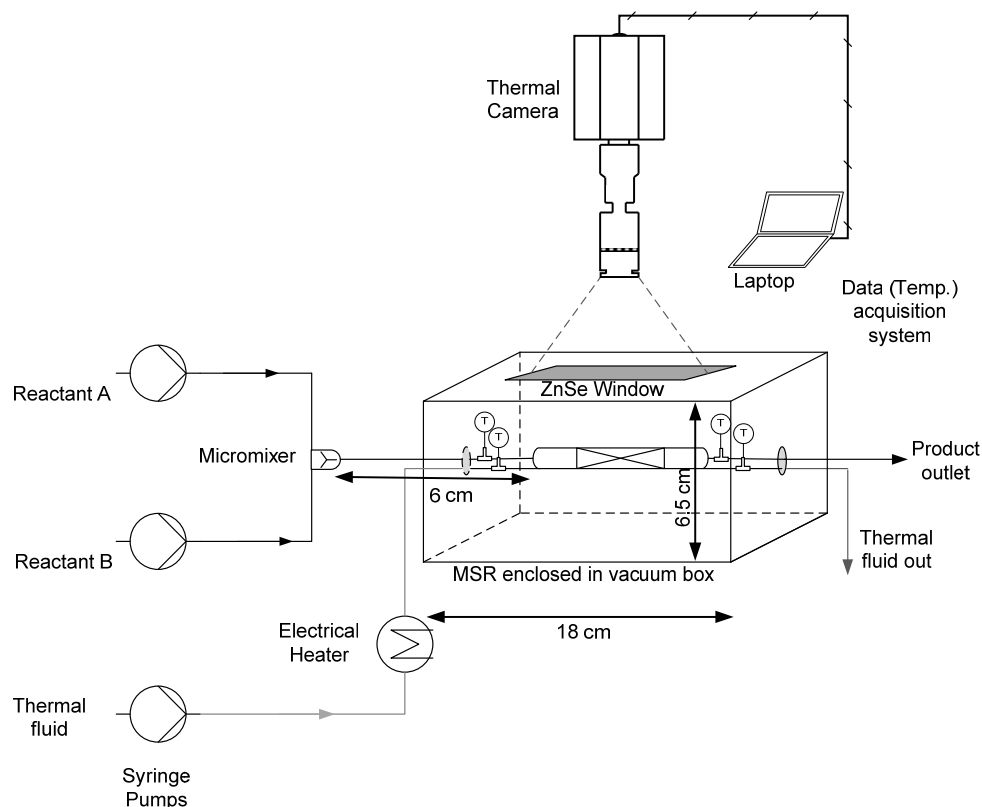


Figure 4.3: Overview of the setup containing a vacuum box with one IR-transmissive ZnSe window.

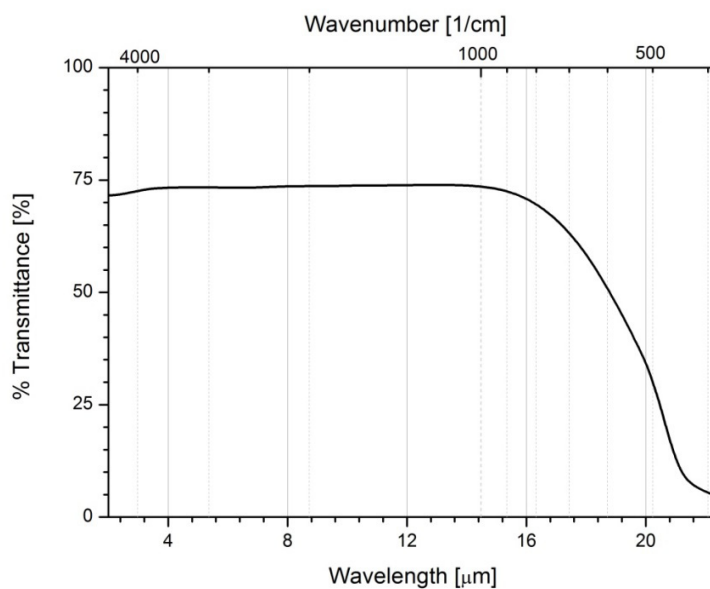


Figure 4.4: Spectral transmittance of zinc selenide. Adapted from ALS Synchrotron Infrared Beamlines [214].

Two liquids are introduced to the micromixer using two syringe pumps. The caterpillar micromixer (CPMM-R150/12-ss-hplc), supplied by Institut für Mikrotechnik Mainz (IMM), Germany [215] is a stainless steel microchannel with varying cross section. The internal bas-relief structures yield a minimum cross section hydraulic diameter of 150 μm . The temperature inside the static mixer and in the connections between mixer and reactor is not monitored by the IR-camera. Therefore it is essential that the space time in the mixer is short to have negligible conversion within the mixing length, and be able to observe the main conversion in the actual reactor. A cooling circuit was built up where the fluid is circulated using a rotary piston pump. The temperature within this circuit was controlled by a heater with a maximal performance of 100 W which was mounted in series with the reactor.

Two plug-in reactors were used which are referred to as first and second generation reactors. The first generation reactor is a perfluoroalkoxy (PFA) capillary with an inner diameter of 1 mm and an outer diameter of 1.6 mm. The total length of the tube monitored by the IR camera is 5 cm. In the first generation reactor, cooling was not applied and therefore, under vacuum, nearly adiabatic conditions can be assumed.

In the second generation reactor, a cooling channel was integrated. By using conventional arrangements as shown in Figure 4.5a, the temperature profile of the reaction channel cannot be determined by infrared thermography. An alternate arrangement by switching the channels can solve this problem as depicted in Figure 4.5b. In this case, the reaction occurs in the annular channel where its thermal profile can be followed with the IR camera. Due to the symmetrical arrangement, a homogeneous heat transfer is warranted. However, the fabrication of this reactor turned out to be difficult as both tubes need to be perfectly centered in the μm -range. Therefore, a reactor with a cross section as shown in Figure 4.5c is used in this study.

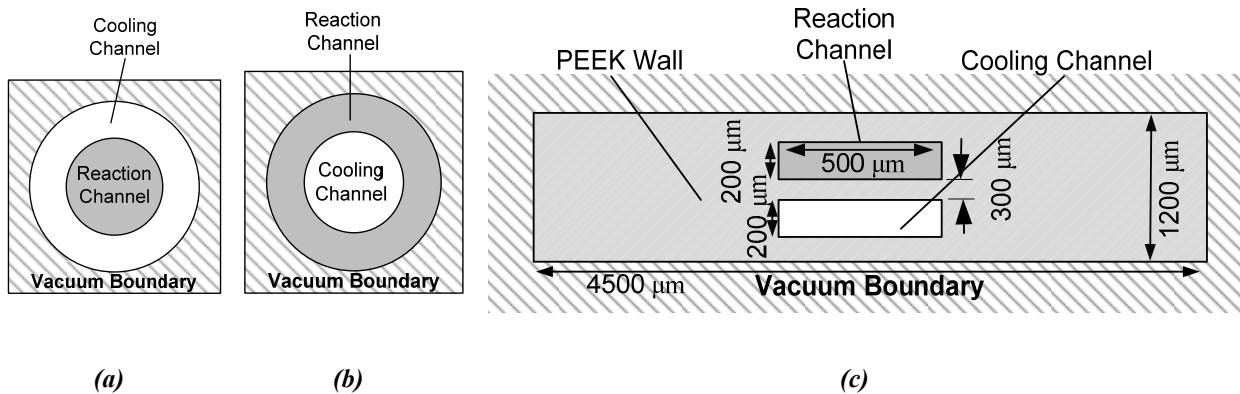


Figure 4.5: Three possible configurations. a) Reaction channel is inside of the cooling channel, b) cooling channel is inside of the reaction channel, c) parallel reaction and cooling channels.

A snapshot of the second generation microreactor is depicted in Figure 4.7. The upper reaction channel is covered by a thin Polyether ether ketone (PEEK) layer of 250 μm . Due to the low thermal conductivity of PEEK ($\lambda_{\text{PEEK}} = 0.29 \text{ W/mK}$) [216] and the small thickness of the layer, diffusion of heat in the plane is avoided and thus, the loss of signal resolution is minimized. In addition, if the heat transfer resistance at the outside of the reactor channel is high (close to adiabatic conditions), the surface temperature of the reactor is close to the temperature inside the channel (see Figure 4.6).

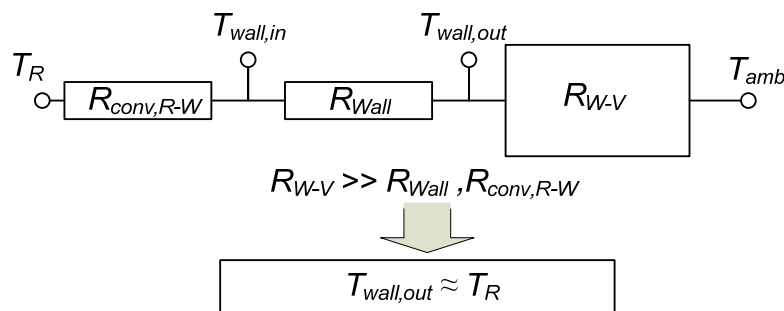


Figure 4.6: Schematic view on the heat transfer resistances in radial direction in the present reactors.

$R_{\text{conv},R-W}$ = Inner convective resistance between wall and reaction mixture, R_{wall} = resistance in the reactor wall, $R_{\text{con},W-V}$ = outer lumped resistance between vacuum and wall.

The bottom channel is used as cooling/heating channel whose temperature profile is not accessible. The heat exchange is carried out through the wall which separates both channels and has a thickness of 300 μm . The height of the channels (h) is 200 μm . Due to the small height, almost homogeneous

temperature distribution within the cross section can be assumed. The width (w) is 500 μm and the total length of the parallel channels is $L = 10$ cm. Due to the physical arrangement of the setup, a reactor length of $L_{\text{obs}} = 4.5$ cm can be monitored through the ZnSe window.

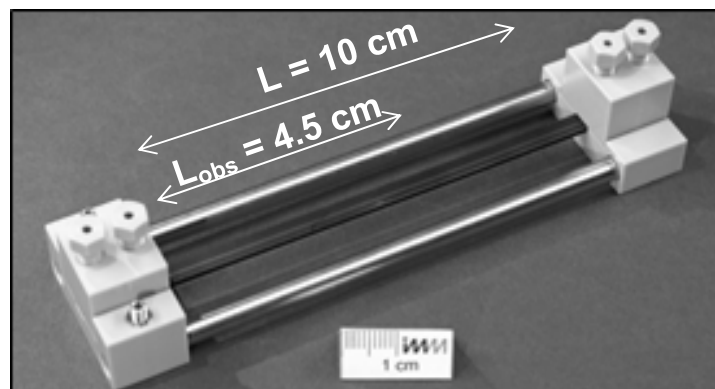


Figure 4.7: 2nd generation reactor: snapshot of the microreactor.

4.3.2 Calibration of the Setup

Using the setup described above, a method for quantitative thermal imaging was developed. As mentioned before, the radiation emitted by a surface is a function of many factors such as the emissivity, the angle of emission and the spectral transmittance through the IR-window. As the unknown sum of these factors influences the signal, the observed temperature θ will deviate from the real temperature inside the microchannel T_{real} . The method presented in this work is based on an external calibration of the IR-camera which subsequently allows obtaining the real temperature inside the microchannel.

For calibration, an inert fluid (ethylene glycol) with known constant temperature was passed through the microchannel with minimized heat losses. The fluid temperatures were measured at the reactor inlet and at the outlet by thermocouples. The outlet temperature of inert fluid was equal to its inlet value within a range of tolerance of 0.5 $^{\circ}\text{C}$. The overall precision of the method increases with suppressed difference of temperature between inlet and outlet. This regime can be reached by reducing the heat losses along the channel and simultaneously increasing the flow rate (reducing the residence time). For each calibration

temperature, one thermal image was taken as well as the real temperature measured by the thermocouples placed inside the tube. The thermal image indicates an observed temperature θ for every pixel of the image, which has to be calibrated with the known temperature T_{real} (see Figure 4.12). For every point in the image, an n^{th} order polynomial is developed which has the form of $T_{\text{real}} = f(\theta)$ by processing using a commercial software, MathWorks Matlab 7.0 .

The overall precision of the presented method is ± 1 °C for the temperature range 30 °C - 50 °C. The experimental inaccuracy is composed of the following factors:

- The signal/noise level of the IR camera: ± 0.1 °C
- Shift of temperature between intervals of internal calibration of the camera: ± 0.7 °C
- Precision of the calibrated thermocouples: ± 0.5 °C
- Temperature difference between inlet and outlet during calibration: ± 0.5 °C

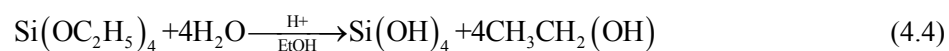
If necessary, a higher accuracy can be obtained by directly using platinum thermal resistance thermometers and averaging the pictures. However, for the present work, the achieved accuracy was estimated to be sufficient.

4.3.3 Experimental Conditions

To validate the presented methodology, the temperature profiles in two different systems i.e. with a reactive and non-reactive system were quantitatively determined. The calibration of the setup with ethylene glycol was carried out before each series of experiments to assure reliable results.

In the reactive system, a fast exothermic reaction is carried out in the 1st generation reactor, which is connected in series with the micromixer. As residence time in the visible area varies from 0.5 s to 3 s, a reaction with characteristic reaction time in the order of seconds is required, referred as type B reaction (in Kockmann *et al.* [55]). In the present work, the hydrolysis of Tetraethoxysilane (TEOS) was used as model reaction. As TEOS has limited solubility in water, the reaction is carried out using ethanol as

solvent to create a homogeneous system. The reaction rate can be controlled by varying the concentration of hydrochloric acid which catalyzes the transformation.



However, one has to be careful when carrying out this reaction in microchannels. As a consecutive polymerization of the product occurs, the risk of channel clogging is high. Therefore, it was decided to work only with one specific mixture which was found to be stable: solution A contains 67 % v/v of TEOS in ethanol. Solution B contains 42 % v/v of water, 17 vol. % v/v of fuming hydrochloric acid (37 % w/w in water) in ethanol. Subsequently, solution A and B are mixed in a volumetric proportion of 2:1. Using these proportions, the molar ratio of TEOS to water is 0.8. The obtained characteristic reaction time is in the order of 5 s at 25 °C and the adiabatic temperature rise measured in a calorimeter is $\Delta T_{\text{ad}} = 37$ °C. The kinetics of this reaction were published by Bessarabov and Shalubov [217], however, they have not been validated within the range of high concentrations of catalyst and reactants as given above.

In the non-reactive system, the second generation reactor was used for carrying out heat exchange experiments. Thereby, in the upper channel ethanol was passed at 25 °C and the bottom channel was supplied by butanol at 58 ± 3 °C. The profile of the upper channel was monitored with the IR camera. Subsequently, the heat transfer coefficient of the reactor was determined by numerical simulation and compared to theoretical estimations.

4.4 Results

First, the overall heat losses in the setup are identified and then quantified. Subsequently, the calibration and the temperature profiles in the reactive system are obtained. Finally, the heat transfer coefficient in the non-reactive system is estimated.

4.4.1 Characterization of Heat Losses

To determine the heat losses in the system, hot ethylene glycol was pumped through the first generation reactor at a velocity of 2 cm/s. The temperature was measured with thermocouples at the inlet and outlet of the reactor as depicted in Figure 4.8 as a function of time and pressure in the vacuum box. When the vacuum pump was switched on, the pressure inside the box was decreased to $2 \cdot 10^{-2}$ mbar. The vacuum pump was then switched off resulting in increased pressure inside the box. At $2 \cdot 10^{-2}$ mbar the measured temperature was found to increase as shown in Figure 4.8 indicating the influence of vacuum on heat losses through capillary surface.

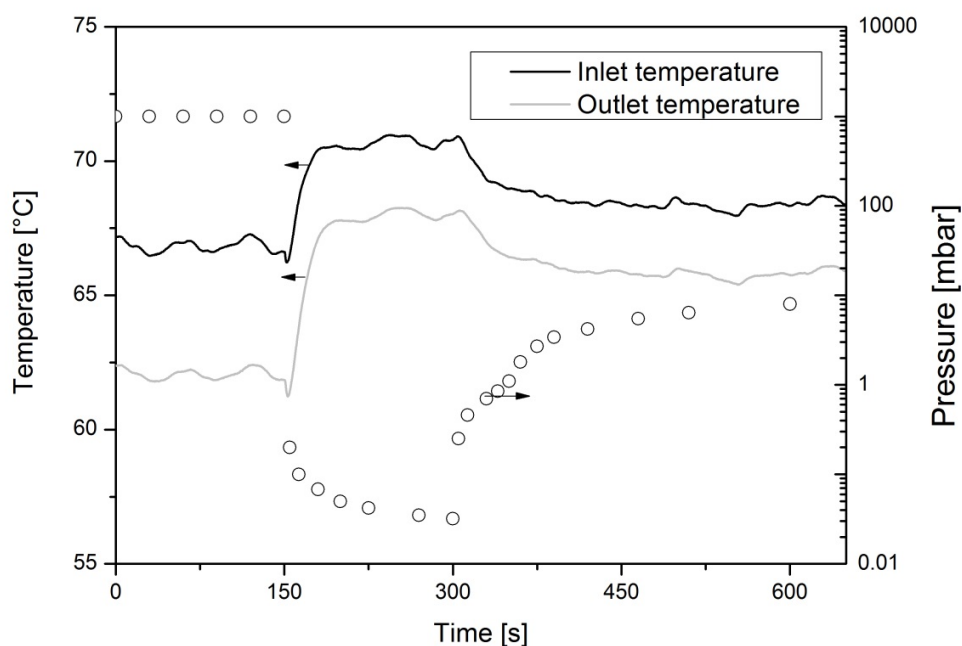


Figure 4.8: Temperature difference between inlet and outlet of the first generation reactor with a flow of 2 cm/s of ethylene glycol.

Assuming that all the heat losses are due to convection, an apparent heat transfer coefficient can be determined using following relation for ideal plug flow reactor [17]:

$$u \cdot \rho_{eg} \cdot c_{p,eg} \cdot \frac{dT}{dz} = -U_{loss} \cdot a_{outer} \cdot (T - T_{amb})$$

$$U_{loss} = \frac{u \cdot \rho_{eg} \cdot c_{p,eg} \cdot \frac{\Delta T}{\Delta z}}{a_{outer} \cdot (T - T_{amb})} \quad (4.5)$$

Where, u , U_{loss} , T_{amb} and a_{outer} are linear velocity, apparent heat transfer coefficient, ambient temperature and specific exchange area of the channel, respectively. The specific exchange area is defined as the ratio between surface area at the capillary outer surface and volume of the liquid inside. The temperature difference between reactor inlet and outlet is ΔT over a reactor length of Δz in this case. The physical properties such as density (ρ_{eg}) and specific heat capacity ($c_{p,eg}$) refer to mean values of the liquid.

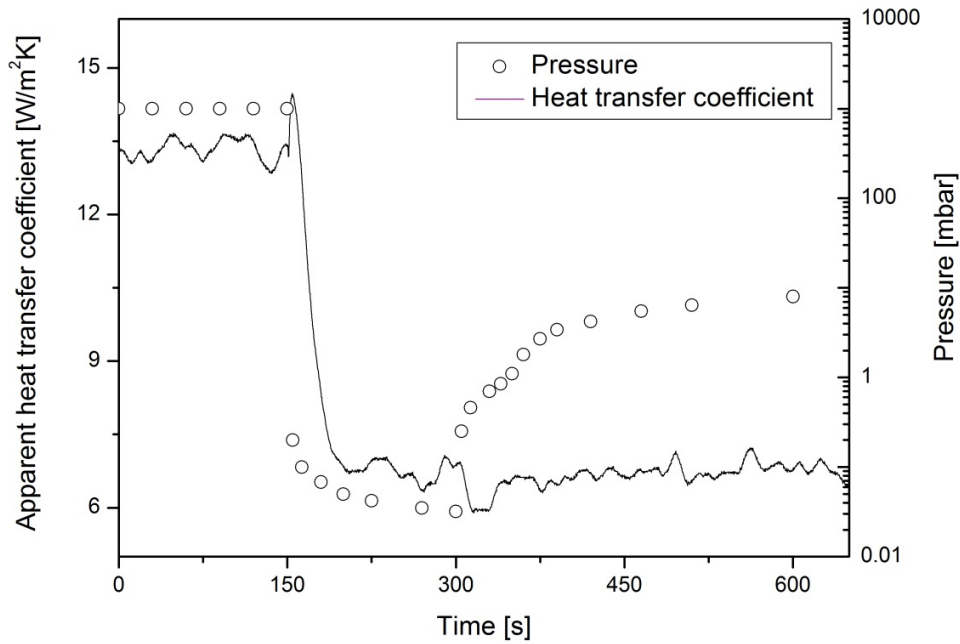


Figure 4.9: Apparent heat transfer coefficient of the first generation reactor with a flow of 2 cm/s of ethylene glycol.

The heat transfer coefficient as a function of time for different pressures is plotted in Figure 4.9. At atmospheric pressure, the resulting apparent heat transfer coefficient is $\sim 13 \text{ W/m}^2\text{K}$. By switching on the vacuum pump, the pressure drops to $2 \cdot 10^{-2}$ mbar. Simultaneously the heat transfer coefficient decreases to

$\sim 7 \text{ W/m}^2\text{K}$. An increase of pressure up to 10 mbar has no major influence on the apparent heat transfer coefficient indicating no further visible impact of reduced pressure on the heat losses. To better understand the nature of the remaining $\sim 7 \text{ W/m}^2\text{K}$ corresponding to a heat dissipation of 0.11 W, these were estimated using a simplified scheme of the set-up, as shown in Figure 4.10.

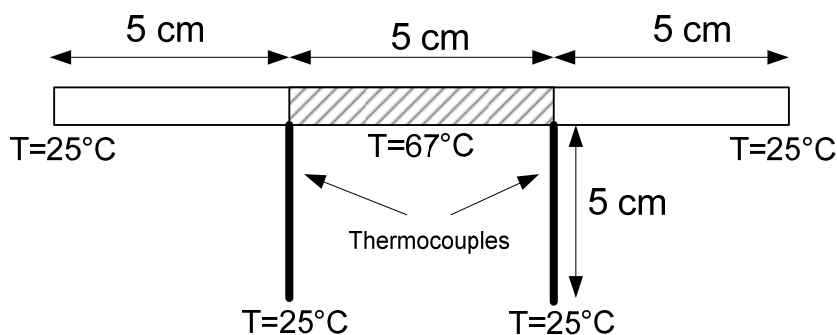


Figure 4.10: Simplified configuration of the setup to determine heat losses.

The three mechanisms of heat transfer were analyzed: convection, conduction (through thermocouples and tubes) and radiation. The convective heat transfer coefficient was estimated using Krischers correlation [37] for convective heat transfer along horizontal cylinders (see Figure 4.11). A value of convective heat transfer coefficient $U_{\text{Conv}} \approx 0.5 \text{ W/m}^2\text{K}$ was obtained which corresponds to about 0.008 W or 7 % of the total heat losses indicating that a vacuum of about 10^{-2} mbar efficiently suppresses convection.

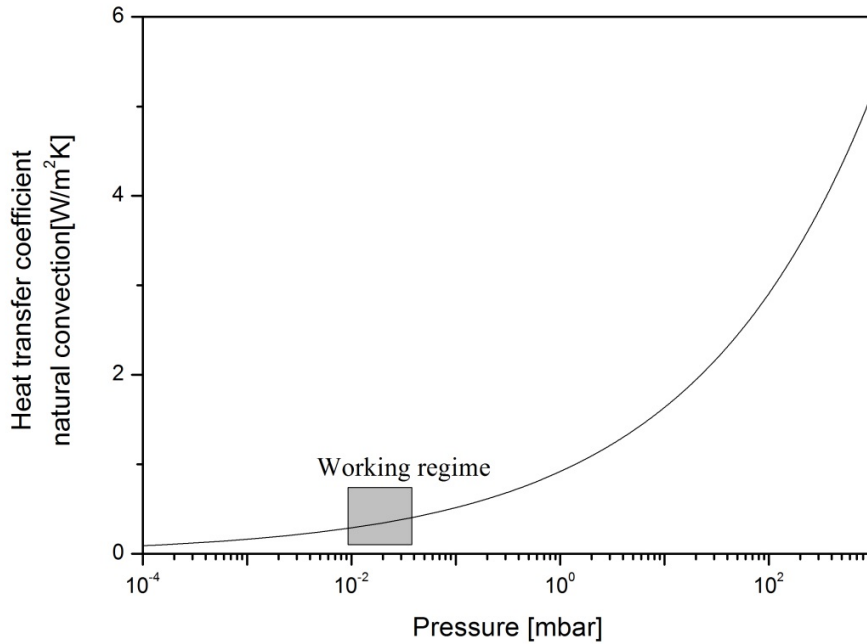


Figure 4.11: Heat transfer coefficient as a function of ambient pressure

The losses through conduction can be estimated using the Fourier law. The heat losses (\dot{Q}_{cond}) in the highly conductive thermocouples $\lambda_{Ni} = 91$ W/mK and in the low conductive but thicker perfluoroalkoxy (PFA) capillary $\lambda_{PFA} = 0.25$ W/mK (assuming a homogeneous cylinder with a diameter of 1.55 cm) should be considered:

$$\begin{aligned}
 \dot{Q}_{cond} &= \dot{Q}_{cond,PFA} + \dot{Q}_{cond,TC} \\
 &= 2 \cdot A_{PFA} \cdot \lambda_{PFA} \cdot \frac{\Delta T}{\Delta l} + 2 \cdot A_{TC} \cdot \lambda_{Ni} \cdot \frac{\Delta T}{\Delta l} \\
 &= 2 \cdot (1.55 \cdot 10^{-3})^2 / 4 \cdot \pi \cdot 0.6 \cdot \frac{67-25}{0.05} + 2 \cdot (0.55 \cdot 10^{-3})^2 / 4 \cdot \pi \cdot 91 \cdot \frac{67-25}{0.05} \\
 &= 1.9 \cdot 10^{-3} \text{ W} + 0.036 \text{ W} = 0.038 \text{ W}
 \end{aligned} \tag{4.6}$$

Thus, the conduction losses through axial conductivity in the capillary are negligible, whereas the losses through the thermocouples account for about 30 % of the total losses. By removing these thermocouples, the losses can be avoided. At last, the radiation losses can be determined through the Stephan-Boltzmann law:

$$\begin{aligned}\dot{Q}_{rad} &= \varepsilon \cdot 5.67 \cdot 10^{-8} \cdot (340^4 - 298^4) \cdot 0.045 \cdot 1.55 \cdot 10^{-3} \cdot \pi \\ &= \varepsilon \cdot 0.075 \text{ W}\end{aligned}\tag{4.7}$$

Where ε is the emissivity of PFA, which is assumed to be close to 1 in the range of measurement [218]. Hence, the radiation losses constitute about 60 % of the total heat losses at 67 °C. These losses cannot be avoided as the emitted radiation is used to determine temperature.

4.4.2 Temperature Profiles of the Reactive System

In this section, the calibration of the thermal image is demonstrated before showing the temperature profiles obtained with the model hydrolysis of TEOS.

4.4.2.1 Calibration for 1st Generation Reactor

For the five calibration experiments shown in Figure 4.12, ethylene glycol was pumped at flow velocities above 20 cm/s through the reactor with constant temperatures between 30 °C and 50 °C. The temperature difference between inlet and outlet was kept below 0.5 °C.

A typical calibration of a pixel from Figure 4.12 fitted to 2nd order polynomial is shown in Figure 4.13. With this function, any observed temperature θ of pixel with coordinates ($x = 16$, $y = 19$) can be transformed into the real temperature inside the reactor T_{real} . In general, a 2nd order polynomial was observed to fit well having a coefficient of determination > 0.99 . The R^2 -value for every pixel of the image is shown in Figure 4.14. It can be noted that pixels located on the border of the reactor are less accurate and should therefore not be used to determine the axial temperature profile. Therefore, to track axial temperature profiles, an average over several pixels located in the middle of the channel was used.

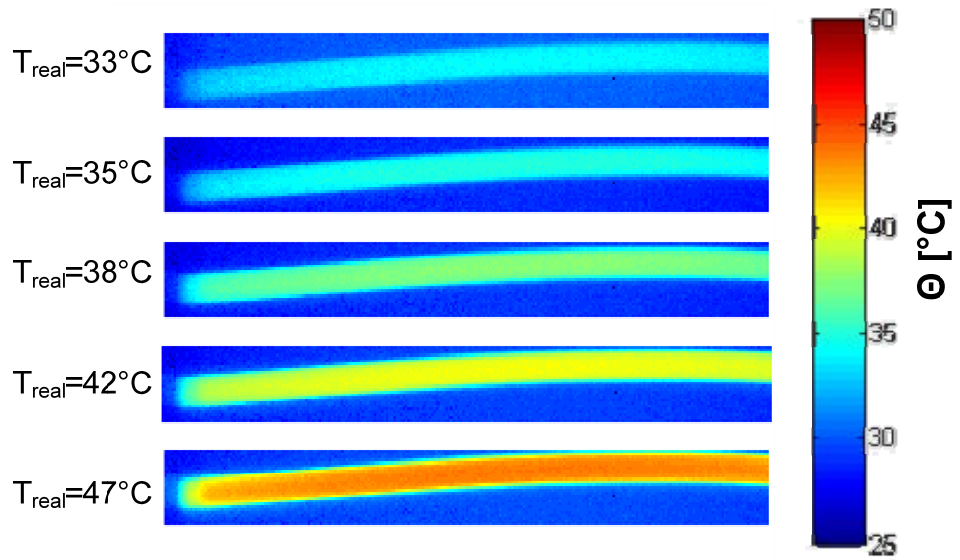


Figure 4.12: Calibration images of the 1st generation reactor taken at 5 different temperatures.

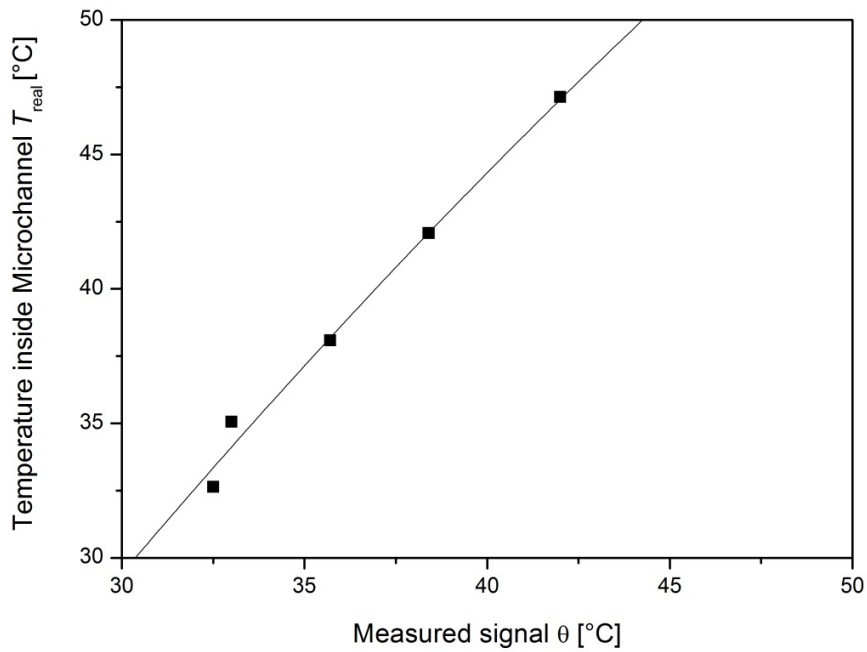


Figure 4.13: Calibration curve for pixel ($x = 16, y = 19$) situated on the left hand side of the picture. The R^2 -value for the fit is 0.99.

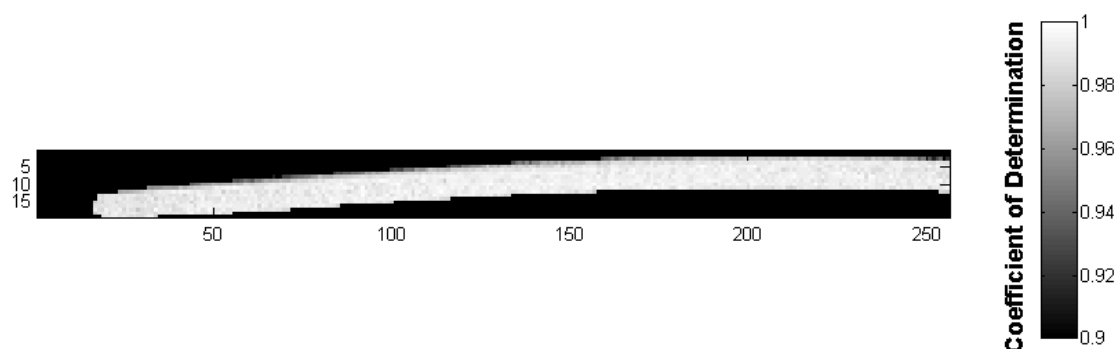


Figure 4.14: Coefficient of determination (R^2 -value) for every pixel of the image after calibration of the 1st generation reactor.

4.4.2.2 Temperature Profiles in 1st generation reactor

Four temperature profiles with the hydrolysis of Tetraethoxysilane without cooling were recorded and are shown in Figure 4.15. The observed window is located 5 cm from the outlet of the micromixer.

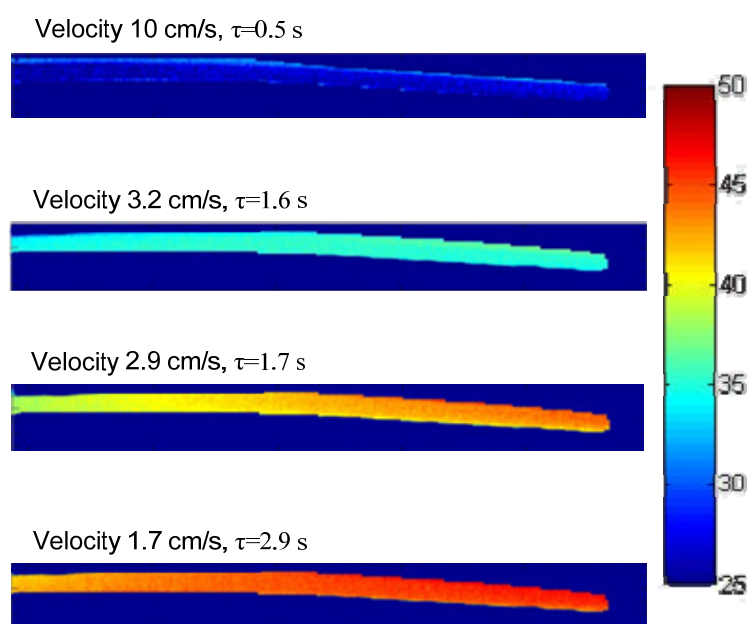


Figure 4.15: Temperature profile of 1st generation reactor during the hydrolysis of Tetraethoxysilane. The inlet of the 5 cm long reactor is located 5 cm from the outlet of the micromixer.

At a flow velocity of 10 cm/s, no temperature rise was observed. The low conversion at this flow velocity can be explained by the short residence time. When the velocity was decreased to 3.2 cm/s, the hot spot

moved to the observing window and temperature rose to 34 °C. Diminishing the flow velocity down to 2.9 cm/s and then to 1.7 cm/s made possible to observe the hot spot at its full magnitude of 47 °C. However, in an ideal adiabatic system at full conversion, a temperature rise up to 62 °C would be expected. Two phenomena are responsible for the difference between theoretical adiabatic temperature and maximum observed temperature: heat losses and segregation of the reactants. The impact of the former effect can be quantified using the apparent heat transfer coefficient calculated in the characterization section. Thus, a total loss of less than 1 °C can be attributed to the non-ideal adiabatic conditions. The remaining difference of temperature is ascribed to the incomplete conversion due to insufficient mixing of the reactants. The Reynolds number inside the caterpillar mixer at this flow rate is relatively low ($Re = 144$), leading only to a limited amount of secondary flows. In addition, the flow ratio of 2:1 (A:B) and the difference of density between the two flows are not favorable for homogenization. To further analyze the mixing quality, solution B was colored using Methylene Blue. As depicted in Figure 4.16, at the outlet of the caterpillar mixer segregation of the flows was observed. Due to gravitational forces, solution A flows on top of the denser solution B.

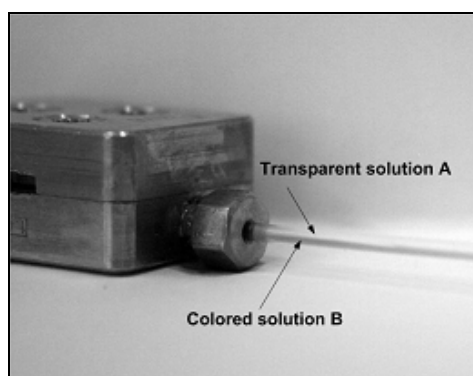


Figure 4.16: Segregation of the flows at the outlet of caterpillar mixer due to difference in density and flow ratio of 2:1 (A:B) at a total flow rate of 1 ml/min.

The further mixing of the flows in the first generation reactor occurs mainly by diffusion, as no mixing structures are embedded. The characteristic diffusion time required for complete mixing is in the order of minutes ($D_m \approx 10^{-9} \text{ m}^2/\text{s}$), explaining the gap between maximum observed temperature and theoretical

adiabatic temperature. Hence, the information gained from the quantitative temperature profile retrieved via “pixel-by-pixel” calibration was successfully used to understand the phenomena inside the microstructured reactor.

4.4.3 Temperature Profiles in the Non-reactive System

The second generation reactor was used for an estimation of the heat transfer coefficient at constant flow of 92 cm/s of hot butanol at 58 ± 3 °C in the bottom channel. In the top channel, three different flow rates of cold ethanol (25 °C) were applied. The corresponding temperature profiles observed through the ZnSe-window within the first 4.5 cm ($z = 0 \dots 4.5$ cm) are given in Figure 4.17. The values measured with 0.5 mm thick thermocouples at the inlets ($T_{Top,in}$) and the outlet ($T_{Top,out}$) are given in Table 4.1.

It has to be pointed out that the thermocouple at the reactor inlet was placed 1 cm before the location defined as $z = 0$ on the thermal image and the one at the outlet at 1 cm after $z = L = 10$ cm. Thus, heat is exchanged already before reaching the point defined as $z = 0$, which leads to $T_{top}(z = 0) > T_{top,in}$. The same effect is observed at the reactor outlet, where heat exchange is occurring after $z = 4.5$ cm before reaching the outlet thermocouple.

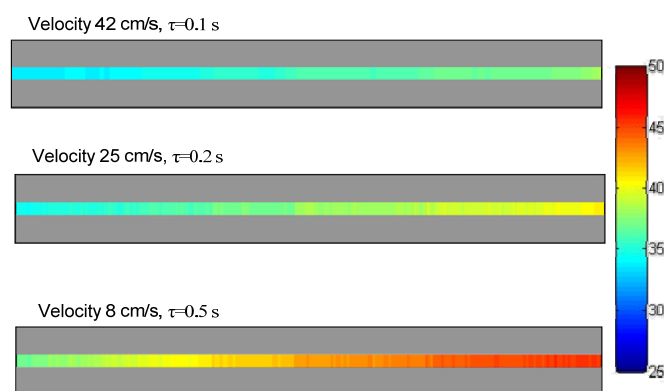


Figure 4.17: Temperature profiles in 2nd generation microreactor at different flow rates.

Table 4.1: Temperature measured by thermocouples at the inlet and outlet of the top and bottom channel; the flow rate in the bottom channel was 92 cm/s.

Flow rate in the top channel [cm/s]	$T_{\text{top,in}}$	$T_{\text{top,out}}$	$T_{\text{bottom,in}}$	$T_{\text{bottom,out}}$
42	27.2	39.6	60.9	54.5
25	26.9	43.6	60.2	54.6
8	26.5	45.2	56.3	52.5

As expected, decreasing the flow rate in the upper channel leads to higher temperatures at its outlet. In general, a discrepancy between temperature measured by thermocouples and the temperature depicted at distances $z = 0$ and $z = L$ is observed due to the heat exchange occurring in the connections.

There are two options to determine the heat transfer coefficient of the reactor. The temperatures can be measured by thermocouples which results in a mean heat transfer coefficient all over the part including the connections. The second possibility is to determine the heat transfer coefficient using the profiles obtained with IR camera. A simple heat balance between the flow in the upper channel and the bottom channel is considered with the heat transfer coefficient U_{ex} used as fitting parameter. The equations to be solved are given in the following:

$$\begin{aligned} \frac{dT_{\text{top}}}{dz} &= U_{ex} \cdot a_{ex} / (u_{\text{top}} \cdot \rho_{\text{top}} \cdot c_{p,\text{top}}) \cdot (T_{\text{bottom}} - T_{\text{top}}) \\ \frac{dT_{\text{bottom}}}{dz} &= U_{ex} \cdot a_{ex} / (u_{\text{bottom}} \cdot \rho_{\text{bottom}} \cdot c_{p,\text{bottom}}) \cdot (T_{\text{top}} - T_{\text{bottom}}) \end{aligned} \quad (4.8)$$

Assuming that the heat exchange only occurs through the wall located between the channels, the specific heat exchange area is $a_{ex} = 5000 \text{ m}^2/\text{m}^3$. As the physical properties of ethanol and butanol are very similar, the density and the heat capacity of both are assumed to be equal and independent of temperature in the considered range. The resulting deviation is less than 3 %, so $\rho_{\text{bottom}} = \rho_{\text{top}} = 775 \text{ kg/m}^3$ and $c_{p,\text{bottom}} = c_{p,\text{top}} = 2400 \text{ J/kgK}$. The temperature profile for the upper channel is known. To find the heat transfer coefficient, an initial temperature for the bottom channel is required. This temperature is obtained

using the values measured by thermocouples ($T_{\text{bottom,in}}$ and $T_{\text{top,in}}$) followed by a heat balance supposing an adiabatic connection piece:

$$u_{\text{top}} \cdot (T_{\text{top,in}} - T_{\text{top}}(z = 0)) = -u_{\text{bottom}} \cdot (T_{\text{bottom}} - T_{\text{bottom}}(z = 0)) \quad (4.9)$$

The values obtained for the global heat transfer coefficient are summarized in Table 4.2 and the corresponding plots are given in Figure 4.18.

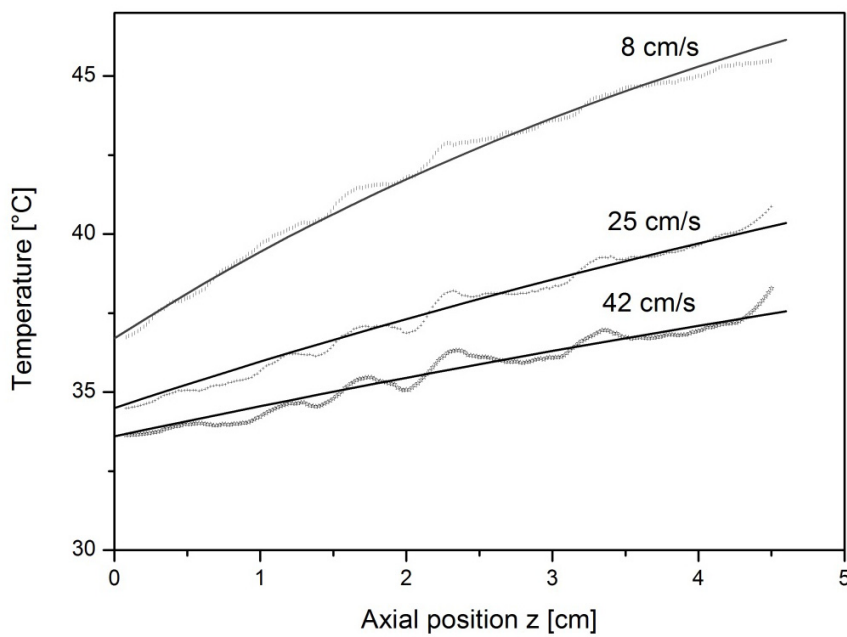


Figure 4.18: Temperature profiles (gray line) and corresponding simulation (dark line) in 2nd generation microreactor.

Table 4.2: Global heat transfer coefficient determined at different flow rates.

u [m/s]	0.42	0.25	0.08
U_{ex} [W/m ² K]	629	598	494

The plot shows that the measured data vary within ± 0.5 °C. This can be explained by the fact that each axial value of temperature is obtained by calculating the mean over two pixels which cover a width of

2x200 μ m of the channel. Depending on the position of the two pixels within the channel, this temperature can slightly vary.

As the flow and the temperature profile are fully developed at $z = 0$ (flow developing length is 3 mm, from [219]), a dependence of the heat transfer coefficient is not expected. The different values obtained are within the range of precision and can be partly explained by an increased influence of the heat losses during the calibration process. If the experiment is carried out over a too narrow temperature range (at the higher flow rates $\Delta T \approx 5$ °C), the heat transfer coefficient gets slightly overestimated. For comparison with literature correlations, a mean value of $U_{ex, mean} = 574$ W/m²K is supposed.

To understand the contribution of the different heat transfer resistances, the results can be compared to the values obtained using correlations given in literature [37]. Therefore, three resistances are considered: the resistance at the ethanol/PEEK interface R_1 , the resistance inside the PEEK R_2 and the resistance at the PEEK/butanol interface R_3 . The global heat transfer coefficient is given by:

$$\frac{1}{U'_{ex}} = R_1 + R_2 + R_3 \quad (4.10)$$

As a first approach, identical physical properties of ethanol and butanol are assumed i.e. $R_1 = R_3$. For the estimation of these resistances, the channels' hydraulic diameter is used and the equivalent resistance is calculated. Since the flow is already developed, the Nusselt number for an isothermal wall has attained its limit value of $Nu_\infty = 3.4$ for rectangular ducts with aspect ratio 0.4 [219]:

$$\begin{aligned} Nu_\infty = 3.4 &= \frac{d_h}{\lambda_{OH} R_1} \\ \Rightarrow R_1 = R_3 &= \left(\frac{Nu_\infty \cdot \lambda_{OH}}{d_h} \right)^{-1} = \left(\frac{3.4 \cdot 0.17 \text{ W}}{286 \cdot 10^{-6} \text{ m}^2\text{K}} \right)^{-1} = \frac{1 \text{ m}^2\text{K}}{2021 \text{ W}} \end{aligned} \quad (4.11)$$

The resistance inside the PEEK wall can be calculated with $\lambda_{PEEK} = 0.25$ W/mK [220]:

$$R_2 = \frac{\lambda_{PEEK}}{\delta} = \left(\frac{0.25 \text{ W}}{300 \cdot 10^{-6} \text{ m}^2\text{K}} \right)^{-1} = \frac{1 \text{ m}^2\text{K}}{833 \text{ W}} \quad (4.12)$$

Thus, the global heat transfer coefficient (U'_{ex}) is 457 W/m²K which is in the same order of magnitude as the value estimated from the experiments ($U_{ex, mean} = 574$ W/m²K). About 50 % of the total resistance comes from the PEEK wall, the other 50 % are due to the heat transfer between liquid and wall.

4.5 Conclusions

A method based on infrared thermometry has been developed allowing quantitative on-line monitoring of axial temperature profiles within microreactors with an accuracy of 1 °C and a resolution of 2500 data points/cm². Heat losses by convection were efficiently suppressed by placing the microreactor at a pressure of 10⁻² mbar. Thereby, the overall heat losses were reduced down to 15 % as compared to ambient environment. The method was applied to a microcapillary without cooling where highly exothermic and fast hydrolysis of tetraethoxysilane was carried out. The location and the magnitude of the hot spot have been determined as a function of the flow rate. Furthermore, using this novel method of quantitative temperature measurement, insufficient mixing of the reactants was detected. The developed method has also been applied to a cooled system where the overall heat transfer coefficient was determined being in good agreement with literature data.

4.6 Notations

A	Surface area, [m ²]
c_p	Mean heat capacity, [J/(kg K)]
c	Concentration, [mol/m ³]
c'	Speed of light, [m/s]
d	Channel diameter, [m]
h	Channel height, [m]
h'	Planck's constant, [J·s]
k	Rate constant, [(m ³ /mol) ^{$n-1$} /s]
k_B	Boltzmann constant, [J/K]
L	Radiance, [W·sr ⁻¹ ·m ⁻²]
L	Length of the reactor, [m]
l	Length of thermocouples/tubes, [m]
n	Reaction order
\dot{Q}	Heat flux, [W]
R	Heat Transfer resistance, [K/W]
R^2	Coefficient of determination, [-]
t_r	Characteristic reaction time $1/(k \cdot c_0^{n-1})$, [s]
T	Temperature, [K]
u	Flow velocity, [m/s]
U	Global heat transfer coefficient, [W/(m ² K)]
w	Channel width, [m]
x	Abscissa, [m]
y	Ordinate, [m]
z	Axial coordinate, [-]

Greek

α	Absorbance, [-]
δ	Wall thickness, [m]
Δ	Symbol for difference
ε	Emissivity, [-]
λ	Thermal conductivity, [W/(m K)]
λ'	Wavelength, [m]
θ	Signal measured by the thermal camera, [°C]
ρ	Mean density, [kg/m ³]

Dimensionless numbers

Nu	Nusselt number $h \cdot d_p / l_{Fluid}$, [-]
Re	Reynolds number $u \cdot d_p / \nu$, [-]

Subscript

0	Initial condition
ad	Adiabatic
amb	Ambient
bottom	Related to the bottom channel
cond	Conduction
conv	Convection
EG	Ethyleneglycol
ex	Experimental
loss	Related to heat losses
max	Maximal
Ni	Nickel
PEEK	Polyether Ketone

PFA	Perfluoroalkoxy
R	Reactor
rad	Radiation
R-W	Reactor-Wall
TC	Thermocouple
Top	Related to the top channel
W-V	Wall-Vacuum

Chapter 5

REACTIVE MIXING PROFILES IN A MICRO-CROSS MIXER

At the short residence times experienced in microstructured reactors while performing fast exothermic reactions, efficient mixing of the inlet flows plays a crucial role. In the present chapter mixing of two flows leading to a fast exothermic reaction in a T-mixer with circular cross section is monitored via the temperature profile using quantitative infrared thermography. It is shown that mixing at such short time scales remains challenging, and two solutions are proposed: the use of micro-batch flow and of structures.

5.1 Introduction

The high heat transfer rates achieved in microstructured reactors [17] render this type of equipment ideal to control temperature of rapid exothermic reactions and to accelerate the kinetics of existing slower reactions by increasing temperature and/or pressure [11, 34, 46]. As shown in Figure 5.1, depending on the characteristic reaction time $t_r = 1/(k \cdot c_0^{n-1})$ and the characteristic mixing time t_{mix} of the system, the reaction can be carried out in four different regimes:

- $t_{mix} \leq 0.01 \cdot t_r$: No influence of mixing on the overall transformation rate
- $t_{mix} \leq 0.1 \cdot t_r$: Negligible influence of mixing on the overall transformation rate
- $0.1 \cdot t_r \leq t_{mix} \leq 10 \cdot t_r$: Overall transformation rate is influenced by mixing of the reactants

- $t_{mix} \geq 10 \cdot t_r$: Overall transformation rate is controlled by mixing of the reactants

To work in a regime where the effect of mixing can be neglected, characteristic mixing time needs to be at least one order of magnitude smaller than characteristic reaction time [125]. When working with rapid exothermic reactions with characteristic reaction times smaller than 1 s, in many cases mixing time which is in the order of milliseconds to seconds [160] cannot be neglected. Therefore, mixing of the reactants plays an essential role in the formation of temperature profiles in microstructured reactors.

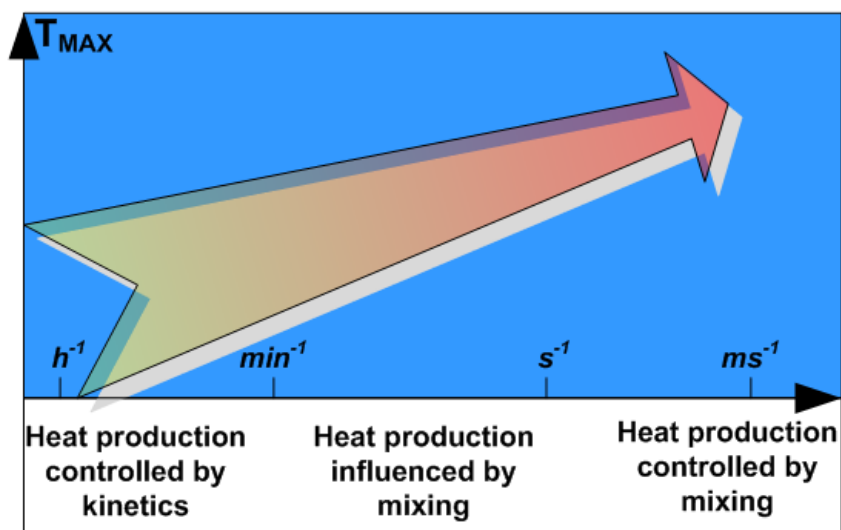


Figure 5.1: Different regimes of operation of a chemical reaction in a microstructured reactor.

Hence, before carrying out a fast chemical reaction in a microstructured reactor, it is necessary to estimate the order of magnitude of mixing time. As a first approach, in a regime where mixing is dominated by convection rather than by diffusion, mixing time can be approximated by the relation proposed by Falk *et al.* [160]:

$$t_{mix} = 0.15 \cdot \varepsilon^{-0.45} \cdot s \cdot (W/kg)^{0.45} \quad (5.1)$$

where ε is the specific power dissipation. In most of the cases, more detailed information is required, which can be obtained either by numerical simulation or experimentally.

The numerical approach has been successfully used during the past 10 years to understand the basic mechanism of mixing in different types of micromixer [107, 141, 147, 154, 221]. It is generally used for geometrical optimization of the mixer avoiding costly iterations of fabrication and testing of devices [147, 154, 222]. Thereby, the simulations have to be carried out in three dimensions and at sufficiently high resolution requiring high computational power. Especially when working with liquids, the low molecular diffusion coefficient can lead to artifacts due to numerical diffusion [146, 147, 223].

Several experimental methods to describe mixing quality in microstructured reactors can be found in literature [224, 225]. They are mainly subdivided in physical and chemical methods of characterization.

The group of physical methods is based on the addition of tracer to the inlet flows. In the simplest method, fluid containing a dye is mixed with a transparent fluid. The homogenization of the color is used as indicator for mixing quality, which has to be monitored along the length of the reactor [226, 227]. As this kind of method only gathers data within two dimensions, the precision is limited. One can imagine a case where two solutions of different densities are contacted: the heavier solution flows on the bottom of the microchannel, whereas the less dense solution flows on top. If observed from the top, one might conclude that both solutions are perfectly mixed due to the apparent homogeneous color all over the channel, which is not the case. By using fluorescent dyes such as fluorescein or rhodamine in combination with confocal microscopy [228-231], three dimensional profiles can be obtained which allows overcoming the abovementioned drawback. However, the resolution of these physical methods is limited by the sampling volume, which cannot record mixing on the molecular level.

When using chemical methods, mixing quality is determined by the conversion/formation of a chemical compound, indicating the quality down to the molecular level. The most straightforward approach is the monitoring of the formation or consumption of a chemical compound along the length. Acid base reactions in presence of an indicator [232, 233] or the coloration of rhodamine [228] constitute important examples of this category. When working with a single reaction, the same disadvantages apply as for the physical methods: visible access to the reactor must be warranted, and only qualitative data is obtained as

generally 2-dimensional images are taken. By carrying out specific complex competitive chemical reactions, the mixing quality can be deduced from the yield of the reaction. In the past 10 years, a lot of effort has been put into obtaining quantitative data from such reaction systems [160, 185, 234, 235]. Among other test reactions [236-238], the Villermaux-Dushman reaction system was widely applied to microstructured reactors [160, 234, 239]. Thereby, the development of an approach for quantitative interpretation of the results enables comparison of mixing between different reactors [160].

Many of the chemical and physical methods presented in literature are based on an aqueous system at equal flow rates. The results obtained in such testing systems can differ from the behavior of the real reaction system mainly due to changes in viscosity, density and flow ratio. In this chapter, a method is presented to track mixing profiles of rapid exothermic reaction directly by quantitative infrared thermal mapping. The data collected along the axial coordinate contains integral information of the whole cross section, preventing misinterpretation such as in other chemical systems with one single reaction. Experiments are carried out in a micro-cross mixer which has three inlets and one outlet each at an angle of 90° one from another. Two model reactions are carried out: the dilution of sulfuric acid (70 % w/w) with water and the organic cyclization of pseudoionone in the presence of acid [240, 241]. Whereas the first reaction is quasi-instantaneous and controlled by mixing, the second reaction is carried out in a regime strongly influenced by mixing. The effective reaction times obtained under homogeneous and under micro-batch flow were compared. Thereby, micro-batch flow is defined as a slug flow pattern induced by the addition of a carrier fluid through the third inlet. Both reactants mix in droplets of typically 1-2 mm length which behave as internally mixed micro-batch reactor [240, 242].

5.2 Experimental Part

The main components of the setup are listed and briefly described before presenting the two model reactions, i.e. the dilution of sulfuric acid in water and the cyclization of pseudoionone in presence of

sulfuric acid. In the present series of experiments biphasic systems are used, which lead to a non-negligible change of the inner heat transfer resistance. The consequences of this effect for the experiments are analyzed in the final part of this section.

5.2.1 Experimental Setup

The core of the experimental setup is the continuous flow micro-cross mixer, where the reactants are contacted and the temperature profile is measured. Before presenting it, an overview of the complete setup is shown.

5.2.1.1 Overview of the Setup

In Figure 5.2 the solutions containing the reactants are pumped via two syringe pumps to the micro-cross mixer. An additional syringe pump provides the reactor with inert liquid (in this case toluene/perfluorohexane) for the creation of a micro-batch type flow pattern (slug flow).

The reactor is placed in a vacuum box under a pressure of 10^{-2} mbar, where convection can be almost completely suppressed. Nevertheless, the losses by radiation cannot be avoided, and need to be considered due to the high outer surface to channel volume ratio (see section 5.2.1). The visible access to the vacuum box (Figure 5.3) is given by two ZnSe windows ($50 \text{ mm} \times 20 \text{ mm} \times 1.8 \text{ mm}$) allowing temperature to be measured in the reactor itself or in the subsequent capillary.

To carry out the calibrations at different reactor temperatures, one of the inlets is equipped with a controllable heater (0-100 W). The temperature at the reactor inlet and outlet is measured by two K-type thermocouples with an outer diameter of 0.5 mm.

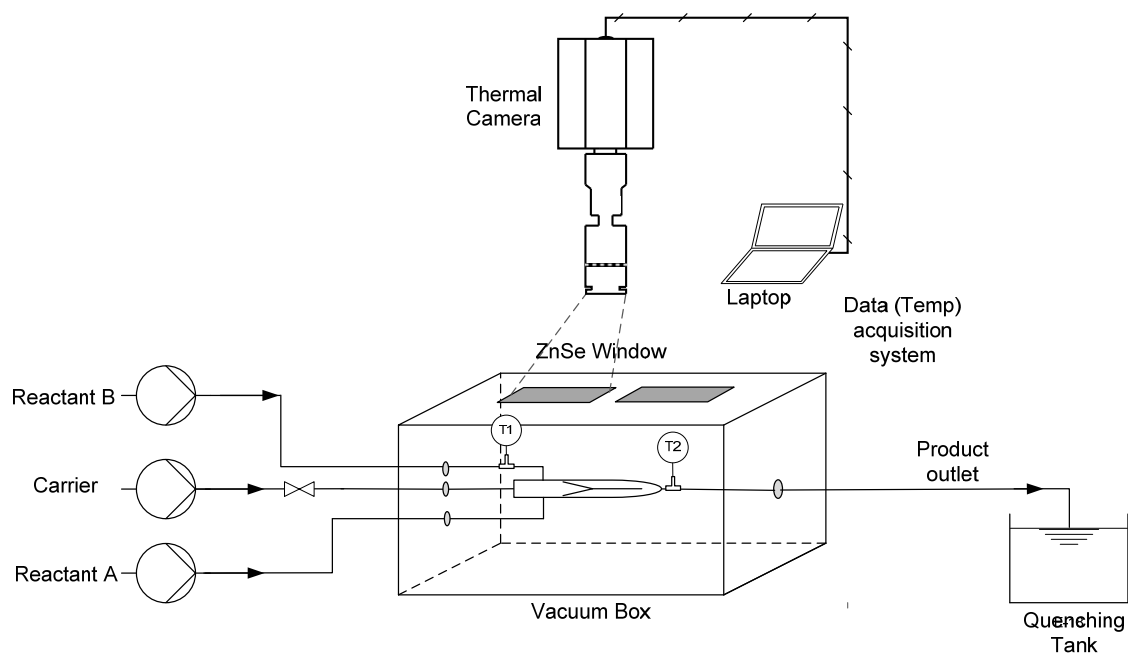


Figure 5.2: Schematic overview of the experimental setup.

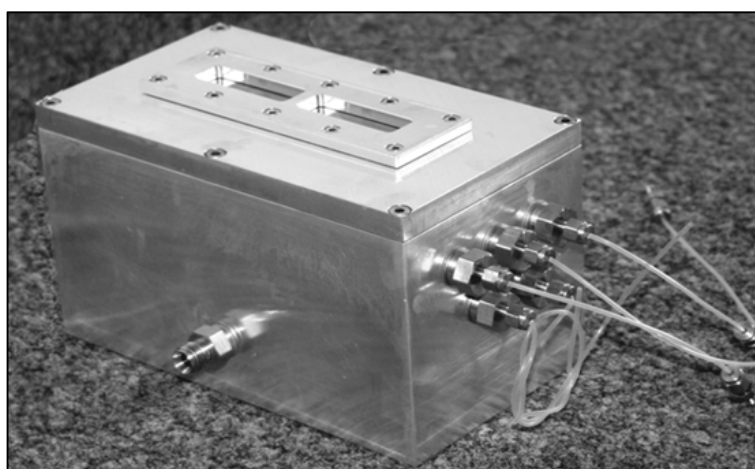


Figure 5.3: In-house constructed vacuum box with two IR-transmissive ZnSe windows.

5.2.1.2 The Micro-cross Mixer

The micro-cross mixer made of polytetrafluoroethylene (PTFE) is placed inside the vacuum box directly under one of the two ZnSe windows. The physical dimensions of the device are given in Figure 5.4.

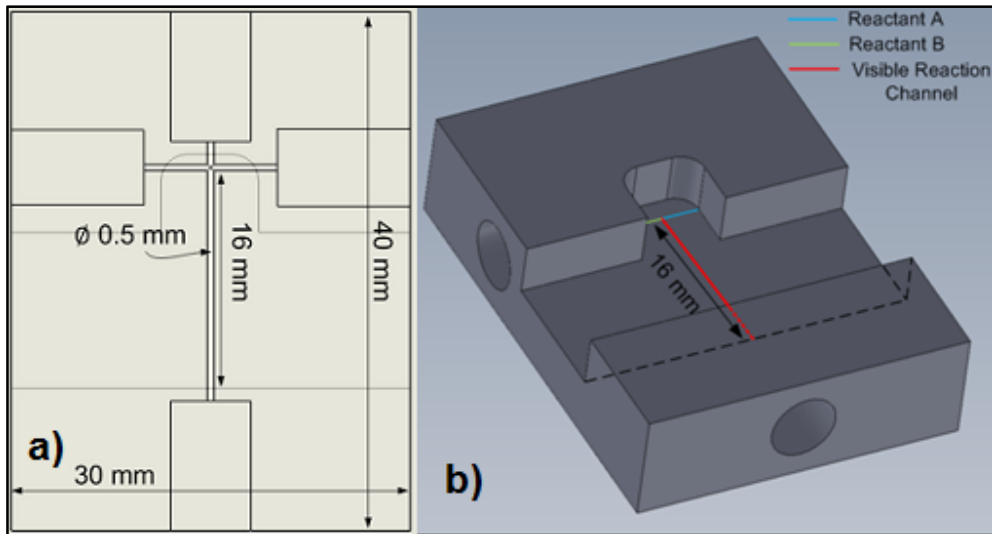


Figure 5.4: Micro-cross mixer with up to three inlets and one outlet: a) Two dimensional schematic containing the dimensions in millimeter and b) three dimensional representation of the reactor highlighting the mixing channel.

As opposed to the setup used for reactive mixing in Chapter 4, where mixing was carried out in a “black box” (the caterpillar mixer), the goal of this device is to observe the temperature profile immediately from the point of contact of the reactive solutions. To minimize diffusion in the plane and have an optimal temperature signal on the reactor surface, the wall thickness on the top part of the reactor was kept at $100\ \mu\text{m}$. This also explains the specific shape of the reactor: whereas initially the piece was box-shaped ($10\ \text{mm} \times 40\ \text{mm} \times 30\ \text{mm}$) allowing the four connections for capillaries of $6\ \mu\text{m}$ to be drilled, material was removed in the center of the part to reduce the surface thickness above the channel to $100\ \mu\text{m}$. This thin upper wall is maintained at a length of $16\ \text{mm}$, representing the reactor part apt for quantitative measurements with the infrared camera. Furthermore, it has to be pointed out that the long reaction channel ($40\ \text{mm}$) was drilled from two sides: from the top and the bottom in Figure 5.4a). As a consequence, at the contact point of the two drilled channels, they are shifted by $300\ \mu\text{m}$ due to the limited precision of the drills. This point is located about $7\ \text{mm}$ from the cross junction and plays an essential role for mixing as shown in section 5.3, and is referred to as “mixing element” in the following.

The micro-cross mixer consists of three inlets and one outlet with circular cross section. In the case of a homogeneous reaction with two reactants, only two of the inlets are used, the third one being blocked. When shifting to a micro-batch flow system, the third inlet is fed with an inert liquid. Thereby, the contact angle between liquid and reactor plays an essential role. The wetting phase (toluene/perfluorohexane) needs to have a smaller contact angle than the non-wetting phase containing the reactants and forming the micro-batches. As a consequence, the reactor needs to be fabricated of a hydrophobic material, i.e. Teflon (PTFE).

5.2.2 The Model Reaction Systems

Two chemically distinct transformations were carried out each under homogeneous conditions and under micro-batch flow. In the following, the specificities of each transformation including concentrations and adiabatic temperature rise are detailed. Subsequently, the flow patterns obtained with these reactions are discussed.

5.2.2.1 Model Reactions

The two transformations carried out in this study are the dilution of sulfuric acid in water and the cyclization of pseudoionone to the protonated form of α -ionone/ β -ionone in the presence of sulfuric acid.

Dilution of sulfuric acid:

The dilution of sulfuric acid is considered as having a characteristic reaction time much smaller than the range of mixing times achieved during this study. Hence, the formation of heat is directly linked to the mixing of the two solutions. The dilution of sulfuric acid comprises many reactions such as dissociations and formation of hydrates. The equilibrium of the different species depends on the concentration of the sulfuric acid solution. As a result, the enthalpy of dilution of acid in water depends on the initial and final concentration of the solutions and can be determined using the data given by Müller *et al.* [243] which is plotted in Figure 5.5.

In the present case, a solution of $\sim 70\%$ w/w sulfuric acid in water is diluted with a stream of pure water (volumetric ratio 1:1) yielding $\sim 41\%$ w/w sulfuric acid in water. Under adiabatic conditions, the observed temperature rise equals $28\text{ }^\circ\text{C}$. The physical properties obtained for the different mixtures of water and sulfuric acid are summarized in Table 5.1.

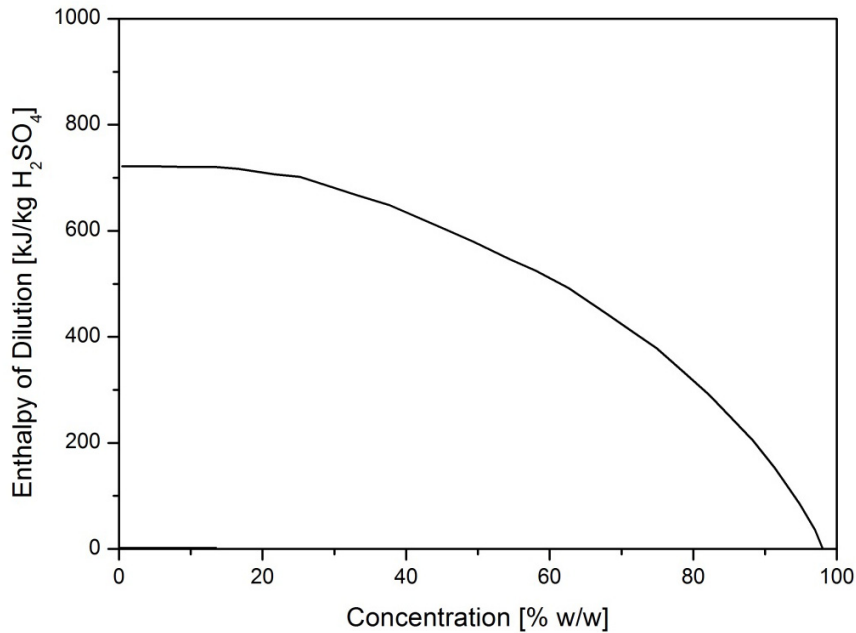


Figure 5.5: Enthalpy of dilution of sulfuric acid in water as function of the concentration of sulfuric acid in the aqueous solution. Data adapted from [243].

Table 5.1: Physical properties of the compounds used for the dilution of sulfuric acid taken from graphs in Müller *et al.* [243].

	Density [kg/m^3]	Heat capacity [$\text{J}/(\text{kg K})$]	Viscosity [m^2/s]
Sulfuric acid	1840	1340	$1.34 \cdot 10^{-5}$
70 % w/w	1615	1890	$5.63 \cdot 10^{-6}$
41 % w/w	1310	2670	$2.23 \cdot 10^{-6}$
Water	997	4187	10^{-6}

Cyclization of Pseudoionone:

The cyclization of pseudoionone is a complex reaction [240, 241] whose simplified reaction scheme is shown in Figure 5.6. Even though the interpretation of the results is challenging, this reaction was chosen as it represents an industrially relevant reaction used in the synthesis of vitamin A and in perfumery [241]. Sulfuric acid and pseudoionone would form a biphasic system; however, the presence of the solvent, 1-nitropropane, added to both solutions enables the formation of one single phase. With a ratio of sulfuric acid to pseudoionone of 5:1, this reaction consists in a quasi-instantaneous protonation followed by the very fast (but not instantaneous!) cyclization. With decreasing concentration of acid, the kinetics of the reaction is slowed down. As opposed to the dilution of sulfuric acid, this reaction is operated in a regime strongly influenced but not strictly controlled by mixing, as the second reaction step is very fast, but, not quasi-instantaneous.

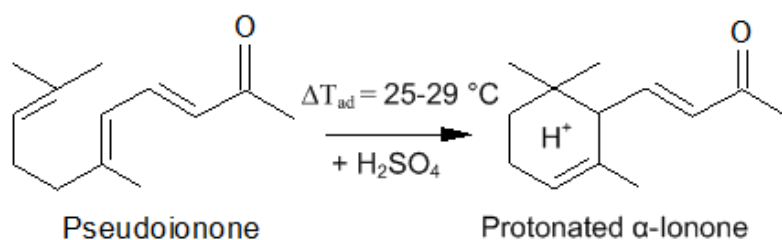


Figure 5.6: Simplified scheme of the quasi-instantaneous protonation of pseudoionone.

In the present study, the reaction was carried out with concentrations of pseudoionone ranging from 1 M to 1.5 M and of sulfuric acid from 6 M to 8 M. The physical properties of the different compounds of the reaction and of the respective solutions obtained by dilution with 1-nitropropane are summarized in Table 5.2.

Table 5.2: Physical properties of the compounds used for the homogeneous cyclization of pseudoionone.

	Density [kg/m ³]	Heat capacity [J/(kg K)]	Viscosity [m ² /s]
1-Nitropropane	998	1972	$7.90 \cdot 10^{-7}$
Pseudoionone	895.1	1930	$6.38 \cdot 10^{-6}$
β-ionone	940	-	$1.15 \cdot 10^{-5}$
Sulfuric acid	1840	1340	$1.34 \cdot 10^{-5}$
Solution A*	970	1962	$2.17 \cdot 10^{-6}$
Solution B*	1372	1596	$8.28 \cdot 10^{-6}$
Product mixture*	1169	1757	$5.60 \cdot 10^{-6}$

*Calculated properties assuming initial solution of 1.25 M of pseudoionone (A) and 7.5 M of sulfuric acid (B). Due to the lack of data regarding α -ionone, physical properties of the very similar β -ionone are used.

5.2.2.2 Flow Pattern

The main objective of the present study was the comparison of overall transformation rate during classic homogeneous mixing with mixing under micro-batch flow conditions, where enhanced mixing performance was expected. Therefore, both flow patterns had to be created for the two model reactions.

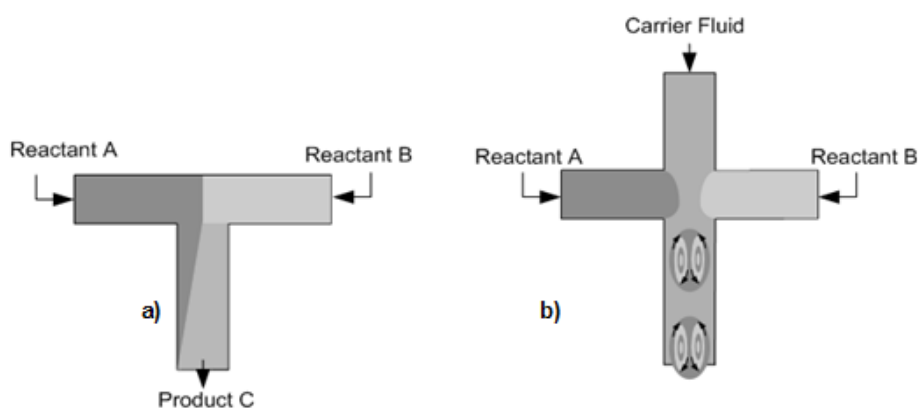


Figure 5.7: Two types of flow regimes analyzed in the present work: a) Homogeneous mixing and b) mixing in micro-batches (slugs)

To work under homogeneous conditions, the third inlet of the micro-cross mixer was blocked. The two reacting solutions were fed at an angle of 90° to the reaction channel (T-type configuration). Within the tested operation conditions ($Re \approx 1-50$) the channel geometry and the flow velocity lead to two

distinguishable parallel streams interlacing due to a tangential velocity compound, which is referred to as “swirling” flow in the following. Thereby, diffusion of the molecules is the ultimate step of mixing, leading to homogenization on the molecular level. If mixing in a channel with a diameter of 500 μm occurs solely by diffusion, this rather slow process takes at least several seconds to be completed. In parallel to the direct diffusion of the streams, shearing leads to the reduction of the characteristic size of a structure in orthogonal direction to its elongation, accelerating the overall mixing process [160].

The inlet concentrations for both reactions can be found in Table 5.3.

Two phase flow patterns were created by supplemental addition of a carrier fluid. For the first reaction system toluene was chosen, and for the cyclization of pseudoionone perfluorohexane [240] was used. The flow pattern was altered by modifying the flow velocity. At low flow velocity micro-batch flow (slug flow) is favored due to the predominance of surface forces [40, 240]. Thereby, both reactants are mixed in droplets with a size between 1-2.5 mm. By increasing the flow rate, the relative importance of the surface forces diminishes leading to a similar flow pattern as observed in the homogeneous case (swirling flow). The inlet concentrations and resulting adiabatic temperature rises obtained under heterogeneous conditions are listed in Table 5.3, and the physical properties of the carrier phase in Table 5.4.

Table 5.3: Inlet concentrations and adiabatic temperature rises for the different experiments.

	Reaction	Inlet 1	Inlet 2	Inlet 3	ΔT_{ad}
Homogeneous	Dilution	Water	H ₂ SO ₄ : 70 % w/w	-	28 °C
	Cyclization	PI: 0.8 M	H ₂ SO ₄ : 6 M	-	25 °C
Micro-batch flow	Dilution	Water	H ₂ SO ₄ : 75 % w/w	Toluene	30 °C
	Cyclization	PI: 1.2 M	H ₂ SO ₄ : 7.5 M	Perfluorohexane	29 °C

Table 5.4: Physical properties of the carrier phase used during micro-batch flow regime.

	Density [kg/m ³]	Heat capacity [J/(kg K)]	Viscosity [m ² /s]
Toluene	867	1720	$6.80 \cdot 10^{-7}$
Perfluorohexane	1669	722	$4.01 \cdot 10^{-7}$

5.2.3 Quantitative Thermal Imaging of Multi-phase Flows

The “pixel-by-pixel” thermal imaging method presented in Chapter 4 allows temperature to be determined inside a reaction channel by measuring the infrared signal emitted by the surface of the microchannel. In principle, such a method of calibration and measurement can only work if the heat transfer resistances between reactor surface and reaction channel remain unchanged. To illustrate the problematic, one can imagine the heat transfer between the reaction channel and the ambient air as limited by three distinct resistances as shown in Figure 5.8: the resistance between liquid and wall R_{L-W} , the wall itself R_W and the transfer from the wall to the surrounding R_{W-Amb} . After calibration, the reactor temperature can be deduced from the wall temperature only if the three resistances remain unchanged. If, for example, the outer surface is exposed to strong convection diminishing R_{W-Amb} to almost zero, the surface temperature becomes close to ambient temperature, independently of the temperature in the reaction channel. Thus, a variation of the resistance induces error.

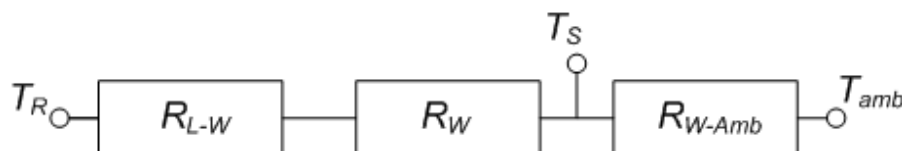


Figure 5.8: Scheme of the heat transfer resistances between reaction channel and ambient temperature. T_R : Reaction channel temperature; T_S : Reactor surface temperature; T_{amb} : Ambient temperature; R_{L-W} : Convective resistance between liquid and wall; R_W : Conductive resistance in the wall; R_{W-Amb} : resistance between wall and ambient.

By placing the microreactor under vacuum, the outer resistance (mainly radiative) can be kept constant with respect to the flow rate. The second resistance, i.e. the wall can be assumed not to vary as well. The only critical point of the system is the convective heat transfer inside the reaction channel, which changes depending on the flow pattern inside the channel [37, 125, 244]. The highest local resistance is observed in developed laminar flow, where the local heat transfer in a circular channel can be described by $Nu_\infty = 3.66$ [245]. The local Nusselt number is improved if the laminar flow and temperature profile is developing or with the appearance of radial exchange of heat by convection. Such a radial exchange

occurs for example in mixers or when working under slug type flow regimes in 2-phase systems [246, 247], as carried out in this study.

To counter the sensibility of the system to a variation of the inner heat transfer resistance, a specific reactor design strategy has to be applied. By increasing the value of the outer resistance to an extent that $R_{W-Amb} \gg R_{L-W} + R_W$, the influence of the inner resistance is diminished, and the surface temperature is close to the temperature inside the reactor. In practice, this is achieved by putting the reactor under vacuum, and by keeping the wall between reaction channel and measurement surface thin. Nevertheless, to estimate the error induced by a change of inner resistance, a thermal Finite Elements Analysis was carried out using the commercially available software Ansys Workbench 12.

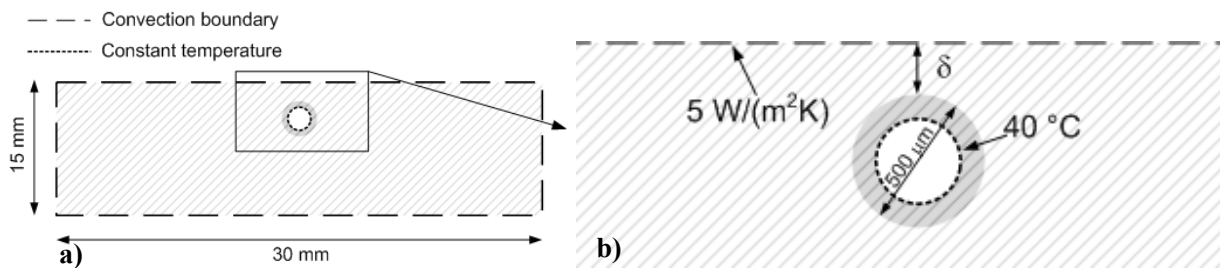


Figure 5.9: Geometry (a) and boundary conditions (b) solved with the commercial software Ansys Workbench 12.

The boundary layer of the fluid is modeled with a 100 μm-thick layer inside the fluid channel (gray).

Two boundary conditions were placed on the cross section of the micro-cross mixer geometry: a constant temperature of $T_R = 40 \text{ °C}$ inside the microchannel and a convective heat exchange of $5 \text{ W/m}^2\text{K}$ with the ambient temperature of 25 °C at the reactor surface. Thereby, the convective heat exchange is a lumped parameter comprising convection and radiation. To simulate the variation of the heat transfer coefficient h within the boundary layer of the reaction channel, inside the microchannel of 500 μm a layer of 100 μm of material (depicted in gray) with variable conductivity was placed. The conductivity of this material was varied between $h/10 = 0.15 \text{ W/(m}\cdot\text{K)}$ and $h = 1.5 \text{ W/(m}\cdot\text{K)}$ corresponding to a 10-fold increase of the inner convective heat transfer. In addition, this experiment was carried out for a wall thickness of $\delta = 100$

μm and $5 \times \delta = 500 \mu\text{m}$ to highlight the effect of the thin wall. The temperature profiles obtained in the four cases are depicted in Figure 5.10.

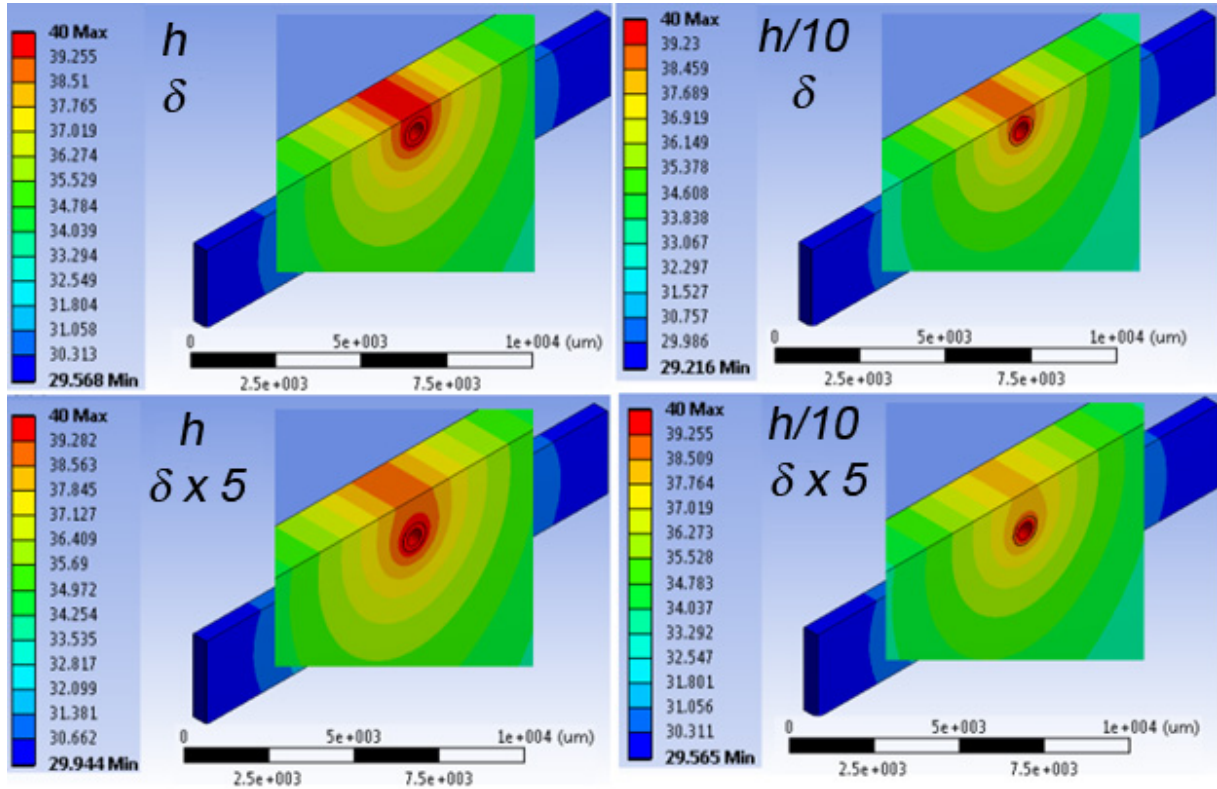


Figure 5.10: Demonstration of the effect of inner heat transfer resistance and wall thickness on the surface temperature of the micro-cross mixer. Boundaries: $T = 40 \text{ }^\circ\text{C}$ inside the microchannel; Heat losses at the surface: $5 \text{ W/m}^2\text{K}$. Mesh: 117 000 elements

In the case of thin walls of $100 \mu\text{m}$, the difference in surface temperature for a 10-fold increase of the inner resistance ($0.8 \text{ }^\circ\text{C}$) lies below the precision of the method ($\pm 1 \text{ }^\circ\text{C}$). For the same experiment with thicker walls, the temperature on the reactor surface is slightly lower; however, the influence of the inner heat transfer resistance remains negligible due to the much higher outer heat transfer resistance. Hence, this method can be readily applied to slug type flow pattern as long as wall thicknesses below $500 \mu\text{m}$ and low heat losses are assured at the reactor surface.

5.3 Results

At first, the heat losses of the system under non-reacting conditions were determined. Subsequently, reproducibility of the curves under reactive conditions is discussed before presenting the results obtained with the first and second model reaction i.e. water and sulfuric acid (dilution) on the one hand, and pseudoionone and sulfuric acid on the other hand (cyclization). In both cases, a regime where effective kinetics are controlled by homogenization of the liquids is assumed. Thus, the obtained temperature profiles can be used to extract information about mixing rate.

5.3.1 Heat losses

When working under an ambient pressure of 10^{-2} mbar, the convection heat losses per unit area can be efficiently reduced to almost zero. Nevertheless, radiative heat losses cannot be suppressed (see Chapter 4). As a result, a low surface specific heat loss coefficient is obtained (by lumping radiation and convection into one coefficient). However, as the ratio between channel volume and heat exchange area with the surrounding is considerable (in the order of $350\,000\text{ m}^2/\text{m}^3$), the volumetric heat loss coefficient cannot be neglected [248]. To estimate the amount of these losses, inert liquid was pumped through the micro-cross mixer. Three different systems with different inner heat transfer resistances were tested: pure butanol, pure water and a biphasic system consisting of slugs of water in pseudoionone as continuous phase. Thereby, the inlet temperature was varied in the range between 45-60 °C and the flow velocity u between 3.4 cm/s and 6.8 cm/s leading to gradients between 0.5 °C/cm and 3 °C/cm. To simplify the modeling of the losses, plug flow behavior was assumed, and the volumetric heat loss coefficient Ua_{loss} was obtained by fitting:

$$\frac{dT}{dz} = Ua_{\text{loss}} / (u \cdot \rho \cdot c_p) \cdot (T_{\text{amb}} - T) \quad (5.2)$$

Where the mean density ρ and the mean heat capacity c_p are estimated using the according values of the pure compounds at 25 °C. The resulting heat loss coefficient is depicted in Figure 5.11.

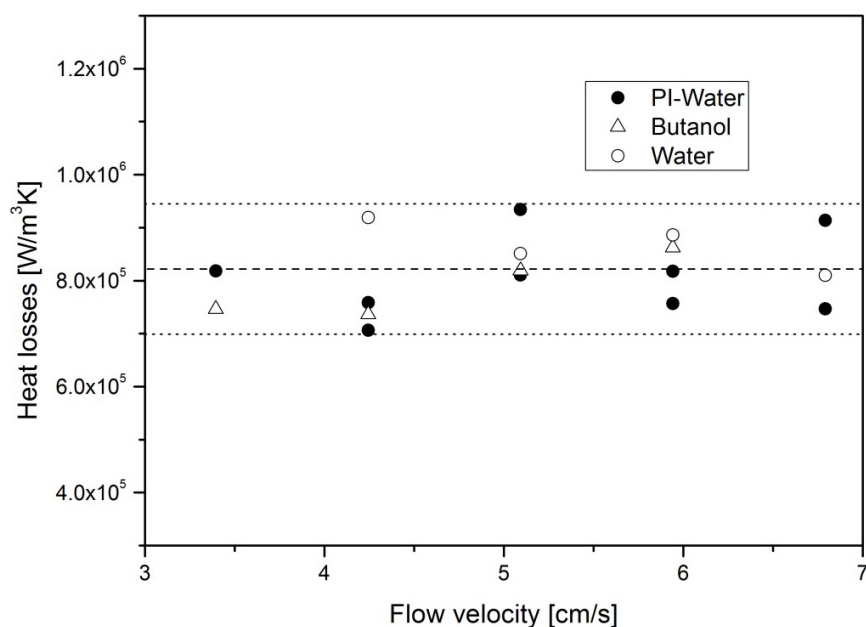


Figure 5.11: Volumetric heat loss coefficient determined in the micro-cross for different liquid systems. Dashed line: Average value of $8.22 \cdot 10^5$ W/m^3K . Dotted Lines: Deviation of $\pm 15\%$ from average value.

As expected, even though the inner heat transfer resistances in the three systems differ by at least a factor 4 [244], no impact on the overall heat losses was noticeable. The bulk amount of heat loss is limited by the heat transfer inside the PTFE material and by convection on the reactor surface. An average value of $8.22 \cdot 10^5$ W/m^3K was obtained with all the values being contained within an interval of $\pm 15\%$. The relatively high deviation is due to the fact that this method is operated at its limits of precision.

To conclude correctly in the upcoming section, the heat losses need to be considered especially at low flow velocity. The temperature losses at different flow rates are summarized in Table 5.5 for the 2-phase system consisting of micro-batch flow of pseudoionone and H_2SO_4 in nitropropane, with perfluorohexane as continuous phase (33 % v/v) to show the impact of heat losses.

Table 5.5: Heat losses at a mean temperature of 40 °C for the micro-batch flow system with pseudoionone and H₂SO₄ in nitropropane, and perfluorohexane as continuous phase (33 % v/v).

Flow velocity [cm/s]	ΔT_{loss} [°C]
0.85	11.5
2.12	4.6
8.15	1.2

5.3.2 Reproducibility of the Temperature Profiles

When measuring temperature curves formed during mixing phenomenon, reproducibility is a crucial issue. During mixing of two or more fluids a complex stationary regime forms, involving inertia, pressure-gradient and surface forces. Especially in the transition phase from slug flow regime to swirling flow, this stationarity is easily disturbed leading to a change of flow pattern. In Figure 5.12 a first example of reproducibility of mixing of sulfuric acid and water in micro-batch flow is given. For this system, at a flow velocity as low as 0.85 cm/s, the flow can be considered as stable resulting in good repeatability of the temperature curves.

As a second representation of reproducibility, the curves shown in Figure 5.13 were chosen. These profiles were recorded during homogeneous mixing of pseudoionone and sulfuric acid at a flow velocity of 13.6 cm/s. Whereas run 1 and run 3 overlap well, run 2 demonstrates the sensitivity of such measurements. Even though the trend is similar, the latter curve shows a steeper rise in temperature indicating faster mixing of the reactants at the mixing element (see section 5.2.1.2). This type of phenomenon can be explained by the sensitivity of the system, which reacts to the slightest perturbances such as induced by discontinuous pumping or external vibrations.

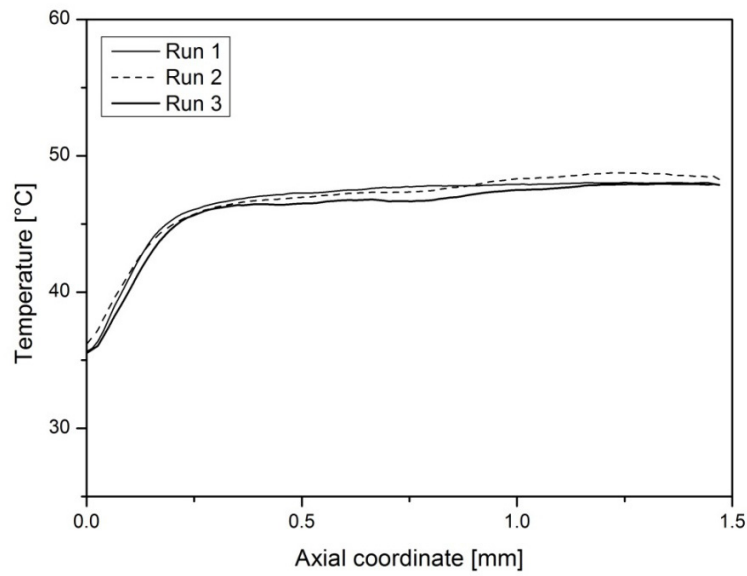


Figure 5.12: Reproducibility of temperature curve compared in three runs of sulfuric acid and water in micro-batch flow at a velocity of 0.85 cm/s.

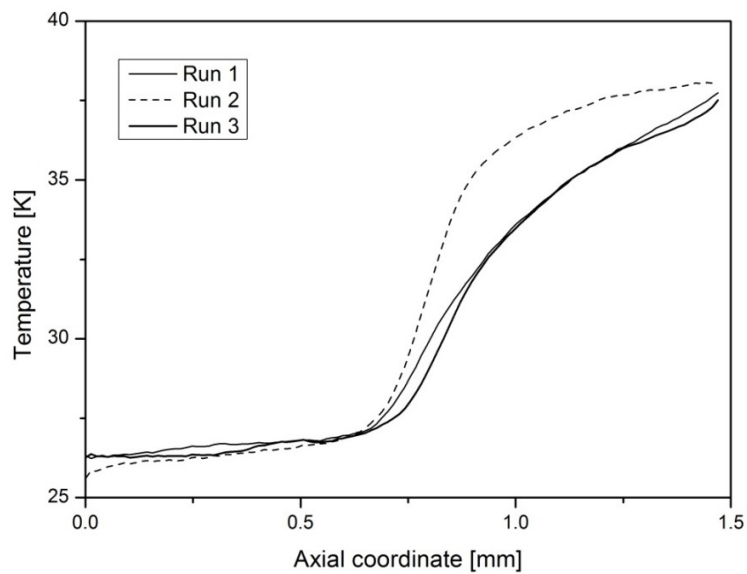


Figure 5.13: Reproducibility of temperature curve compared in three runs of homogeneous mixing of pseudoionone and sulfuric acid at a flow velocity of 13.6 cm/s.

In the case of appearance of fluctuations, only the reproducible curves, i.e. run 1 or run 2 in the present case, was used for further processing.

5.3.3 Mixing in homogeneous systems

Homogeneous mixing of sulfuric acid and water, and subsequently, of sulfuric acid with pseudoionone (cyclization) was carried out without the third inlet of the micro-cross mixer resulting in a contact angle of both mixing streams of 180° .

5.3.3.1 Dilution of Sulfuric Acid

The axial temperature profiles obtained for the homogeneous mixing of sulfuric acid and water are depicted in Figure 5.14.

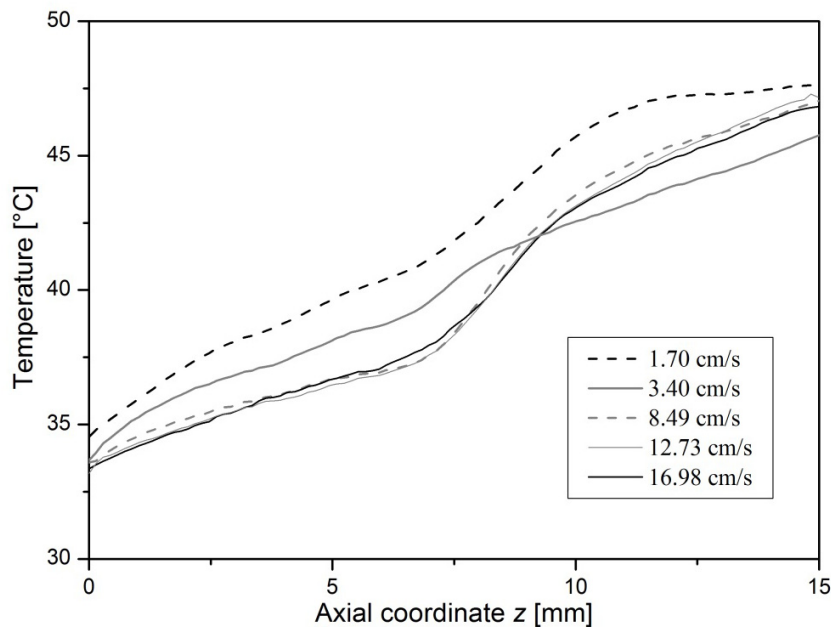


Figure 5.14: Comparison of axial temperature profiles obtained during homogeneous mixing of sulfuric acid and water.

The initial temperature monitored at the coordinate $z = 0$ differs from the inlet temperature of 25°C . In fact, a considerable temperature rise between 7°C and 10°C occurs immediately at the beginning of the mixing process. This increase represents the heat release during the first contact of the reactants and its magnitude depends on the interfacial area between the two inlet streams and on the diffusion coefficient (depth of penetration). It can be seen that with decreasing flow rate, the initial temperature increases

which can be explained by residence time: the more time a molecules spends in the intersection (at $z \rightarrow 0$), the more diffusion occurs at this precise position, which, in turn, leads to a higher initial temperature. Temperature rises almost linearly along the length due to shearing and diffusion. At the axial position $z = 7$ mm, a slight effect of the mixing element (see section 5.2.1.2) is observed which gets more pronounced at higher flow rate. Thereby, the formation of secondary flows enhances mixing rate shortly after the element.

To simplify the description of the above system, for further calculation only the first 6 mm of the reactor without the mixing element are considered. In this part, the heat production is controlled by shearing and diffusion, and the flow can be readily described with the Hagen-Poiseuille equation.

As already mentioned, the temperature is the result of interaction between heat produced by the reaction and heat loss to the surrounding. To estimate the conversion along the length, the heat losses need to be considered by integration:

$$u \cdot \rho \cdot c_p \cdot \frac{dT'}{dz'} = Ua_{loss} \cdot (T_{amb} - T') + u \cdot \frac{dc'}{dz'} \cdot (-\Delta H_r) \quad (5.3)$$

$$\Rightarrow dX' = \frac{\rho \cdot c_p}{c_0 \cdot (-\Delta H_r)} \cdot dT' + \frac{Ua_{loss}}{u \cdot c_0 \cdot (-\Delta H_r)} \cdot (T - T_{amb}) \cdot dz' \quad (5.4)$$

Assuming a constant reaction enthalpy, the following expression is obtained:

$$\Rightarrow X = \frac{T - T_0}{\Delta T_{ad}} + \int_{z'=0}^{z'=z} \frac{Ua_{loss}}{\rho \cdot c_p} \cdot \frac{(T - T_{amb})}{u \cdot \Delta T_{ad}} \cdot dz' \quad (5.5)$$

Using equation (5.5), the conversion can be expressed as function of the axial distance from the junction. The only additional data required to solve the equation is the adiabatic temperature rise ΔT_{ad} and the volumetric heat capacity of the mixture $\rho \cdot c_p$.

When diluting sulfuric acid with water, the heat release is not proportional to conversion. Hence, further corrections need to be made considering the reaction enthalpy at different dilution stages [243].

The resulting curves obtained by numerical integration are plotted in Figure 5.15.

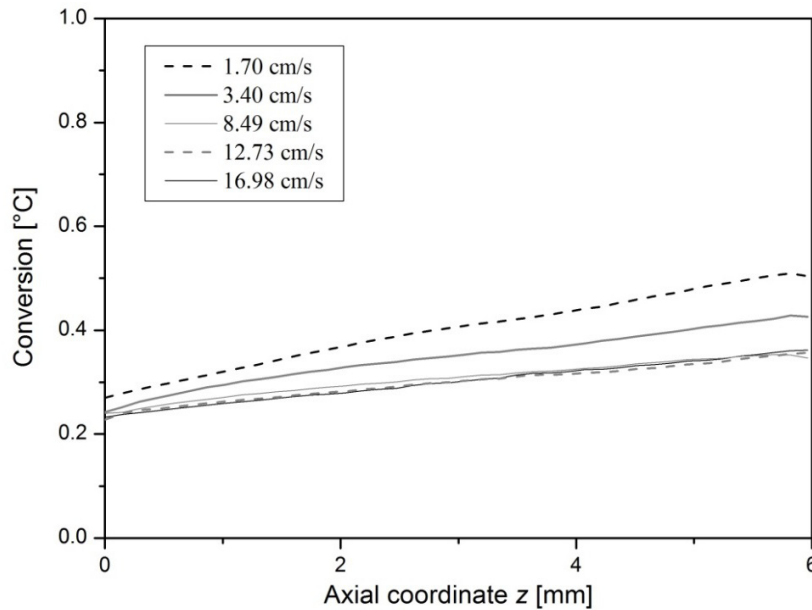


Figure 5.15: Axial conversion profile obtained for homogeneous mixing of sulfuric acid and water.

Even though the flow velocity undergoes a 10-fold increase, the axial temperature gradient remains almost constant for all the curves. Thereby, highest conversion is obtained at the lower flow rates, whereas no change in conversion is observed for flow velocities above 12 cm/s. The explanation to this behavior lies in the diffusion phenomenon. One has to consider the ratio of characteristic diffusion time to residence time of the molecules in the reactor, i.e. the Fourier number $Fo = t_{diff}/\tau$, where $t_d = d^2/(4 \cdot D_m)$ and $\tau = L/u$. The former is constant and in the order of 6 s (for the diffusion of protons in water $D_m = 10^{-8} \text{ m}^2/\text{s}$ [249]), and the latter parameter varies from 1 s down to 100 ms leading to $Fo \approx 6 \dots 60$. At $Fo < 10$ number, characteristic diffusion time is less than one order of magnitude greater than residence time. Therefore, the observed temperature profile is a superposition of both mixing processes: creation of interfacial area by

shearing and penetration by diffusion. At higher Fo , the diffusion becomes negligible, and heat release is mainly controlled by shearing.

While the 10-fold increase does not affect considerably the axial temperature gradient, the temporal gradient is strongly affected. When looking at the curves monitored at a flow velocity of 8.5 cm/s and at 17 cm/s, the fact that they are identical when plotted versus the z axes results in mixing that is twice as efficient on the temporal scale at the higher flow rate. To compare the mixing rates at the different flow velocities, the conversion rate was deduced according to the following calculations:

$$\left(\frac{\Delta X}{\Delta \tau}\right)_{z \rightarrow 0} = \left(\frac{\Delta X}{\Delta z}\right)_{z \rightarrow 0} \cdot u \quad (5.6)$$

The mixing rates obtained at different flow velocities are plotted in Figure 5.16.

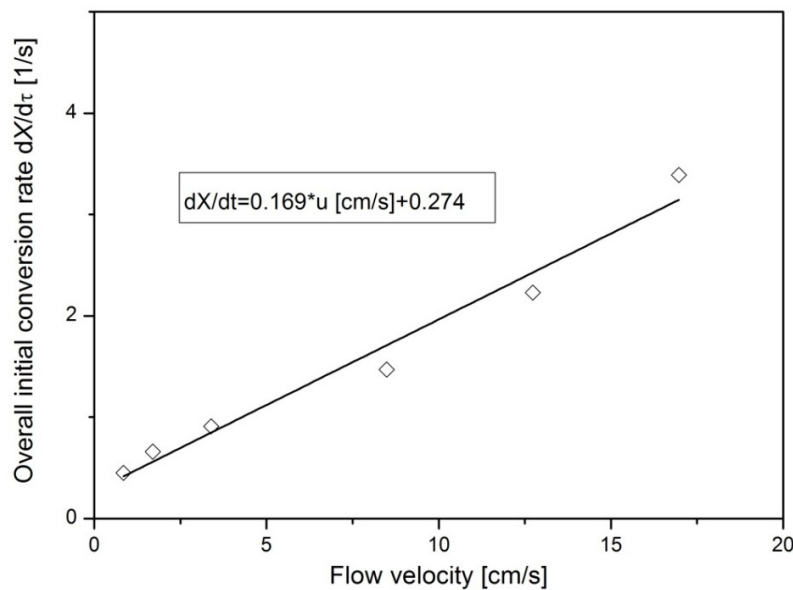


Figure 5.16: Linear trend of initial conversion rate plotted as function of flow velocity obtained for homogeneous mixing of sulfuric acid and water.

A linear behavior of conversion rate with flow velocity is observed. The first order polynomial is described by the equation:

$$(dX / d\tau)_{z \rightarrow 0} = a' \cdot u + b' \quad (5.7)$$

With the slope $a' = 16.9 \text{ m}^{-1}$ and the y-intercept $b' = 0.27 \text{ s}^{-1}$. Assuming a first order reaction for mixing, the characteristic reaction time defined as $t_r = t_{mix} = 1/k_{eff}$ is obtained by taking the invert of conversion rate:

$$(t_{mix})_{z \rightarrow 0} = [(dX / d\tau)_{z \rightarrow 0}]^{-1} = \frac{1}{a' \cdot u + b'} \quad (5.8)$$

Using equation (5.8), two extreme cases can be distinguished: 1) mixing strongly influenced by the diffusion between the two inlet streams ($Fo = t_{diff}/\tau \ll 1$), and 2) mixing where diffusion between the two ingoing streams plays a minor role as the process is too slow compared to the residence time in the reactor ($Fo \gg 1$). Whereas in the former case high conversion is attained in any configuration, in the latter case the conversion at the reactor outlet relies on the formation of secondary surface area due to shearing (see section 5.2.2.2). In the first case, the extreme is $Fo = 0$ where residence time is infinitely long for the given system. In this case, the flow velocity tends towards 0 leading to:

$$(t_{mix})_{z \rightarrow 0} = [(dX / d\tau)_{z \rightarrow 0}]^{-1} = \frac{1}{b'} = 3.6 \text{ s} \quad (5.9)$$

For the other extreme, $Fo \gg 1$, the mixing time can be expressed as following:

$$(t_{mix})_{z \rightarrow 0} = [(dX / d\tau)_{z \rightarrow 0}]^{-1} = \frac{1}{a' \cdot u} \propto u^{-1} \quad (5.10)$$

Such a behavior of mixing time with respect to flow velocity confirms the findings of Falk *et al.* [160], who obtained the same results with the Villermaux-Dushman reaction system.

To understand the effect of flow rate on the conversion at the outlet of a microreactor (the overall conversion at position L), the Damköhler number defined as $DaI_{mix} = \tau / t_{mix}$ is used for each of the two regimes described above:

- Mixing controlled by diffusion ($Fo \gg 1$)

$$DaI_{mix} = \frac{\tau}{t_{mix}} \approx \frac{\tau}{t_{diff}} \propto u^{-1} \quad (5.11)$$

The DaI_{mix} shows that in this regime, conversion at the outlet decreases with increasing flow rate. This is due to the fact that diffusion has less time to occur at higher flow rates which leads to less conversion.

- Mixing controlled by shearing ($Fo \ll 1$)

$$DaI_{mix} = \frac{\tau}{t_{mix}} = \frac{L \cdot a \cdot \cancel{u}}{\cancel{u}} = const. = 0.1 \quad (5.12)$$

Amazingly, for a given system (L and a fixed), the conversion at the reactor outlet is independent of the flow velocity inside the channel. As an increase of flow velocity reduces residence and mixing time to the same extent, the conversion at the reactor outlet is not affected when working at high Fo . This behavior is observed for the curves with flow velocities equal and higher than 8.49 cm/s.

It has to be pointed out, that this result is only valid in a regime where the flow profile is described by the Hagen-Poiseuille equation. With the appearance of secondary flows (eddies), the relationship between pressure drop and flow velocity is described with an exponent $q > 1$ ($\Delta p \propto u^q$). Thereby, an increased flow velocity results in supplemental power dissipation compared to the linear case, which, in turn leads to higher conversion at the reactor outlet.

5.3.3.2 Cyclization of Pseudoionone

The temperature profiles obtained from the cyclization of pseudoionone with sulfuric acid are given in Figure 5.17.

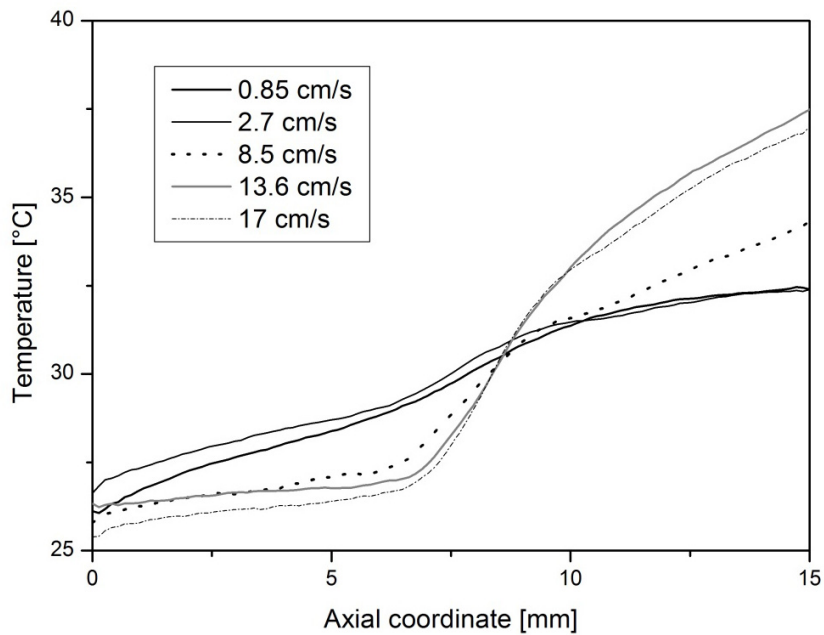


Figure 5.17: Comparison of axial temperature profiles obtained during homogeneous mixing of pseudoionone and sulfuric acid.

Compared to the results obtained with sulfuric acid, the initial temperature rise at the axial position $z = 0$ is much smaller. The equivalent conversion lies around 0.01-0.05 compared to a conversion of 0.22-0.25 in the intersection for the former system. This can be explained on the one hand, by the diffusion coefficient, which is one order of magnitude smaller than in the previous system. On the other hand, as this reaction can be considered as instantaneous only at ratios of sulfuric acid and pseudoionone close to 5, which is not fulfilled locally, the reaction is controlled by the slower kinetics in these areas.

The mixing element (see section 5.2.1.2) plays an essential role in mixing. As conversion due to creation of secondary surface area is the dominant phenomenon, a more pronounced effect of the mixing element is observed. Applying the same procedure as before, the conversion rate can be plotted as function of flow velocity.

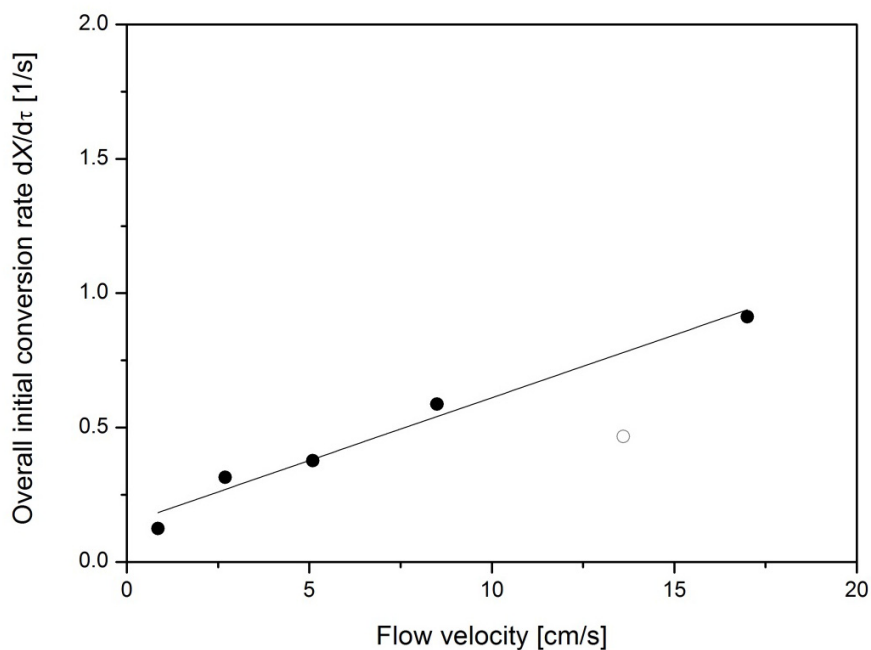


Figure 5.18: Linear trend of initial conversion rate plotted as function of flow velocity obtained for homogeneous mixing of a solution of pseudoionone and of sulfuric acid.

Due to the small conversion during the first 6 mm and the restricted ability to resolve small temperature gradients, it remains challenging to draw quantitative conclusions in this area. Nevertheless, a linear trend of conversion rate is observed.

5.3.4 Mixing in Micro-batch Flow System

The reactions previously presented in homogeneous mode, were carried out in micro-batch flow. An immiscible and inert liquid is fed through the third inlet resulting in the formation of slug flow pattern at lower flow rates and swirling parallel flow pattern at higher flow rates where the surface forces are dominated by inertia forces.

5.3.4.1 Dilution of Sulfuric Acid

The temperature profiles obtained in the system sulfuric acid-water-toluene are depicted in Figure 5.19.

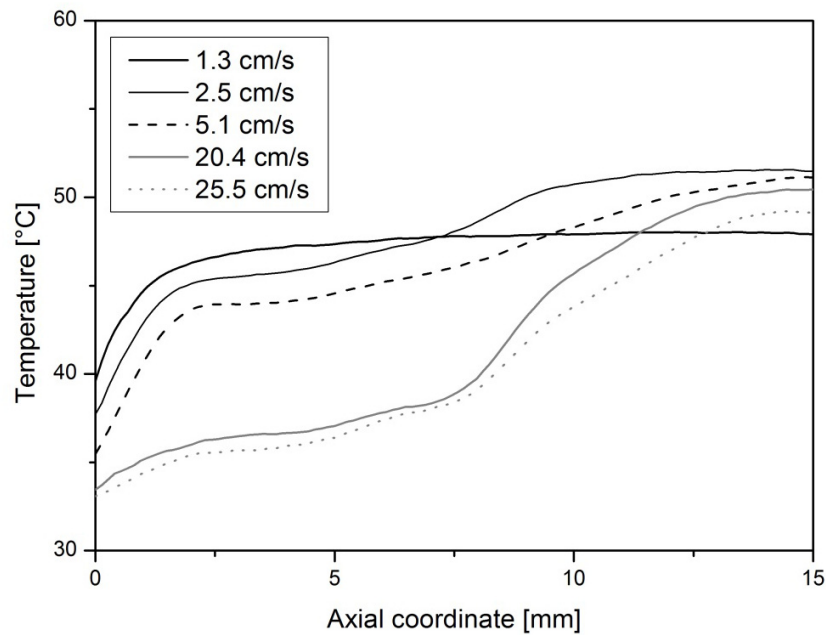


Figure 5.19: Comparison of axial temperature profiles obtained during mixing in micro-batch flow of sulfuric acid and water.

As seen in the homogeneous case, high temperatures form already in the intersection point itself. From the initial temperatures, one can deduce an initial conversion in the order of 0.2 which is comparable to the homogeneous case. After the intersection, a strong temperature gradient is observed for the three lower flow rates, whereas this behavior is not seen for the higher flow rates. The latter curves resemble the profiles observed in the homogeneous case. The difference between these two set of curves can be explained by a change of flow pattern: while at low flow rates the pattern is the desired micro-batch flow, the inertia forces become predominant for flow velocities above 20 cm/s. In fact, this change of flow pattern was observed in the PFA tube located at the outlet of the cross reactor: when shifting to higher flow velocities a swirling flow appeared, as described in section 5.2.2.2.

When comparing the initial conversion rates at different flow velocities, the difference between the two flow patterns is evident (Figure 5.20)

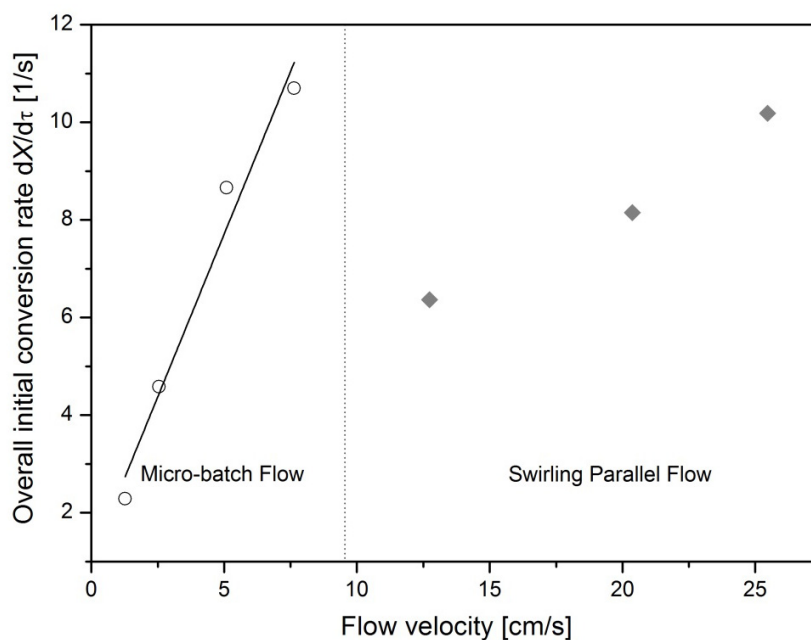


Figure 5.20: Comparison of conversion rates obtained during mixing in micro-batch flow of sulfuric acid and Water.

A linear increase of initial conversion rate is observed within the window of micro-batch flow achieving values between 2 s^{-1} and 10 s^{-1} which correspond to characteristic mixing times of a few hundred ms. When moving to higher flow rates, a drop of conversion rate is seen: about three times higher flow velocities are needed to obtain mixing rate similar to the ones observed with the micro-batch flow pattern.

5.3.4.2 Cyclization of Pseudoionone

When the heterogeneous system was operated at flow velocities lower than 0.85 cm/s , no stationary temperature profiles were formed on the reactor surface since the single slugs were seen travelling through the channel. For the system with lower diffusion coefficient, temperature curves obtained in the micro-batch flow clearly differ from temperature curves obtained at higher flow rates (Figure 5.21).

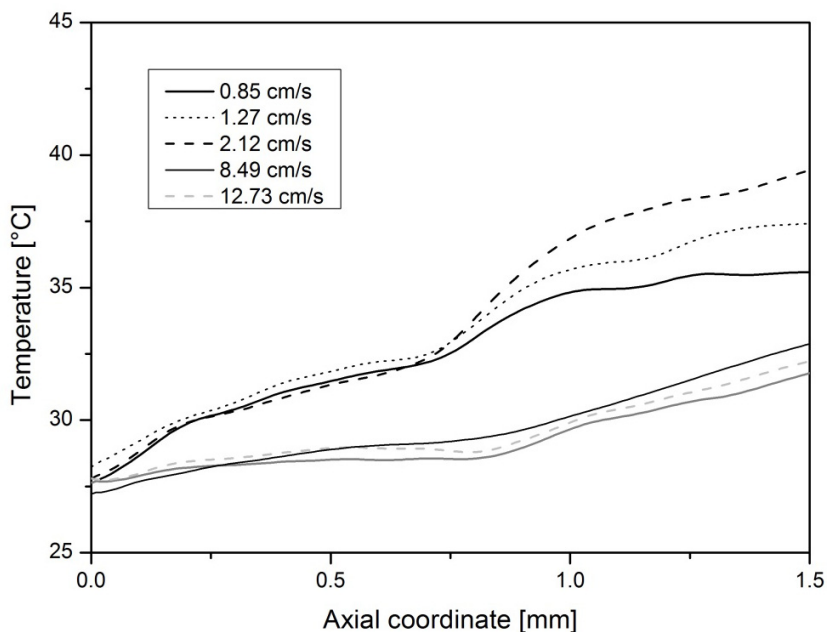


Figure 5.21: Comparison of axial temperature profiles obtained during mixing in micro-batch flow of pseudoionone and sulfuric acid.

As before, in the micro-batch regime much higher conversions are attained. However, due to the insufficient length of the reactor, the conversion at the outlet is only in the order of 0.5 (compared to 1 for the previous system). When looking at the capillary connected to the outlet of the reactor, temperature was found to be rising for several more centimeters. Interestingly, an influence of the mixing element is already seen at the lowest flow rates showing the enhanced recirculation inside the micro-batch due to a change of orientation of the slug. As expected, the conversion rates found in Figure 5.22 are relatively small resulting in mixing times in the order of a few seconds. The points monitored at flow rates higher than 8.49 cm/s don't follow the linear trend of the previous points, indication the change of flow regime.

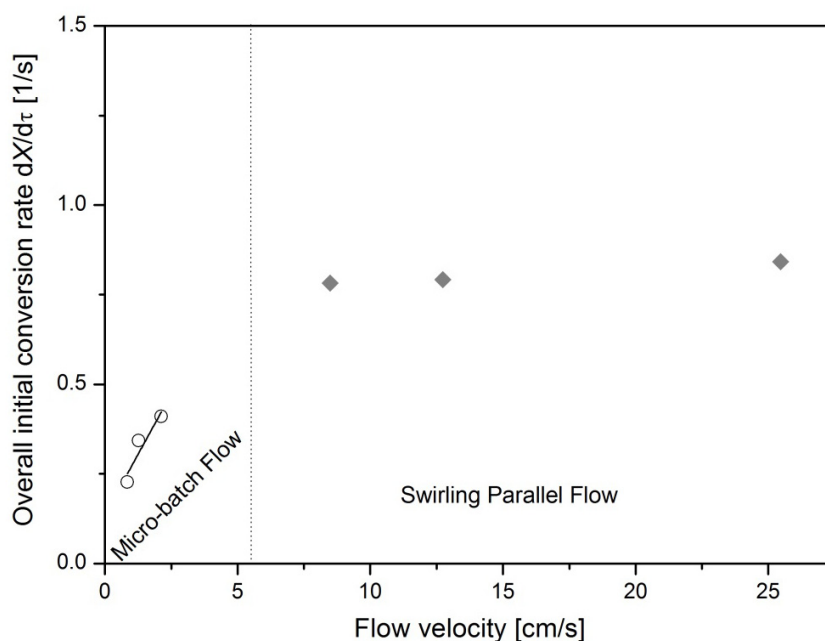


Figure 5.22: Comparison of conversion rates obtained during mixing in micro-batch flow of pseudoionone and sulfuric acid.

5.3.5 Comparison of the Systems

In Figure 5.23, all of the linearized mixing rates curves obtained in this work are plotted together.

When comparing effective conversion rates in the dilution of sulfuric acid system (denoted with squares) with the cyclization system (denoted with triangles), one clearly recognizes a faster overall transformation rate in the former. This can be mainly attributed to a fast homogenization of water and sulfuric acid, which can be explained by the fast diffusion coefficient of protons in water. The poor heat release in the cyclization system is a superposition of two effects: as mixing is incomplete, the required ratio for instantaneous reaction of acid/pseudoionone is only reached in a small volume of the reactor. Hence, in addition to the mixing limitation, kinetic limitation is observed.

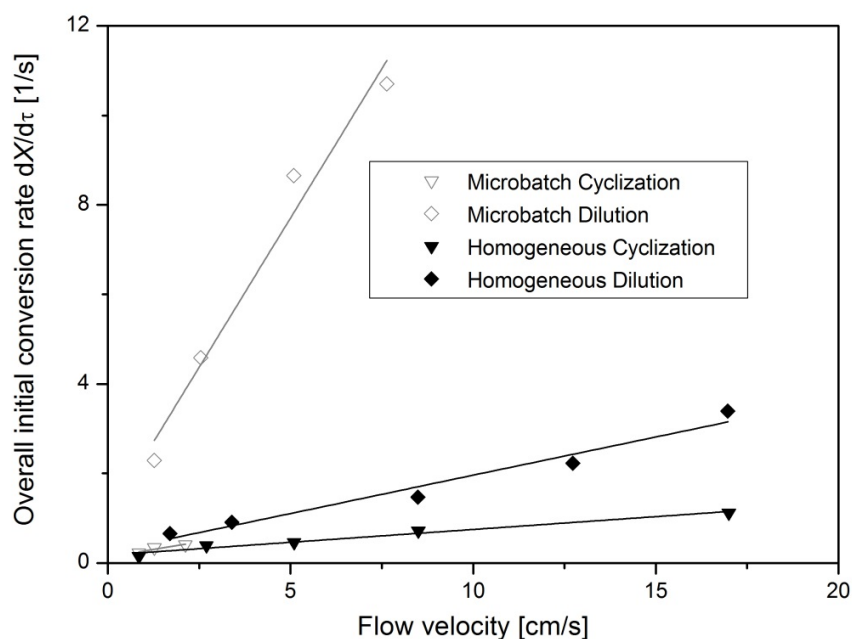


Figure 5.23: Comparison of mixing rates obtained in the four types of systems analyzed in this study.

Hence, mixing times measured with chemical systems based on protons in aqueous system, such as acid-base neutralizations or the Villermaux-Dushman [160] reaction system, always represent “best case” results. Thereby, one has to keep in mind that diffusion times for organic compounds are at least one order of magnitude higher.

On the other hand, for both reactions the comparison between homogeneous mixing and mixing in microbatch flow shows better mixing in the latter case. Whereas the difference is impressive for the dilution of H_2SO_4 (factor 3-4), the benefit for the cyclization reaction is limited to about a factor of 1.5. Hence, moving from a classical homogeneous mixing system to micro-batch flow pattern is beneficial if an increased mixing time is required. However, mixing time can only be reduced to a limited extent, as at some point an increase of flow velocity leads to a change of flow pattern leading to a drop of mixing rates.

5.4 Conclusion

A chemical method based on infrared thermal imaging to measure mixing time as a function of axial coordinate was successfully applied to highly exothermic single phase systems as well as to multi-phase systems. An integral value of mixing quality within the whole cross section (for high Sc/Pr i.e. ratio of diffusivity of mass and of heat) was obtained, preventing artifacts such as observed with many classical methods.

This novel method was applied to two different quasi-instantaneous reactions: the dilution of sulfuric acid in water and the cyclization of pseudoionone to the protonated form of α -ionone in the presence of sulfuric acid. It was demonstrated that mixing rates of the former system are up to one order of magnitude higher than for the latter system due to the fast diffusion of protons in water. In both cases, an increase of mixing rate was observed by switching from homogeneous conditions to micro-batch flow regime. This increase was much more pronounced for the fast diffusing system (3 to 4-fold). Moreover, it has to be pointed out that even though an improved mixing time can be achieved using micro-batch flow, this type of flow regime is very challenging to stabilize. Especially when numbering-up, high pressure drops and low manufacturing tolerances are required to achieve the needed precision [66].

Finally, the effect of flow velocity on conversion at the reactor outlet (equivalent to DaI_{mix}) was analyzed, and it was shown that at high Fourier numbers (mixing controlled by diffusion) the conversion at the outlet increases with decreasing flow velocity, whereas at low Fourier numbers (mixing controlled by shearing) the conversion at the outlet of the reactor is independent of flow velocity: on the one hand, higher flow velocity leads to faster mixing, on the other hand, the residence time is reduced.

5.5 Notations

a	Specific surface area, [1/m]
a'	Fit variable, [1/m]
b'	Fit variable, [1/m]
c_p	Mean heat capacity, [J/(kg K)]
c	Concentration, [mol/m ³]
c'	Concentration, [mol/m ³]
d	Channel diameter, [m]
D_m	Molecular diffusion coefficient, [m ² /s]
h	Heat transfer coefficient, [W/(m ² ·K)]
H_r	Reaction enthalpy, [J/mol]
k	Rate constant, [(m ³ /mol) ⁿ⁻¹ /s]
L	Length of the reactor, [m]
n	Reaction order
p	Pressure, [Pa]
R	Heat Transfer resistance, [K/W]
t_{diff}	Characteristic diffusion time, [s]
t_{mix}	Characteristic mixing time, [s]
t_r	Characteristic reaction time $1/(k \cdot c_0^{n-1})$, [s]
T	Temperature, [K]
T'	Temperature, [K]
u	Flow velocity, [m/s]
U	Global heat transfer coefficient, [W/(m ² K)]
X	Conversion, [-]
z	Axial coordinate, [-]

z' Axial coordinate, [-]

Greek

δ Wall thickness, [m]

Δ Symbol for difference

ε Specific power dissipation, [W/kg]

ρ Mean density, [kg/m³]

τ Residence time, [s]

Dimensionless numbers

Da_{mix} Damköhler number τ / t_{mix}

Fo Fourier number t_d / τ

Nu Nusselt number $h \cdot d_h / l_{fluid}$, [-]

Re Reynolds number $u \cdot d_h / \nu$, [-]

Subscript

0 Initial condition

∞ Infinity, after infinite length

ad Adiabatic

amb Ambient

eff Effective

loss Related to heat losses

L-W Liquid-Wall

R Reactor

S Surface

R-W Reactor-Wall

W Wall

W-Amb Wall-Ambient

Chapter 6

DEVELOPMENT AND EXPERIMENTAL INVESTIGATION OF A MULTI-INJECTION REACTOR

This chapter gathers the knowledge collected in the previous chapters (the theoretical behavior of multi-injection reactors, monitoring temperature in microchannels and efficient mixing of liquids) to develop an efficient multi-injection reactor. Using the technology of low temperature co-fired ceramics (LTCC), a multi-injection reactor embedding herringbone mixing structures is designed and manufactured. With the model reaction, i.e. cyclization of pseudoionone, it is demonstrated how process intensification can be achieved with this kind of devices while maintaining temperature control.

6.1 Introduction

In this introductory part, at first the multi-injection reactor concept is addressed. Herein, the experience gained from the numerical simulations (Chapter 3) is reviewed together with existing prototypes described in literature. Subsequently, the model reaction chosen for this study, i.e. the cyclization of pseudoionone, is discussed by addressing its thermodynamics, kinetics and processing modes. In the third part of the introduction, the motivation for carrying out the cyclization of pseudoionone in a multi-injection reactor is put forward.

6.1.1 Multi-Injection Reactor

The injection of one reagent at several points along the length of a tubular reactor to gain in selectivity was studied and optimized numerically in publications by Cougnon *et al.* and Lu *et al.* [250, 251]. Whereas in the present study the motivation to use multiple injection points lies in the thermal control of the reactor, in the cited publications the focus was put on the creation of an optimized concentration profile for the molecules travelling through the reactor. In the past, the injection of feed at several points in a fixed bed reactor has also been carried out to maintain thermal control over a reactor [252]. Such cold-shot injection reactors are especially used to create optimal temperature profiles for exothermic reactions with equilibrium issues: whereas high temperature is favorable for the kinetics, low temperature is needed for thermodynamics.

Only recently the multi-injection reactor concept has been applied to the small scale [170, 171]. As the reactor performance of these heat transfer limited processes is directly related to the characteristic cooling time of the reactor ($t_r = \rho \cdot c_p / (U \cdot a)$), high space-time yields can be achieved using multi-injection milli- or microreactors. Thereby, the hot spot temperature is mainly controlled by the amount of injection points, preventing the use of excessively small channel dimensions. As trade-off, one has to accept a broadened residence time distribution of the injected flow and a high pressure drop related to the flow distribution.

Barthe *et al.* [170] and Roberge *et al.* [171] described the development and characterization of a multi-injection reactor. Their main goal was to increase selectivity in a model reaction involving organo-metallic reagents, i.e. the reaction of phenylethyl magnesium bromide with 2-chloropropionylchloride, by controlling the axial temperature profile. Productivities up to 100 g/min were achieved in a 35 mm³ continuous multi-injection reactor. The exothermic and quasi-instantaneous reaction showed sensitivity to mixing quality and hot spot temperature. A glass reactor (Figure 6.1) was designed in a modular flexible manner for the use in multiple processes. For each specific function required for an optimal performance in a multi-injection reactor, a separate module was built:

- DT: pre-cooling of the feed
- MF: flow distribution, splitting one flow into four using channel length to create equal pressure drop. Equal flow distribution is attained by $\pm 8\%$ relative variation.
- MJ: multi-injection unit, containing 4 injection points. Each injection point is followed by a mixing zone containing mixing elements. Each mixing zone leads into a residence time channel of 5 mm width, 0.6 mm height and 0.8 m length designed to evacuate the heat produced before reaching the following injection point.

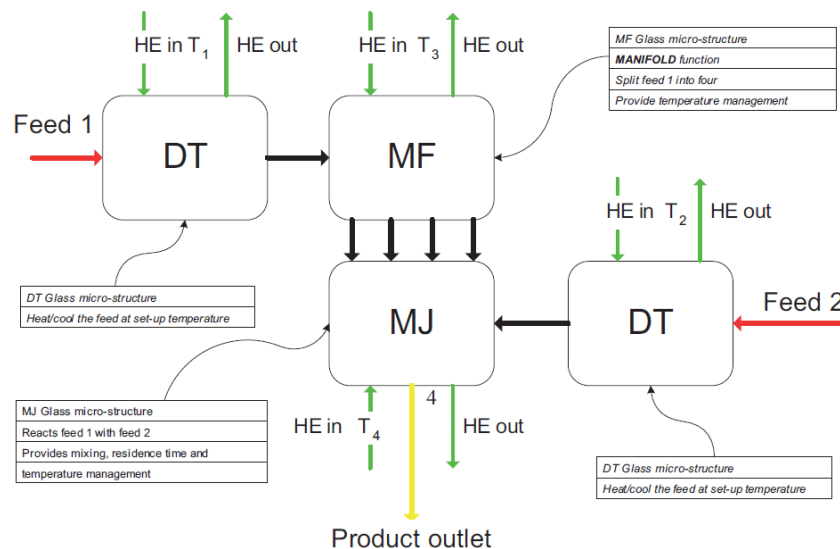


Figure 6.1: Scheme of a modular multi-injection reactor adapted from Barthe *et al.* [170].

In the reactor presented by Barthe *et al.* [170], the key design criteria for an efficient multi-injection reactor are respected:

- 1) Injection of a controlled flow rate of reactant at each injection point.
- 2) Assure complete mixing of the reactants at the end of the mixing zone by efficient mixing structures.
- 3) Evacuation of heat within the larger residence time channel before the subsequent injection.

To avoid accumulation of mass and heat, it is essential that each function is lead to completion before the induction of the subsequent step.

6.1.2 Cyclization of Pseudoionone

The cyclization of pseudoionone in the presence of sulfuric acid was chosen as model reaction, with α -ionone and β -ionone being the desired products. This reaction represents the class of cyclization reactions, which are widely carried out in the fine chemical industry. Due to their olfactory properties, the ionones are used for the creation of essential oils and in various other products in perfumery [241]. Furthermore, β -ionone is an important compound in the synthesis of vitamin A molecules.

While the pure reactants (pseudoionone and sulfuric acid) form two separate phases, by using an appropriate solvent (e.g. nitropropane or nitromethane) one can achieve a homogeneous system. In the following, the studies carried out under heterogeneous conditions are reviewed before summarizing the results obtained in homogeneous systems.

First reports about the cyclization of pseudoionone can be found already in 1946, where E.E. Royals [253] demonstrated that the yield of β -ionone increases with dissociation constant of the catalyzing acid. With a mixture of sulfuric acid and glacial acetic acid he achieved a yield of 71.5 % after more than 35 min of reaction at 20 °C. By operating at higher temperatures of 110 °C, Karshan *et al.* [254] managed to increase the molar ratio of pseudoionone:acid to 20:1. They obtained a yield of 97 % of cyclized ionones (14.6 % β -ionone and 85.2 % α -ionone) after 40 min in a batch reactor. Panfilov *et al.* [255] carried out the reaction using hydrofluoric acid as catalyst in semi-batch mode. At lower temperatures, they achieved yields as high as 93 % of β -ionone at 5 °C with ratios of pseudoionone:acid of 1:11 down to 1:15. Other authors propose the use of continuous processes for the cyclization of pseudoionone. Hertel *et al.* [256] carried out the cyclization of pseudoionone in a continuous glass tube with 2 cm diameter and a thin film reactor respectively. They evacuated the heat of reaction by evaporative cooling of a low boiling solvent

and obtained β -ionone yields of 83 % within a reaction time in the order of a few seconds at 41 °C. With a similar approach, Rheude *et al.* [257] produced β -ionone in a reaction mixing pump yielding 92 % surface area in the gas chromatograph.

Working under homogeneous conditions gave access to the intrinsic kinetics of the system. The reaction mechanism was first studied by Semenovskii *et al.* [258, 259] using nitropropane and nitromethane as solvent to form a single-phase system of sulfuric acid and pseudoionone. They claimed that the rate of reaction is independent of the isomer configuration of pseudoionone. Thereby, the cyclization leads mainly to the formation of α -ionone (90 %) accompanied by a parallel formation of β -ionone (10 %). Under certain reaction conditions, α -ionone can be transformed to β -ionone (isomerization). Kashid *et al.* [240, 241] recently published a study giving deeper insight into the reaction mechanism of cyclization. At first, they carried out kinetic measurements of the relatively slow and slightly endothermic isomerization reaction in a batch reactor with nitropropane as solvent maintaining the molar ratio of pseudoionone to H_2SO_4 at 1:4.8. An increase of this ratio led to a diminished yield of the sum of α -ionone and β -ionone. The isomerization turned out to follow first order kinetics with respect to α -ionone with an activation energy of 65 kJ/mol and a frequency factor of $5.4 \cdot 10^{10}$ 1/s [241]. As a second step, the overall very exothermic cyclization of pseudoionone to the final product β -ionone was studied [240]. Due to the rapidity of the reaction, they switched from a batch vessel to a microreactor based system. This allows on the one hand, sampling after short residence time, and on the other hand, evacuation of the heat produced during the exothermic reaction steps. By introducing a non-miscible solvent (perfluorohexane), they managed to obtain a narrow residence time distribution. The proposed reaction scheme is depicted in Figure 6.2. The first step is a quasi-instantaneous protonation of the pseudoionone molecule, followed by the very fast cyclization of the molecule to the intermediate (6). The low activation energy obtained for these reaction steps indicate a mixing influenced regime. Intermediate (6) is in equilibrium with the protonated α -ionone and γ -ionone, and a part of the intermediate is irreversibly transformed to the protonated form of β -ionone. In the last reaction step, quenching by the addition of water, the final

products α -ionone, β -ionone and γ -ionone are obtained. Herein, the selectivity to γ -ionone is negligible in comparison to α -ionone and β -ionone due to the chosen conditions. When working at higher temperatures (> 10 °C), a loss of selectivity towards the sum of α -ionone and β -ionone was observed due to polymerization of the products [241, 253].

Kashid *et al.* [241] also determined the enthalpies of the different reaction steps by combining calorimetric measurements with the theoretical method of group contribution. The obtained enthalpies are summarized in a scheme in Figure 6.3. Herein, the protonation and the cyclization turn out to be extremely exothermic steps. Hence, in combination with the high reaction rate, this very fast and highly exothermic step (-128 kJ/mol) makes it particularly critical to carry out this reaction. The second key point regarding heat release is the quenching of the reactants. However, a temperature rise at this point is less critical than in the first step, where subsequent reactions can be triggered.

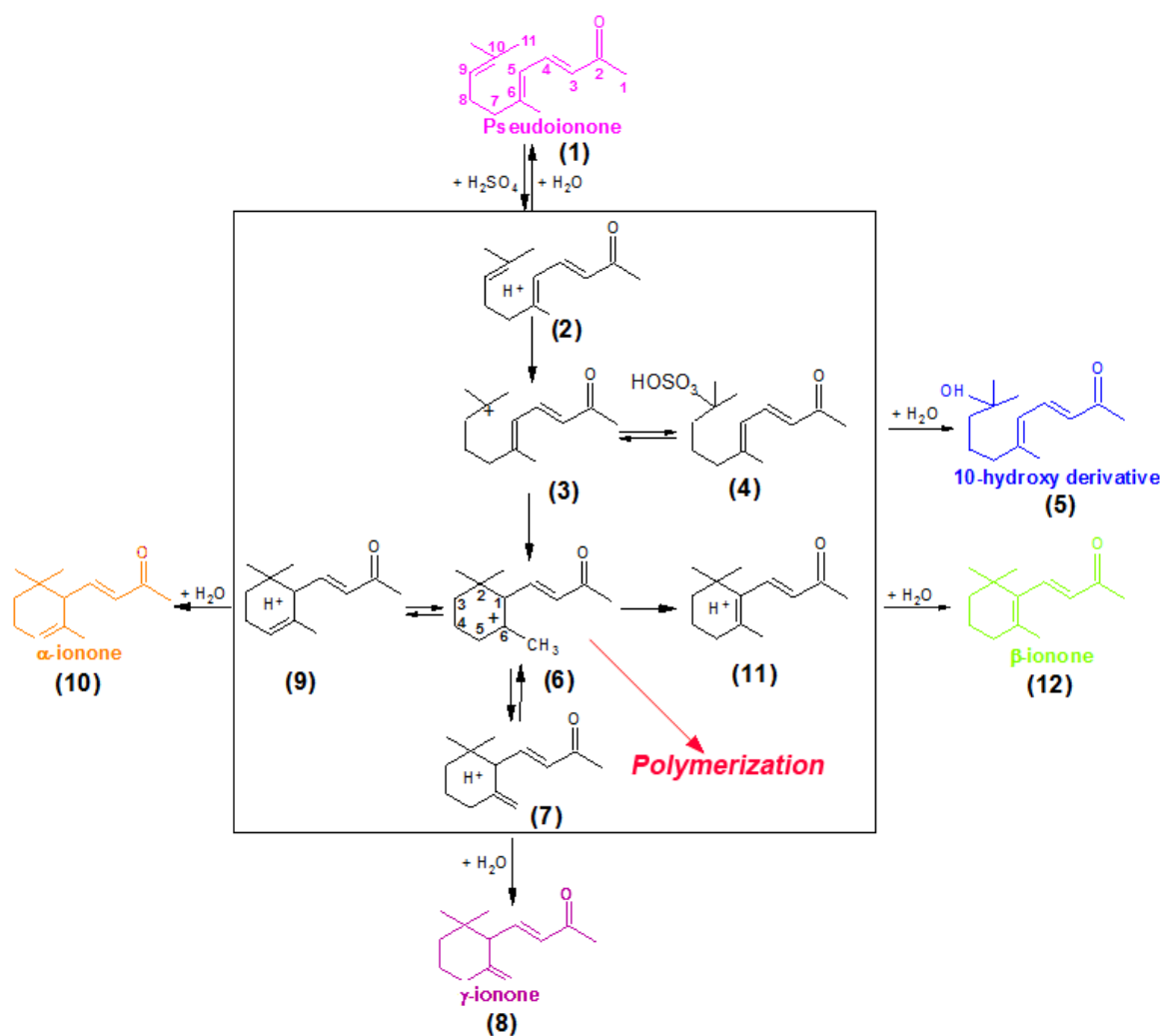


Figure 6.2: Reaction scheme of cyclization of Pseudoionone.

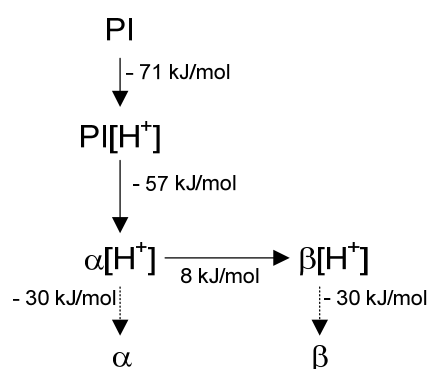


Figure 6.3: Reaction enthalpies proposed by Kashid *et al.* [241]. PI: pseudoionone, α : α -ionone β : β -ionone. The reaction enthalpy of -30 kJ/mol is obtained by superposition of the deprotonation enthalpy (71 kJ/mol) and the enthalpy released by the dilution of sulfuric acid to 60 % w/w.

Despite the effort that has been done in the past decades, the state of the art of industrial production of β -ionone remains a semi-batch production with dosing times around 60 min at temperatures around 0 °C. As a consequence, low space-time yields are achieved and a part of the product is lost due to consecutive polymerization. A more extensive review on this reaction can be found in literature [241].

6.1.3 Scope of the work

In this chapter, a multi-injection microreactor is designed and used to carry out the cyclization of pseudoionone to α -ionone and β -ionone. The reactor design is directed by the two-fold aim:

- 1) Process intensification and optimization for the combined yield of α -ionone and β -ionone.
- 2) Experimental demonstration of the temperature profile in a multi-injection reactor.

Regarding the first point, the primary target is to obtain a maximal yield of α -ionone and β -ionone. Thereby, it is crucial to prevent the highly exothermic, and therefore, dangerous product decomposition (polymerization), which leads to a loss in yield of the sum of α -ionones and β -ionones. As the target molecule of the overall process is β -ionone, it is preferential to shift the composition towards β -ionone. As the isomerization from α -ionone to β -ionone is only slightly endothermic, this reaction can be easily carried out in a subsequent isothermal residence time loop [240].

The second aim, i.e. the experimental study of the temperature profile using an infrared thermography based method sets some constraints to the reactor design, especially regarding its size.

In the upcoming sections, the novel reactor design is presented followed by the experimental setup and the obtained results.

6.2 Design of the Multi-injection Reactor

The development of a multi-injection reactor was carried out in collaboration with the Ceramics Laboratory (LC) and the Laboratory of Microengineering for Manufacturing 2 (LPM2) of EPFL. At the beginning, a list of requirements was set up, highlighting the needs for a successful design. Subsequently, it was found that these requirements could be met by manufacturing the multi-injection reactor using low temperature co-fired ceramic (LTCC) materials. As a first proof of concept, two different mixing structures were constructed and tested. Finally, the most suitable structures (the herringbone mixer) was integrated in the final multi-injection reactor design which is shown at the end of this section.

6.2.1 List of Requirements

As already mentioned in the description of the scope of the work, the reactor design is a compromise between the requirements for the best possible process performance and the boundaries needed for the quantitative monitoring of temperature inside the reaction channels. Hence, the list of requirements can be subdivided into two parts: The requirements by the process and the requirements by the method. The requirements are listed according to their priorities, starting from the most important aspect.

Requirements by the process:

- The material is corrosion resistive up to temperatures of 100 °C, withstanding the extreme concentrations of sulfuric acid (> 55 % w/w)
- Efficient microstructures ensure complete mixing at the end of the mixing zone
- Integrated cooling system with high volumetric heat transfer coefficient to evacuate the heat of the exothermic reaction
- Allow for sufficient residence time τ_i between the injection points to prevent accumulation of heat and mass: $\tau_i > t_{cool}$ and $\tau_{cool} > t_{r,eff}$

6 Development and Experimental Investigation of a Multi-injection Reactor

- A maximal pressure drop of 1 bar which can be handled by the available syringe pump
- Maximize the amount of injection points

Requirements by the method:

- Due to the trade-off between resolution and field of vision, the reactor is comprised within an area of 6 cm × 6 cm to measure with a resolution of 150-200 μm.
- The cooling channel does not interfere with the infrared signal emitted by the reaction channel.
- The wall separating the reaction channel from the ambient on the camera side is thinner than 500 μm to reduce the effect of inner channel resistance on the surface temperature.
- Low conductivity in the plane for the best possible contrast

6.2.2 Microstructured Reactor from Low Temperature Co-fired Ceramics

Low temperature co-fired ceramics (LTCC) was chosen as a manufacturing technology to build up the ceramic multi-injection reactor. It is derived from the thick-film technology area (film thicknesses of typically 10 μm) [260], where it has been used for the creation of electronic substrates for high frequency applications. Within this area of applications, noble metals are used as conductors and electrodes as they exhibit thermodynamic stability under air at the common range of operation temperatures (800 °C – 1100 °C). However, these noble metals have relatively low melting temperatures: Ag, Au and Cu at 961 °C, 1063 °C and 1083 °C. Hence, to prevent melting of the electrodes during the sintering process (“co-firing” of both), the processing temperature of LTCC has to be below their melting point. The substrates are typically sintered at temperatures between 800 °C and 900 °C.

The properties of the LTCC substrates render this material very attractive for the development of microstructured reactors: it is chemically inert even in harsh environments and one can easily create complex 3-D structures through punching, milling and laser cutting processes [261-263]. The application

of this technology to the field of microfluidics is very recent, and the use of LTCC for such a complex development as the multi-injection reactor has not been reported so far [260, 264-268].

Figure 6.2 shows a simplified fabrication process scheme of the LTCC technology [267]. The reactor is fabricated out of several plain layers of LTCC tapes. The commercial glass-ceramic composition DuPont 951 was chosen for the construction because of its chemical inertness against acids and bases [269-271]. Ceramics are composed of non-organic, non-metallic elements that are sintered at high temperature forming the ceramic. Such tapes are commercially available in different thicknesses between 50 and 250 μm . In the first step, the designed channel patterns are applied by means of laser ablation (1064 μm Nd:YAG, LS9000 Laser Systems GmbH) (A). Subsequently, the tapes are stacked together using a pin-alignment leading to a 3 dimensional structure (B). The lamination of the stacked tapes was achieved through the novel progressive lamination process that not only enables inter-penetration of ceramic particles in the LTCC by diffusion of the organic binders, but, also guarantees the quality of embedded cavities (C) [269]. The firing of the stack is generally carried out in two phases: removal of the organics via evaporation and oxidation at about 400 $^{\circ}\text{C}$ followed by the liquid phase sintering [272] of the ceramic layers at 900 $^{\circ}\text{C}$ [267] (D). Thereby, shrinkage of the reactors in the order of 30 % has to be taken into account. In the final steps of the process, the reactor is cut to the right size and the fluidic connections are made (E, F).

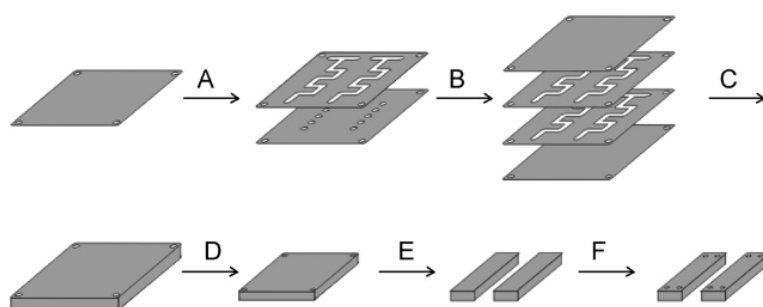


Figure 6.2: Schematic of the fabrication of Low Temperature Co-fired Ceramic microstructured reactors. A: Structuring by laser ablation B: Stacking of the layers C: Isostatic lamination D: Firing E: Dicing F: Fluidic opening by laser ablation. Image adopted from Große *et al.* [21].

The physical properties and the flexibility of the process render LTCC greatly attractive for the development of the multi-injection reactor with the requirements as described in the previous section:

- Within this study, the LTCC material was shown to be extremely corrosion resistant towards strong sulfuric acid: the sintered material sustained 14 days in 60 % w/w of aqueous sulfuric acid without weight loss or visible changes.
- Due to the high precision obtained with laser ablation, fine structures with dimensions down to 200 μm can be created.
- Due to the stacking procedure, the creation of three dimensional structures and superposed channels is enabled.
- The thermal conductivity of 3.3 W/(m·K) [273] is low enough to avoid loss of contrast by diffusion in the plane (x-y).
- The low thickness of the layers (z-direction) essentially nullifies the heat transfer resistance in the wall as compared to the resistance within the reaction channels resulting in high heat transfer rates.

6.2.3 Mixing zone

As illustrated in Chapter 5, fast and complete mixing of the inlet streams is crucial when carrying out rapid exothermic reactions with short residence time in the reactor. Due to the low diffusion coefficients in liquid phase [274], the small sizes of microstructured reactors do not assure fast mixing. Especially in the case of organic solutions, mixing structures are needed to prevent accumulation of the reactants in the multi-injection reactor.

Several mixing structures can be found in literature [38, 275], among which two distinct designs were chosen: the tangential mixer [275, 276] and the herringbone mixer [110, 153-156, 277]. Both structures

were manufactured on 25 mm × 62 mm plates using low temperature co-fired ceramics and tested regarding their suitability for the integration in the multi-injection reactor (see section 6.4.1).

In the tangential mixer, the fluid flows through a series of narrow channels followed by a recirculation zone (Figure 6.5A). The recirculation increases the mixing quality with increasing Reynolds number [276]. In the ideal case, this type of mixer can be assimilated to a cascade of continuous stirred tank reactors. As a consequence, when working with an amount of structures less than 10, one has to take into account a broadened residence time distribution. For the present design, it was chosen to work with eight consecutive recirculation zones with a diameter in the x-y plane of 2 mm and a channel height of 500 μm. The width of the transfer channels connecting one zone with the following was set to 500 μm. The total reactor volume from the contacting point of the reactants to the reactor outlet is 18 μl. A scheme and a picture of the complete mixer design is given in Figure 6.5A.

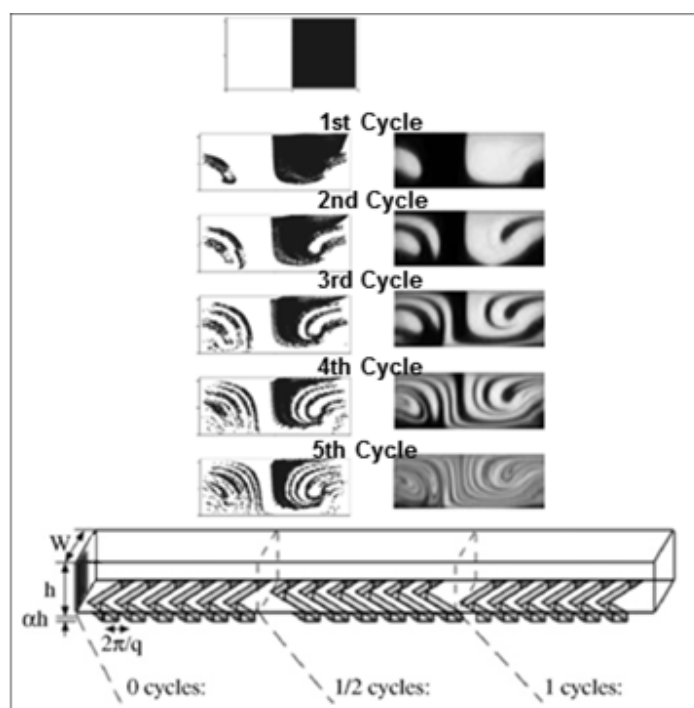


Figure 6.4: Mixing of the herringbone mixer by creation of transverse flow compounds (from [155]).

The herringbone mixing structure was first time shown to work about 10 years ago [277]. Since that time, several studies have been carried out regarding the mixing mechanism and the geometric optimization of this structure using numerical simulation [153-156]. The addition of grooves on the bottom of the channel induces a flow velocity component that is normal to the flow direction. By alternating the direction of the grooves, the two inlet flows are successively “folded” on top of each other even at low Reynolds number ($Re < 10$). As shown in Figure 6.5, a sequence of grooves with same orientation constitute half a cycle. Thereby, the grooves reach only a certain percentage α of the total channel height H .

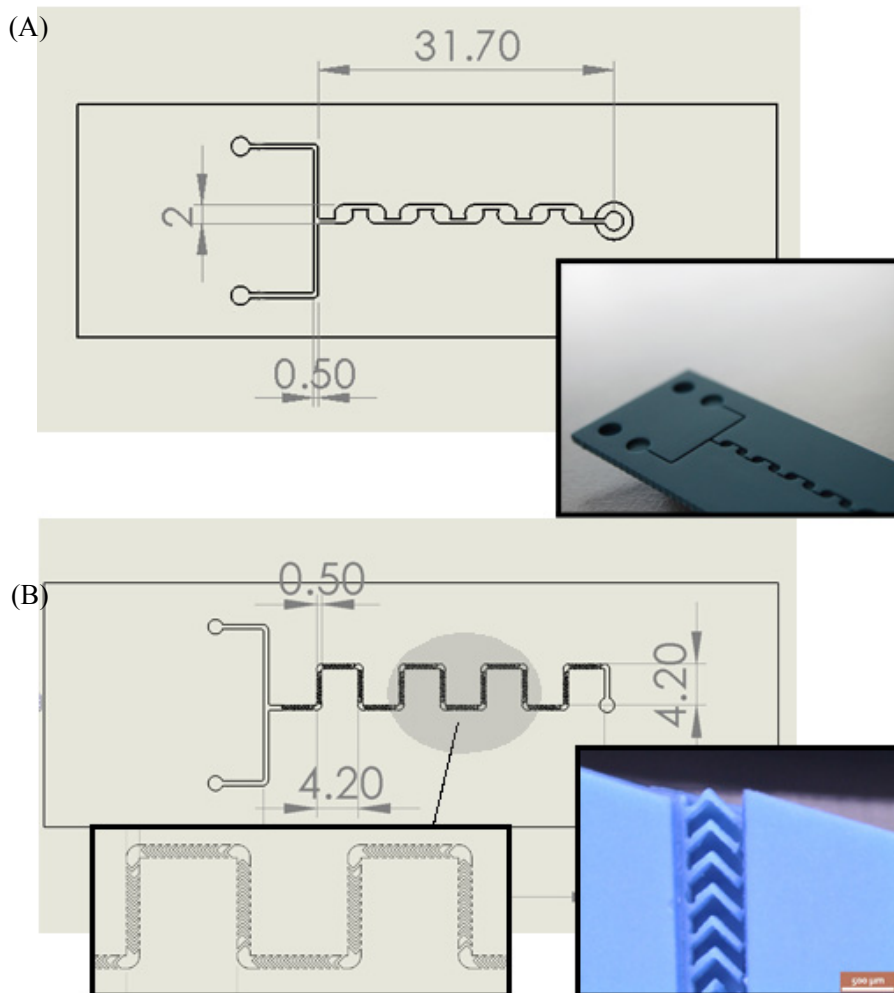


Figure 6.5: Scheme of the tangential mixer (A) and the herringbone mixer (B). The dimensions are given in millimeter.

For the present herringbone mixer, 7.5 cycles of 10 grooves per half cycle were built up. The groove thickness is $100\ \mu\text{m}$ with a space of $100\ \mu\text{m}$ between the grooves ($2\pi/q = 200\ \mu\text{m}$). The channel cross section is $560\ \mu\text{m} \times 500\ \mu\text{m}$ ($(h + h\cdot\alpha) \times W = H \times W$) with $\alpha = 0.30$. The mixer with a total channel length of $L = 68\ \text{mm}$ and a volume of approximately $19\ \mu\text{l}$ is depicted in Figure 6.5B.

6.2.4 The Multi-injection Reactor Design

The overall size of the multi-injection reactor plate is $65\ \text{mm} \times 35\ \text{mm}$. The mixing and cooling channels are confined to a window of $30\ \text{mm} \times 30\ \text{mm}$ in the center of the plate, which can be almost completely monitored by the infrared camera. The amount of injection points was set to three due to the limited availability of surface on the plate. For an efficient mixing of the reactants, the herringbone structure was chosen (see section 6.4.1).

The reactor was constructed out of a total of 11 layers of ceramic green type (Dupont 951). Some of these layers are identical to each other which is used to built-up the required thickness, e.g. to obtain an overall height of the herringbones of $150\ \mu\text{m}$ (before shrinkage), 3 layers of $50\ \mu\text{m}$ are needed. After firing, shrinkage of the layer thicknesses of 15 % has to be considered. Hence, 8 different structures were created by laser ablation (see Figure 6.6), and are shortly described in the following together with their thickness in the unfired state:

- The connection plane (156 μm) contains an overall of 11 holes with a diameter of 1 mm allowing all the connections to be done from the top of the reactor. The system used to make the connections is described in 6.3.1.1. With a thickness of only $156\ \mu\text{m}$ (before shrinkage), the influence of the inner heat transfer resistance on the temperature signal can be neglected, as the main heat transfer resistance lies between the wall and the surrounding.
- The fluidic channel (508 μm) layer creates the void space above the herringbone structures. Together with the herringbone layer, the resulting cross section is $560\ \mu\text{m} \times 500\ \mu\text{m}$ ($(h + h\cdot\alpha) \times$

W) in the mixing module and $560 \mu\text{m} \times 2000 \mu\text{m}$ in the residence time module. The total length of one mixing module is 66 mm followed by 33 mm of residence time module before reaching the subsequent injection point.

- The herringbone layer (150 μm) contains a total of 7 cycles of herringbones with the same geometry as described in 6.2.3.
- The cooling wall 1 (156 μm) separates the reaction channel from the cooling channel. Its low thickness provides almost no resistance to heat transfer between both channels.
- The cooling layer (508 μm) contains three identical cooling channels having each 9 mm of width and about 5 cm of length. Each of these channels is exactly superposed to one single module of mixing and residence time on the fluidic channel layer. For manufacturing reasons and to avoid maldistribution of coolant between the channels, this layer is fed by separate inlets.
- The cooling wall 2 (254 μm) separates the cooling channel from the reactant inlet channel. Its low thickness provides almost no resistance to heat transfer between both channels.
- The inlet layer (508 μm) has the function to preheat the inlet flow before it reaches the first injection point located on the top of the reactor. The channel dimensions are identical to the dimensions of the residence time module.

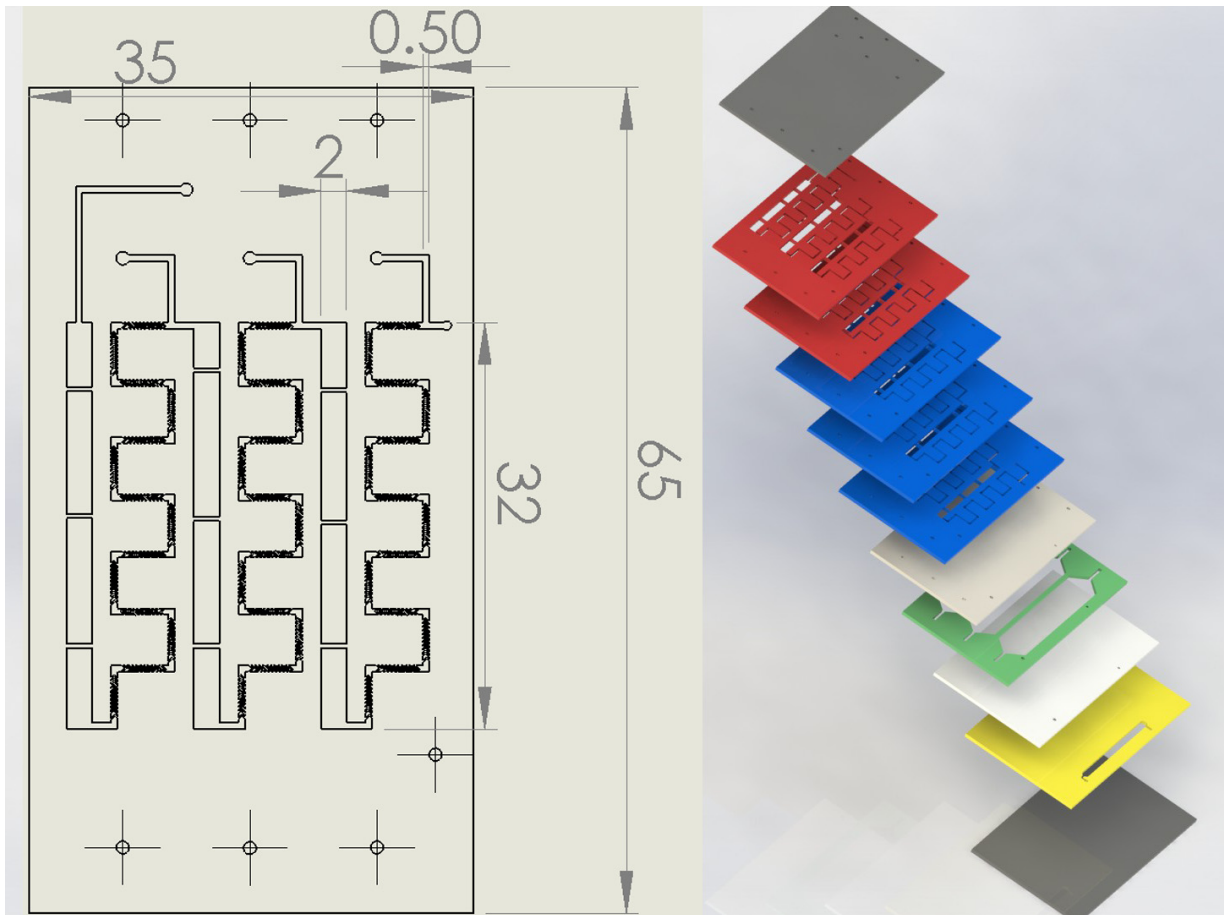


Figure 6.6: Scheme of the second layer of the multi-injection reactor containing the dimensions in millimeter (left), and the complete reactor built-up from 11 layers of green tape (right).

For the stability of the green tape during the manufacturing process, the channels are crossed by “bridges”. As their positions are shifted from one layer to another, the passage of the liquid is not hindered.

6.3 Experimental Part

This section focuses on the setup built to carry out the measurements with the previously described reactors, and on the methods used to characterize the reactors.

6.3.1 Experimental Setup

The integration of the mixers and the multi-injection reactor into an experimental setup is described in this section. First it is shown, how the flat laser ablated holes can be connected to standard tubing. Subsequently, an overall picture of the setup and methods of analysis is given.

6.3.1.1 Embedding the Reactor into the Setup

To make the connections between the standard 1/8" tubing and the inlet of the ceramic microstructured reactors, a connection device was manufactured out of alumina. By fixing the reactor into this construction, leak proof connections can be made between the perfluoroalkoxy (PFA) tubes and the reactor openings by using commercially available ethylene tetrafluoroethylene (ETFE) flangeless ferrules. A snapshot of the device fabricated for the multi-injection reactor allowing the 11 connections to be done is given in Figure 6.7.

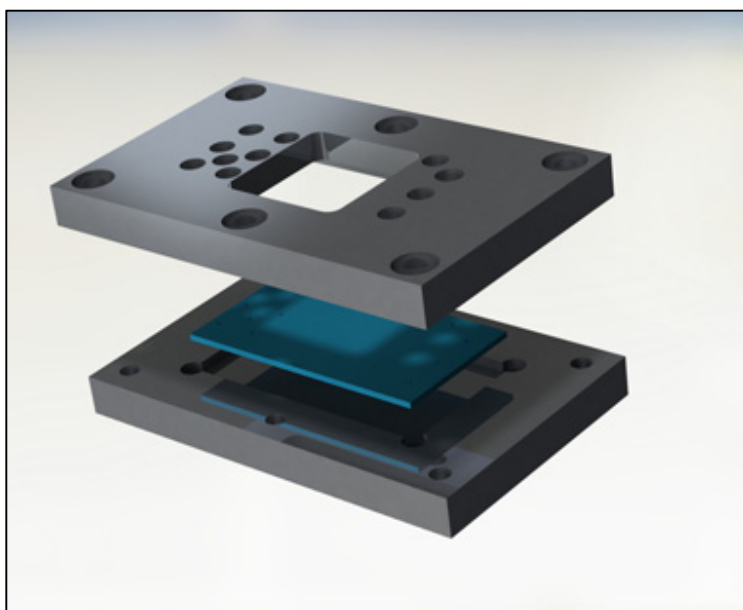


Figure 6.7: Device constructed to connect the multi-injection reactor to standard 1/8" tubing using flangeless ferrules.

6.3.1.2 *Overview of the Setup*

The reactor embedded in the connection device is integrated in a similar setup as described in the previous chapters. To have reproducible results, the boundary conditions of the reactor were fixed by two different manners leading to two distinct setups:

- 1) The tangential and herringbone mixer, which do not contain an integrated heat exchange channel, were analyzed in the vacuum box as presented in chapter 4. While, the heat losses by convection are efficiently suppressed, the heat losses by radiation cannot be suppressed, leading to a lumped heat loss coefficient in the order of $1.4 \cdot 10^6 \text{ W}/(\text{m}^3\text{K})$ to $2.1 \cdot 10^6 \text{ W}/(\text{m}^3\text{K})$.
- 2) The multi-injection reactor with integrated cooling unit (containing a liquid as coolant) was monitored under a constant convective flow of air. Thereby, the aim was to maintain the heat losses via the cover of the reactor to the environment constant by avoiding natural convection, which exhibits a strong dependence on temperature and disturbances from the outside. As the heat losses coefficient on the top surface of the channel is much lower than the heat transfer coefficient with the cooling channel (effect on the overall heat balance is less than 15 %), the vacuum box was omitted.

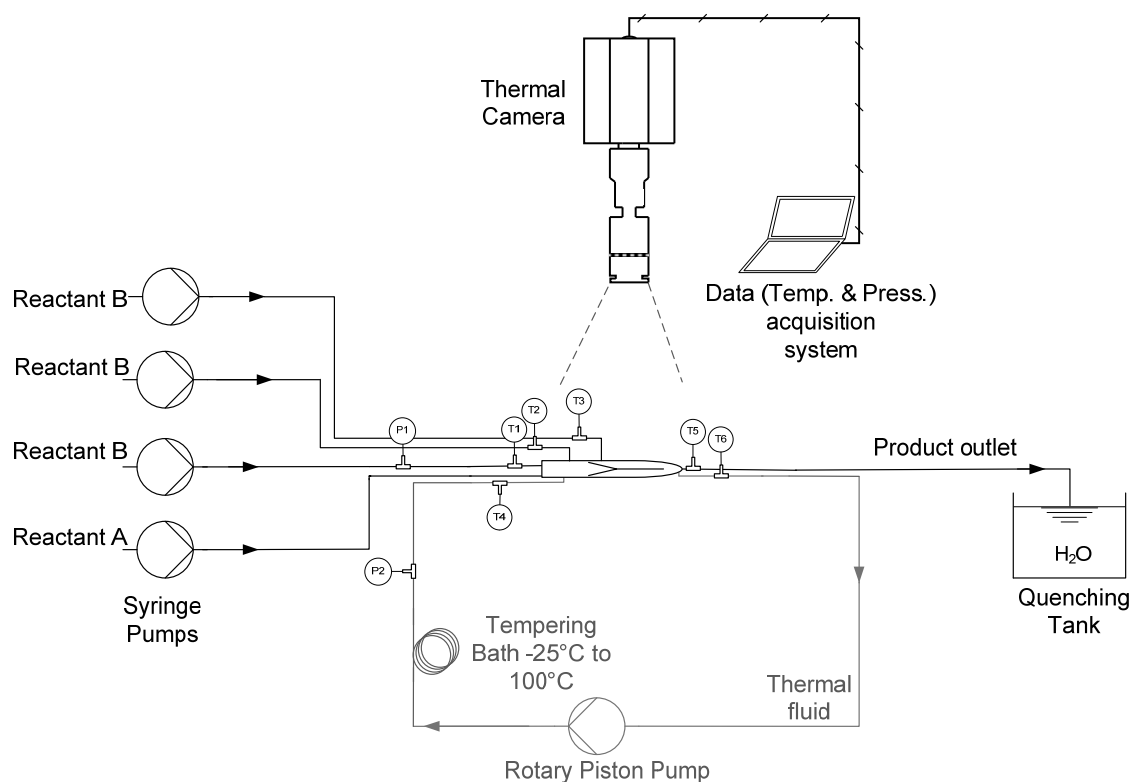


Figure 6.8: Setup for experimental analysis of the multi-injection microreactor.

The reactants are fed through four separate syringe pumps, thus, avoiding flow maldistribution. For the experiments, two homogeneously miscible solutions A and B are prepared:

- A) 1.25...2.75 M pseudoionone in 1-nitropropane
- B) 7.5...12 M sulfuric acid in 1-nitropropane

The main physical properties of the compounds are summarized in Table 6.1 together with an estimation of the properties of the solutions.

Table 6.1: Physical properties at 25 °C of the compounds used for the homogeneous cyclization of pseudoionone.

	Density [kg/m ³]	Heat capacity [J/(kg K)]	Kinematic viscosity [m ² /s]
1-Nitropropane	998	1972	$7.90 \cdot 10^{-7}$
Pseudoionone	895.1	1930	$6.38 \cdot 10^{-6}$
β-ionone	940	-	$1.15 \cdot 10^{-5}$
Sulfuric acid	1840	1340	$1.34 \cdot 10^{-5}$
Solution A*	970	1962	$2.17 \cdot 10^{-6}$
Solution B*	1372	1596	$8.28 \cdot 10^{-6}$
Product mixture*	1169	1757	$5.60 \cdot 10^{-6}$

*Calculated properties assuming an initial solution of 1.25 M of pseudoionone and 7.5 M of sulfuric acid.

It is worthwhile to point out that the sulfuric acid solution is fed through the main channel (reactant A) whereas the pseudoionone solution is fed to the three injection points (reactant B). If the flows were inverted, the yield would be shifted towards higher amounts of α -ionone due to an insufficient ratio of acid to pseudoionone within the first injection points. The products are quenched at the outlet with a 150 g/l solution of sodium carbonate at 0 °C. Temperature at the inlets and outlets is measured by 0.5 mm thick K-type thermocouples and pressure is monitored at the first injection point using pressure gauges with a working range of 0...28 bar and a precision of ± 0.15 bar.

6.3.2 Methods of Analysis

The main tool of analysis used in the present study was the quantitative monitoring of temperature using an infrared thermography based method similar to the method presented in the previous chapter. The product composition at the reactor outlet was characterized using a gas chromatograph.

6.3.2.1 *Quantitative Infrared Measurement*

As mentioned in section 6.3.1.2, the temperature profiles of the two micromixers (the herringbone and the tangential mixer) were monitored in the vacuum box. To get quantitative data, a “pixel-by-pixel” calibration of the setup was carried out prior to the measurements as thoroughly described in chapter 4.

Compared to the mixers, the volume of the multi-injection reactor is larger due to longer channels. As a consequence, heat losses between inlet and outlet play a more important role, which decreases the accuracy of the “pixel-by-pixel” calibration. For this reason, the calibration procedure was adapted to the multi-injection reactor: a uniform emissivity can be assumed all over the reactor surface due to its flat and homogeneous surface. As the signal emitted by the reactor is not interfering with an infrared transparent window, the dependence on emission angle can also be neglected (see chapter 4). Hence, the calibration between liquid temperature inside the reactor channel and signal measured by the camera can be carried out at one single point, and be used for the whole reactor. To validate the assumptions, the calibration was carried out at the three injection points respectively:

Inert liquid (Butanol) was fed at temperatures between 25 °C and 50 °C to one of the three injection point inlets at high flow rates. The temperature was monitored by a thermocouple directly at the inlet of the injection point and compared to the average of the camera signal θ over 10 pixels located on top of the respective injection channel. Due to the short distance between thermocouple and calibration pixels (≈ 4 mm), and because of the high flow rates (≈ 20 ml/min), it can be assumed that the temperatures were identical at the two locations within ± 0.25 °C. The calibration plot in Figure 6.9 shows that a homogeneous emissivity of $\varepsilon = 1$ can be readily applied all over the reactor allowing temperature to be monitored within an overall precision range of ± 1 °C.

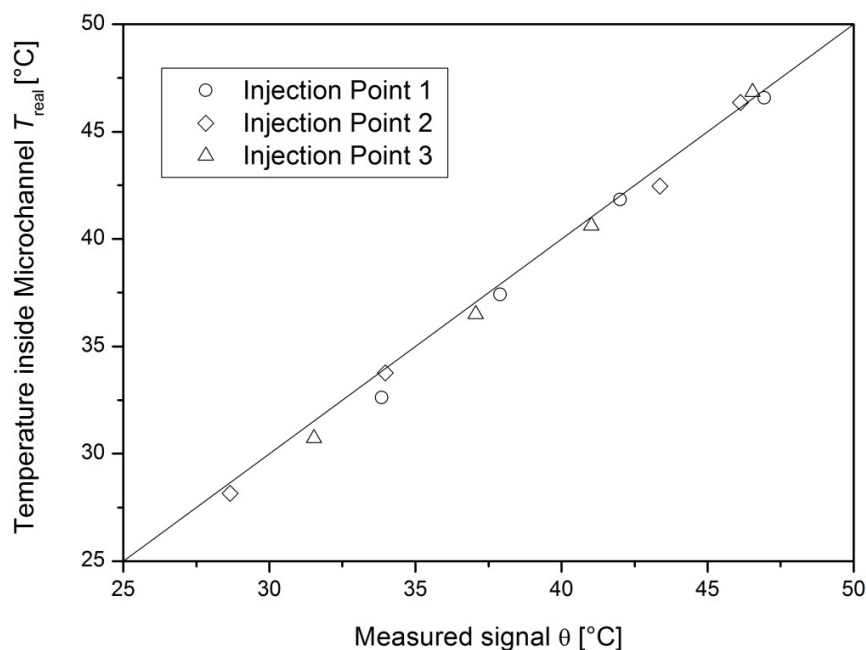


Figure 6.9: Calibration of camera signal to the temperature measured by thermocouples at three injection point inlets.

6.3.2.2 Gas chromatography

After separating the organic phase from the aqueous phase, analysis of the product distribution is carried out in a Perkin-Elmer Auto System XL chromatograph equipped with a programmed split/splitless injector and a flame ionization detector employing a Stabilwax (Cross-bond Carbowax-PEG, Restek, USA) capillary column (i.d. = 0.32 mm, length = 30 m, film thickness = 0.25 μm). The calibration of the chromatograph was carried out with 90 % pseudoionone supplied by Aldrich, 96 % β -ionone supplied by Acros, and 90 % solution of α -ionone supplied by Aldrich. Thereby, the calibration curve was found to be quasi identical for the three molecules. As internal standard, 99.5 % butanol by Alfa Aesar was added to the outlet solution before the injection into the chromatograph. A typical chromatogram showing the analyzed molecules is given in Figure 6.10. To obtain a representative product composition, the analysis of each sample was performed three times.

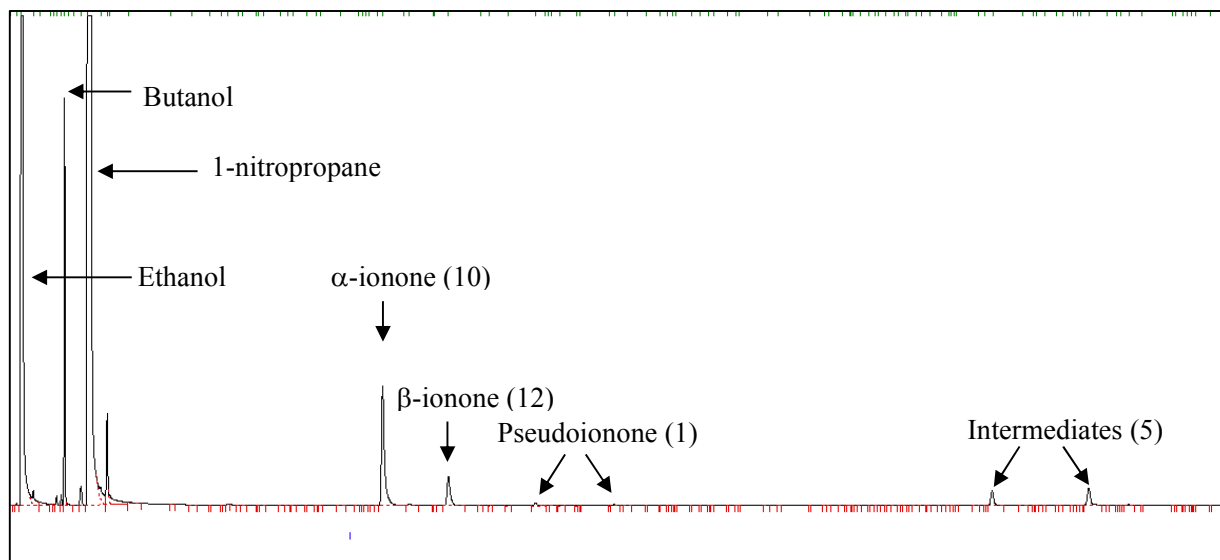


Figure 6.10: Chromatogram showing a typical product distribution after cyclization of pseudoionone. The molecule designated as “Intermediates (5)” was found to be 6,10-dimethylundeca-3,5-dione-10-hydroxy-2-one [240]. Ethanol was used for the dilution of the product mixture to obtain concentrations in the measurable range.

6.4 Experimental Results

At first, quantitative infrared thermography was used as tool to evaluate both mixing structures, and chose the one to be integrated into the multi-injection reactor. Subsequently, the multi-injection reactor was characterized thermally on the one hand, regarding the heat transfer under non-reactive conditions, and on the other hand, regarding the temperature profile during the cyclization of pseudoionone. Finally, the product composition at the reactor outlet was determined with respect to flow rate, temperature and inlet concentrations.

6.4.1 Mixing structure

To avoid accumulation of reactant in the multi-injection reactor, an efficient mixing structure had to be found that is able to provide almost complete mixing of the reactants which is especially challenging due

to the considerable difference of density ($\Delta\rho \approx 0.4 \text{ kg/m}^3$) between the two inlet streams (sulfuric acid and pseudoionone). Therefore, the temperature profiles were monitored in the two selected mixing structures, i.e. the tangential mixer and the herringbone mixer, that have been shown to work efficiently with aqueous solutions in literature [38, 110, 153-156, 275, 277]. The temperature profile provides integral information of the conversion of the reactants inside the mixing structure, provided the system is adiabatic. Assuming a quasi-instantaneous reaction, conversion is directly proportional to the advancement of mixing inside the reactor. As especially radiation heat losses cannot be completely avoided, a characteristic heat losses time in the order of $t_{\text{loss}} \approx 1 \text{ s}$ had to be taken into account.

In the following, the profiles obtained with the tangential mixer and with the herringbone mixer are separately presented, before comparing one with another.

6.4.1.1 *Tangential Mixer*

Quantitative temperature profiles of the strongly mixing controlled reaction between pseudoionone (1.2 M) and sulfuric acid (7.5 M) are given in Figure 6.11. The adiabatic temperature rise of the mixture is $\Delta T_{ad} = 37 \text{ }^\circ\text{C}$. As an orientation, a total flow rate of 1 ml/min corresponds to a flow velocity of 0.067 m/s, a residence time of about 1 s in the mixer and to a Reynolds number of around $Re \approx 10$ (at the contacting point, assuming an average viscosity of the mixture).

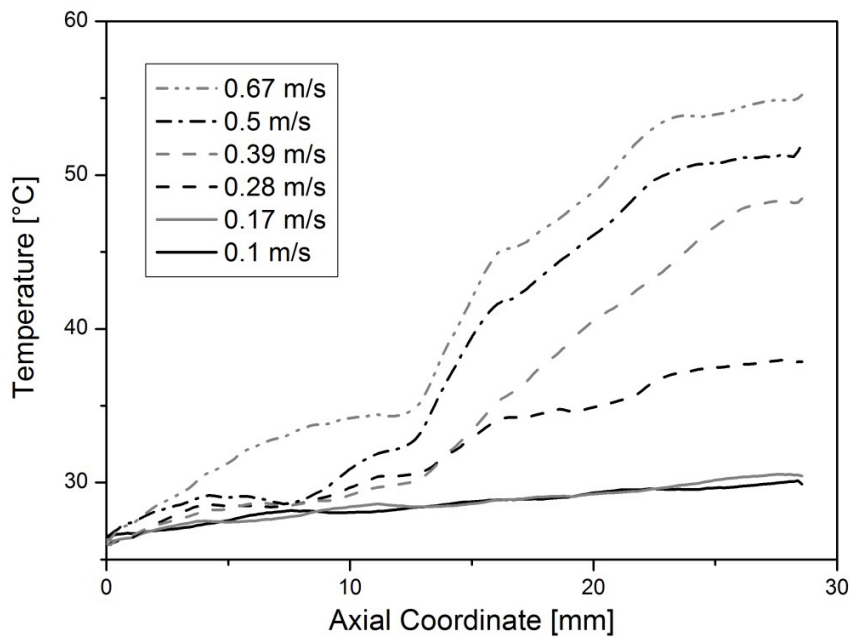


Figure 6.11: Mixing profiles obtained in the tangential mixing structure while mixing pseudoionone (1.2 M) with sulfuric acid (7.5 M).

For flow velocities lower than 0.17 m/s, almost no formation of heat is observed. Only at flow rates above 4.2 ml/min (0.28 m/s), a noticeable conversion of the reactants is seen. To confirm the poor quality of mixing at low flow rates, microscope pictures were taken during the mixing of water with dyed water in an identical reactor with glass cover. The results in Figure 6.12 show that at low Reynolds numbers ($Re < 60$), mixing occurs solely by diffusion.

When exceeding velocities of 0.5 m/s (corresponding to $Re \approx 70$), more than 50 % of the adiabatic temperature is reached, while at 0.67 m/s already 80 %, indicating almost complete mixing. When comparing with the microscope results obtained with water in Figure 6.12, one can clearly notice the appearance of secondary flow leading to fast homogenization.

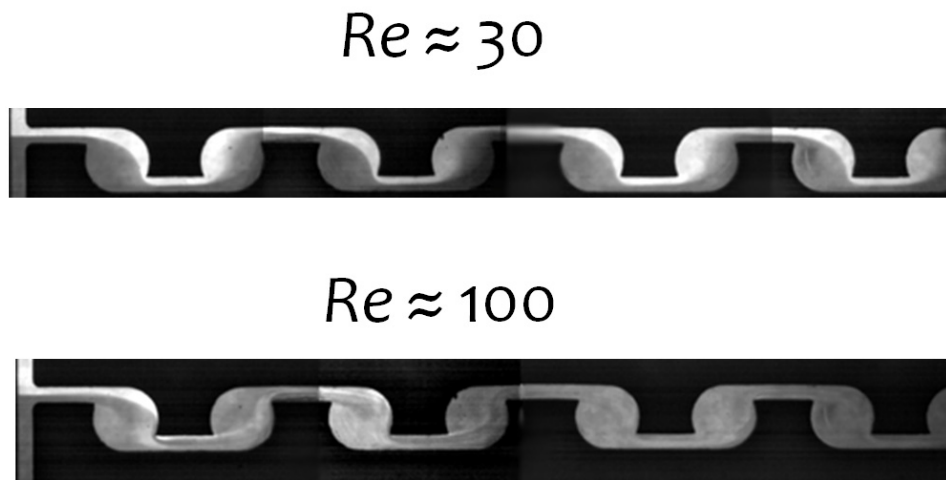


Figure 6.12: Mixing of dyed water with pure water at low (top) and higher (bottom) Reynolds number.

As expected, this type of mixing structure relies on the formation of secondary flows, which do not clearly appear until $Re \approx 70$. Hence, when applying this type of structure to the model reaction, one needs to work at flow rates higher than 7 ml/min (velocities higher than 0.47 m/s) in order to benefit from efficient mixing.

6.4.1.2 *Herringbone Mixer*

The results obtained with the herringbone mixing structure are depicted in Figure 6.13. As this reactor has approximately the same volume as the tangential mixer, the same approximation for Reynolds number and residence time holds: 1 ml/min corresponding to a flow velocity of 0.06 m/s, $\tau \approx 1.1$ s and $Re \approx 10$ (at the contacting point).

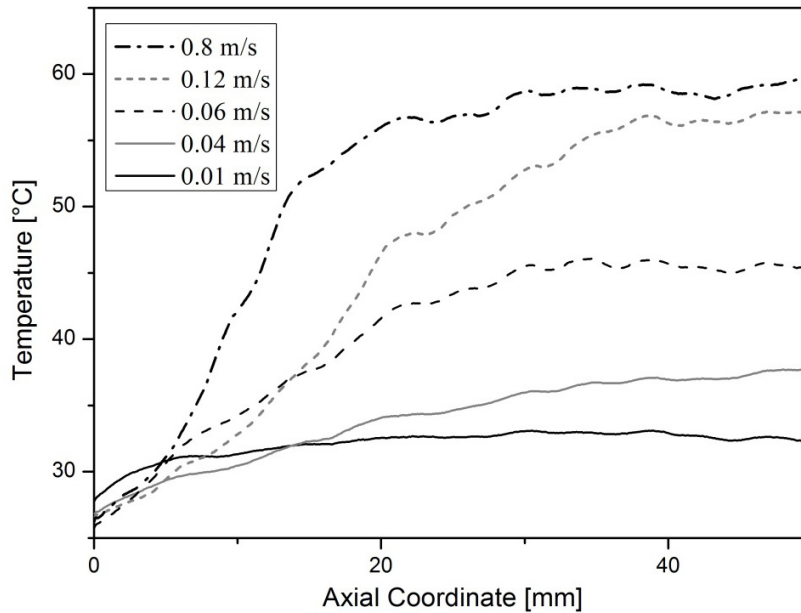


Figure 6.13: Mixing profiles obtained in the herringbone mixing structure while mixing pseudoionone (1.2 M) with sulfuric acid (7.5 M).

Compared to the tangential mixer, where an onset of the reaction is observed at a length of about 12 mm, this type of mixer leads to an immediate and almost linear increase in temperature. At flow rates as low as 2 ml/min (0.12 m/s), efficient mixing of the reactants is observed. This corresponds to a 4-fold reduction of the required Reynolds number compared to the previous structure. Furthermore, even when lowering flow velocity down to 0.04 m/s, temperature rises up to 35 °C. As heat losses become considerable at such high residence times, it is likely that the drop in temperature at lower flow rates can be ascribed to the increasing importance of the losses rather than to a loss of mixing quality. More interestingly, this structure which is supposed to fail at higher Re numbers [156] exhibits its best performance at $Re \approx 130$. This deviation might be explained by the fact that the Reynolds number is obtained by using average physical parameters of both inlet solutions.

6.4.1.3 Comparison of the Structures

For a comparison of both mixing structures, the heat losses were taken into account as follows:

$$\Rightarrow X = \frac{T - T_0}{\Delta T_{ad}} + \int_{z'=0}^{z'=z} \frac{Ua_{loss}}{\rho \cdot c_p} \cdot \frac{1}{u} \cdot \frac{(T - T_w)}{\Delta T_{ad}} \cdot dz' \quad (6.1)$$

Thereby, the volumetric heat loss coefficient was estimated by flowing hot inert liquid (butanol) through the structure prior to the experiments, leading to values of $2.1 \cdot 10^6 \text{ W}/(\text{m}^3\text{K})$ and $1.4 \cdot 10^6 \text{ W}/(\text{m}^3\text{K})$ for the tangential and the herringbone mixer respectively. For simplification, no dependence on the flow velocity was considered. Assuming a first order behavior, the conversion at the outlet of the reactor was transformed into the Damköhler number:

$$DaI = -\ln(1 - X) \quad (6.2)$$

The Damköhler numbers obtained for both mixers are shown in Figure 6.14.

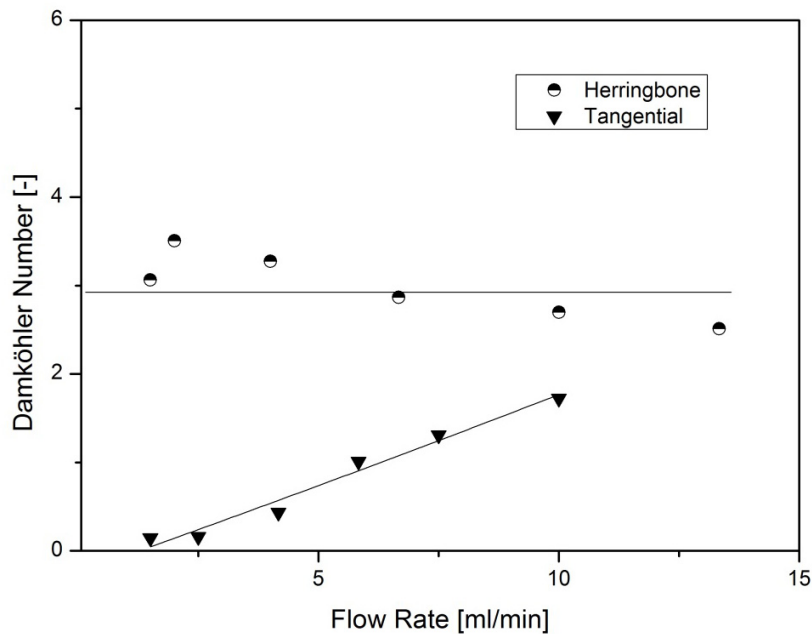


Figure 6.14: Conversion at the mixer outlet ($DaI = \tau/t_{r,eff}$) as a function of the flow rate.

The trend observed for the tangential mixer is exactly opposed to the curves expected from a reaction working in the kinetic regime, where an increase of flow rates results in a reduced residence time and hence, in a linearly diminishing $DaI = \tau/t_{r,eff}$. In the present case, the increase of the flow rate not only

affects DaI , but, overproportionally reduces $t_{r,eff}$ due to the creation of vortices. This turbulent aspect of the laminar flow leads to an increased conversion with increasing flow rates.

Figure 6.14 shows that for the tangential mixer a minimum flow rate of about 7 ml/min is required to obtain sufficient conversion ($X = 0.73$ corresponding to $DaI = 1.30$) at the reactor outlet. On the other hand, a constant high value of Damköhler number is observed for the herringbones mixer in the range of 2 ml/min to 13 ml/min (0.12-0.8 m/s). The points at lower flow rates were removed due to insufficient accuracy to make solid conclusions. Nevertheless, a much broader range of flow rates is accessible when using the herringbone structure. For this reason, the latter structure was chosen for the integration into the multi-injection reactor.

6.4.2 Characterization of Heat-Transfer in the Multi-Injection Reactor

The temperature profiles developed within the mixing structures presented in the previous section are a result of the interaction between the heat source, i.e. the exothermic reaction, and the heat losses to the surrounding. As opposed to these mixing structures, the multi-injection reactor has an additional integrated cooling layer to maintain the reaction at a constant level of temperature. To evaluate the heat transfer performance between the cooling layer and the reaction layer, heat exchange experiments were carried out. Thereby, the channels on the reaction layer are fed with ethanol and butanol respectively (via the first injection point) at room temperature, which is heated up by the coolant passed with a temperature of 40 °C / 50 °C. Two types of coolants are used: isopropanol and water with thermal conductivities of 0.138 W/(mK) [37] and 0.638W/(mK) [37] at 45 °C, respectively. As the heat losses by radiation and convection are neglected for the estimation of the heat transfer coefficient, the value obtained for the volumetric heat transfer coefficient is a superposition between the actual heat transfer coefficient and the heat losses to the surroundings. Hence, the real heat transfer coefficient between the reaction and the

cooling layer is always higher than the value obtained from the experiments. A typical profile obtained with ethanol in the reaction channel and water in the cooling channel is presented in Figure 6.15.

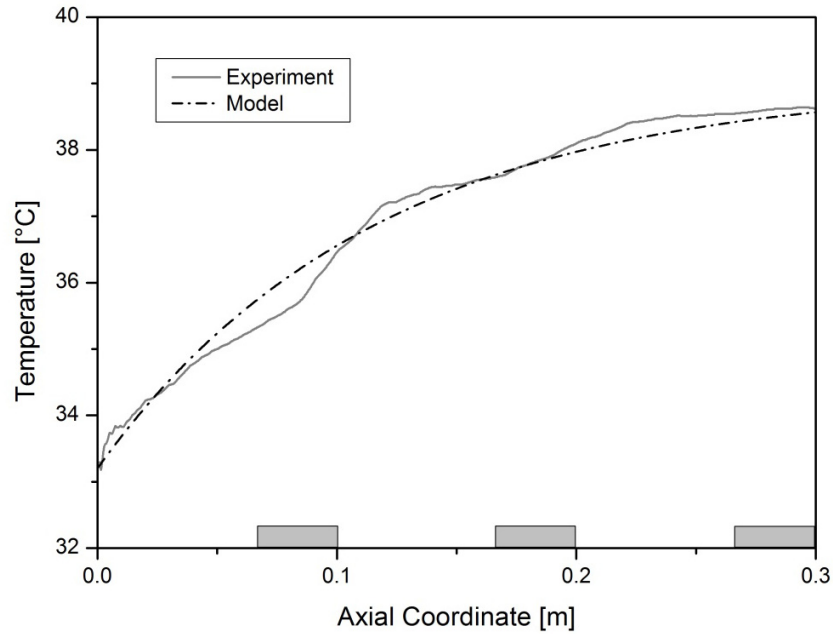


Figure 6.15: Temperature profile measured (experiment) and modeled (model) in the multi-injection reactor using a simple heat transfer model with constant coolant temperature. The gray rectangles indicate the location of the three larger residence time channels. Cooling channel: water at 39 °C and flow rate > 80 ml/min. Reaction channel: ethanol at 10.6 ml/min (0.63 m/s). Modeling: see descriptions in the text.

When looking at the heat balance, the experiment can be described using the following simplified equations:

$$\begin{aligned}
 u \cdot \rho \cdot c_p \cdot \frac{dT}{dz} &= Ua_{global} \cdot (T - T_{Cool}) \\
 \Rightarrow \frac{dT}{dz} &= \frac{Ua_{global}}{\rho \cdot c_p} \cdot \frac{1}{u} \cdot (T - T_{Cool})
 \end{aligned}
 \tag{6.3}$$

Hence, assuming that the volumetric heat transfer coefficient Ua_{global} is identical in the mixing channel ($H \times W = 560 \mu\text{m} \times 500 \mu\text{m}$) and in the residence time channel ($H \times W = 560 \mu\text{m} \times 2000 \mu\text{m}$), one would expect a steeper temperature gradient dT/dz in the residence time channel due to the 4-fold reduced flow velocity. However, the curve obtained in Figure 6.15 shows no clear difference between the larger

residence time channels and the narrow mixing channels. From this observation, it was concluded that the volumetric heat transfer coefficient in the wider channels is about 4 times smaller than in the structured mixing channels. This difference was ascribed to two phenomena:

- 1) The presence of structures leading to an improved convection in radial direction.
- 2) In spite the fact that the heat exchange occurs mostly through the bottom of the reaction channel, due to the short distances, the side walls are not adiabatic. Hence, the specific heat exchange area is 2-fold smaller for the wider channels.

For the modeling, a lumped volumetric heat transfer coefficient was calculated, assuming a uniform flow velocity in empty channels with a cross section of $H \times W = 560 \mu\text{m} \times 500 \mu\text{m}$ all over the reactor. The value obtained for the mixing channels is $Ua_{global} = 1 \cdot 10^7 \text{ W}/(\text{m}^3\text{K})$ corresponding to a characteristic cooling time of 0.2 s. At this place, it has to be pointed out again that the volumetric heat transfer coefficient in the larger channels is 4-fold smaller than Ua_{global} .

Furthermore, it has to be pointed out that the initial temperature in Figure 6.15 differs from room temperature, as heat exchange occurs within a length of 6 mm prior to the area monitored by the infrared camera.

The volumetric heat exchange coefficients obtained under different conditions are summarized in Figure 6.16.

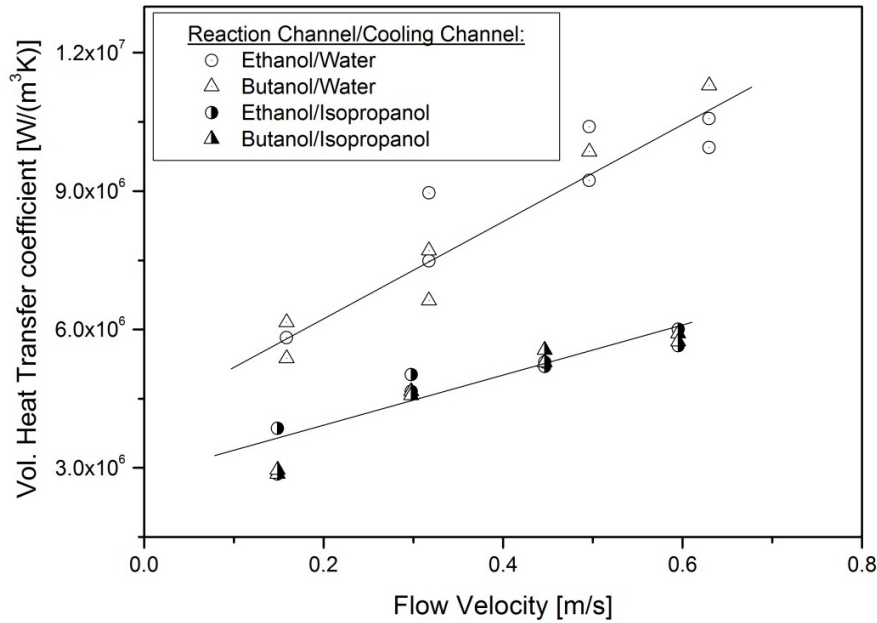


Figure 6.16: Comparison of the heat transfer coefficient estimated by heat exchange experiments with two different heat exchange media, i.e. water ($\lambda_{\text{H}_2\text{O}} = 0.638 \text{ W/(mK)}$) and isopropanol ($\lambda_{\text{OH}} = 0.138 \text{ W/(mK)}$).

Generally, the volumetric heat transfer coefficient is increasing with the flow rate which was varied up to 10.6 ml/min. The increased heat transfer was ascribed to the improved radial mixing with flow rate due to the herringbone structures, as demonstrated in section 6.4.1. While changing the cold flow from ethanol to slightly more viscous butanol had no noticeable impact, the volumetric heat transfer coefficient in the working range (about 0.18 m/s corresponding to 3 ml/min) was improved almost 2-fold by changing from isopropanol to more conductive water as coolant. By comparing the results obtained with isopropanol and with water respectively, one can estimate the relative impact of the heat transfer resistance on the reaction layer and on the cooling layer side respectively. The overall heat transfer resistance between reaction layer and cooling layer is described as follows:

$$\begin{aligned}
 1/Ua_{\text{global}} &= R_{\text{global}} = R_{\text{reaction}} + R_{\text{wall}} + R_{\text{cool}} \\
 &= \frac{1}{C'} + \frac{\delta}{\lambda_{\text{wall}}} \cdot a + \frac{1}{B \cdot \lambda_{\text{fluid}}}
 \end{aligned} \tag{6.4}$$

Thereby, C and B are two parameters describing the thermal resistance located on the reactor and on the cooling side respectively. As with the available experiments the wall resistance cannot be distinguished from the reaction layer side resistance, both resistances are lumped into one constant C :

$$1/Ua_{global} \approx \frac{1}{C} + \frac{1}{B \cdot \lambda_{fluid}} \quad (6.5)$$

Thus, the ratio between the resistance obtained with isopropanol R_{OH} and with water R_{H2O} is:

$$\begin{aligned} \frac{R_{global,OH}}{R_{global,H2O}} &= \frac{\frac{1}{C} + \frac{1}{B \cdot \lambda_{OH}}}{\frac{1}{C} + \frac{1}{B \cdot \lambda_{H2O}}} \\ &= \frac{1 + M / \lambda_{OH}}{1 + M / \lambda_{H2O}} \quad \text{with} \quad M = \frac{C}{B} \end{aligned} \quad (6.6)$$

The ratio of both resistances obtained at a flow rate of 3 ml/min is 1.8 (see Figure 6.16). Solving the first order equation system, a value of $M = 0.18$ is obtained. Hence, the impact of the resistances can be determined as follows:

$$\frac{R_{reaction} + R_{wall}}{R_{cool,OH}} = \frac{\lambda_{OH}}{M} = 0.76 \quad (6.7)$$

$$\frac{R_{reaction} + R_{wall}}{R_{cool,H2O}} = \frac{\lambda_{H2O}}{M} = 3.54 \quad (6.8)$$

Whereas in the case of cooling with isopropanol more than 50 % of the resistance is located on the cooling layer side due to the larger channel and the absence of mixing structures, when exchanging the coolant to water the resistance drops to about 20 % of the total resistance.

For the experiments described in the following sections, isopropanol was always used as a coolant allowing temperatures around 0 °C to be accessed. The coolant was fed with a minimum flow rate of 80 ml/min leading to a maximal temperature difference of 4 °C between inlet and outlet.

6.4.3 Thermal Characterization of the Cyclization of Pseudoionone in the Multi-injection Reactor

The cyclization of pseudoionone was performed in the multi-injection reactor by injecting three equal flows of pseudoionone solution (1.5 M) into the main stream of sulfuric acid solution (7.5 M) keeping the total flow ratio at 1:1. Under adiabatic conditions, a temperature rise of 48 °C would occur. Furthermore, at temperature above 70 °C, the highly exothermic and unwanted polymerization of the products is triggered. Hence, it is crucial to control temperature during this reaction. For the following series of experiments, the coolant (isopropanol) temperature was kept at 48 °C. To extract the temperature profile from the thermal image (Figure 6.17 left), the exact position of the reactor channels had to be identified prior to the experiments. This can be done by injecting pulses of hot fluid, allowing the channels to be distinguished from the rest of the reactor surface. Subsequently, the thermal image of the reactor surface can be transformed into the temperature profile inside the reaction channels (Figure 6.17 right).

By taking the average temperature over the cross section, the 1-dimensional temperature profile was deduced (Figure 6.18). As expected, temperature rises along the three herringbone mixers and decreases in the residence time channels. However, especially for the first mixing structure located in the bottom of the picture, a wavelike increase of temperature is observed. The explanation for this behavior can be found in the thermal image: the three temperature minima are reached at the positions close to the cold reactor edge (bottom of the picture), whereas the maxima are reached when the flow passes through the regions located close to the center of the plate. In fact, the cooling is more effective on the reactor edge due to increased heat losses compared to the reactor center where slight thermal interactions between the channels cannot be neglected. Furthermore, the hot spot after each injection point is reached just in the beginning of the residence time channel, which is due to the about 4-fold reduced volumetric heat transfer coefficient (see section 6.4.2) in combination with ongoing mixing/reaction.

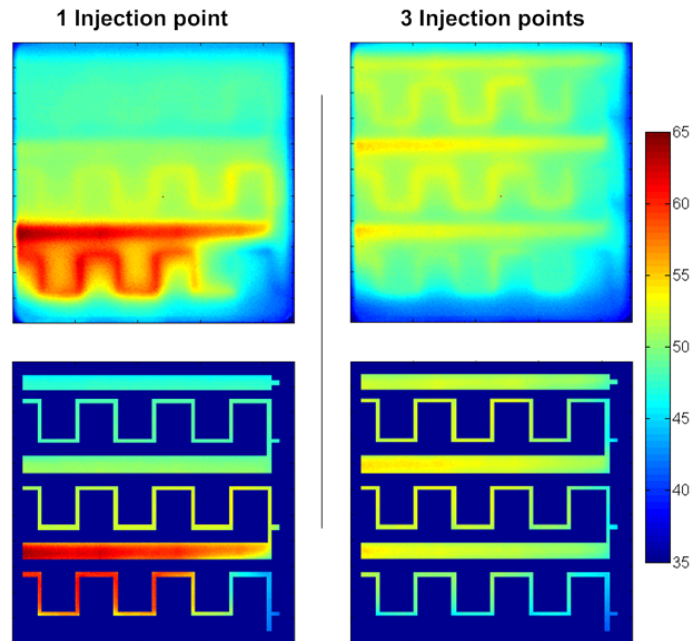


Figure 6.17: Temperature profile during the cyclization of pseudoionone in the multi-injection MSR with one injection point (left) and with three injection points (right). In the bottom pictures, the top pictures are covered by a mask highlighting the reaction channels. The first injection point is located in the bottom of the picture. Initial concentration of the two inlet solution: $c_{\text{H}_2\text{SO}_4} = 7.5 \text{ M}$ and $c_{\text{PI}} = 1.5 \text{ M}$; Total flow rate: 3 ml/min (0.18 m/s); $\Delta T_{ad} = 48 \text{ }^\circ\text{C}$; $T_c = 48 \text{ }^\circ\text{C}$.

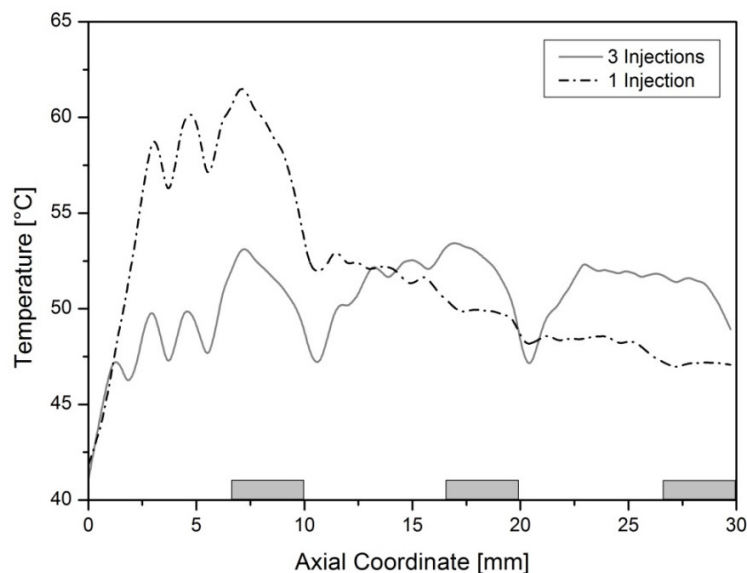


Figure 6.18: Axial temperature profile during the cyclization of pseudoionone in the multi-injection reactor with one injection point and with three injection points. Conditions identical to Figure 6.17. The gray rectangles indicate the location of the three larger residence time channels.

Using the multi-injection reactor, the temperature rise can be kept below 6 °C compared to the cooling temperature, which is the equivalent of an 8-fold reduced hot spot temperature compared to the adiabatic temperature rise. The low hot spot temperature is mainly attained due to three distinct effects:

- 1) The high heat transfer coefficient attained in microchannels
- 2) The gradual mixing in the herringbone structure leads to a decelerated release of heat, thus, reducing the overall transformation rate.
- 3) The injection of pseudoionone at three distinct injection points.

To analyze the impact of the latter phenomenon, in Figure 6.18 the temperature profile obtained with 3 injection points was compared to the one obtained by injecting the whole flow of pseudoionone via the first injection point. In the latter case, the temperature rises up to a maximum value of 62 °C, corresponding to a temperature rise of 14 °C with respect to the cooling channel. Hence, the increase in temperature is more than 2-fold higher than with 3 injection points. The maximum temperatures found at different flow rates within the two configurations (1 and 3 injection points) are given in Figure 6.19.

As expected, an enhanced temperature control all over the flow rate range is observed using three injection points. The slight increase in temperature with the flow rate is mainly due to two reasons:

- 1) The overall transformation rate is increased with flow rate due to the reduced mixing time
- 2) The evacuation of heat between two injection points is less effective due to the reduced residence time.

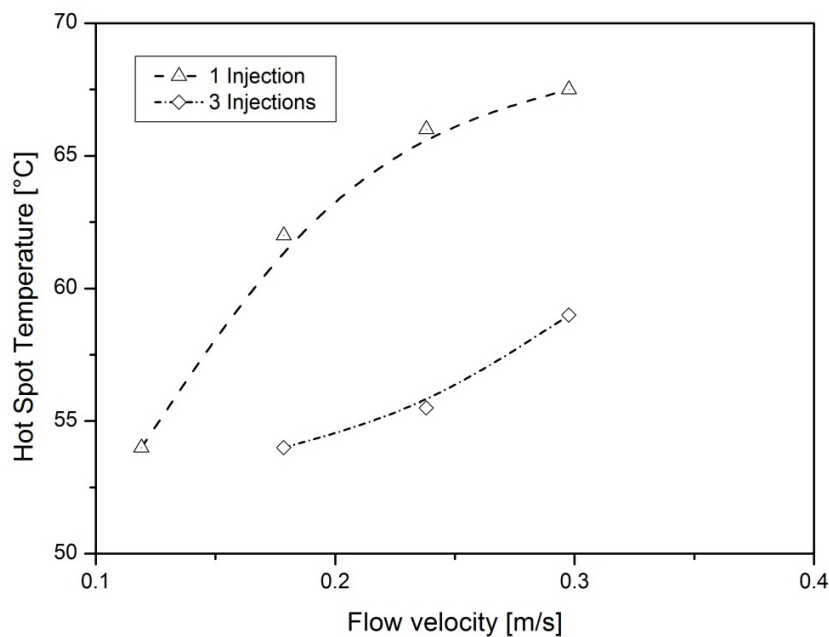


Figure 6.19: Maximum temperature while carrying out cyclization of pseudoionone in the multi-injection reactor with one injection point and with three injection points. Initial concentration of the two inlet solutions:

$$c_{\text{H}_2\text{SO}_4} = 7.5 \text{ M and } c_{\text{PI}} = 1.5 \text{ M; } \Delta T_{\text{ad}} = 48 \text{ }^\circ\text{C; } T_{\text{cool}} = 48 \text{ }^\circ\text{C.}$$

6.4.4 Product Distribution in the Multi-injection Reactor

The distribution of the products at the reactor outlet was characterized by gas chromatography with a precision of $\pm 5\%$. As not all of the molecules could be detected, a mass balance analysis was performed after each experiment. Thereby, a deficit of the mass balance indicates either that the molecules are in an intermediate form not monitored by the gas chromatograph or have entered the unwanted consecutive polymerization. To distinguish both phenomena, the yield of the intermediate isomers 6,10-dimethylundeca-3,5-dione-10-hydroxy-2-one is used as indicator for the occurrence of the first type of mass balance deficit.

In the following, the effect of flow rate and temperature on product distribution is analyzed at the reference concentrations of $c_{\text{PI}} = 1.25 \text{ M}$ and $c_{\text{H}_2\text{SO}_4} = 7.5 \text{ M}$ which is in the working range of the industrial

state of the art batch process. Subsequently, the possibility to work at increased reactant concentrations i.e. at reduced amounts of solvent in the multi-injection reactor is investigated.

6.4.4.1 Yield as Function of Flow Rate

The effect of the flow rate on mixing quality was already extensively discussed in section 6.4.1 and it was concluded that with a flow rate above 2 ml/min (0.12 m/s), complete mixing can be assured. However, it was difficult to make a clear statement regarding mixing quality at lower flow rates due to the increasing impact of heat losses. In Figure 6.20, the product composition at the reactor outlet was determined at different flow rates for a fixed working temperature of 51 °C.

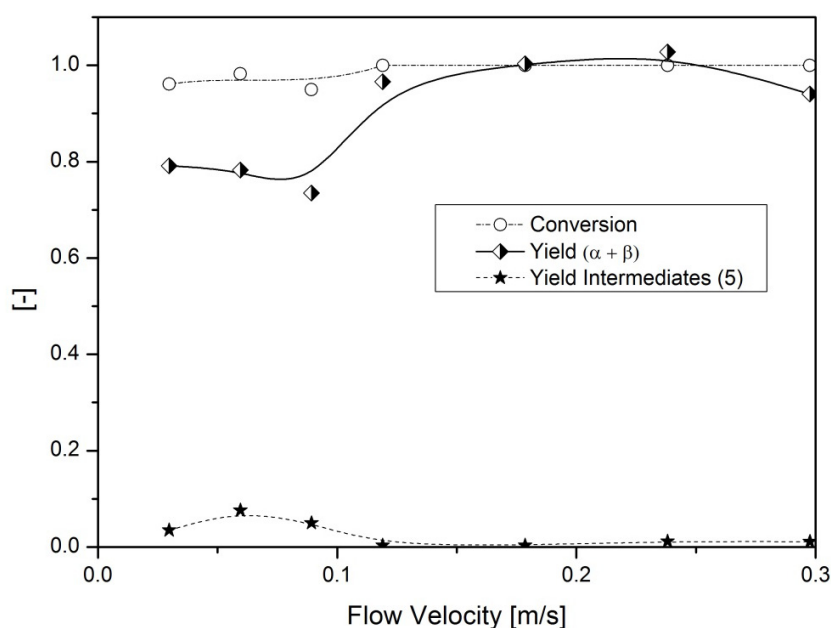


Figure 6.20: Yields and conversion at the outlet of the multi-injection reactor during cyclization of pseudoionone as function of flow rate. Temperature: 51 °C, initial concentrations of the respective solutions: $c_{PI} = 1.25$ M; $c_{H_2SO_4} = 7.5$ M.

Conversion all over the velocity range is above 0.95. Thereby, the lowest values are monitored at the lower range of flow velocities, with a constant conversion of almost 1 at flow velocities higher than 0.12 m/s. As in an ideal kinetically controlled system the conversion increases with the residence time, one can conclude that mixing plays an essential role in this range of flow rates. At a total flow rate of less

than 2 ml/min (0.12 m/s) the inefficiency of mixing has an impact on the product composition, confirming the results obtained in section 6.4.1.1. The yield of α -ionone and β -ionone is lower compared to the higher flow rates where a yield of $Y_{\alpha + \beta} > 98\%$ is achieved. The increased concentration of intermediates indicates that the loss of yield is due to the presence of intermediate molecules rather than due to the loss to the unwanted consecutive reactions. The increased segregation at lower flow rates leads to areas of low concentrations of acid. Kashid *et al.* [241] demonstrated that below a ratio of acid:pseudoionone of 2.4:1, the reaction cannot be completed.

To assure good mixing quality, experiments are carried out at a flow rate of 3 ml/min (0.18 m/s).

6.4.4.2 Yield as Function of Temperature

In the first series of experiments, the flow rate was kept constant at a total of 3 ml/min corresponding to a residence time of $\tau_1 \approx 4.1$ s for the molecules entering via the first injection point, of $\tau_2 \approx 2.5$ s for the molecules entering via the second injection point and $\tau_3 \approx 1.1$ s for the molecules entering via the third injection point. Simultaneously, the temperature in the cooling unit was varied between 0 °C and 80 °C with isopropanol as coolant at a flow rate > 80 ml/min. The coolant temperature could be kept constant with a maximum difference between inlet and outlet of 4 °C at 80 °C. The yields obtained are depicted in Figure 6.21.

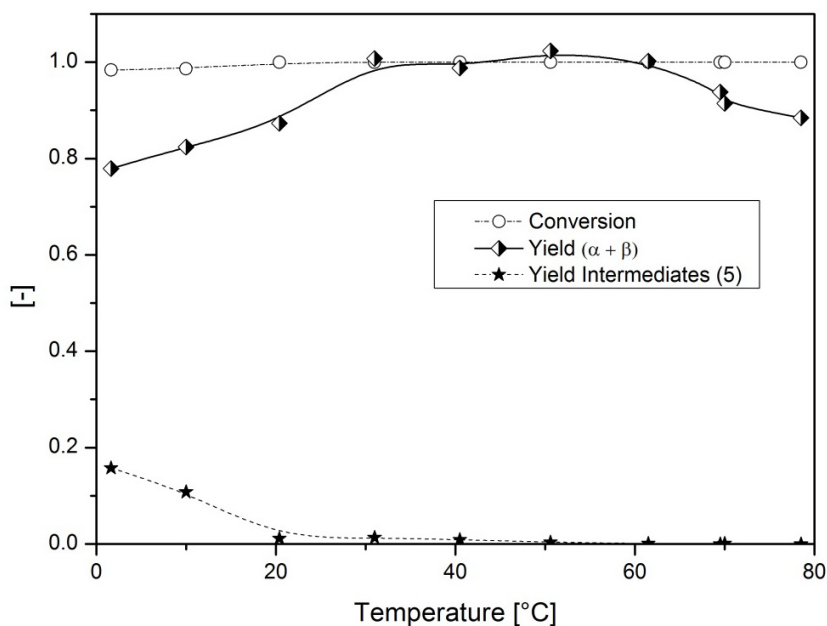


Figure 6.21: Yield and conversion at the outlet of the multi-injection reactor during cyclization of pseudoionone as function of coolant temperature. Thereby α and β denote α -ionone and β -ionone, and intermediates (5) are two isomers of 6,10-dimethylundeca-3,5-dione-10-hydroxy-2-one. Total flow rate: 3 ml/min (0.18 m/s), initial concentrations of the respective solutions: $c_{PI} = 1.25$ M; $c_{H_2SO_4} = 7.5$ M.

The conversion of the reactants is close to 1 all over the temperature range, indicating almost complete mixing of the reactants. Thereby, slightly lower conversions (0.98) were observed at the lower temperatures, which is either a kinetic effect or linked to a decreased mixing quality at increased viscosity. It results in an increased amount of intermediates at low temperature and causes a slight deficit of mass balance. In turn, the yield of the sum of α -ionone and β -ionone is at 0.8 at temperatures around 0 °C and increases until a plateau of $Y_{\alpha+\beta} > 98\%$ reached at 30 °C. The plateau is constant in the range of 30 °C to 60 °C, which constitutes an optimal operation window. The on-set of the unwanted consecutive polymerization reaction is observed at temperatures above 70 °C. The short residence time of this microstructured reactor allows working at much higher temperatures compared to a classical batch system, where the residence time in the order of 1 h causes a loss of $Y_{\alpha+\beta}$ at temperatures above 10 °C [241].

When looking at the product distribution between α -ionone and β -ionone in Figure 6.22, with higher temperatures the ratio of $\beta/(\alpha + \beta)$ increases with temperature as the kinetics of the isomerization reaction is accelerated.

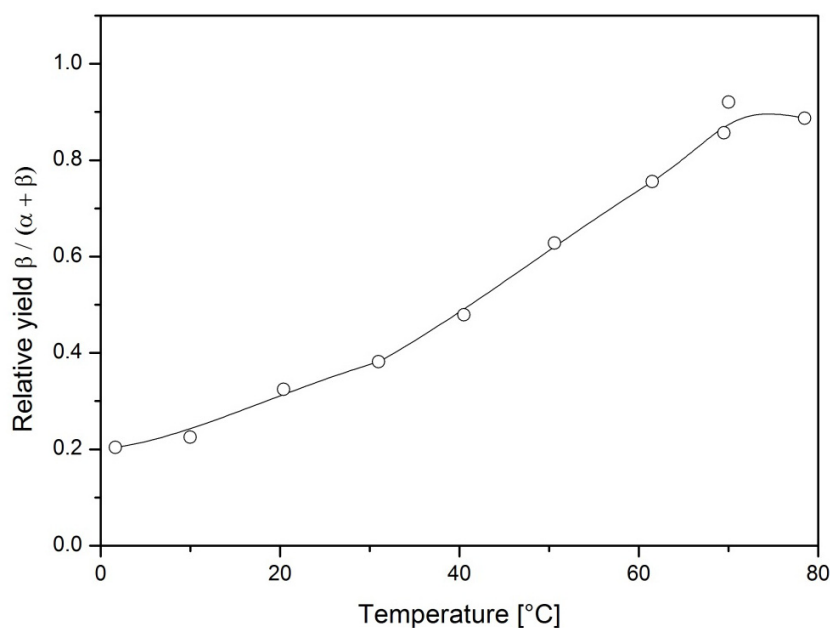


Figure 6.22: Product repartition of α -ionone and β -ionone with respect to cooling temperature. Total flow rate: 3ml/min, initial concentrations of the respective solutions: $c_{PI} = 1.25$ M; $c_{H_2SO_4} = 7.5$ M.

Thereby, 80 % α -ionone is obtained at temperatures around 0 °C and about 80 % of β -ionone at 65 °C. As for the target process, the yield of β -ionone has to be improved, high temperatures are favorable. Thereby, working under almost isothermal conditions as shown in the previous section allows the optimum point to be approached while preventing the induction of unwanted consecutive reactions. Hence, by carrying out the cyclization at 50 °C, one can estimate the additional residence time needed in an isothermal loop for a conversion of 0.99 from pseudoionone to β -ionone to be in the order of ≈ 2 s [240, 241]. Compared to the semi-batch process with a residence time in the order of hours, a space-time yield improvement of a factor more than $\tau_{\text{batch}}/\tau_{\text{Multi-Injection}} \approx 500$ is achieved due to the improved temperature control.

6.4.4.3 Reducing the Amount of Solvent

As final step, the inlet concentrations were raised with the aim of reducing the required amount of the solvent 1-nitropropane and of the excess reactant sulfuric acid. This was done in two consecutive steps:

- 1) The concentration of the inlet solution of pseudoionone (PI) was approximately doubled from 1.25 M to 2.75 M while raising the concentration of sulfuric acid from 7.5 M to 12 M. Thereby, the ratio of acid to pseudoionone was diminished from 6 to 4.4.
- 2) In a next step, the acid concentration was further reduced to 7.5 M yielding a ratio of acid:pseudoionone of 2.7.

While increasing the inlet concentrations, on the one hand, the adiabatic temperature rise increases, which renders temperature control a key issue. This was overcome by the multi-injection reactor (see Figure 6.24), where the temperature rise was limited to below 10 °C. On the other hand, the increased viscosity of the solution limits the throughput with the setup used, as pressure drop above 1 bar could not be realized with syringe pumps. The working conditions and the product distribution achieved are summarized in Table 6.2 and in Figure 6.23.

When comparing the product quality of Set 1 to the Reference, an almost identical product distribution is observed with a slightly lower yield of β -ionone. The appearance of a non-negligible amount of intermediates can be linked to the reduced flow rate compared to the reference, and could be eliminated by increasing the flow rate with appropriate pumps. While changing from the reference to set 1, the required amount of solvent is reduced from 600 g / (liter of solution) to 250 g / (liter of solution).

A further reduction of the ratio sulfuric acid:pseudoionone as shown for Set 2 considerably reduces the yield of $Y_{\alpha+\beta}$ while an important amount of intermediates is found. This confirms the results published by Kashid *et al.* [240, 241], who showed that a ratio in the order of 5 is required for the reaction to complete.

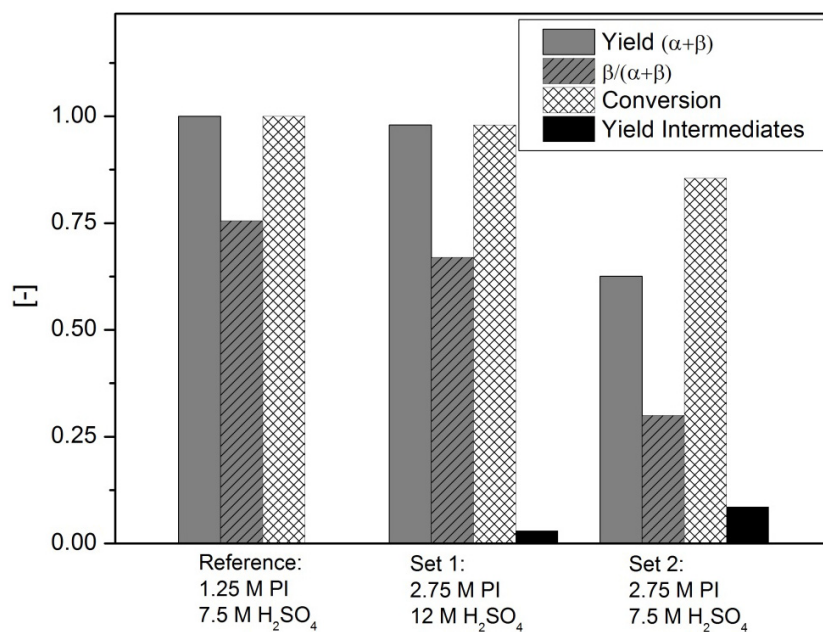


Figure 6.23: Yields and conversion obtained at the outlet of the multi-injection reactor during cyclization of pseudoionone. The respective experimental conditions are given in Table 6.2.

Table 6.2: Conditions used for comparison of increased concentration in Figure 6.23.

	Flow velocity [m/s]	Temperature [°C]	ΔT_{ad} [°C]
Reference	0.18	60 °C	37 °C
Set 1	0.12	27 °C	81 °C
Set 2	0.18	27 °C	85 °C

In the temperature profile obtained with the concentration Set 2 (Figure 6.24), a hot spot temperature of 38 °C corresponding to a temperature rise of 10 °C, i.e. 13 % of the adiabatic temperature rise, is found. Thus, even at high concentration this reaction can be carried out in a controlled manner using the multi-injection reactor.

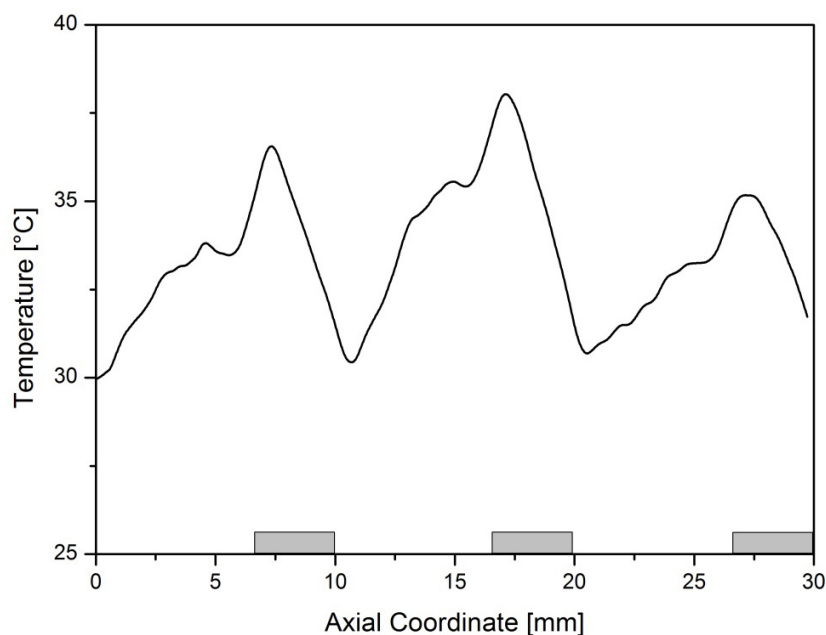


Figure 6.24: Axial temperature profile while carrying out cyclization of pseudoionone in the multi-injection reactor with three injection points. The reaction conditions are summarized in Set 2 in Table 6.2.

6.5 Conclusions

Within this study, it was successfully demonstrated how quantitative thermal mapping can be used as a tool to characterize and develop efficient microstructured reactors. By measuring the temperature profiles under quasi-adiabatic conditions and deducing the mixing profile inside a tangential and a herringbone mixer, it was shown that the herringbone mixing structure provides efficient mixing in a large range within the laminar flow regime ($Re = 20 \dots 130$).

The incorporation of the herringbone structure in a multi-injection microreactor enabled carrying out the highly exothermic and quasi-instantaneous model reaction under continuous flow while reducing the hot spot temperature 8-fold compared to conventional large scale batch reactors, where a temperature near adiabatic temperature rise would be obtained. The improved temperature control was ascribed to three aspects of the reactor:

6 Development and Experimental Investigation of a Multi-injection Reactor

- 1) The high heat transfer coefficient attained in the microchannels ($Ua \approx 4 \cdot 10^6 \text{ W}/(\text{m}^3\text{K})$)
- 2) The gradual mixing in the herringbone structure leads to a decelerated release of heat, thus, reducing the overall transformation rate.
- 3) The injection of pseudoionone at three distinct injection points provided a 2-fold reduced hot spot temperature compared to an operation mode with one single injection point.

Within a temperature range of 30 °C to 60 °C, a combined yield of α -ionone and β -ionone of $Y_{\alpha+\beta} > 98\%$ was achieved with a residence time of 4.1 s. Using this type of setup, a more than 500-fold improved space-time yield was achieved compared to the conventional semi-batch setup with typical processing times in the order of hours. Furthermore, by doubling the concentrations, the solvent quantity required during the reaction was reduced by a factor of 2.

Finally, during this study, low temperature co-fired ceramics was shown to be a very flexible technology permitting an integrated design of microstructured reactors which exhibit high chemical resistance to harsh acidic and basic environments.

6.6 Notations

a	Specific surface area, [1/m]
B	Fit variable, [1/m ²]
C	Fit variable, [W/(m ³ K)]
c	Concentration, [mol/m ³]
c_p	Heat capacity, [J/(kg K)]
h	Height of the void channel, [m]
H_r	Reaction enthalpy, [J/mol]
L	Channel length, [m]
M	Fit variable = C/B , [W/(mK)]
q	Groove wave factor, [-]
R	Volumetric Heat Transfer resistance, [(m ³ K)/W]
t_{cool}	Characteristic cooling time $\rho \cdot c_p / Ua_{cool}$, [s]
t_{loss}	Characteristic heat loss time $\rho \cdot c_p / Ua_{loss}$, [s]
T	Temperature, [K]
u	Flow velocity, [m/s]
Ua_{global}	Global volumetric heat transfer coefficient, [W/(m ² K)]
Ua_{losses}	Global heat losses to surrounding coefficient, [W/(m ² K)]
W	Channel width, [m]
X	Conversion, [-]
Y	Yield, [-]
z	Axial coordinate, [-]
z'	Axial coordinate, [-]

Greek

α	Factor describing the ratio of herringbone height to void channel height, [-]
α	Designates the α -ionone molecule

β	Designates the β -ionone molecule
$\alpha(H^+)$	Designates the α -ionone molecule in its protonated state
$\beta(H^+)$	Designates the β -ionone molecule in its protonated state
λ	Thermal conductivity, [W/(mK)]
Δ	Symbol for difference
ε	Emissivity, [-]
ρ	Mean density, [kg/m ³]
τ	Residence time, [s]

Dimensionless numbers

DaI	Damköhler number $\tau / t_{r,eff}$
Re	Reynolds number $u \cdot d_h / \nu$, [-]

Subscript

0	Initial condition
ad	Adiabatic
cool	In the cooling layer
eff	Effective
loss	Related to heat losses
LTCC	Low temperature co-fired ceramics
PI	Pseudoionone
Wall	Wall
W-Amb	Wall-Ambient

Chapter 7

GENERAL CONCLUSIONS

Compared to the conclusions made in every single chapter, this chapter summarizes the outcome in a less detailed manner, while making the links between the individual conclusions of each chapter.

Process intensification of rapid and highly exothermic reactions with microstructured reactors (characteristic dimensions in the range of 100-1000 μm) has been first analyzed numerically. Thereby, special attention was put to maintain temperature within a narrow window, i.e. isothermal conditions in the ideal case. One of the main simplifications done during the modeling was the assumption of a reaction controlled by its very fast or even quasi-instantaneous kinetics, neglecting the influence of mixing. The outcome of the three concepts of hot spot reduction is summarized in the following:

- 1) Increasing thermal conductivity of the microchannel walls to spread the heat formed at the hot spot along the whole channel: Two distinct scenarios were observed. a) If the inlet temperature is equal to the cooling temperature, backmixing of heat leads to an increase of inlet temperature, which, in turn, results in an earlier and more pronounced run-away. b) If the inlet temperature is lower than the cooling temperature, at high thermal conductivity the heat from the hot spot is used to heat up the inlet stream, leading to a reduced hot spot temperature. Hence, this concept works only with the presence of a heat sink in the reactor, such as a cold inlet stream or endothermic reactions.

- 2) The multi-injection reactor, i.e. stepwise injection of one of the reactants along the main channel: Thereby, the heat production is spread over the reactor length, leading to a minimized maximum temperature. In the model, the hot spot temperature diminished with an increasing amount of injection points. Furthermore, instead of dosing equal amounts of solution at each injection point, it was shown that increasing the amount from one injection points to the next can lead to a further reduction of temperature of 15 %.
- 3) The micro-annular reactor, i.e. continuous injection of one of the reactants along the main channel of the reactor with a concentric shape. It is the analog to a multi-injection reactor with a quasi-infinite amount of injection points. In the model, for quasi-instantaneous reaction a zero order behavior was observed as dosing is the rate limiting step. As a consequence, an almost isothermal temperature profile is obtained if effective characteristic reaction time is one order of magnitude smaller than residence time.

The decisive difference between model and reality lies in the mixing of the reactants. Especially for quasi-instantaneous reactions, despite the small sizes of microstructured reactors, they operate in a regime strongly influenced or even controlled by mixing. It was demonstrated that mixing in circular channels without structured walls is not fast enough, leading to incomplete reactions at the outlet of the reactor. Only by designing efficient structures, such as the herringbone and the tangential mixer, one can assure the reaction to occur within the reactor, and obtain the desired product quality. Thereby, one has to operate at the minimum Reynolds number required for the structure to mix efficiently. The minimal value for sufficient mixing in the tangential and the herringbone mixer found in this study are:

$$\begin{array}{ll} \text{Tangential:} & 70 \leq \text{Re} \\ \text{Herringbone:} & 20 \leq \text{Re} \end{array} \quad (6.9)$$

Despite the fact that the micro-annular reactor showed the best results in the simulation, the integration of such efficiently mixing structures in a perfectly concentric reactor is technically very challenging. For this

reason, the multi-injection reactor was chosen as the device for process intensification of quasi-instantaneous reactions.

A calibration method for infrared thermography was developed which allows monitoring of temperature inside microchannels with a precision of ± 1 °C. The main requirement of the method for the reactor design is a thin top cover (< 500 μm). Compared to thermocouples, a much higher resolution of 100 points/ mm^2 is achieved while preventing artifacts due to the non-intrusive way of measurement. As validation of the method, it was shown that temperature profiles can be determined in non-reactive systems to obtain heat transfer coefficients for example, and in reactive systems to measure effective reaction kinetics.

In the last part of the study, an efficient multi-injection reactor was developed using low temperature co-fired ceramic technology (LTCC) with its versatile advantages such as inertness to harsh reaction conditions and straightforward creation of 3-d structures. While carrying out the model reaction, i.e. cyclization of pseudoionone to α -ionone and β -ionone, an 8-fold reduction of hot spot temperature compared to the adiabatic temperature rise was demonstrated by quantitative infrared thermal mapping. Furthermore, this technique allowed the decreased product quality at low flow rates to be attributed to low mixing quality. When working at a sufficient velocity of 0.18 m/s corresponding to a throughput of about 20 g of pseudoionone per hour, within a temperature range of 30 °C to 60 °C, a combined yield of α -ionone and β -ionone of $Y_{\alpha + \beta} > 98\%$ was achieved with a residence time of 4.1 s. Thereby, the highly exothermic and unwanted consecutive polymerization was efficiently suppressed due to the excellent temperature control and the short residence time. Using this type of setup, a more than 500-fold improved space-time yield was achieved compared to the conventional semi-batch setup with typical processing times in the order of hours. Furthermore, the solvent quantity required during the reaction was reduced by a factor of 2.

7 General Conclusions

As mentioned in the beginning, by definition quasi-instantaneous reactions are operated in a regime where the overall transformation rate corresponds to the mixing rate. Thus, the application of the multi-injection reactor developed in the present thesis is not limited to the cyclization of pseudoionone, but, it can be used for any quasi-instantaneous reaction such as acid-base reactions or organo-metallic reactions.

REFERENCES

- [1] Report of the World Commission on Environment and Development: Our Common Future; Transmitted to the General Assembly as an Annex to document A/42/427 - Development and International Co-operation: Environment; Our Common Future, Chapter 2: Towards Sustainable Development; <http://www.un-documents.net/ocf-02.htm>; Accessed: 2013
- [2] R. Kemp, J. Schot, R. Hoogma, Regime shifts to sustainability through processes of niche formation: The approach of strategic niche management, *Technology Analysis and Strategic Management*, 10 (1998) 175-195.
- [3] J. Ranke, S. Stolte, R. Störmann, J. Arning, B. Jastorff, Design of Sustainable Chemical Products The Example of Ionic Liquids, *Chemical Reviews*, 107 (2007) 2183-2206.
- [4] S. Baumgärtner, M. Faber, J. Schiller, Joint Production and Responsibility in Ecological Economics, Edward Elgar Publishing Ltd, 2006.
- [5] R.A. Sheldon, Atom efficiency and catalysis in organic synthesis, *Pure and Applied Chemistry*, 72 (2000) 1233-1246.
- [6] R.A. Sheldon, The E Factor: fifteen years on, *Green Chem*, 9 (2007) 1273-1283.
- [7] R.A. Sheldon, Organic synthesis. Past, present and future, *Chemistry and Industry (London)*, (1992) 903-906.
- [8] D.M. Roberge, M. Gottsponer, M. Eyholzer, N. Kockmann, Industrial design, scale-up, and use of microreactors, *Teknoscienze, Milano, ITALIE*, 2009.
- [9] M. Braungart, W. McDonough, *Cradle to Cradle: Beyond Sustainability*, 2002.
- [10] <http://www.wbcsd.org/vision2050.aspx>; Accessed: 2013
- [11] V. Hessel, Novel Process Windows – Gate to Maximizing Process Intensification via Flow Chemistry, *Chem. Eng. Technol.*, 32 (2009) 1655-1681.
- [12] A. Stankiewicz, J.A. Moulijn, Process Intensification, *Ind. Eng. Chem. Res.*, 41 (2002) 1920-1924.
- [13] A.I. Stankiewicz, J.A. Moulijn, Process intensification: Transforming chemical engineering (vol 96, pg 22, 2000), *Chem. Eng. Prog.*, 96 (2000) 8-8.
- [14] K. Jähnisch, V. Hessel, H. Löwe, M. Baerns, Chemistry in Microstructured Reactors, *Angew. Chem., Int. Ed.*, 43 (2004) 406-446.
- [15] N. Kockmann, M. Gottsponer, B. Zimmermann, D.M. Roberge, Enabling continuous-flow chemistry in microstructured devices for pharmaceutical and fine-chemical production, *Chem. Eur. J.*, 14 (2008) 7470-7477.
- [16] L. Kiwi-Minsker, A. Renken, Microstructured reactors for catalytic reactions, *Catalysis Today*, 110 (2005) 2-14.
- [17] J. Haber, M.N. Kashid, A. Renken, L. Kiwi-Minsker, Heat management in single and multi-injection microstructured reactors: Scaling effects, stability analysis, and role of mixing, *Ind. Eng. Chem. Res.*, 51 (2012) 1474-1489.
- [18] W. Ehrfeld, Hessel V., Löwe H., *Microreactors: New Technology for Modern Chemistry*, Wiley-VCH Verlag GmbH, Weinheim, 2000.
- [19] P. Watts, C. Wiles, Recent advances in synthetic micro reaction technology, *Chem Commun*, 0 (2007) 443-467.

References

- [20] V. Hessel, T. Noël, Micro Process Technology, 1. Introduction, in: Ullmann's Encyclopedia of Industrial Chemistry, Wiley-VCH Verlag GmbH & Co. KGaA, 2000.
- [21] K. Schubert, W. Bier, G. Linder, D. Seidel, Herstellung und Test von kompakten Mikrowärmeüberträgern, *Chemie Ingenieur Technik*, 61 (1989) 172-173.
- [22] IMM website, http://www.imm-mainz.de/ueber_uns.html; Accessed: 2013
- [23] P.S. Dittrich, A. Manz, Lab-on-a-chip: microfluidics in drug discovery, *Nat Rev Drug Discov*, 5 (2006) 210-218.
- [24] P. Yager, T. Edwards, E. Fu, K. Helton, K. Nelson, M.R. Tam, B.H. Weigl, Microfluidic diagnostic technologies for global public health, *Nature*, 442 (2006) 412-418.
- [25] M. Brivio, W. Verboom, D.N. Reinhoudt, Miniaturized continuous flow reaction vessels: influence on chemical reactions, *Lab Chip*, 6 (2006) 329-344.
- [26] W. Ehrfeld(ed.), *Microreaction Technology - Proc. of the 1st International Conference on Microreaction Technology, IMRET1*, Springer-Verlag, Berlin, 1997.
- [27] I. Dencic, V. Hessel, M.H.J.M. de Croon, J. Meuldijk, C.W.J. van der Doelen, K. Koch, Recent Changes in Patenting Behavior in Microprocess Technology and its Possible Use for Gas-Liquid Reactions and the Oxidation of Glucose, *Chemsuschem*, 5 (2012) 232-245.
- [28] Scopus, <http://www.scopus.com/home.url>; Accessed: 2013
- [29] M.M. Mentele, J. Cunningham, K. Koehler, J. Volckens, C.S. Henry, Microfluidic Paper-Based Analytical Device for Particulate Metals, *Analytical Chemistry*, 84 (2012) 4474-4480.
- [30] O. Görke, P. Pfeifer, K. Schubert, Kinetic study of ethanol reforming in a microreactor, *Applied Catalysis A: General*, 360 (2009) 232-241.
- [31] Y. Voloshin, R. Halder, A. Lawal, Kinetics of hydrogen peroxide synthesis by direct combination of H₂ and O₂ in a microreactor, *Catalysis Today*, 125 (2007) 40-47.
- [32] A. Renken, V. Hessel, P. Löb, R. Miszczuk, M. Uerdingen, L. Kiwi-Minsker, Ionic liquid synthesis in a microstructured reactor for process intensification, *Chem. Eng. Process.*, 46 (2007) 840-845.
- [33] I.V. Gürsel, Q. Wang, T. Noël, V. Hessel, Process-Design Intensification - Direct synthesis of adipic acid in flow, *Chemical Engineering Transactions*, 29 (2012) 565-570.
- [34] A.-L. Dessimoz, C. Berguerand, A. Renken, L. Kiwi-Minsker, Kinetic and thermodynamic study of the aqueous Kolbe-Schmitt synthesis of beta-resorcylic acid, *Chem. Eng. J.*, 200-202 (2012) 738-747.
- [35] D. Kralisch, I. Streckmann, D. Ott, U. Krtschil, E. Santacesaria, M. Di Serio, V. Russo, L. De Carlo, W. Linhart, E. Christian, B. Cortese, M.H.J.M. de Croon, V. Hessel, Transfer of the Epoxidation of Soybean Oil from Batch to Flow Chemistry Guided by Cost and Environmental Issues, *Chemsuschem*, 5 (2012) 300-311.
- [36] S. Pissavini, E. Kakes, S. Walton, P. Watts, A. Weiler, F. Pavlou, Microreactor technology: Is the industry ready for it yet?, *Pharmaceutical Technology Europe*, 21 (2009) 22-32.
- [37] Verein Deutscher Ingenieure, *VDI-Wärmeatlas*, VDI-Verlag GmbH, Düsseldorf 1984.
- [38] V. Hessel, H. Lowe, F. Schonfeld, Micromixers - a review on passive and active mixing principles, *Chem Eng Sci*, 60 (2005) 2479-2501.
- [39] M.N. Kashid, A. Renken, L. Kiwi-Minsker, Gas-liquid and liquid-liquid mass transfer in microstructured reactors, *Chem Eng Sci*, 66 (2011) 3876-3897.
- [40] M.N. Kashid, W. Kowaliński, A. Renken, J. Baldyga, L. Kiwi-Minsker, Analytical method to predict two-phase flow pattern in horizontal micro-capillaries, *Chem Eng Sci*, 74 (2012) 219-232.
- [41] M.N. Kashid, D.W. Agar, Hydrodynamics of liquid-liquid slug flow capillary microreactor: Flow regimes, slug size and pressure drop, *Chem. Eng. J.*, 131 (2007) 1-13.
- [42] S. Hardt, *Micromixers - Modeling and Simulation*, in: Ullmann's Encyclopedia of Industrial Chemistry, Wiley-VCH Verlag GmbH & Co. KGaA, 2000.

- [43] H. Krummradt, U. Koop, J. Stoldt, Experiences with the use of microreactors in organic synthesis, in: W. Ehrfeld (Ed.) *Microreaction Technology: Industrial Prospects*, Springer Berlin Heidelberg, 2000, pp. 181-186.
- [44] N. Kockmann, Scale-up-fähiges Equipment für die Prozessentwicklung
Scalable Equipment for Process Development, *Chemie Ingenieur Technik*, 84 (2012) 646-659.
- [45] G. Vesper, Experimental and theoretical investigation of H₂ oxidation in a high-temperature catalytic microreactor, *Chem Eng Sci*, 56 (2001) 1265-1273.
- [46] V. Hessel, B. Cortese, M.H.J.M. de Croon, Novel process windows – Concept, proposition and evaluation methodology, and intensified superheated processing, *Chem Eng Sci*, 66 (2011) 1426-1448.
- [47] C. Amador, A. Gavriilidis, P. Angeli, Flow distribution in different microreactor scale-out geometries and the effect of manufacturing tolerances and channel blockage, *Chem. Eng. J.*, 101 (2004) 379-390.
- [48] M.N. Kashid, A. Gupta, A. Renken, L. Kiwi-Minsker, Numbering-up and mass transfer studies of liquid–liquid two-phase microstructured reactors, *Chem. Eng. J.*, 158 (2010) 233-240.
- [49] R. Schenk, V. Hessel, C. Hofmann, J. Kiss, H. Löwe, A. Ziogas, Numbering-up of micro devices: a first liquid-flow splitting unit, *Chem. Eng. J.*, 101 (2004) 421-429.
- [50] O. Tonomura, T. Tominari, M. Kano, S. Hasebe, Operation policy for micro chemical plants with external numbering-up structure, *Chem. Eng. J.*, 135, Supplement 1 (2008) S131-S137.
- [51] A. Yamamoto, S. Mori, M. Suzuki, Scale-up or numbering-up of a micro plasma reactor for the carbon dioxide decomposition, *Thin Solid Films*, 515 (2007) 4296-4300.
- [52] R. Schenk, V. Hessel, C. Hofmann, H. Löwe, F. Schönfeld, Novel Liquid-Flow Splitting Unit Specifically Made for Numbering-Up of Liquid/Liquid Chemical Microprocessing, *Chem. Eng. Technol.*, 26 (2003) 1271-1280.
- [53] M. Matlosz, J.-M. Commenge, From Process Miniaturization to Structured Multiscale Design: The Innovative, High-Performance Chemical Reactors of Tomorrow, *CHIMIA International Journal for Chemistry*, 56 (2002) 654-656.
- [54] T.R. Dietrich, *Microchemical Engineering in Practice*, in, John Wiley & Sons, Inc., New Jersey, 2009.
- [55] N. Kockmann, M. Gottsponer, D.M. Roberge, Scale-up concept of single-channel microreactors from process development to industrial production, *Chem. Eng. J.*, 167 (2011) 718-726.
- [56] N. Viswanadham, The past, present, and future of supply-chain automation, *Robotics & Automation Magazine*, IEEE, 9 (2002) 48-56.
- [57] D.M. Roberge, L. Ducry, N. Bieler, P. Cretton, B. Zimmermann, *Microreactor Technology: A Revolution for the Fine Chemical and Pharmaceutical Industries?*, *Chem. Eng. Technol.*, 28 (2005) 318-323.
- [58] J. Bucko, M. Mayer, W. Benzinger, W. Augustin, S. Scholl, R. Dittmeyer, Untersuchungen zum Kristallisationsfouling in Mikrowärmeübertragern
Investigation on Crystallization Fouling in Micro Heat Exchanger, *Chemie Ingenieur Technik*, 84 (2012) 491-502.
- [59] U. Krtschil, V. Hessel, D. Kralisch, G. Kreisel, nther, M. pper, R. Schenk, Cost Analysis of a Commercial Manufacturing Process of a Fine Chemical Compound Using Micro Process Engineering, *CHIMIA International Journal for Chemistry*, 60 (2006) 611-617.
- [60] T. Iwasaki, N. Kawano, J.-i. Yoshida, Radical Polymerization Using Microflow System: Numbering-up of Microreactors and Continuous Operation, *Organic Process Research & Development*, 10 (2006) 1126-1131.

References

- [61] M. Saber, J.M. Commenge, L. Falk, Microreactor numbering-up in multi-scale networks for industrial-scale applications: Impact of flow maldistribution on the reactor performances, *Chem Eng Sci*, 65 (2010) 372-379.
- [62] T. Van Gerven, A. Stankiewicz, Structure, Energy, Synergy, Time -The Fundamentals of Process Intensification, *Ind. Eng. Chem. Res.*, 48 (2009) 2465-2474.
- [63] E.V. Rebrov, J.C. Schouten, M.H.J.M. de Croon, Single-phase fluid flow distribution and heat transfer in microstructured reactors, *Chem. Eng. Sci.*, 66 (2011) 1374-1393.
- [64] N. de Mas, A. Günther, T. Kraus, M.A. Schmidt, K.F. Jensen, Scaled-Out Multilayer Gas-Liquid Microreactor with Integrated Velocimetry Sensors, *Ind. Eng. Chem. Res.*, 44 (2005) 8997-9013.
- [65] M. Al-Rawashdeh, F. Yu, T.A. Nijhuis, E.V. Rebrov, V. Hessel, J.C. Schouten, Numbered-up gas-liquid micro/milli channels reactor with modular flow distributor, *Chem. Eng. J.*, 207-208 (2012) 645-655.
- [66] M.m. Al-Rawashdeh, X. Nijhuis, E.V. Rebrov, V. Hessel, J.C. Schouten, Design methodology for barrier-based two phase flow distributor, *AIChE Journal*, 58 (2012) 3482-3493.
- [67] N. Kockmann, D.M. Roberge, Scale-up concept for modular microstructured reactors based on mixing, heat transfer, and reactor safety, *Chemical Engineering and Processing: Process Intensification*, 50 (2011) 1017-1026.
- [68] M. Sommerfeld, S. Horender, Fluid Mechanics, in: *Ullmann's Encyclopedia of Industrial Chemistry*, Wiley-VCH Verlag GmbH & Co. KGaA, 2000.
- [69] M. Gad-el-Hak, The fluid mechanics of microdevices - The Freeman Scholar Lecture, *J. Fluids Eng.-Trans. ASME*, 121 (1999) 5-33.
- [70] S.G. Jennings, The mean free path in air, *Journal of Aerosol Science*, 19 (1988) 159-166.
- [71] P.W. Atkins, *Physical Chemistry*, 5th edition ed., Oxford University Press, Oxford, 1994.
- [72] W.a.H. Loose, S., Rheology of Dense Fluids via Nonequilibrium Molecular Hydrodynamics: Shear Thinning and Ordering Transition, *Rheologica Acta*, 28 (1989) 91-101.
- [73] V. Hessel, A. Renken, J.C. Schouten, J. Yoshida, *Micro Process Engineering WILEY-VCH*, 1 (2009).
- [74] H.H. Bau, Transport Processes Associated with Micro-Devices, *Thermal Science and Engineering*, 2 (1994) 172-178.
- [75] J. Pfahler, Harley, J., Bau, H., and Zemel, J.N., Gas and Liquid Flow in Small Channels, *Symposium on Micromechanical Sensors, Actuators, and Systems, ASME DSC-Vol. 32* (1991) 49-60.
- [76] J. Pfahler, J. Harley, H. Bau, J. Zemel, Liquid transport in micron and submicron channels, *Sensors and Actuators A: Physical*, 22 (1989) 431-434.
- [77] Z. Guo, Z. Li, Size effect on microscale single-phase flow and heat transfer, *Int. J. Heat Mass Transfer*, 46 (2003) 149.
- [78] Z.-Y. Guo, Z.-X. Li, Size effect on single-phase channel flow and heat transfer at microscale, *International Journal of Heat and Fluid Flow*, 24 (2003) 284-298.
- [79] H. Herwig, O. Hausner, Critical view on "new results in micro-fluid mechanics": an example, *International Journal of Heat and Mass Transfer*, 46 (2003) 935-937.
- [80] G.L. Morini, Scaling effects for liquid flows in microchannels, *Heat Transf. Eng.*, 27 (2006) 64-73.
- [81] W.M. Kays, Crawford, M. E, Weigand, B., *Laminar Flow Forced Convection in Ducts: a source Book for Compact Heat Exchanger Analytical Data*, in, McGraw-Hill Higher Education, Boston, 2005.
- [82] R.K. Shah, A.L. London, F.M. White, *Laminar Flow Forced Convection in Ducts*, *Journal of Fluids Engineering*, 102 (1980) 256-257.
- [83] *CRC Handbook of Chemistry and Physics*, 60th ed., CRC Press, Inc., Florida, 1980.

-
- [84] K.S.a.H. Drese, S., Characterization of micro heat exchangers, in *MicroTec2000: World Microtechnologies Congress, Topical Conference Preprints*, VDE Verlag, Berlin, 2000.
- [85] S. Hardt, W. Ehrfeld, V. Hessel, K.M.V. Bussche, Strategies for size reduction of microreactors by heat transfer enhancement effects, *Chemical Engineering Communications*, 190 (2003) 540 - 559.
- [86] T. Stief, O.-U. Langer, K. Schubert, Numerical Investigations of Optimal Heat Conductivity in Micro Heat Exchangers, *Chem. Eng. Technol.*, 22 (1999) 297-303.
- [87] D.G. Norton, E.D. Wetzel, D.G. Vlachos, Thermal Management in Catalytic Microreactors, *Ind. Eng. Chem. Res.*, 45 (2005) 76-84.
- [88] C. Horny, A. Renken, L. Kiwi-Minsker, Compact string reactor for autothermal hydrogen production, *Catalysis Today*, 120 (2007) 45-53.
- [89] B. Xu, K.T. Ooi, C. Mavriplis, M.E. Zaghoul, Viscous Dissipation Effects For Liquid Flow In Microchannels, *Technical Proceedings of the 2002 International Conference on Modeling and Simulation of Microsystems*, 1 (2002).
- [90] G.P. Celata, G.L. Morini, V. Marconi, S.J. McPhail, G. Zummo, Using viscous heating to determine the friction factor in microchannels - An experimental validation, *Exp. Therm. Fluid Sci.*, 30 (2006) 725-731.
- [91] J. Koo, C. Kleinstreuer, Liquid flow in microchannels: experimental observations and computational analyses of microfluidics effects, *J. Micromech. Microeng.*, 13 (2003) 568.
- [92] Z.G. Liu, C.W. Zhang, X.B. Zhao, Experimental study on influence of microscale effects on liquid flow characteristic in microtubes, *Heat Mass Transf.*, 45 (2009) 297-304.
- [93] E.A. Mansur, M. Ye, Y. Wang, Y. Dai, A State-of-the-Art Review of Mixing in Microfluidic Mixers, *Chinese Journal of Chemical Engineering*, 16 (2008) 503-516.
- [94] G.L. Morini, Viscous heating in liquid flows in micro-channels, *International Journal of Heat and Mass Transfer*, 48 (2005) 3637-3647.
- [95] G.L. Morini, M. Spiga, The role of the viscous dissipation in heated microchannels, *J. Heat Transf.-Trans. ASME*, 129 (2007) 308-318.
- [96] G. Mohiuddin Mala, D. Li, J.D. Dale, Heat transfer and fluid flow in microchannels, *International Journal of Heat and Mass Transfer*, 40 (1997) 3079-3088.
- [97] C. Yang, D. Li, J.H. Masliyah, Modeling forced liquid convection in rectangular microchannels with electrokinetic effects, *International Journal of Heat and Mass Transfer*, 41 (1998) 4229-4249.
- [98] O. Levenspiel, *Chemical Reaction Engineering*, 3rd ed., 1999.
- [99] D. Boskovic, S. Loebbecke, Modelling of the residence time distribution in micromixers, *Chem. Eng. J.*, 135 (2008) S138-S146.
- [100] J. Aubin, L. Prat, C. Xuereb, C. Gourdon, Effect of microchannel aspect ratio on residence time distributions and the axial dispersion coefficient, *Chemical Engineering and Processing: Process Intensification*, 48 (2009) 554-559.
- [101] A. Rouge, B. Spoetzl, K. Gebauer, R. Schenk, A. Renken, Microchannel reactors for fast periodic operation: the catalytic dehydration of isopropanol, *Chem Eng Sci*, 56 (2001) 1419-1427.
- [102] R. Aris, On the dispersion of a solute in a fluid flowing through a tube, *Proc. Roy. Soc. London A*, 235 (1956) 67-77.
- [103] G.I. Taylor, Dispersion of soluble matter in solvent flowing slowly through a tube, *Proc. Roy. Soc. A.*, 219 (1953) 186-203.
- [104] T.H. Chilton, A.P. Colburn, Mass Transfer (Absorption) Coefficients Prediction from Data on Heat Transfer and Fluid Friction, *Ind. Eng. Chem.*, 26 (1934) 1183-1187.
- [105] F. Trachsel, A. Günther, S. Khan, K.F. Jensen, Measurement of residence time distribution in microfluidic systems, *Chem Eng Sci*, 60 (2005) 5729-5737.
-

References

- [106] S. Lohse, B.T. Kohnen, D. Janasek, P.S. Dittrich, J. Franzke, D.W. Agar, A novel method for determining residence time distribution in intricately structured microreactors, *Lab Chip*, 8 (2008) 431-438.
- [107] J.T. Adeosun, A. Lawal, Numerical and experimental studies of mixing characteristics in a T-junction microchannel using residence-time distribution, *Chem Eng Sci*, 64 (2009) 2422-2432.
- [108] S. Kuhn, R.L. Hartman, M. Sultana, K.D. Nagy, S. Marre, K.F. Jensen, Teflon-Coated Silicon Microreactors: Impact on Segmented Liquid-Liquid Multiphase Flows, *Langmuir*, 27 (2011) 6519-6527.
- [109] D. Bošković, S. Loebbecke, G.A. Gross, J.M. Koehler, Residence Time Distribution Studies in Microfluidic Mixing Structures, *Chem. Eng. Technol.*, 34 (2011) 361-370.
- [110] A. Cantu-Perez, S. Barrass, A. Gavriilidis, Residence time distributions in microchannels: Comparison between channels with herringbone structures and a rectangular channel, *Chem. Eng. J.*, 160 (2010) 834-844.
- [111] D.G. Norton, D.G. Vlachos, A CFD study of propane/air microflame stability, *Combustion and Flame*, 138 (2004) 97-107.
- [112] M. Baerns, A. Renken, *Chemische Reaktionstechnik*, in Winnacker-küchler: *Chemische Technik: Prozesse und Produkte*, Wiley-VCH, Weinheim, 2004.
- [113] K.-H. Grote, Feldhusen, J., *Dubbel - Taschenbuch für den Maschinenbau*, 21st ed., Springer Berlin Heidelberg New York, Berlin, 2005.
- [114] O. Klais, F. Westphal, W. Benaïssa, D. Carson, Guidance on Safety/Health for Process Intensification including MS Design; Part I: Reaction Hazards, *Chem. Eng. Technol.*, 32 (2009) 1831-1844.
- [115] J. Fischer, C. Liebner, H. Hieronymus, E. Klemm, Maximum safe diameters of microcapillaries for a stoichiometric ethene/oxygen mixture, *Chem Eng Sci*, 64 (2009) 2951-2956.
- [116] S. Chattopadhyay, G. Vesper, Heterogeneous-homogeneous interactions in catalytic microchannel reactors, *AIChE Journal*, 52 (2006) 2217-2229.
- [117] A. Leclerc, M. Alame, D. Schweich, P. Pouteau, C. Delattre, C. de Bellefon, Gas-liquid selective oxidations with oxygen under explosive conditions in a micro-structured reactor, *Lab Chip*, 8 (2008) 814-817.
- [118] J.C. EtcHELLS, Process Intensification: Safety Pros and Cons, *Process Safety and Environmental Protection*, 83 (2005) 85-89.
- [119] C.H. Barkelew, Stability of chemical reactors, *AIChE symposium series*, 55 (1959) 38-46.
- [120] N. Semenoff, Zur Theorie des Verbrennungsprozesses, *Zeitschrift für Physik A Hadrons and Nuclei*, 48 (1928) 571-582.
- [121] N. Semenoff, Some problems of Chemical Kinetics and Reactivity, in, London: Pergamon, 1959.
- [122] A. Varma, Morbidelli, M., Wu, H., *Parametric Sensitivity in Chemical Systems*, Cambridge University Press, New-York, 1999.
- [123] D.A. Frank-Kamenetskii, Raspredelenie temperatur v reaktsionnom sosude i stacionarnaya teoriya teplovogo vzry va, *Zh. Fiz. Khim.*, 13 (1939) 738.
- [124] A. Renken, L. Kiwi-Minsker, Chemical reactions in continuous flow micro-structured reactors, in: N. Kockmann (Ed.) *Micro Process Engineering*, Wiley-VCH, Weinheim, 2006, pp. 173-201.
- [125] M. Kashid, A. Renken, L. Kiwi-Minsker, *Microstructured Devices for Chemical Processing*, Wiley-VCH Verlag GmbH & Co. KGaA, 2013.
- [126] O. Klais, F. Westphal, W. Benaïssa, D. Carson, J. Albrecht, Guidance on Safety/Health for Process Intensification Including MS Design. Part III: Risk Analysis, *Chem. Eng. Technol.*, 33 (2010) 444-454.
- [127] J. Baldyga, J.R. Bourne, S.J. Hearn, Interaction between chemical reactions and mixing on various scales, *Chem Eng Sci*, 52 (1997) 457-466.

- [128] M.N. Kashid, A. Renken, L. Kiwi-Minsker, *Microstructured Devices for Chemical Processing*, Wiley-VCH Verlag GmbH, 2013.
- [129] V. Kumar, M. Paraschivoiu, K.D.P. Nigam, Single-phase fluid flow and mixing in microchannels, *Chem Eng Sci*, 66 (2011) 1329-1373.
- [130] R.H. Liu, R. Lenigk, R.L. Druyor-Sanchez, J. Yang, P. Grodzinski, Hybridization Enhancement Using Cavitation Microstreaming, *Analytical Chemistry*, 75 (2003) 1911-1917.
- [131] R.H. Liu, J. Yang, M.Z. Pindera, M. Athavale, P. Grodzinski, Bubble-induced acoustic micromixing, *Lab Chip*, 2 (2002) 151-157.
- [132] W.K. Tseng, J.L. Lin, W.C. Sung, S.H. Chen, G.B. Lee, Active micro-mixers using surface acoustic waves on Y-cut 128 degrees LiNbO₃, *Journal of Micromechanics and Microengineering*, 16 (2006) 539-548.
- [133] M.Z. Huang, R.J. Yang, C.H. Tai, C.H. Tsai, L.M. Fu, Application of electrokinetic instability flow for enhanced micromixing in cross-shaped microchannel, *Biomed. Microdevices*, 8 (2006) 309-315.
- [134] M.H. Oddy, J.G. Santiago, J.C. Mikkelsen, Electrokinetic instability micromixing, *Analytical Chemistry*, 73 (2001) 5822-5832.
- [135] Z.M. Wu, D.Q. Li, Micromixing using induced-charge electrokinetic flow, *Electrochim. Acta*, 53 (2008) 5827-5835.
- [136] A. Rida, M.A.M. Gijs, Manipulation of Self-Assembled Structures of Magnetic Beads for Microfluidic Mixing and Assaying, *Analytical Chemistry*, 76 (2004) 6239-6246.
- [137] Y. Wang, J. Zhe, B. Chung, P. Dutta, A rapid magnetic particle driven micromixer, *Microfluidics and Nanofluidics*, 4 (2008) 375-389.
- [138] Z.-H. Wei, C.-P. Lee, Magnetic fluid micromixer with tapered magnets, *Journal of Applied Physics*, 105 (2009) 07B523-507B523-523.
- [139] L.H. Lu, K.S. Ryu, C. Liu, A magnetic microstirrer and array for microfluidic mixing, *J. Microelectromech. Syst.*, 11 (2002) 462-469.
- [140] G.A. Mensing, T.M. Pearce, M.D. Graham, D.J. Beebe, An externally driven magnetic microstirrer, *Philos. Trans. R. Soc. Lond. Ser. A-Math. Phys. Eng. Sci.*, 362 (2004) 1059-1068.
- [141] M. Engler, N. Kockmann, T. Kiefer, P. Woias, Numerical and experimental investigations on liquid mixing in static micromixers, *Chem. Eng. J.*, 101 (2004) 315-322.
- [142] M. Kashid, A. Renken, L. Kiwi-Minsker, Mixing efficiency and energy consumption for five generic microchannel designs, *Chem. Eng. J.*, 167 (2011) 436-443.
- [143] D. Bothe, C. Stemich, H.-J. Warnecke, Fluid mixing in a T-shaped micro-mixer, *Chem Eng Sci*, 61 (2006) 2950-2958.
- [144] S.H. Wong, M.C.L. Ward, C.W. Wharton, Micro T-mixer as a rapid mixing micromixer, *Sensors and Actuators B: Chemical*, 100 (2004) 359-379.
- [145] M. Hoffmann, M. Schlüter, N. Rübiger, Experimental investigation of liquid-liquid mixing in T-shaped micro-mixers using μ -LIF and μ -PIV, *Chem Eng Sci*, 61 (2006) 2968-2976.
- [146] A. Soleymani, H. Yousefi, I. Turunen, Dimensionless number for identification of flow patterns inside a T-micromixer, *Chem Eng Sci*, 63 (2008) 5291-5297.
- [147] A. Soleymani, E. Kolehmainen, I. Turunen, Numerical and experimental investigations of liquid mixing in T-type micromixers, *Chem. Eng. J.*, 135, Supplement 1 (2008) S219-S228.
- [148] M.A. Ansari, K.-Y. Kim, K. Anwar, S.M. Kim, Vortex micro T-mixer with non-aligned inputs, *Chem. Eng. J.*, 181-182 (2012) 846-850.
- [149] www.mathworks.com; Accessed: 2013
- [150] F. Jiang, K.S. Drese, S. Hardt, M. Küpper, F. Schönfeld, Helical flows and chaotic mixing in curved micro channels, *AIChE Journal*, 50 (2004) 2297-2305.

References

- [151] F. Schönfeld, S. Hardt, Simulation of helical flows in microchannels, *AIChE Journal*, 50 (2004) 771-778.
- [152] V. Mengeaud, J. Josserand, H.H. Girault, Mixing Processes in a Zigzag Microchannel: Finite Element Simulations and Optical Study, *Analytical Chemistry*, 74 (2002) 4279-4286.
- [153] R. Choudhary, T. Bhakat, R.K. Singh, A. Ghubade, S. Mandal, A. Ghosh, A. Rammohan, A. Sharma, S. Bhattacharya, Bilayer staggered herringbone micro-mixers with symmetric and asymmetric geometries, *Microfluidics and Nanofluidics*, 10 (2011) 271-286.
- [154] S. Hossain, A. Husain, K.Y. Kim, Shape optimization of a micromixer with staggered-herringbone grooves patterned on opposite walls, *Chem. Eng. J.*, 162 (2010) 730-737.
- [155] S.P. Kee, A. Gavriilidis, Design and characterisation of the staggered herringbone mixer, *Chem. Eng. J.*, 142 (2008) 109-121.
- [156] M.S. Williams, K.J. Longmuir, P. Yager, A practical guide to the staggered herringbone mixer, *Lab Chip*, 8 (2008) 1121-1129.
- [157] J. Aubin, D.F. Fletcher, C. Xuereb, Design of micromixers using CFD modelling, *Chem Eng Sci*, 60 (2005) 2503-2516.
- [158] I. Glasgow, N. Aubry, Enhancement of microfluidic mixing using time pulsing, *Lab Chip*, 3 (2003) 114-120.
- [159] L. Ducry, D.M. Roberge, Dibal-H reduction of methyl butyrate into butyraldehyde using microreactors, *Organic Process Research and Development*, 12 (2008) 163-167.
- [160] L. Falk, J.M. Commenge, Performance comparison of micromixers, *Chem Eng Sci*, 65 (2010) 405-411.
- [161] J. Villiermaux, Micromixing phenomena in stirred reactors, in: *Encyclopedia Fluid Mech.*, Gulf Publishing Company, Houston, TX, 1986.
- [162] J. Baldyga, J.R. Bourne, Mixing and fast chemical reaction-VIII: Initial deformation of material elements in isotropic, homogeneous turbulence, *Chem Eng Sci*, 39 (1984) 329-334.
- [163] J. Baldyga, A. Rozen, F. Mostert, A model of laminar micromixing with application to parallel chemical reactions, *Chem. Eng. J.*, 69 (1998) 7-20.
- [164] C. Guinand, Temperature management of very fast and exothermic reactions in Microstructured Reactors, in: *GGRC, EPFL, Lausanne*, 2011.
- [165] M.a.A.R. Baerns, *Chemische Reaktionstechnik*, in: *Winnacker-Küchler: Chemische Technik: Prozesse und Produkte*, Wiley-VCH, Weinheim, 2004, pp. 453-643.
- [166] D.W. Flick, M.C. Huff, Oxidative dehydrogenation of ethane over a Pt-coated monolith versus Pt-loaded pellets: Surface area and thermal effects, *Journal of Catalysis*, 178 (1998) 315-327.
- [167] O. Klais, J. Albrecht, D. Carson, M. Kraut, P. Lö, C. Minnich, F. Olschewski, C. Reimers, A. Simoncelli, M. Uerdingen, Guidance on Safety/Health for Process Intensification Including MS Design. Part IV: Case Studies, *Chem. Eng. Technol.*, 33 (2010) 1159-1168.
- [168] O. Klais, F. Westphal, W. Benaissa, D. Carson, Guidance on Safety/Health for Process Intensification including MS Design; Part II: Explosion Hazards, *Chem. Eng. Technol.*, 32 (2009) 1966-1973.
- [169] C.H. Bartholomew, Mechanisms of catalyst deactivation, *Applied Catalysis A: General*, 212 (2001) 17-60.
- [170] P. Barthe, C. Guerneur, O. Lobet, M. Moreno, P. Woehl, D.M. Roberge, N. Bieler, B. Zimmermann, Continuous Multi-Injection Reactor for Multipurpose Production – Part I, *Chem. Eng. Technol.*, 31 (2008) 1146-1154.

- [171] D.M. Roberge, N. Bieler, M. Mathier, M. Eyholzer, B. Zimmermann, P. Barthe, C. Guerneur, O. Lobet, M. Moreno, P. Woehl, Development of an industrial multi-injection microreactor for fast and exothermic reactions - Part II, *Chem. Eng. Technol.*, 31 (2008) 1155-1161.
- [172] Z. Anxionnaz, M. Cabassud, C. Gourdon, R. Tochon, Heat exchanger/reactors (HEX reactors): Concepts, technologies: State-of-the-art, *Chem. Eng. Process.*, 47 (2008) 2029-2050.
- [173] www.upchurch.com/; Accessed: 2013
- [174] <http://www.swagelok.com/>; Accessed: 2013
- [175] R. Krishna, S.T. Sie, Strategies for multiphase reactor selection, *Chem Eng Sci*, 49 (1994) 4029-4065.
- [176] A. Julbe, D. Farrusseng, C. Guizard, Porous ceramic membranes for catalytic reactors — overview and new ideas, *J Membrane Sci*, 181 (2001) 3-20.
- [177] S. Thomas, S. Pushpavanam, A. Seidel-Morgenstern, Performance Improvements of Parallel-Series Reactions in Tubular Reactors Using Reactant Dosing Concepts, *Ind. Eng. Chem. Res.*, 43 (2004) 969-979.
- [178] H. Hausen, *Allgemeine Wärmetechnik* 9, 1959.
- [179] D. Gilbarg, N.S. Trudinger, *Partial Differential Equations of Second Order*, Springer-Verlag, Berlin, 1998.
- [180] A. Große Böwing, A. Jess, Kinetics and reactor design aspects of the synthesis of ionic liquids-- Experimental and theoretical studies for ethylmethylimidazole ethylsulfate, *Chem Eng Sci*, 62 (2007) 1760-1769.
- [181] H.D. Young, *University Physics*, 7th ed., Addison Wesley, 1992.
- [182] J.N. Sweet, E.P. Roth, M. Moss, Thermal conductivity of Inconel 718 and 304 stainless steel, *Int J Thermophys*, 8 (1987) 593-606.
- [183] M.J. Stutz, D. Poulikakos, Effects of microreactor wall heat conduction on the reforming process of methane, *Chem Eng Sci*, 60 (2005) 6983-6997.
- [184] R.J. Boersma, N.M. Sammes, Distribution of gas flow in internally manifolded solid oxide fuel-cell stacks, *J. Power Sources*, 66 (1997) 41-45.
- [185] J.M. Commenge, L. Falk, J.P. Corriou, M. Matlosz, Optimal design for flow uniformity in microchannel reactors, *AIChE Journal*, 48 (2002) 345-358.
- [186] M. Pan, Y. Tang, L. Pan, L. Lu, Optimal design of complex manifold geometries for uniform flow distribution between microchannels, *Chem. Eng. J.*, 137 (2008) 339-346.
- [187] M. Pan, Y. Tang, H. Yu, H. Chen, Modeling of velocity distribution among microchannels with triangle manifolds, *AIChE Journal*, 55 (2009) 1969-1982.
- [188] R. Fu, B. Xu, D. Li, Study of the Temperature Field in Microchannels of a PDMS Chip With Embedded Local Heater Using Temperature-Dependent Fluorescent Dye, *ASME Conference Proceedings*, 2005 (2005) 427-432.
- [189] D. Ross, M. Gaitan, L.E. Locascio, Temperature Measurement in Microfluidic Systems Using a Temperature-Dependent Fluorescent Dye, *Analytical Chemistry*, 73 (2001) 4117-4123.
- [190] A. Günther, P. Rudolf von Rohr, Structure of the temperature field in a flow over heated waves, *Experiments in Fluids*, 33 (2002) 920-930.
- [191] V.N. Hoang, G.V. Kaigala, C.J. Backhouse, Dynamic temperature measurement in microfluidic devices using thermochromic liquid crystals, *Lab Chip*, 8 (2008) 484-487.
- [192] A. Iles, R. Fortt, A.J. de Mello, Thermal optimisation of the Reimer-Tiemann reaction using thermochromic liquid crystals on a microfluidic reactor, *Lab Chip*, 5 (2005) 540-544.
- [193] M. Basson, T.S. Pottebaum, Measuring the temperature of fluid in a micro-channel using thermochromic liquid crystals, *Experiments in Fluids*, (2012) 1-12.

References

- [194] C.H. Fan, J.P. Longtin, Laser-based measurement of liquid temperature or concentration at a solid-liquid interface, *Exp. Therm. Fluid Sci.*, 23 (2000) 1-9.
- [195] K. Swinney, D.J. Bornhop, Noninvasive picoliter volume thermometry based on backscatter interferometry, *ELECTROPHORESIS*, 22 (2001) 2032-2036.
- [196] K.L. Davis, K.L.K. Liu, M. Lanan, M.D. Morris, Spatially resolved temperature measurements in electrophoresis capillaries by Raman thermometry, *Analytical Chemistry*, 65 (1993) 293-298.
- [197] S.H. Kim, J. Noh, M.K. Jeon, K.W. Kim, L.P. Lee, S.I. Woo, Micro-Raman thermometry for measuring the temperature distribution inside the microchannel of a polymerase chain reaction chip, *Journal of Micromechanics and Microengineering*, 16 (2006) 526-530.
- [198] M.E. Lacey, A.G. Webb, J.V. Sweedler, Monitoring temperature changes in capillary electrophoresis with nanoliter-volume NMR thermometry, *Analytical Chemistry*, 72 (2000) 4991-4998.
- [199] G. Yaralioglu, Ultrasonic heating and temperature measurement in microfluidic channels, *Sensors and Actuators A: Physical*, 170 (2011) 1-7.
- [200] G. Hetsroni, A. Mosyak, E. Pogrebnyak, R. Rozenblit, Infrared temperature measurements in microchannels and micro-fluid systems, *International Journal of Thermal Sciences*, 50 (2011) 853-868.
- [201] J. Barber, D. Brutin, K. Sefiane, J.L. Gardarein, L. Tadrist, Unsteady-state fluctuations analysis during bubble growth in a “rectangular” microchannel, *International Journal of Heat and Mass Transfer*, 54 (2011) 4784-4795.
- [202] J.L. Xu, Y.H. Gan, D.C. Zhang, X.H. Li, Microscale heat transfer enhancement using thermal boundary layer redeveloping concept, *International Journal of Heat and Mass Transfer*, 48 (2005) 1662-1674.
- [203] Y. Mishan, A. Mosyak, E. Pogrebnyak, G. Hetsroni, Effect of developing flow and thermal regime on momentum and heat transfer in micro-scale heat sink, *International Journal of Heat and Mass Transfer*, 50 (2007) 3100-3114.
- [204] J. Antes, D. Boskovic, H. Krause, S. Loebbecke, N. Lutz, T. Tuercke, W. Schweikert, Analysis and Improvement of Strong Exothermic Nitrations in Microreactors, *Chemical Engineering Research and Design*, 81 (2003) 760-765.
- [205] C. Pradere, C. Hany, J. Toutain, J.C. Batsale, Thermal analysis for velocity, kinetics, and enthalpy reaction measurements in microfluidic devices, *Experimental Heat Transfer*, 23 (2010) 44-62.
- [206] G.A. Bennett, S.D. Briles, Calibration procedure developed for IR surface-temperature measurements, *Components, Hybrids, and Manufacturing Technology*, *IEEE Transactions on*, 12 (1989) 690-695.
- [207] D.R. Joshi, *Engineering Physics*, Tata McGraw Hill Education Private Limited, Delhi, 2010.
- [208] Y.A. Çengel, *Heat and mass transfer: a practical approach*, Mcgraw Hill Higher Education, 2006.
- [209] M. Vollmer, K.-P. Möllmann, *Infrared Thermal Imaging*, Wiley-VCH, Weinheim, 2010.
- [210] N. Sahba, T.J. Rockett, Infrared Absorption Coefficients of Silica Glasses, *J. Am. Ceram. Soc.*, 75 (1992) 209-212.
- [211] D.P. De Witt, G.D. Nutter, *Theory and Practice of Radiation Thermometry*, John Wiley & Sons, Inc., New York.
- [212] J.M. Lloyd, *Thermal Imaging Systems (Optical Physics and Engineering)* 1975.
- [213] www.crystan.co.uk: Accessed: 2013
- [214] Infrared.als.lbl.gov/ ALS Synchrotron Infrared Beamlines Accessed:
- [215] V. Hessel, C. Hofmann, H. Löwe, A. Meudt, S. Scherer, F. Schönfeld, B. Werner, Selectivity Gains and Energy Savings for the Industrial Phenyl Boronic Acid Process Using Micromixer/Tubular Reactors, *Organic Process Research & Development*, 8 (2004) 511-523.

- [216] K. Sung-Ryong, K. Dae-Hoon, K. Dong-Ju, K. Min-Hyung, P. Joung-Man, Study on Thermal Conductivity of Polyetheretherketone/Thermally Conductive Filler Composites, *Solid State Phenomena*, 124-126 (2007) 1079-1082.
- [217] A.M. Bessarabov, B.Z. Shalumov, Kinetics of catalytic hydrolysis of tetraethoxysilane by polycomponent solutions of neutral salts, *Reaction Kinetics and Catalysis Letters*, 34 (1987) 29-34.
- [218] M. Isogai, T. Ito, T. Oonishi, T. Yamada, N. Yonekawa, Fixing device for image forming apparatus, in: *Patent Genius*, Japan, 1998.
- [219] J.P. Hartnett, M. Kostic, Heat Transfer to Newtonian and Non-Newtonian Fluids in Rectangular ducts, Academic Press. Inc., 1989.
- [220] A.M. Díez-Pascual, B. Ashrafi, M. Naffakh, J.M. González-Domínguez, A. Johnston, B. Simard, M.T. Martínez, M.A. Gómez-Fatou, Influence of carbon nanotubes on the thermal, electrical and mechanical properties of poly(ether ether ketone)/glass fiber laminates, *Carbon*, 49 (2011) 2817-2833.
- [221] D. Bothe, A. Lojewski, H.-J. Warnecke, Computational analysis of an instantaneous chemical reaction in a T-microreactor, *AIChE Journal*, 56 (2010) 1406-1415.
- [222] X. Shi, Y. Xiang, L.X. Wen, J.F. Chen, CFD analysis of flow patterns and micromixing efficiency in a Y-type microchannel reactor, *Ind. Eng. Chem. Res.*, 51 (2012) 13944-13952.
- [223] N. Kockmann, T. Kiefer, M. Engler, P. Woias, Convective mixing and chemical reactions in microchannels with high flow rates, *Sensors and Actuators B: Chemical*, 117 (2006) 495-508.
- [224] J. Aubin, M. Ferrando, V. Jiricny, Current methods for characterising mixing and flow in microchannels, *Chem Eng Sci*, 65 (2010) 2065-2093.
- [225] A.R. V. Hessel, J.C. Schouten and J. Yoshida, *Micro Process Engineering Volume 1*, WILEY-VCH, (2009).
- [226] F. Schönfeld, V. Hessel, C. Hofmann, An optimised split-and-recombine micro-mixer with uniform 'chaotic' mixing, *Lab Chip*, 4 (2004) 65-69.
- [227] S.W. Lee, D.S. Kim, S.S. Lee, T.H. Kwon, A split and recombination micromixer fabricated in a PDMS three-dimensional structure, *Journal of Micromechanics and Microengineering*, 16 (2006) 1067-1072.
- [228] V. Hessel, S. Hardt, H. Löwe, F. Schönfeld, Laminar mixing in different interdigital micromixers: I. Experimental characterization, *AIChE Journal*, 49 (2003) 566-577.
- [229] C.-P. Jen, C.-Y. Wu, Y.-C. Lin, C.-Y. Wu, Design and simulation of the micromixer with chaotic advection in twisted microchannels, *Lab Chip*, 3 (2003) 77-81.
- [230] M. Hoffmann, M. Schlüter, N. Rübiger, Experimental investigation of liquid-liquid mixing in T-shaped micro-mixers using -LIF and -PIV, *Chem Eng Sci*, 61 (2006) 2968-2976.
- [231] T.J. Johnson, D. Ross, L.E. Locascio, Rapid microfluidic mixing, *Analytical Chemistry*, 74 (2002) 45-51.
- [232] R.H. Liu, M.A. Stremmer, K.V. Sharp, M.G. Olsen, J.G. Santiago, R.J. Adrian, H. Aref, D.J. Beebe, Passive mixing in a three-dimensional serpentine microchannel, *Microelectromechanical Systems, Journal of*, 9 (2000) 190-197.
- [233] K. Dong Sung, L. In Hwan, K. Tai Hun, C. Dong-Woo, A barrier embedded Kenics micromixer, *Journal of Micromechanics and Microengineering*, 14 (2004) 1294.
- [234] J.-M. Commenge, L. Falk, Villermaux-Dushman protocol for experimental characterization of micromixers, *Chemical Engineering and Processing: Process Intensification*, 50 (2011) 979-990.
- [235] P. Guichardon, L. Falk, Characterisation of micromixing efficiency by the iodide-iodate reaction system. Part I: experimental procedure, *Chem Eng Sci*, 55 (2000) 4233-4243.
- [236] A. Kölbl, S. Schmidt-Lehr, The iodide iodate reaction method: The choice of the acid, *Chem Eng Sci*, 65 (2010) 1897-1901.

References

- [237] B.K. Johnson, R.K. Prud'homme, Chemical processing and micromixing in confined impinging jets, *AIChE Journal*, 49 (2003) 2264-2282.
- [238] S. Ehlers, K. Elgeti, T. Menzel, G. Wießmeier, Mixing in the offstream of a microchannel system, *Chemical Engineering and Processing: Process Intensification*, 39 (2000) 291-298.
- [239] A. Kölbl, M. Kraut, K. Schubert, The iodide iodate method to characterize microstructured mixing devices, *AIChE Journal*, 54 (2008) 639-645.
- [240] M. Kashid, O. Detraz, M.S. Moya, I. Yuranov, P. Prechtel, J. Membrez, A. Renken, L. Kiwi-Minsker, Micro-batch reactor for catching intermediates and monitoring kinetics of rapid and exothermic homogeneous reactions, *Chem. Eng. J.*, 214 (2013) 149-156.
- [241] M.N. Kashid, I. Yuranov, P. Raspail, P. Prechtel, J. Membrez, A. Renken, L. Kiwi-Minsker, Cyclization of Pseudoionone to β -Ionone: Reaction Mechanism and Kinetics, *Ind. Eng. Chem. Res.*, 50 (2011) 7920-7926.
- [242] B. Ahmed, D. Barrow, T. Wirth, Enhancement of Reaction Rates by Segmented Fluid Flow in Capillary Scale Reactors, *Adv Synth Catal*, 348 (2006) 1043-1048.
- [243] H. Müller, Sulfuric Acid and Sulfur Trioxide, in: *Ullmann's Encyclopedia of Industrial Chemistry*, Wiley-VCH Verlag GmbH & Co. KGaA, 2000.
- [244] A. Asthana, I. Zinovik, C. Weinmueller, D. Poulikakos, Significant Nusselt number increase in microchannels with a segmented flow of two immiscible liquids: An experimental study, *International Journal of Heat and Mass Transfer*, 54 (2011) 1456-1464.
- [245] A. Cybulski, J.A. Moulijn, Monoliths in Heterogeneous Catalysis, *Catal. Rev. - Sci. Eng.*, 36 (1994) 179-270.
- [246] D. Lakehal, G. Larrignon, C. Narayanan, Computational heat transfer and two-phase flow topology in miniature tubes, *Microfluidics and Nanofluidics*, 4 (2008) 261-271.
- [247] A.R. Betz, D. Attinger, Can segmented flow enhance heat transfer in microchannel heat sinks?, *International Journal of Heat and Mass Transfer*, 53 (2010) 3683-3691.
- [248] J. Haber, M.N. Kashid, N. Borhani, J. Thome, U. Krtschil, A. Renken, L. Kiwi-Minsker, Infrared imaging of temperature profiles in microreactors for fast and exothermic reactions, *Chem. Eng. J.*, 214 (2013) 97-105.
- [249] C.A. Wraight, Chance and design-Proton transfer in water, channels and bioenergetic proteins, *Biochimica et Biophysica Acta - Bioenergetics*, 1757 (2006) 886-912.
- [250] P. Cougnon, D. Dochain, M. Guay, M. Perrier, Real-time optimization of a tubular reactor with distributed feed, *AIChE Journal*, 52 (2006) 2120-2128.
- [251] Y. Lu, A.G. Dixon, W.R. Moser, Y.H. Ma, Analysis and optimization of cross-flow reactors with distributed reactant feed and product removal, *Catalysis Today*, 35 (1997) 443-450.
- [252] M. Baerns, A. Behr, A. Brehm, J. Gmehling, H. Hofmann, U. Onken, A. Renken, *Technische Chemie*, 4 Edition ed., Wiley-VCH, Weinheim, Germany, 2006.
- [253] E.E. Royals, Cyclization of Pseudoionone by Acidic Reagents, *Ind. Eng. Chem.*, 38 (1946) 546-548.
- [254] M.A. Kharshan, A.A. Kron, I.S. Aulchenko, Method of producing ionone or homologs thereof, S.U. Patent 695,164, (1986).
- [255] A.V. Panfilov, D. Markovich Yu, A.A. Zhirov, L.A. Gorbach, A.T. Kirsanov, V.N. Ionin, D.V. Davydovich, Method of beta-ionone synthesis, R.U. Patent 2,075,473, (1997).
- [256] O. Hertel, H. Kiefer, L. Arnold, Preparation of ionones, U.S. Patent 4,565,894, (1986).
- [257] U. Rheude, U. Horcher, D. Weller, M. Stroezel, Process for preparing ionones, U.S. Patent 6,288,282, (2000).
- [258] A.V. Semenovskii, V.A. Smith, V.F. Kucherov, The Mechanism of Pseudoionone Cyclization, *Dokl. Akad. Nauk. SSSR*, 132 (1960) 1107-1107.

- [259] V.A. Smith, A.V. Semenovskii, V.M. Medvedeva, V.F. Kucherov, On Pseudoionone Cyclization - A New Method of Alpha-Ionone Production for Pseudoionone Cyclization, *Dokl. Akad. Nauk. SSSR+*, 124 (1959).
- [260] H. Birol, Fabrication of low temperature co-fired ceramic (LTCC)-based sensor and micro-fluidic structures, EPFL, Lausanne, 2007.
- [261] B. Jiang, T. Maeder, P. Muralt, A new platform concept for micro-scale SOFC using low temperature co-fired ceramic technology, in: *PowerMEMS 2010, 10th International Workshop on Micro and Nanotechnology for Power Generation and Energy Conversion Applications*, Leuven, Belgium, 2010.
- [262] M. Eberstein, W.A. Schiller, Development of high-permittivity glasses for microwave LTCC tapes, *Deutsche Glastechnische Gesellschaft*, Frankfurt, 2003.
- [263] M. Valant, D. Suvorov, Chemical Compatibility between Silver Electrodes and Low-Firing Binary-Oxide Compounds: Conceptual Study, *J. Am. Ceram. Soc.*, 83 (2000) 2721-2729.
- [264] L.J. Golonka, Technology and applications of Low Temperature Cofired Ceramic (LTCC) based sensors and microsystems, *Bulletin of the Polish Academy of Sciences: Technical Sciences*, 54 (2006) 221-231.
- [265] L.J. Golonka, H. Roguszczak, T. Zawada, J. Radojewski, I. Grabowska, M. Chudy, A. Dybko, Z. Brzozka, D. Stadnik, LTCC based microfluidic system with optical detection, *Sens. Actuators, B*, 111-112 (2005) 396-402.
- [266] L.J. Golonka, T. Zawada, J. Radojewski, H. Roguszczak, M. Stefanow, LTCC microfluidic system, *Int. J. Appl. Ceram. Technol.*, 3 (2006) 150-156.
- [267] G.A. Groß, T. Thelemann, S. Schneider, D. Boskovic, J.M. Köhler, Fabrication and fluidic characterization of static micromixers made of low temperature cofired ceramic (LTCC), *Chem Eng Sci*, 63 (2008) 2773-2784.
- [268] B. Smith, M. Pleskach, C. Gamlen, Microfluidics for thermal management: Applications, fabrication, and demonstration in LTCC, in, 2003, pp. 217-222.
- [269] B. Jiang, J. Haber, L. Kiwi-Minsker, P. Muralt, A. Renken, T. Maeder, Fine structuration of LTCC and its application to the microreactor engineering, in preparation.
- [270] T. Thelemann, M. Fischer, A. Groß, J. Müller, LTCC-based fluidic components for chemical applications, *Journal of Microelectronics and Electronic Packaging*, 4 (2007) 167-172.
- [271] W. Zhang, R.E. Eitel, Biostability of low-temperature co-fired ceramic materials for microfluidic and biomedical devices, *Int. J. Appl. Ceram. Technol.*, 9 (2012) 60-66.
- [272] R. German, P. Suri, S. Park, Review: liquid phase sintering, *J Mater Sci*, 44 (2009) 1-39.
- [273] <http://www2.dupont.com/home/en-us/index.html>; Accessed: 2013
- [274] F. Gharagheizi, Determination of Diffusion Coefficient of Organic Compounds in Water Using a Simple Molecular-Based Method, *Ind. Eng. Chem. Res.*, 51 (2012) 2797-2803.
- [275] C.P. Holvey, D.M. Roberge, M. Gottsponer, N. Kockmann, A. Macchi, Pressure drop and mixing in single phase microreactors: Simplified designs of micromixers, *Chemical Engineering and Processing: Process Intensification*, 50 (2011) 1069-1075.
- [276] J. Lee, S. Kwon, Mixing efficiency of a multilamination micromixer with consecutive recirculation zones, *Chem Eng Sci*, 64 (2009) 1223-1231.
- [277] A.D. Stroock, S.K.W. Dertinger, A. Ajdari, I. Mezić, H.A. Stone, G.M. Whitesides, Chaotic Mixer for Microchannels, *Science*, 295 (2002) 647-651.

CURRICULUM VITAE

EDUCATION

- 01/2010 - 07/2013 Ph.D. in the Group of Catalytic Reaction Engineering,
École Polytechnique Fédérale de Lausanne, Switzerland
- 02/2007 - 11/2009 Master degree (Diplom) in Process Engineering at University of Bayreuth,
Germany
Overall grade: 1.1 « With Distinction »
- 10/2004 - 02/2007 Bachelor degree (Vordiplom) in Process Engineering at University of
Bayreuth, Germany
Overall grade: 1.7 « Very Good »
- 09/1997- 07/2004 Baccalaureat at “Lycée des Garçons Luxembourg”, Luxembourg
Overall grade: « Very Good »

PROFESSIONAL EXPERIENCE

- 01/2010 – 08/2013 Research Assistant in the Group of Catalytic Reaction Engineering, École
Polytechnique Fédérale de Lausanne, Switzerland
- 10/2007-03/2008 Internship in a photovoltaic production plant (Gällivare Photovoltaic AB),
Gällivare, Sweden
Responsibilities:
- ◆ *Detection and elimination of bottlenecks in the production of solar panels*
 - ◆ *Quality control of the chemical resistance of sealing material*
- 11/2006-07/2007 Student assistant at Department of Measurement and Control Technologies
Bayreuth, Germany

Responsibilities:

- ◆ *Participation in the development of a surface acoustic wave device and supervision of students*

08/2004-09/2004

Internship at a waste-management company (IDELUX), Habay, Belgium

Responsibilities:

- ◆ *Monitoring waste water quality and testing novel methods of purification*

PROJECTS

PhD Project: *Heat Management for Process Intensification of Fast Exothermic Reactions in Microstructured Reactors*

- ◆ Aim: To enhance temperature control during chemical reaction to increase product quality
- ◆ Design and construction of Microstructured Reactors in a collaboration, finding the best compromise between necessity and feasibility
- ◆ Development of a method to quantitatively measure temperature inside microchannels
- ◆ Supervision of students and teaching in courses of Prof. Kiwi and Prof. Renken.

Master Project: *Thermogravimetric Analysis on the vapor pressure and the thermal decomposition of pure and water containing Ionic liquids.*

- ◆ Aim: To describe the kinetics of evaporation and decomposition of Ionic liquids.

LANGUAGES

<u>French</u>	<i>Mother tongue</i>	<u>Luxembourgish</u>	<i>Fluent</i>
<u>German</u>	<i>Mother tongue</i>	<u>Russian</u>	<i>Level A2</i>
<u>English</u>	<i>Fluent</i>		

EXTRA CURRICULAR ACTIVITES

Hobbies Ultimate Frisbee (Player & Coach), Generally Sports, Fishing

Part of Organizing Chemical Engineering Day 2010 & 2011

Committee Several Ultimate Frisbee Tournaments (up to 100 people)

LIST OF PUBLICATIONS

J. Haber, M.N. Kashid, N. Borhani, J. Thome, U. Krtshil, A. Renken, L. Kiwi-Minsker, Infrared imaging of temperature profiles in microreactors for fast and exothermic reactions, *Chemical Engineering Journal*, 214 (2013) 97-105.

J. Haber, B. Jiang, T. Maeder, A. Renken, L. Kiwi-Minsker, Multi-injection Microstructured Reactor for Intensification of Fast Exothermic Reactions: Proof of Concept, *Green Processing & Synthesis*, submitted (2013)

J. Haber, B. Jiang, T. Maeder, N. Borhani, J. Thome, A. Renken, L. Kiwi-Minsker, Heat Management for Process Intensification of the Cyclisation of Pseudoionone in a Multi-injection Microstructured Reactor, *Chemical Engineering and Processing: Process Intensification*, in preparation (2013)

B. Jiang, J. Haber, L. Kiwi-Minsker, P. Muralt, A. Renken, T. Maeder, Fine structuration of LTCC and its application to the microreactor engineering, in preparation (2013)

R. Turco, J. Haber, I. Yuranov, V. Russo, E. Santacesaria, L. Kiwi-Minsker, Sintered Metal Fibers Coated with Transition Metals as Catalysts for Hydrogen Peroxide Decomposition, *Chemical Engineering and Processing: Process Intensification*, submitted (2013)

J. Haber, M.N. Kashid, A. Renken, L. Kiwi-Minsker, Heat management in single and multi-injection microstructured reactors: Scaling effects, stability analysis, and role of mixing, *Industrial and Engineering Chemistry Research*, 51 (2012) 1474-1489.

F. Heym, J. Haber, W. Korth, B.J.M. Etzold, A. Jess, Vapor Pressure of Water in Mixtures with Hydrophilic Ionic Liquids – A Contribution to the Design of Processes for Drying of Gases by Absorption in Ionic Liquids, *Chemical Engineering & Technology*, 33 (2010) 1625-1634.

LIST OF PRESENTATIONS

9th European Congress of Chemical Engineering, April 21-25, 2013, Den Haag, The Netherlands: *Oral presentation*

Swiss Chemical Society – 2012 Fall Meeting, September 13, 2012, Zürich, Switzerland

22nd International Symposium on Chemical Reaction Engineering, September 2-5, 2012, Maastricht, The Netherlands: *Oral presentation*

12th International Conferences on Microreaction Technology, February 20-22, 2012, Lyon, France: *Oral presentation*

AWARDS

Award from the Chemistry and Chemical Engineering Section for outstanding teaching activities (2011).